

FOURTH QUARTER

DOE/BC/14875-13
(DE96001276)

RESEARCH PROGRAM ON FRACTURED PETROLEUM RESERVOIRS

Final Report

By
Dr. Abbas Firoozabadi

May 1997

RECEIVED
JUN 03 1997
OSTI

Performed Under Contract No. DE-FG22-93BC14875

Reservoir Engineering Research Institute
Palo Alto, California

MASTER

**National Petroleum Technology Office
U. S. DEPARTMENT OF ENERGY
Tulsa, Oklahoma**



DISTRIBUTION OF THIS DOCUMENT IS UNLIMITED

ng

DISCLAIMER

This report was prepared as an account of work sponsored by an agency of the United States Government. Neither the United States Government nor any agency thereof, nor any of their employees, makes any warranty, expressed or implied, or assumes any legal liability or responsibility for the accuracy, completeness, or usefulness of any information, apparatus, product, or process disclosed, or represents that its use would not infringe privately owned rights. Reference herein to any specific commercial product, process, or service by trade name, trademark, manufacturer, or otherwise does not necessarily constitute or imply its endorsement, recommendation, or favoring by the United States Government or any agency thereof. The views and opinions of authors expressed herein do not necessarily state or reflect those of the United States Government.

This report has been reproduced directly from the best available copy.

Available to DOE and DOE contractors from the Office of Scientific and Technical Information, P.O. Box 62, Oak Ridge, TN 37831; prices available from (615) 576-8401.

Available to the public from the National Technical Information Service, U.S. Department of Commerce, 5285 Port Royal Rd., Springfield VA 22161

DOE/BC/14875-13
Distribution Category UC-122

Research Program On Fractured Petroleum Reservoirs

Final Report

By
Dr. Abbas Firoozabadi

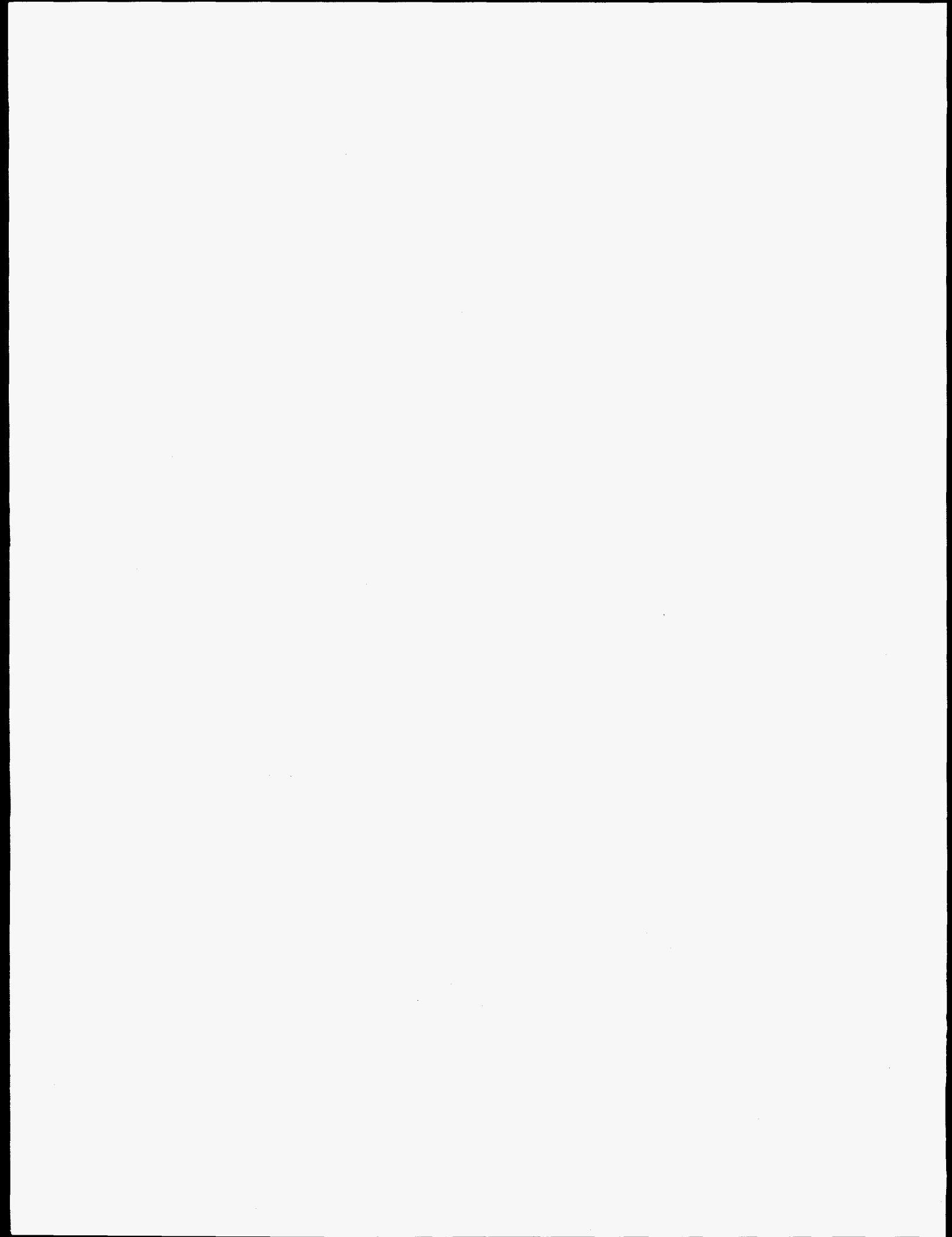
May 1997

Work Performed Under Contract No. DE-FG22-93BC14875

Prepared for
U.S. Department of Energy
Assistant Secretary for Fossil Energy

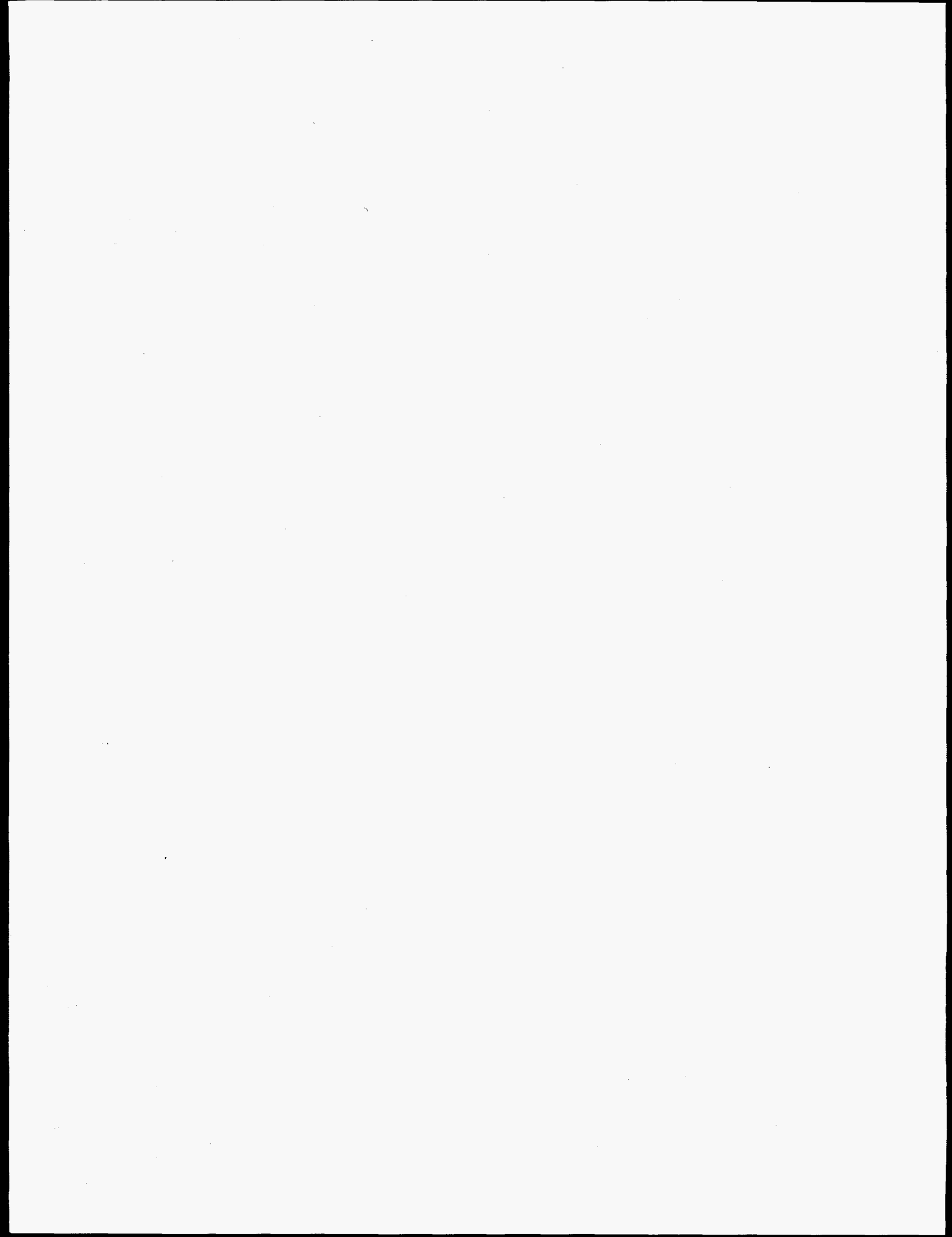
Robert Lemmon, Project Manager
Bartlesville Project Office
P.O. Box 1398
Bartlesville, OK 74005

Prepared by:
Reservoir Engineering Research Institute
845 Page Mill Road
Palo Alto, CA 94304



DISCLAIMER

Portions of this document may be illegible in electronic image products. Images are produced from the best available original document.



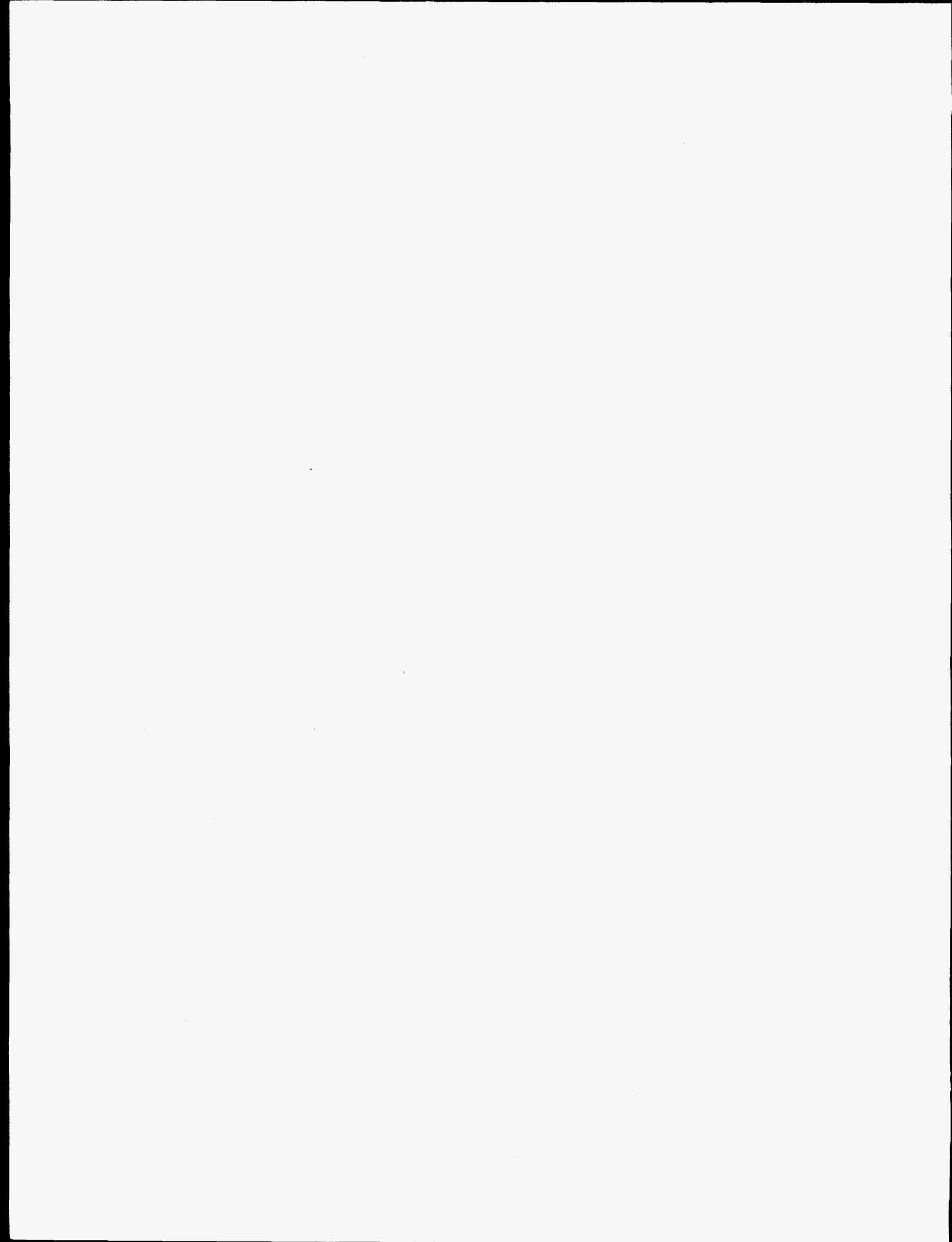
Acknowledgments

The work presented in this final report is the result of the efforts of a group of able scientists and some world class researchers -- a very unique blend of scholars with backgrounds in mathematics, mechanical engineering, chemical engineering, and petroleum reservoir engineering. The special talents and hard work provided the scientific environment to attack one of the most difficult problems in petroleum reservoir engineering -- the physics of multiphase flow in fractured porous media.

Dr. Birol Dindoruk, Dr. James Tan, and Engineers Tore Markeset and Andy Aronson all four, former staff scientists at the Institute, Dr. Mehran Pooladi-Darvish a research engineer, and Dr. Eric Chang of the ARCO Exploration and Production Technology have all contributed to various studies.

The funding for the work presented in this report was from two sources : 1) the United States Department of Energy under Contract No. DE-FG22-93BC14875., and 2) oil companies from the United States, Europe, Japan, the Middle East, and South America. The supporting oil companies include: 1) Abu Dhabi National Oil Company, UAE; 2) Amoco Production Company, USA.; 3) ARCO Exploration and Production Technology, USA; 4) Chevron Petroleum Technology Company, USA; 5) Elf Aquitaine Production, France; 6) Exxon Production Research Company, USA; 7) Japan National Oil Corporation, Japan; 8) Landmark Graphics Corporation, USA; 9) Marathon Oil Company, USA; 10) Mobil Research and Development Corporation, USA; 11) Norsk Hydro Production, A.S., Norway; 12) Petrobras, S.A., Brazil; 13) Petrofina, S.A., Belgium; 14) Petronas Research and Scientific Services , Malaysia; 15) Phillips Petroleum Company, USA; 16) SAGA Petroleum A.S., Norway; 17) Shell Exploration and Production Company, USA; 18) Statoil, A.S., Norway; 19) Texaco, Inc., USA; 20) Total Minatome Corporation, USA and France; and 21) Union Pacific Resources Company, USA.

We also thank our project manager, Dr. Bob Lemmon from the US DOE- Bartlesville's project office for his active interest and support of the research program.



Executive Summary

Multiphase flow in fractured porous media is a complex problem. While the study of single phase flow in a fractured or a layered medium can be pursued by some kind of averaging process, there is no meaning to averaging two-phase flow when capillarity is an active force. For a two-layer system comprised of high and low permeable layers, the performance of gas-oil gravity can be less efficient than the homogeneous low permeable medium. On the other hand, heterogeneity may enhance water imbibition due to capillarity. Due to the above and various other complexities, current tools for predicting the performance of fractured hydrocarbon reservoirs are not reliable. Based on the research work carried out at the Reservoir Engineering Research Institute, and some other Institutions, a good deal of progress has been made in recent years. But still we are a long way from good predictive reservoir models. In this final report, we summarize some of our achievements in the understanding of multiphase flow in fractured media. Since some of the features of two-phase flow in fractured and layered many are similar due to the capillary forces, the work includes progress in both types of media. There are some basic issues of flow in both fractured and unfractured media that are currently unresolved. These issues include: 1) new phase formation such as the formation of liquid phase in gas condensate reservoirs, and gas phase formation in solution gas drive process and 2) composition variation due to thermal convection and diffusion processes. In the following, a brief summary of our findings in the last three years during the course of the project is presented.

In Chapter I, we present the laboratory data and then analyze the data on the effect of viscous displacement in fractured media. The incentive for the work is that in certain fractured reservoirs where a fluid is injected, a pressure gradient in the fractures is established. The viscous pressure gradient may result in additional oil recovery. The experimental data show that up to 10 percent extra recovery may be obtained when the fracture pressure gradient is 0.1 psi/ft.

Chapter II presents a mathematical model to study crossflow between 1) a fracture and a matrix of fractured media; and 2) the less and more permeable layers of a layered media. The incentive for the work in this chapter is to understand how an injected fluid flows through fractured media. The examples selected for the layered media show that most of the oil is first transferred from the low permeability to the high permeability layer and then produced. The examples for fractured media reveal a significant contribution of crossflow to recovery performance.

In Chapter III, we discuss co-current and counter-current imbibition in a water-wet matrix block. The work is based on the mathematical analysis of the process. Despite the general belief, our theoretical and experimental studies indicate that co-current imbibition may be the dominant mechanism in water

displacement of fractured media. In counter-current imbibition, oil is forced to flow in the two-phase region; in co-current imbibition, oil can flow in the single phase. This study reveals that co-current imbibition is much more efficient than counter-current imbibition. The conclusion from the study is that the use of imbibition data by immersing a single block in water and its scale-up provide pessimistic recovery information.

Chapter IV presents an experimental study of gas-oil gravity drainage in layered media. In a previous theoretical study, we discovered that gas-oil gravity drainage in layered media has important features that are different from drainage in homogeneous media. As an example, while in homogeneous media, the process efficiency is high, in layered media, the recovery efficiency may be low. The capillary contrast between different media reduces drainage rate. From the analysis of the experimental data, it is concluded that unlike homogeneous media, where drainage characteristics are often weakly related to gas relative permeability, drainage in layered media can be sensitive to gas phase mobility.

In Chapter V, the dual-porosity model for the simulation of fractured reservoirs is modified to account for reinfiltration and capillary continuity concepts. In this work, the results for a single gridcell is presented. The proposed method requires fine grid simulation of a three-block stack. The information is then used to construct the drainage curves of different gridcells that may contain a large number of matrix blocks. Variation of capillary pressure, block height, and permeability of various blocks within a gridcell are accounted for without the need for fine grid simulation.

Chapter VI presents a simple and clear problem formulation which accounts for 1) thermal convection, 2) thermal diffusion, 3) molecular diffusion, and 4) pressure diffusion. The formulation is aimed towards the understanding of fluid distribution in both fractured and unfractured reservoirs. Field data indicate that fluid distribution in fractured reservoirs are very different from unfractured reservoirs. In this chapter, only the combined effect of pressure, thermal, and molecular diffusion in the one-D vertical case is studied. The results show that thermal diffusion can both enhance or weaken the segregation in a hydrocarbon reservoir.

Chapter VII deals with the study of solution gas drive in light and heavy oil reservoirs. A new high pressure visual coreholder is used to observe the formation of new gas phase and its pattern of growth. We used 11-API and 35-API gravity crudes in the study. The most important conclusion of the work is that solution gas-drive for the heavy oil is much more efficient than the light oil. The bubble density (number of bubbles per unit volume) is very high for the heavy oil. Other conclusions from this work are 1) the number of bubbles is a function of the rate of pressure decline; the higher the rate of pressure decline, the higher the number

of bubbles, and 2) the nucleation in porous media is an instantaneous nucleation process.

Chapter VIII discusses a phenomenological network model for critical condensate saturation. The model reveals that critical condensate saturation is a function of surface tension and contact angle hysteresis. On the other hand, residual oil saturation does not have such a dependency. The model will provide a framework for our future study on gas phase mobility which is the most important parameter of gas well deliverability.

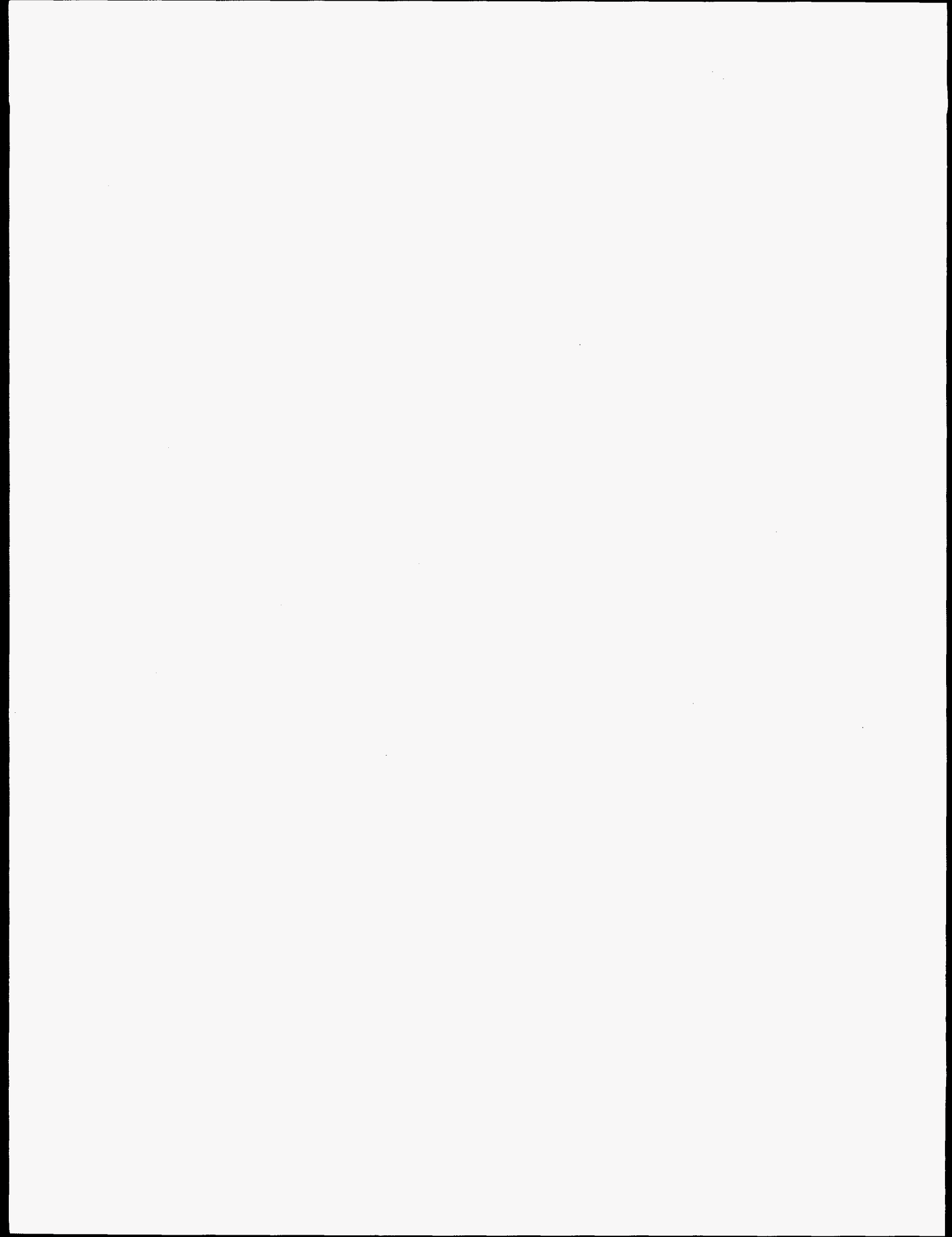


TABLE OF CONTENTS

Acknowledgments

Executive Summary

Chapter I - Viscous Displacement in Fractured Porous Media	1-43
Chapter II - Crossflow in Fractured/Layered Media Incorporating Gravity, Viscous and Phase Behavior Effects	44-82
Chapter III - Co-Current and Counter-Current Imbibition in a Water-Wet Water-Wet Matrix Block	83-109
Chapter IV - Gravity Drainage in Layered Media: Experimental Data And Analysis	110-133
Chapter V - Dual-Porosity Simulation Incorporating Reinfiltration and Capillary Continuity Concepts Part I: Single Gridcell	134-152
Chapter VI - Areal and Vertical Composition Variations in Hydrocarbon Reservoirs: Formulation and One-D Binary Results	153-180
Chapter VII - Visualization and Measurement of Gas Evolution and Flow of Heavy and Light Oil in Porous Media	181-200
Chapter VIII - A Phenomenological of Network Model of Critical Condensate Saturation	201-218

LIST OF TABLES

1.1	Dimensions of blocks and slabs, $L_x \times L_y \times L_z$	40
1.2	Matrix data	41
1.3	Fracture permeability and fracture capillary pressure parameters	42
1.4	Measured and calculated final saturations for the matrix blocks slabs of test 4a and test 4 b	43
2.1	Rock and fluid properties - layered media	69
2.2	Rock and fluid properties - fractured media	69
3.1	Data for the base case example	101
4.1	Summary of test results	118
5.1	S_{ge} values for single blocks	147
5.2	S_{ge} values for individual matrix blocks in the stack	147
7.1	Gas and oil production data for test 4	193
8.1	Different groups of radii (μm)	213

LIST OF FIGURES

1.1	Viscous displacement experimental setup	16
1.2	Matrix-fracture configurations used in the experiments	17
1.3	Comparison of cumulative production and rate data of configuration a.	18
1.4	Injection pressure data	19
1.5	Injection rate data for test 4a	20
1.6	Comparison of cumulative production and rate data of configuration b	21
1.7	Cumulative production and rate data, and simulation results - test 1a.	22
1.8	Calculated saturation profiles at different times -test 1a.	23
1.9	Cumulative production and rate data, and simulation results - test 2a.	24
1.10	Injection pressure data and simulation results	25
1.11	Calculated saturation profiles at different times - test 2a.	26
1.12	Cumulative production and rate data, and simulation results - test 3a.	27
1.13	Calculated saturation profiles at different times - test 3a.	28
1.14	Injection rate data and input rate for simulation - test 4a.	29
1.15	Cumulative production and rate data, and simulation results - test 4a.	30
1.16	Calculated saturation profiles at different times - test 4a.	31
1.17	Cumulative production and rate data, and simulation results - test 1 b.	32

1.18	Calculated saturation profiles at different times - test 1b.	33
1.19	Cumulative production and rate data, and simulation results - test 2b.	34
1.20	Calculated saturation profiles at different times - test 2b.	35
1.21	Cumulative production and rate data, and simulation results - test 3b.	36
1.22	Calculated saturation profiles for test 3b at different times	37
1.23	Cumulative production and rate data, and simulation results - test 4b.	38
1.24	Calculated saturation profiles at different times - test 4b.	39
2.1	Composition profiles at $t_D = 0.25$ PV injection (with and without crossflow) at different pressures and inlet gravity numbers	70
2.2	Close look at the composition profiles at $t_D = 0.25$ PV for $CH_4 - C_{10}$ displacement (with crossflow) at 1000 psia and $N_{gr} = 0$ -- layered media.	71
2.3	Flow rate profiles at $t_D = 0.25$ PV injection (with crossflow) at different pressures and inlet gravity numbers -- layered media.	72
2.4	Saturation profiles at $t_D = 0.25$ PV injection (with crossflow) at different pressures and inlet gravity numbers -- layered media	73
2.5	Recovery plots (with crossflow) at different pressures and inlet gravity numbers -- layered media	74
2.6	Inlet rate history (without crossflow) at different pressures and inlet gravity numbers -- layered media	75
2.7	Recovery plots (without crossflow) at different pressures and gravity numbers -- layered media	76
2.8	Composition profiles at $t_D = 0.00025$ PV injection (with crossflow) at different inlet gravity numbers at 4000 psi -- fractured media	77
2.9	Composition profiles at $t_D = 0.5$ PV injection (with and without crossflow) for different inlet gravity numbers at 4000 psia	78

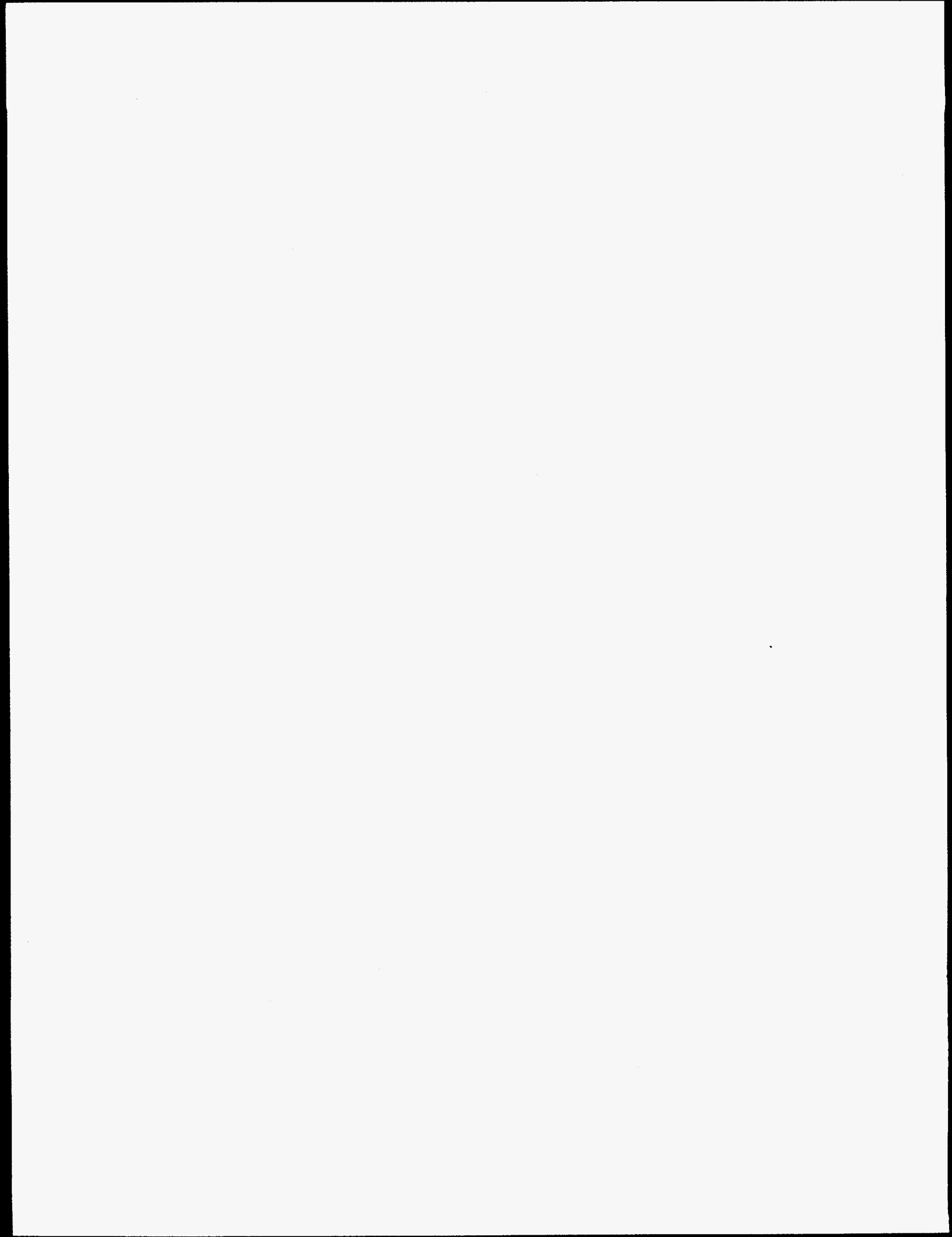
2.10	Flow rate profiles at $t_D = 0.5$ PV injection (with crossflow) for different inlet gravity numbers at 4000 psia -- fractured media . .	79
2.11	Saturation profiles at $t_D = 0.5$ PV injection (with crossflow) at different inlet gravity numbers at 4000 psia -- fractured media . .	80
2.12	Recovery plots for (with and without crossflow) for different gravity numbers at 4000 psia -- fractured media	81
2.13	Inlet rate history (without crossflow) for different gravity numbers at 4000 psia -- fractured media	82
3.1	Oil and water pressure distribution for 1-D counter-current imbibition	101
3.2	Oil and water pressure distribution for 1-D co-current imbibition	101
3.3	Saturation distribution for 1-D counter-current imbibition	102
3.4	Recovery for 1-D counter-current imbibition	102
3.5	Saturation distribution for 1-D co-current imbibition	102
3.6	Recovery for 1-D co- and counter-current imbibition	102
3.7	Scaling law for 1-D co- and counter-current imbibition	103
3.8	Comparison between 1-D co- and counter-current imbibition . . .	103
3.9	Behavior of co-current imbibition at small dimensionless time . . .	103
3.10	Recovery for 2-D co-current and counter-current imbibition	103
3.11	Comparison between 2-D co- and counter-current imbibition (base case)	103
3.12	Saturation and oil velocity profiles for 2-D counter-current imbibition	104
3.13	Oil and water pressure profiles for 2-D counter-current imbibition .	105
3.14	Saturation and oil velocity profiles for 2-D co-current imbibition . .	106
3.15	Oil and water pressure profiles for 2-D co-current imbibition	107

3.16	Superposition for co-current imbibition	108
3.17	Superposition for counter-current imbibition	108
3.18	Schematic diagram of apparatus during a run	108
3.19	Oil production data for co- and counter-current imbibition	109
4.1	Stable and unstable regions of gravity drainage in layered media ...	119
4.2	Schematic of layered-media apparatus	120
4.3	Measured capillary pressures of Berea and sand	121
4.4	Measured and simulated production and rate for tests 2 and 3	122
4.5	Position of gas-liquid front in the sand layer	123
4.6	Production and rate data of tests 15 and 16	124
4.7	Gas-liquid front from interface for test 15	125
4.8	Measured and simulated production and rate for tests 5 and 6 ...	126
4.9	Measured and simulated production and rate for tests 7 and 9 ...	127
4.10	Gas-liquid front from interface for tests 7 and 9	128
4.11	Measured and simulated production and rate for tests 10, 11, and 12	129
4.12	Gas-liquid front from interface for tests 10, 11, and 12	130
4.13	Measured and simulated production and rate for test 13	131
4.14	Gas relative permeabilities	132
4.15	Production for the Berea layer in a two-layer and in a homogeneous system	133
5.1	Drainage rate vs. S_{gi} for various matrix blocks in a 10-block stack	148
5.2	Cumulative production vs. time for a (a) 3, (b) 5, and (c) 10-block stack	148

5.3	Saturation history for various matrix blocks in a 10-block stack . .	148
5.4	Drainage rate vs. \bar{S}_{gi} -- case 1	149
5.5	Saturation history: (a) individual blocks, and (b) entire stack -- case 1	149
5.6	Drainage rate vs. \bar{S}_{gi} -- case 2	149
5.7	Saturation history: (a) individual blocks, and (b) entire stack -- case 2	149
5.8	Schematic of stacked blocks -- cases 3, 4, and 7	150
5.9	Saturation history: (a) individual blocks, and (b) entire stack -- case 3	150
5.10	Drainage performance of a single matrix block	150
5.11	Drainage performance of a four-block stack, $P_{cf} = 0$	150
5.12	Saturation history: (a) individual blocks, and (b) entire stack -- case 4	151
5.13	Drainage rate vs. \bar{S}_{gi} for various blocks in a 10-block stack, $h = 60$ cm.	151
5.14	Drainage rate vs. \bar{S}_{gi} for various blocks in a 10-block stack, $h = 180$ cm.	151
5.15	Saturation history: (a) individual blocks, and (b) entire stack -- case 5	151
5.16	Saturation history: (a) individual blocks, and (b) entire stack -- case 6	152
5.17	Saturation history: (a) individual blocks, and (b) entire stack -- case 7	152
5.18	Drainage performance of a four-block stack, $P_{cf} \neq 0$	152
6.1	Depth vs. composition for a C1/C3 system in the liquid state ($P = 7.24$ MPa, $T = 346$ K @ depth = 0)	166

6.2	Depth vs. composition for a C1/C3 system in a gas state (P = 4.05 MPa, T = 346 K @ depth = 0).	167
6.3	Depth vs. composition for the C1/C3 system in the liquid state (PL = 10.3 MPa, T = 346 K @ depth = 0)	168
6.4	Phase envelope for the C1/C3 system at T = 346 K, and pressure- composition relationship for the example of Fig. 1	169
6.5	Depth vs. composition for the C1/nC4 system in the liquid state (P = 19.3 MPa, T = 334 K @ depth = 0)	170
6.6	Depth vs. composition for the C1/nC10 system in the liquid state (P = 20.7 MPa, T = 346 R @ depth = 0	171
6.7	Phase envelope for the C1/nC10 system at T = 344 K and pressure- composition relationship for the example of Fig. 6.	172
6.8	Depth vs. composition relationship for the nC7/nC16 liquid system (P = 13.8 MPa, T = 308 K @ depth = 0	173
6.9	Thermal diffusion coefficient for the C1/C3 binary at 72.8 C and 5.59 MPa	174
6.10	Thermal diffusion factors for the C1/C3 binary at 72.8 C and 0.34 mole fraction C1	175
6.11	Phase diagram of the C1/C3 system at 72.8 C and the data points used by Kempers	176
6.12	Thermal diffusion factors for the C1/nC4 binary at 40 mole percent methane	177
6.13	Thermal diffusion factors for the C1/nC4 binary at 49 mole percent methane	178
6.14	Thermal diffusion coefficient for the nC7/nC16 binary at atmos- pheric pressure and 35 C	179
6.15	Thermal diffusion factors for various hydrocarbon systems	180
7.1	Apparatus diagram for critical gas experiments	194
7.2	Pressure-volume expansion data for tests 1 and 2	195

7.3	Pressure-volume expansion data for test 3	196
7.4	Pressure-volume expansion data for test 4	196
7.5	Growth of gas bubbles at various expansions for test 4	197
7.6	Gas production from the core into the top cap	198
7.7	Pressure-volume expansion for test 5 and the isolated pump	198
7.8	Growth of gas bubbles at various expansions for test 5	199
7.9	Pressure-volume expansion for test 5 and 6	200
8.1	Imbibition P_c - S_w plots for a single tube of different shapes	213
8.2	Advancing and receding interfaces of liquid column in a circular capillary tube	214
8.3	Capillary rise in triangular and curved triangular tubes	214
8.4	Liquid holdup in a triangular or curved triangular tube	214
8.5	Schematics of liquid formation and flow in intersections	215
8.6	Radii's distribution of the network	216
8.7	Network size distribution of 20 x 20	216
8.8	Liquid distributions at different stages of condensation	217
8.9	S_{cc} vs. surface tension at different contact angle hysteresis network sizes 20 x 20	217
8.10	S_{cc} vs. surface tension for two different network sizes	217
8.11	Basic mechanism of imbibition (after Lenormand, et. al.)	218
8.12	S_{α} vs. surface tension	218
8.13	Liquid distribution at the end of imbibition	218



CHAPTER I

Viscous Displacement in Fractured Porous Media

Abbas Firoozabadi

Tore Marketset

Birol Dindoruk

Reservoir Engineering Research Institute

SUMMARY

In some fractured reservoirs, a gas pressure gradient of the order of 3-5 kPa/m may be established in the fractures due to flow. Such a pressure gradient could result in recovery enhancement of the matrix oil. Several tests are conducted to study viscous displacement in fractured porous media with artificial fractures. These tests are analyzed by using a fully-implicit finite difference simulator with appropriate fracture capillary pressure. The results show that there is considerable recovery improvement due to viscous displacement. For a gas pressure gradient of 3 kPa/m, the matrix oil recovery increases by 10 percent of PV in one of the tests.

INTRODUCTION

In fractured porous media comprised of matrix blocks and a fracture network, gravity and capillary forces affect the two-phase flow in the matrix blocks and the fractures. Capillary forces play a major role in the interaction between the matrix blocks via the capillary continuity mechanism.¹ Gravity forces affect the drainage performance of the matrix blocks and the reinfiltration process.² In addition to capillary and gravity forces, in certain cases, viscous forces are expected to affect the production performance of fractured reservoirs.

Gas injection in some fractured reservoirs with low oil viscosity (say 0.2 mPa·s and an effective permeability to matrix permeability ratio of less than say 30) may result in a small pressure gradient in the fractures between an injection and production well. The gas pressure gradient in the fractures away from the well could be of the order of 3-5 kPa/m. Such a pressure gradient in the fractures improves matrix oil recovery by reducing the matrix capillary threshold height for gravity drainage and the capillary end effect in the horizontal direction. There is no published data in the literature on viscous displacement in fractured porous media.

The purpose of this work is to: 1) provide experimental data on viscous displacement in fractured porous media for gas-oil displacement processes, and 2) analyze the data to

examine the nature of displacement improvement from viscous forces. In the following, we first discuss the experimental setup and present the data, and then analyze the data using a finite difference simulator.

EXPERIMENTAL

The apparatus schematic is depicted in Fig. 1. It consists of a glass-walled case with metal top and bottom plates supported by metal framing. The metal framing allows the 0.95 cm-thick glass plates to be forced against the rock faces. Design allows the setup to be tilted through 240° about a central horizontal axis. The glass case was sealed using fuel resistant room temperature vulcanizing fluorosilicone rubber. The bottom and the top end plates were made of 2.54 cm and 0.64 cm thick aluminum plates, respectively. Both plates provided connections for vacuum, ventilation, gas injection, fluid loading and drainage (see Fig. 1). A valve mounted 6 cm above the bottom face of the coreholder allows gas to flow out freely without interfering with liquid flow. The liquid is produced from the outlet at the bottom plate.

Peripheral accessory equipment consist of vacuum pump, vacuum gauge, heat tapes, balance, gas bottle, gas mass flowmeter and controller, pressure transducer, multiloop controller with proportional, integral, and derivative (PID) control capabilities, resistance temperature detector (RTD), air conditioning unit, convection oven, and a personal computer (PC). The RTD, air conditioning unit, convection oven, pressure transducer, and the gas mass flowmeter and controller are interfaced to the multiloop controller. The multiloop controller is interfaced to the PC. A computer program allows logging of pressure, gas flow rate, and temperature. The same program also simultaneously provides temperature control of the laboratory room ($24.5 \pm 0.2^\circ\text{C}$). The balance is also interfaced to the PC. Another computer program allows logging of mass flow rate data. Constant gas flow rate is provided by the gas mass flowmeter and controller. By utilizing PID control capability of the multiloop controller, the injection pressure can be also held constant while gas injection flow rate varies.

Matrix-Fracture Configurations and Properties

Two different matrix-fracture configurations are used to study viscous displacement in fractured porous media (see Fig. 2). Both configurations are assemblies of matrix blocks and matrix slabs of the Berea sandstone. Block areal dimensions are 15×30 cm, and 60 cm in height. Slab dimensions are 3.75×30 cm areal, and 60 cm in height. In both configurations (see Fig. 2a and Fig. 2b), the rock faces are in direct contact. To ensure uniform fractures and tight mounting in the coreholder, the rock material is grinded to a dimensional tolerance of ± 25 microns. Care is taken to ensure all faces are normal (90°) to adjoining faces.

In Fig. 2a, the slabs in the middle contain 7 vertical fractures; three fractures from the space between the opposing faces of the matrix slabs and four fractures in the space between the glass walls and the slab faces. Visual observations led us to conclude that the four fractures between the glass walls and matrix slabs are thinner than the fractures between

matrix slab faces. For the top and bottom matrix blocks of Fig. 2a, in each four corners a large channel allows free flow of injected gas without any appreciable pressure drop. These channels have a prism shape; the base triangle dimensions are $4 \times 4 \times 5.6$ mm (see Fig. 2c). Therefore, both top and bottom matrix slabs are only subject to gravity drainage.

For Fig. 2b, the fractures for the top and bottom matrix slabs are similar to the fractures of the middle slabs of Fig. 2a. The middle matrix block is surrounded by four large corner fractures to free allow free flow of gas. Fig. 2c provides a top view of the matrix block(s) showing the corner fracture channels.

The effective permeability of the fracture/matrix configurations of Fig. 2a is $6.22 \mu\text{m}^2$ and that of Fig. 2b is $4.15 \mu\text{m}^2$. The effective permeabilities were measured by single phase liquid flow of normal decane. The effective permeability across the matrix blocks are very large (due to channels); one may imply that calculated effective permeabilities correspond to the slab/fracture assemblies. The average permeability of the Berea sandstone used in this work is around $0.87 \mu\text{m}^2$. The hydraulic fracture aperture between the matrix slabs is estimated to be around 150 microns for configuration "a" and 125 microns for configuration "b" of Fig. 2. These values are calculated from $k_f = t_f^2/12$, where t_f is the fracture aperture, and k_f is the intrinsic fracture permeability.³ The aperture of the fracture space between the glass wall and the matrix slab is assumed to be $t_f/2$. Note that the hydraulic aperture is affected by the matrix grain size and how are the fractures created.

The pore volume of the matrix/fracture configurations of Figs. 2a and 2b are $17,830 \text{ cm}^3$, and $18,150 \text{ cm}^3$, respectively. The dead-volume including corner channels, valve, fittings and tubing, and dead-space at the outlet is estimated to be 70 cm^3 . The fracture volumes (which includes horizontal and vertical fracture between rock and slabs, and vertical fractures between rock and glass) are 164 and 208 cm^3 for configurations a and b, respectively. The fracture volume is established from the early drainage behavior of the matrix-fracture system. The porosity of the Berea sandstone is 22 percent. For both configurations in Fig. 2, the glass-walled case extends 2 cm above the top rock matrix face. The open space ensures uniform distribution of gas at the entrance.

Test Procedure

The rock material were evacuated to remove adsorbed fluid and then saturated with normal decane (see Fig. 1) at 24.5°C . Viscosity and density of normal decane at this temperature and atmospheric pressure are $0.866 \text{ mPa}\cdot\text{s}$ and 0.724 g/cm^3 , respectively. A period of two days was allowed to achieve full saturation with liquid normal decane. The rock matrix was submerged in the liquid with about 2 cm of excess liquid ($\approx 900 \text{ cm}^3$) above the horizontal face of the top slab/block. Downward flow of this liquid, until the liquid level reached the horizontal face of the top block gave the effective permeability of the matrix-fracture system. Negligible resistance in the inlet and outlet connections was assumed. Gravity drainage by atmospheric pressure was allowed until both the vertical space between the rock and the glass was empty before nitrogen gas injection was initiated. The viscosity of nitrogen at room conditions is $0.0183 \text{ mPa}\cdot\text{s}$. The produced liquid was accumulated in a container and

recorded by a PC. Separate outlets were provided for liquid and gas. Gas injection pressure was measured at the inlet of the system and recorded by a PC (outlet pressure was atmospheric). For every test, the drying of the rock material and saturation was repeated.

Test Results

A total of eight tests were conducted. In the first four tests, the matrix-fracture configuration of Fig. 2a was used. The other four tests were conducted with configuration of Fig. 2b. Most tests were conducted at a constant injection rate; only one test was performed at a constant pressure drop across the system. In every test, except one, the matrix-fracture configuration was held vertical. The liquid production and the injected gas were measured in every test. In addition, slab saturations were measured at the end of two tests. In the following, the results are presented.

Matrix-Fracture Configuration of Fig. 2a

Test 1a - Gravity Drainage - Free gravity drainage provides a reference to examine the effect of viscous forces on displacement from the other tests. Fig. 3 displays the production and rate data for Test 1a for free gas-oil gravity drainage. The initial flow rate is around 3,200 cm³/hr, but after 3 minutes the drainage rate decreases to about 1,640 cm³/hr. During this period, the fluid in all the fractures is drained as can be observed through the glass case. Matrix desaturation may also occur during this period. As the fractures become empty, film flow along vertical faces of the matrix blocks and matrix slabs continues to about $t = 10$ min. The film flow along vertical faces of the matrix are described in Ref. 4. From $t = 10$ min to the end of the test only the matrix desaturates. The drainage rate at 15, 500 and 3,000 minutes are 735, 169, and 17.5 cm³/hr, respectively. At the end of the test ($t = 18,509$ min - about 12.8 days) the drainage rate decreases to 2.8 cm³/hr. The cumulative production at $t = 3,000$, and 18,509 min are 5,041 and 6,549 cm³ corresponding to matrix liquid saturations of 71.7 and 63.3 percent, respectively. Therefore, the liquid recovery at the end of Test 1a is 36.7 percent.

Test 2a - Gas Injection at 60,000 cm³/hr and Gravity Drainage - In the previous test, there is no forced gas injection; air replaces the drained liquid. In Test 2a, nitrogen is injected at a rate of 60,000 cm³/hr from $t = 0.5$ to $t = 5,432$ min at the inlet, and the pressure at the outlet is held at atmospheric pressure. In the first half minute, gravity drainage is allowed to occur and bulk of the liquid in the fractures is produced. At $t = 5,432$ min, gas injection is stopped and the system is allowed to drain by gravity to $t = 8,732$ min. Fig. 3 shows the production and rate data and Fig. 4a provides the inlet pressure data. At the start of nitrogen injection, the production rate is over 10,000 cm³/hr but decreases rapidly to 4,200 cm³/hr at $t = 1.2$ min. The production rate further decreases to 1,439 cm³/hr at $t = 6$ min. At $t = 15$ min, the rate reduces further to 1,284 cm³/hr which is higher than the 735 cm³/hr gravity drainage rate in Test 1a at the same time. Fig. 3b reveals that the production rate for Test 2a is higher than Test 1a to $t = 500$ min; thereafter the rates become nearly identical.

The production rate at the end of gas injection (i.e., $t = 5,432$ min) is $8.6 \text{ cm}^3/\text{hr}$. Then the system is allowed to drain by gravity to $t = 8,372$ min when the injection is stopped. From $t = 5,432$ to $t = 6,092$ min, there is no production. Production at a rate of $1.9 \text{ cm}^3/\text{hr}$ begins at $t = 6,092$ min. At $t = 6,213$ min, it increases to $3.5 \text{ cm}^3/\text{min}$ and at the end of the test, rate is $3.1 \text{ cm}^3/\text{min}$. The cumulative production at the end, $t = 8,372$ min, is $6,602 \text{ cm}^3$ which corresponds to an average liquid saturation of 63.0 percent. Fig. 3a implies that the matrix desaturates substantially due to viscous forces.

Fig. 4a depicts the inlet pressure versus time. The pressure decreases rapidly from a maximum of 8.71 kPa at $t = 1.2$ min to 3.51 kPa at $t = 4$ min. From then on, the pressure decreases slowly to 2.3 kPa at $t = 5,432$ min when the gas injection is stopped. Therefore, a steady state gas pressure gradient of around 3.8 kPa/m is established in this test.

Test 3a - Gravity Drainage and Gas Injection at $60,000 \text{ cm}^3/\text{hr}$ - In this test, the system is allowed to drain by gravity to $t = 3,217$ min, and then nitrogen is injected at a flow rate of $60,000 \text{ cm}^3/\text{hr}$. Cumulative production and rate data are shown in Fig. 3. The inlet injection pressure is displayed in Fig. 4a. In the gravity drainage period, the drainage performance is almost the same as the first test. At $t = 3,217$ min, just before the start of gas injection, the drainage rate is $14.9 \text{ cm}^3/\text{hr}$, and the cumulative production is $4,913 \text{ cm}^3$. When gas injection starts, the rate rapidly increases to $332 \text{ cm}^3/\text{hr}$. The production rate at the end of the test at $t = 10,054$ min is $4.6 \text{ cm}^3/\text{hr}$ which is slightly lower than Test 1a at the same time. The cumulative production at the end is $6,707 \text{ cm}^3$ corresponding to 37.6 percent recovery.

At the start of gas injection, pressure at the inlet increases very rapidly to 2.55 kPa , then after 5 minutes stabilizes at 2.40 kPa which is about 0.15 kPa higher than Test 2a at the same time. It decreases to 2.34 kPa at $t = 6,000$ min, and decreases very slowly towards the end.

From Fig. 3, it is observed that at the end of Test 3a, the drainage performance approaches Test 2a. If we extrapolate the drainage performance of Test 2a to $10,000$ min, the difference in cumulative production of Tests 2a and 3a would be about 180 cm^3 , or 1 percent of PV.

Test 4a - Gas Injection at $\Delta P = 2.1 \text{ kPa}$ - This test is performed at a constant injection pressure of 2.1 kPa , and therefore the rate of gas injection varies. Note that the injection pressure is 0.2 kPa lower than the injection pressure at the end of Test 2a. Fig. 5 shows the injection rate; rate fluctuations are due to very small pressure fluctuations around the set value of 2.1 kPa . The fluctuations in pressure are caused by change in the resistance of the system and the time lag in the rate adjustment to keep ΔP constant. However after some time, the injection rate becomes nearly constant - the average gas injection rate approaches $51,000 \text{ cm}^3/\text{hr}$.

In this test, the results are similar to Test 2a, but both the cumulative production and rate at corresponding times are somewhat lower. This is to be expected since both injection rate and the injection pressure are also less.

At the end of Test 4a, the experimental setup was dismantled and the slabs were weighed.

The liquid saturation of the three slabs were 46.7, 45.0, and 44.0 percent. The liquid saturation of the fourth slab was not measured. As will be discussed later, the saturation data imply the strong influence of viscous displacement in fractured porous media.

Matrix-Fracture Configuration of Fig. 2b

Test 1b - Gravity Drainage - This test is similar to Test 1a in which gravity drainage is allowed to take place. Fig. 6 displays production and rate data. Similar to Test 1a, the initial rate is high, around 4,415 cm³/hr. The high initial rate is mainly due to fracture desaturation. The rate at $t = 15$ min decreases to 813 cm³/hr. At $t = 500, 3,000,$ and 11,473 min, the corresponding rates are 217, 22, and 5.0 cm³/hr. The cumulative production at $t = 3,000$ and 11,473 min are 6,210 cm³ (65.8 percent matrix saturation), and 7,697 cm³ (57.6 percent matrix saturation). There is a substantial difference between the gravity drainage recovery of Tests 1a and 1b. The main reason is the high capillary threshold height of the bottom matrix block in Fig. 2a. As we will discuss later, the gravity drainage threshold height of the bottom matrix block in configuration "a" is about 53.5 cm whereas that of the bottom slabs in configuration "b" is around 31 cm. Test 1b will be used as a reference for the other tests described next.

Test 2b - Gas Injection at 60,000 cm³/hr - In the first minute, free gravity drainage is allowed to take place. Gas injection starts at $t = 1$ min, when the gas/liquid interface in the fracture reaches the bottom face of the lower slabs (see Fig. 2b). Production and rate data are shown in Fig. 6. After an initial rate increase due to injection, the rate decreases rapidly to 1,753 cm³/hr at $t = 6$ min. At $t = 15, 500,$ and 3,000 min, the production rate becomes 1,489, 219, and 23.5 cm³/hr, respectively.

Pressure data are shown in Fig. 4b. There is a rapid decrease from a maximum of 11.04 kPa at $t = 1.6$ min to 5.72 kPa at $t = 4.8$ min. From then on, the pressure decreases very slowly to 3.52 kPa at 20,216 min when the experiment is stopped. At the end, the rate is 2.3 cm³/hr and the cumulative production is 10,186 cm³ (average liquid saturation of 43.9 percent). Comparison of production data of Tests 2a and 2b shows a similar effect of viscous displacement on recovery. In this test, the gas pressure gradient in the fractures is around 2.93 kPa/m at steady state conditions.

Test 3b - Gravity Drainage and Gas Injection at 60,000 cm³/hr - First the system is drained by gravity to $t = 14,700$ min. Then, nitrogen is injected at the top inlet at a rate of 60,000 cm³/hr to the end of the test ($t = 24,840$ min). During the gravity drainage period, Test 3b is nearly identical to Test 1b. Prior to nitrogen injection at $t = 14,700$ min, the rate is 4.2 cm³/hr, but it increases to 2000 cm³/hr when nitrogen is injected. Then the rate drops rapidly. The production from $t = 14,700$ to 24,840 min is about 1,700 cm³ which is a significant recovery resulting mainly from viscous displacement. Injection pressure data are shown in Fig. 4b.

Test 4b - Tilted Stack with Gravity Drainage and Gas Injection at 60,000 cm³/hr - In this last test, the matrix-fracture configuration of Fig. 2b is tilted 45° along the side edge. From the start to 17,340 min, gravity drainage is allowed to take place. From $t = 17,340$ min to the end at $t = 27,420$ min, nitrogen at a rate of 60,000 cm³/hr is injected at the top inlet. The production and rate data for Test 4b are shown in Fig. 6. The rate of drainage is initially less than Tests 1b and 2b due to the effect of gravity. But in later stages, the rate and even cumulative production become close to the vertical tests.

At $t = 17,340$ min, prior to nitrogen injection the rate is 3 cm³/hr. When nitrogen is injected, the rate increases to 400 cm³/hr but drops very rapidly. As Fig. 6 shows, nitrogen injection results in a substantial increase in recovery; 1,600 cm³ from $t = 14,700$ to $t = 27,420$ min.

Inlet pressure response is very similar to Test 3b. Injection increases very rapidly to 3.9 kPa and drops fast to a value of about 3.6 kPa (see Fig. 4b).

At the end of Test 4b, the saturations of the slabs were measured by weighing. The measured saturations of the three slabs in the top are 0.293, 0.298, and 0.299. The average saturation of the three slabs in the bottom are 0.668, 0.690, and 0.678. Since these saturations are very close, the average saturations of fourth slab at the top and bottom are assumed to be 0.297, 0.678 respectively. From the overall material balance, the average liquid saturation of the matrix block at the center (see Fig. 2b) is calculated as 0.440.

The above tests reveal that viscous displacement in fractured porous media can have a significant effect on matrix oil recovery. Next we will analyze the tests using a finite difference simulator.

NUMERICAL SIMULATION

In a previous study, we simulated gas-oil gravity drainage in fractured porous media⁵; the results showed that fracture capillary pressure is an important two-phase flow parameter for a matrix/fracture system. We proposed the following expression for the fracture capillary pressure,

$$P_{cf} = P_{cf}^o - \sigma_f \left| \ln \left(\frac{S_o - S_{orf}}{1 - S_{orf}} \right) \right|^{n_f}, \quad P_{cf} \geq P_{cf}^o \quad (1)$$

where S_{orf} is the residual liquid saturation of the fracture medium, P_{cf}^o is the fracture threshold capillary pressure, and σ_f is the slope of the logarithmic term. The residual liquid saturation in a fracture is generally low and the simulated results do not show high sensitivity to this parameter⁵. We assume $S_{orf} = 0.01$ in this study. Parameter n_f is used to change the slope of the capillary pressure around the residual liquid saturation; $n_f = 2$ provides a sharp change and seems to be an appropriate value for both this study and the work of Ref. 5.

Effective fracture permeability in the direction perpendicular to fracture planes can be expressed by,⁶

$$k_f = 3.45 \times 10^5 Rl^2 \sqrt{l} \quad (2)$$

where R is film aspect ratio in the fracture, \mathcal{I} is the shape factor of the liquid bridge and l is the half-fracture aperture (in microns). Ref. 6 provides the details of Eq. 2. In this study, $R=1$ and $\mathcal{I}=7.5$ are used to estimate fracture permeability and is assumed to be constant due to the short desaturation period for fractures.

In Ref. 5, as well as in this study, parameters σ_f and P_{cf} of the fracture capillary pressure model are obtained from history matching of one set of data for a given system.

For configuration "a" of Fig. 2, matrix slabs were located between two matrix blocks. The matrix block at the top is designated by A, the four slabs in the middle by B, and the bottom matrix block by C. For configuration "b" of Fig. 2, the four slabs designated by B are used in the top, the matrix block A in the middle and a set of four bottom slabs designated by D. The dimensions of the matrix blocks and slabs are provided in Table 1.

The capillary pressure of the Berea sandstone for the normal decane/air fluid system has been measured previously⁷. The model of Bentsen and Anli⁸ given by,

$$P_{cm} = P_{cm}^o - \sigma_m \ln \left(\frac{S_o - S_{orm}}{1 - S_{orm}} \right), \quad P_{cm} \geq P_{cm}^o \quad (3)$$

describes matrix rock capillary pressure well. The measured threshold capillary pressure, P_{cm}^o , in the previous study is around 2.8 kPa which is equivalent to a gravity-capillary equilibrium threshold height of about 40 cm. Parameter σ_m is in the range of 0.97 to 1.24 kPa⁵.

Liquid relative permeability of the Berea sandstone has been estimated previously⁵. We will use the expression,

$$k_{rom} = \left(\frac{S_o - S_{orm}}{1 - S_{orm}} \right)^{3.5} \quad (4)$$

without any adjustment. In Eq. 4, $S_{orm}=0.26$ is the residual oil saturation of the Berea sandstone.

Next, we will analyze the tests described above using the Eclipse finite difference simulator⁹ with the implicit scheme. In the numerical studies, 10 grids per section (block or slabs) in the vertical direction were used with smaller grids near the fractures to capture the saturation and pressure changes near the boundaries of the rock matrix. The gridding data are $N_x = 9$, $N_y = 3$, $N_z = 35$; $\Delta x = 0.01, 3.74, 0.01, 3.74, 0.01, 3.74, 0.01, 3.74, 0.01, 3.74$ and 0.01 cm; $\Delta y = 0.01, 30, 0.01$ cm; $\Delta z = 0.5, 0.5, 8 \times 7.375, 0.5, 0.1, 0.5, 8 \times 7.375, 0.5, 0.01, 0.5, 8 \times 7.375, 0.5, 0.01, 0.5$ cm. The top and bottom two grids (i.e., $N_z = 1$, $N_z = 34$ and 35) are not part of the fractured porous media, and are initially saturated with gas while the rest of the system both the rock matrix and the fractures are initially saturated with the liquid. The two bottom grids are assigned very high permeabilities and are imposed with $P_c = 0$. This gridding structure is used for configurations "a" and "b" of Fig.2 with appropriate porosities and permeabilities. Liquid film flow along the matrix and slab walls⁴ dominates the flow process in the early period of drainage ($t \leq 10$ minutes). Film flow was not considered in the numerical simulation.

Cumulative production, rate, pressure, and average block/slab saturation data were matched. Saturation measurements were available only for Test 4a, and Test 4b. All the

tests were performed using the coreholder in the vertical position, except Test 4b, where the coreholder was tilted 45° along a long edge.

Matrix-Fracture Configuration of Fig. 2a

Test 1a - Gravity Drainage - The major unknown quantity in the numerical simulation is the fracture capillary pressure. By matching the production and rate data of Test 1a, fracture capillary pressure and other parameters were estimated. The capillary pressures of the matrix block A and slabs B are very similar to the measured data of Ref. 5. For matrix block C, the threshold capillary pressure is significantly higher. Table 2 provides the parameters of the matrix capillary pressure which are also obtained by history matching.

The parameters of the fracture capillary pressure are shown in Table 3. These parameters correspond to an aperture of 30 microns⁵. The fracture aperture in this context differs from the hydraulic fracture aperture which is based on the inferred permeability from the flow parallel to the fracture planes. The aperture of 30 microns is based on the experiments analyzed in Ref. 5 where the blocks were separated from each other by 50 and 100 micron spacers. In Ref. 5, the 50 micron aperture was assigned to the fracture capillary pressure which gave the best match to the experiment with 50 micron spacers. The P_{cf} of the test with 100 micron spacers was calculated by dividing the P_{cf} corresponding to 50 micron spacers by 2 which was the ratio of the assigned apertures of the two separate tests. For those tests with the blocks or slabs in direct contact, there is no similar yard-stick. The nature of capillary pressure continuity of the direct-contact experiments is not fully known; P_{cf} is a function of surface roughness, grain size and probably the weight of the top blocks. Due to the deformation of the spacers under the weight of the top blocks, the exact fracture aperture was not known even for the tests where spacers were used. Among all the parameters, the surface roughness of the matrix blocks and slabs is the most important factor for the nature of capillary continuity in the direct contact experiments. Roughness of the fracture surfaces and the number of contact points are related to cementation as well as the size of the sand grains. For example, fine sand grains have diameter of 64 to 125 microns. Such diameters are the same order as the fracture apertures considered here.

In the simulation of all the experiments, the fracture permeability in the direction parallel to fracture planes was assigned a value of 2000 μm^2 . This permeability is estimated from Poiseuille's law for $t_f=150$ microns. The fracture permeability in the direction perpendicular to fracture planes is estimated from Eq. 2 and the values are listed in Table 3.

Comparison of the production data and the simulation results are shown in Fig. 7. Both cumulative production and rate data show good agreement with the simulation results. Calculated saturation profiles at various times are shown in Fig. 8. As can be seen, the bottom block (block C) drains much less than the top block and middle slabs. The main reason is the high threshold capillary height of the bottom block. Calculated average block and slab saturations at the termination of the experiment from top to bottom are 0.453, 0.455, and 0.985, respectively. Desaturation of the top block and the middle slabs to the same value is mainly attributed to different fracture and matrix capillary pressures.

Test 2a - Gas Injection at 60,000 cm³/hr and Gravity Drainage - In the numerical simulation of this test, all the quantities from Test 1a were used. Figs. 9 and 10a show the comparison of the simulated results and measured data. Considering the complexity of the problem, the agreement between the production and pressure data and the simulation results shown in these two figures is very good. As stated above, in the numerical simulation, the early film flow in the fracture planes is not accounted for and, therefore, the measured early drainage rate is higher than simulation results.

The calculated saturation profiles at various times are shown in Fig. 11. Although the shape of the saturation profiles of the top block and middle slabs are different, they both produce to a liquid saturation of 0.51 at 90.4 hours, whereas the top block and middle slabs produce to a liquid saturation of 0.55 at 90.5 hours in Test 1a. The calculated average saturation of the bottom block at the termination of the experiment is 0.92 (at $t = 90.5$ hrs). This saturation value is less than the corresponding saturation value of Test 1a (0.987) at 90.5 hours. Due to capillary continuity, the viscous force results in desaturation of all the blocks and slabs.

As nitrogen injection proceeds, the top block and the middle slabs are stripped by nitrogen beyond the gravity drainage production. However, the amount of extra production from these segments is not as much as the bottom block (the bottom block has more producible oil than the top block and the middle slabs due to the effect of capillary threshold pressure).

The second part of the experiment undergoes saturation direction change. The matrix imbibition capillary pressure data are not available, and therefore, the simulation is not extended to the end of this test.

Test 3a - Gravity Drainage and Gas Injection at 60,000 cm³/hr - Similar to the numerical simulation of Test 2a, the simulation results for Test 3a are performed without parameter adjustment. Fig. 12 shows that the simulation results for both cumulative production and rate are in excellent agreement with data. The kick in rate (at $t = 53.6$ hr) is due to nitrogen injection. Comparison of the calculated and measured injection pressures shown in Fig. 10b reveals a good match. The sudden increase in pressure is also reflected in the rate history with a corresponding sharp peak. At the early stage of the nitrogen injection, nitrogen mobilizes the liquid in the matrix, and the mobilized liquid fills the fractures causing higher pressure drop than nitrogen-filled fractures. But, desaturation of the fractures is rather fast due to limited supply of the excess liquid (excess as compared to gravity effect), and high permeability of the fractures.

Calculated saturation profiles of the blocks and slabs are shown in Fig. 13. A pronounced effect of nitrogen injection at $t = 53.6$ hr on liquid production can be observed from the progress of saturation profiles. At the end of the experiment, the saturation profiles are about the same as the saturation profiles of Test 2a (Fig. 11). The difference between the liquid productions of Test 2a and Test 3a is minor (about 2 %). This means that nitrogen injection can accelerate the production at late stages of gravity drainage.

Test 4a - Gas Injection at $\Delta P = 2.1$ kPa - In our simulation study, we could not impose $\Delta P = 2.1$ kPa throughout simulation period due to a very low value of ΔP ; instead we imposed a multi-rate injection scheme to keep the pressure drop somewhat constant. In order to implement multi-rate injection, we used the injection rate history that is shown in Fig. 14. As seen from this figure, the injection rate history is divided into separate segments with injection rates of 22,500 cm³/hr ($0 < t \leq 5.4$ min), 45,000 cm³/hr ($5.4 < t \leq 613$ min), and 51,000 cm³/hr ($613 < t \leq 11,256$ min). The rates are the average values of the corresponding time intervals.

The comparison of the production and pressure data and simulation results are shown in Figs. 15 and 10c. The match between the simulation results and the pressure data at late times could have been improved by discretizing the rate further (considering the rate fluctuations). However, since our main purpose is to understand the mechanisms of displacement, this was not carried out.

The calculated saturation profiles at various times are shown in Fig. 16. For this test, the average block and slab saturations are measured at the termination of the experiment. The measured and calculated values are shown in Table 4. Note that the middle slabs desaturate more than the top matrix block. The non-monotonic saturation behavior of the middle slabs is due to the influence of viscous forces on displacement. In the design of the configuration of Fig. 2a, gas pressure gradient in the fractures is mainly imposed on the middle slabs. As a result, these slabs can drain more than the top matrix block.

It should be noted that consistent numerical simulation of the experiments presented in this paper is a real challenge. As independently measured sets of data increase, prediction becomes more difficult. Nevertheless, the predicted production, rate, pressure, and saturation results are in good agreement with measured data.

Matrix-Fracture Configuration of Fig. 2b

Test 1b - Gravity Drainage - As in Test 1a, the fracture capillary pressure is obtained from the match of production data. The P_{cf}^o and σ_f parameters of the fracture capillary pressure (see Table 3) correspond to an aperture of 26 microns which is 13 % less than the corresponding aperture of the configuration in Fig. 2a. Similar to Test 1a, the 26-micron fracture aperture value is for the purpose of correlating fracture capillary pressure.

The comparison of the production data and the simulation results is shown in Fig. 17. The agreement between the data and the simulation results is very good. The production response of Test 1b is somewhat different from Test 1a. The main reason for difference is the threshold height of the bottom block (see Table 2). Calculated saturation profiles are shown in Fig. 18. This figure provides the desaturation history of the top, middle, and bottom segments. As can be seen, the bottom block is desaturated more than the bottom block of Test 1a (Fig. 2). Calculated final average saturations are 0.336, 0.460, and 0.805, for the top, middle, and bottom segments, respectively.

Test 2b - Gas Injection at 60,000 cm³/hr - The only difference between Test 1b and Test

2b is the injection of nitrogen from the top at a rate of 60,000 cm³/hr (the same as Test 2a). The fracture capillary pressure is available from the simulation of Test 1b. Fig. 19 shows that the simulation results are in agreement with the production data.

The simulation and pressure data are shown in Fig. 10d; the agreement is very good. Comparison of the pressure responses of Tests 2a and 2b indicates that the pressure drop in both tests is consistent with the single phase permeability measurements of each configuration. The permeability ratio of Test 2a/Test 2b is approximately the same as the stabilized pressure ratio of both tests (Test 2a/Test 2b : 6.22 μm²/4.15 μm² ≈ 3.52 kPa/2.28 kPa).

Calculated saturation profiles are shown in Fig. 20. Comparison of this figure with Fig. 18 reveals that the bottom slabs and the middle block drain significantly by viscous forces as compared to Test 1b. Note that the capillary threshold height of the bottom slabs has reduced significantly due to viscous forces (compare Figs. 18 and 20). The calculated average saturation values for the top, middle, and bottom sections are 0.312, 0.365, and 0.665, respectively.

Test 3b - Gravity Drainage and Gas Injection at 60,000 cm³/hr - Measured and simulation results for this test are shown in Fig. 21. The gravity drainage portion of the production data is the same as Test 2b showing the reproducibility of the experiments. The response to nitrogen injection is fast and rate increases to about 2000 cm³/hr from 4.2 cm³/hr. However, the peak rate drops rapidly. The match between pressure data and simulation is also good. Fig. 22 provides the calculated saturation profiles to show the progress of drainage with respect to time and space. The extra desaturation due to injection is not significant for the top slabs of the stack. This may be due to high desaturation prior to gas injection. Similar to Test 2b, forced injection results in significant additional recovery from the bottom slabs due to the reduction in the capillary threshold height. Fig. 10e shows the comparison of the measured and simulated injection pressures.

Test 4b - Tilted Stack with Gravity Drainage and Gas Injection at 60,000 cm³/hr - Due to the non-symmetrical orientation of the slabs and the blocks with respect to the gravity direction, the matrix is additionally gridded in the direction perpendicular to the fractures between the slabs.

For this test, the fracture capillary pressure from Test 1b did not yield a good match of the data and simulation. This could be the result of the changes of contact properties between the blocks and slabs or other effects. Due to tilting, some blocks and especially the slabs slightly slid over each other crushing some of the surface sand grains. The gravity drainage portion of this experiment is used to obtain P_{cf}^o and σ_f (see Table 3). The corresponding aperture value (20 μ) is about 20 % less than the aperture value found from Test 1b (26 μ).

As shown in Fig. 23, the production data match the simulation results before and after nitrogen injection. The injection pressure match is shown in Fig. 10f; the pressure response is very similar to other tests with a peak at the beginning of injection, then a stabilized response at later times.

The calculated saturation profiles are shown in Fig. 24. Similar to Test 4a, the average

saturation of the slabs was measured at the end. The measured saturations are compared with simulation results in Table 4. Agreement between data and calculated results is very good. Maximum deviation belongs to the saturation value of the middle block. Average saturation of the middle block is inferred from the overall material balance and the saturation measurements of the slabs. Therefore, it has some uncertainty with respect to the other slabs. Similar to Test 4a, the measured average block and slab saturations reveal the effect of viscous forces to displace additional liquid. The middle matrix block and the bottom slabs of this test desaturate significantly due to nitrogen injection; especially, the bottom slabs desaturate beyond capillary/gravity equilibrium.

DISCUSSION AND CONCLUSIONS

In the experiments that was simulated above, due to high hydraulic fracture aperture—120 to 150 microns, a large amount of gas was injected to establish a pressure gradient of some 3 to 3.8 kPa/m in the fractures. In some naturally fractured reservoirs containing a light oil of 0.2 mPa·s, fracture aperture is of the order of 10 to 30 microns. Therefore, the gas rate for the same gas pressure gradient in the fractures is much less than those of the tests conducted in this work. We performed a numerical simulation for the system of configuration of Fig. 2b with a fracture aperture of 20 microns. Both gravity drainage and gas injection schemes were modeled. Results revealed that gas injection rates of 10 to 20 times less than the rates of the tests will provide comparable additional recoveries. All the tests except one, were conducted with the coreholder in the vertical direction and therefore the enhancement in recovery from viscous forces is compared to gravity-capillary conditions. The test with 45° tilt reveals that the reduction of end effects by viscous forces also enhances the recovery.

The two main conclusions of this study are:

1. Viscous displacement in some fractured porous media can result in significant additional recovery beyond the gravity-capillary equilibrium.
2. Viscous displacement in fractured porous media is mainly influenced by gas pressure gradient across the displacement length. This gradient in a fracture depends on the fracture aperture and the injection rate.

NOMENCLATURE

h_m^o	=	matrix threshold height for gravity/capillary equilibrium, cm
\mathcal{I}	=	liquid film shape factor
k_m	=	absolute permeability of matrix, μm^2
k_f	=	absolute permeability of fracture, μm^2
k_{rom}	=	matrix relative permeability of liquid (oil) phase
l	=	half fracture aperture, micron

L_x = thickness of the block in x -direction, cm
 L_y = thickness of the block in y -direction, cm
 L_z = height of the block (z -direction), cm
 n_f = exponent in Eq. 1
 N_x = number of grids in the x -direction
 N_y = number of grids in the y -direction
 N_z = number of grids in the z -direction
 P_{cm} = matrix capillary pressure, kPa
 P_{cf} = fracture capillary pressure, kPa
 P_{cm}^o = matrix threshold capillary pressure, kPa
 P_{cf}^o = fracture threshold capillary pressure, kPa
 R = liquid film aspect ratio
 S_o = liquid (oil) saturation
 S_{orm} = residual liquid (oil) saturation in matrix
 S_{orf} = residual liquid (oil) saturation in fracture
 t = time, hours
 t_f = hydraulic fracture aperture, micron

Greek Symbols

σ_m = logarithmic slope of the matrix capillary pressure, kPa
 σ_f = logarithmic slope of the fracture capillary pressure, kPa
 ϕ_m = matrix porosity
 θ = tilt angle (Degrees)
 μ_o = liquid (oil) viscosity, mPa.s
 Δx = x -direction grid size
 Δy = y -direction grid size
 Δz = z -direction grid size

REFERENCES

1. Firoozabadi, A., and Hauge, J.: "Capillary Pressure in Fractured Porous Media," *Journal of Petroleum Technology* (June 1990) 784 - 791, Trans. AIME, 289.
2. Firoozabadi, A., and Ishimoto, K.: "Reinfiltration in Fractured Porous Media - Part 1 - One Dimensional Model," *SPE Advanced Technology Series* (April 1994) 35-44.
3. Amyx, J.W., Bass D.M. Jr., and Whiting, R.L.: *Petroleum Reservoir Engineering, Physical Properties*, McGraw-Hill Book Co., 1960.
4. Firoozabadi, A., and Markeset, T.: "Fracture-Liquid Transmissibility in Fractured Porous Media," *SPE Reservoir Engineering Journal* (August 1994) 201-207.

5. Dindoruk, B. and Firoozabadi, A.: "Computation of Gas-Liquid Drainage in Fractured Porous Media Recognizing Fracture Liquid Flow," *Journal of Canadian Petroleum Technology* (May 1995) 39-49.
6. Dindoruk, B. and Firoozabadi, A.: "Liquid Film Flow In a Fracture Between Two Porous Blocks," *Physics of Fluids* (December 1994) 3861-3869.
7. Firoozabadi, A. and Markeset, T.: "Laboratory Studies in Fractured Porous Media Part I: Reinfiltration for Gas-Liquid Systems," *In Situ* (February 1995) 1-21.
8. Bentsen, R.G. and Anli, J.: "A New Displacement Capillary Pressure Model," *Journal of Canadian Petroleum Technology* (September-October 1991) 75-79.
9. "Eclipse Reference Manual," Version 92A, Exploration Consultants Ltd. (1992).

ACKNOWLEDGMENT

This work was supported by the US Dept. of Energy (Contract No: DE-FG22-93BC14875), and by the members of the Research Consortium on Fractured Petroleum Reservoirs of the Reservoir Engineering Research Institute. Their support is greatly appreciated.

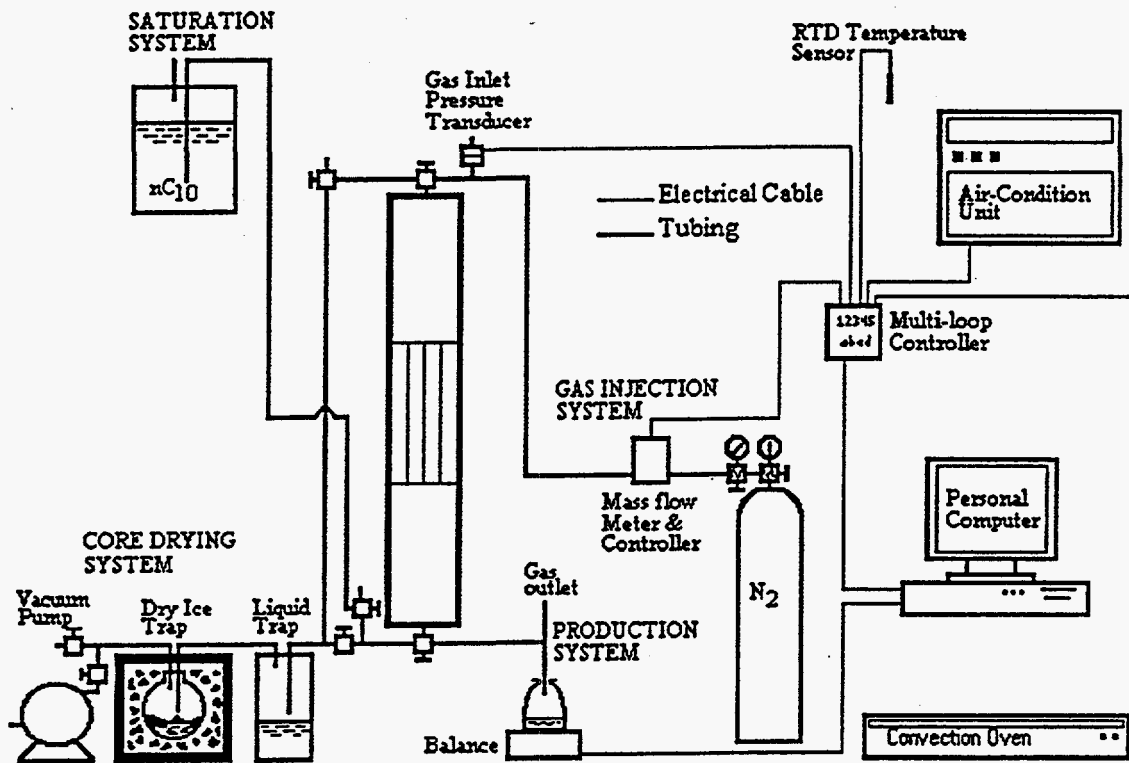


Fig. 1: Viscous Displacement Experimental Setup

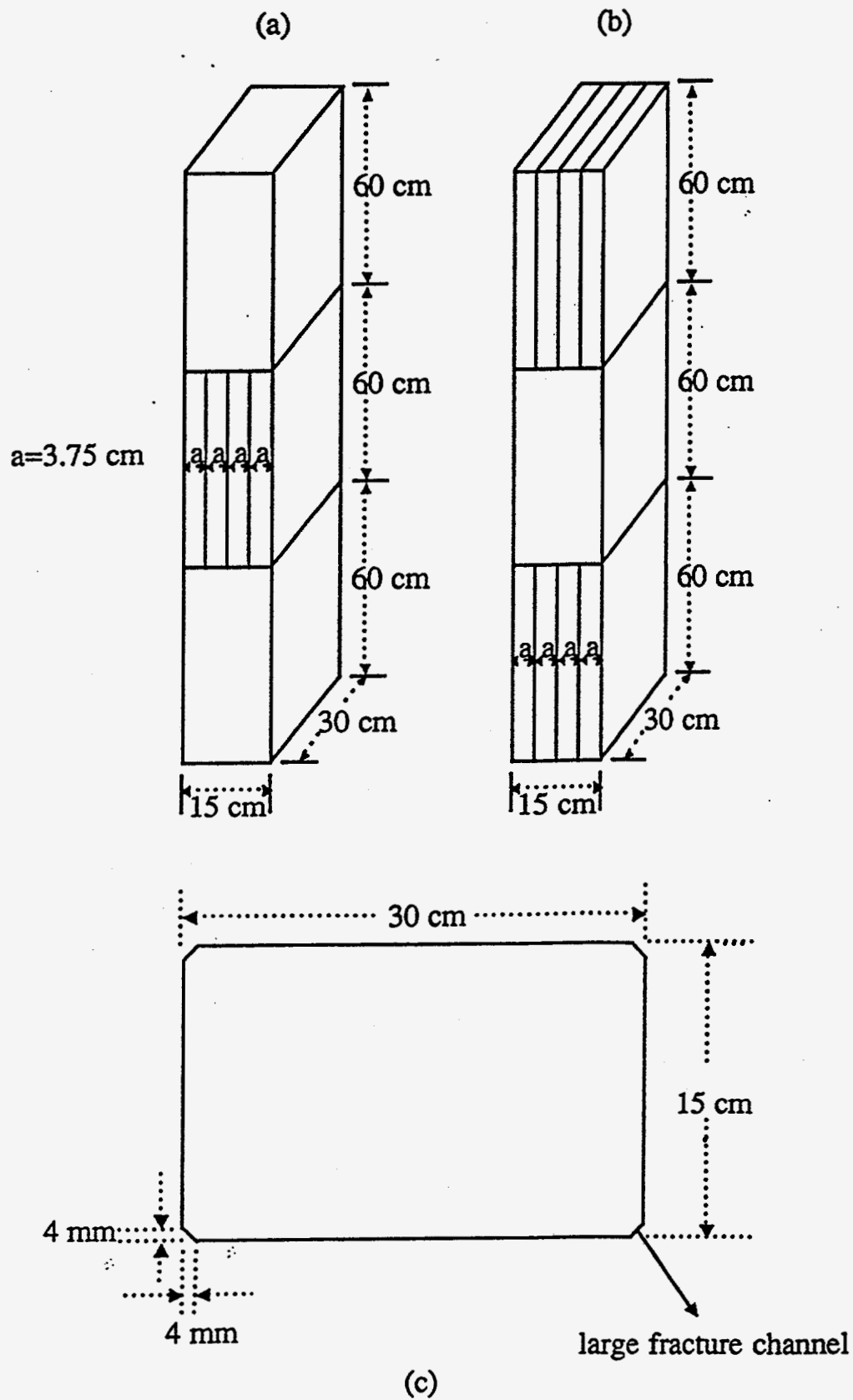


Fig. 2: Matrix-fracture configurations used in the experiments (drawn not to scale)

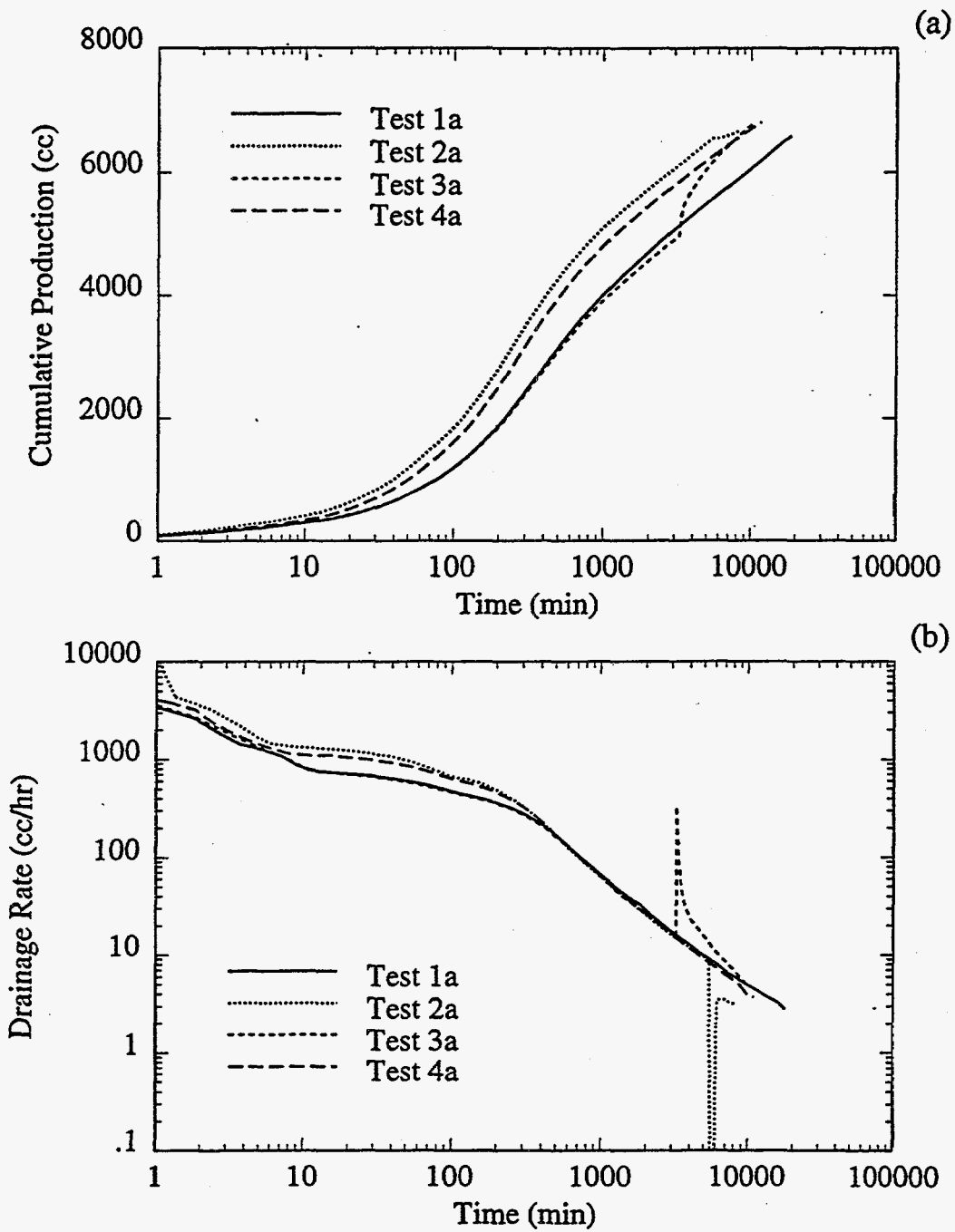
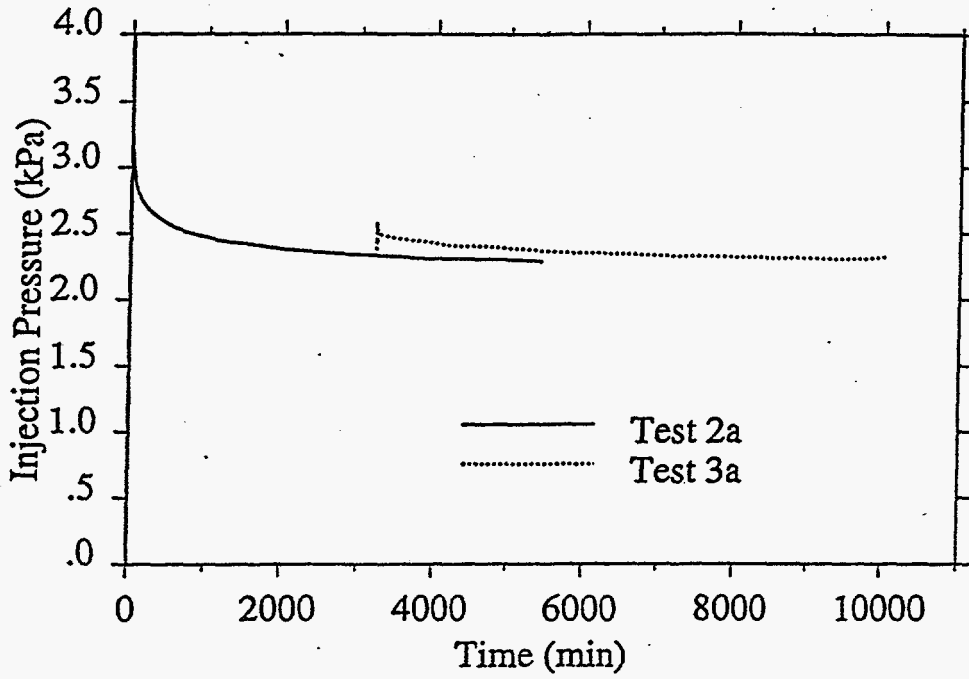


Figure 3: Comparison of cumulative production and rate data of configuration a.

(a) Tests 2a and 3a



(b) Tests 2b, 3b, and 4b

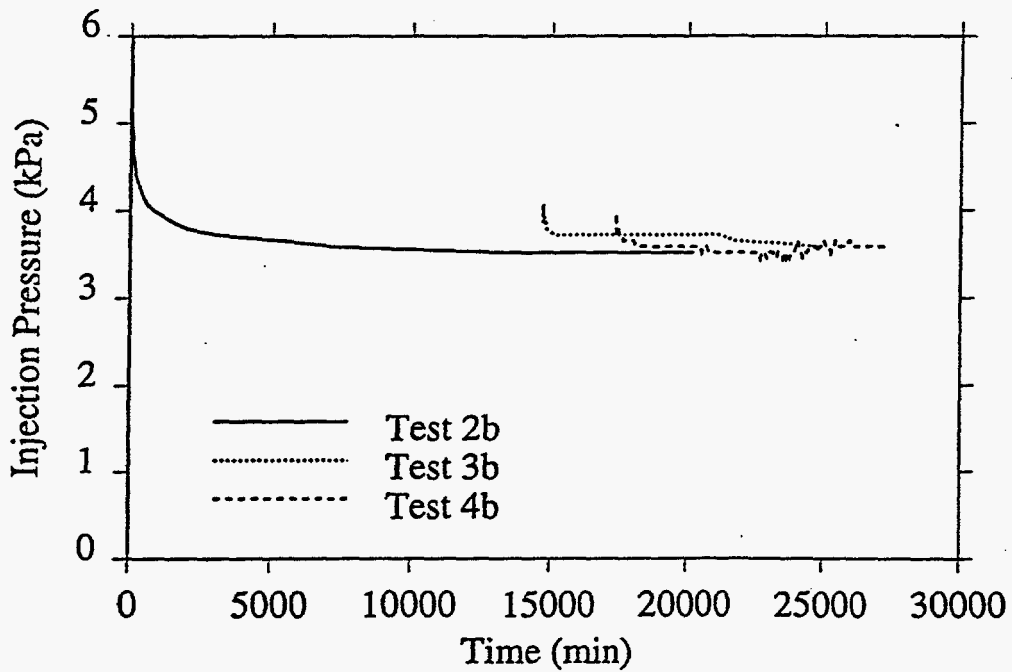


Figure 4: Injection pressure data.

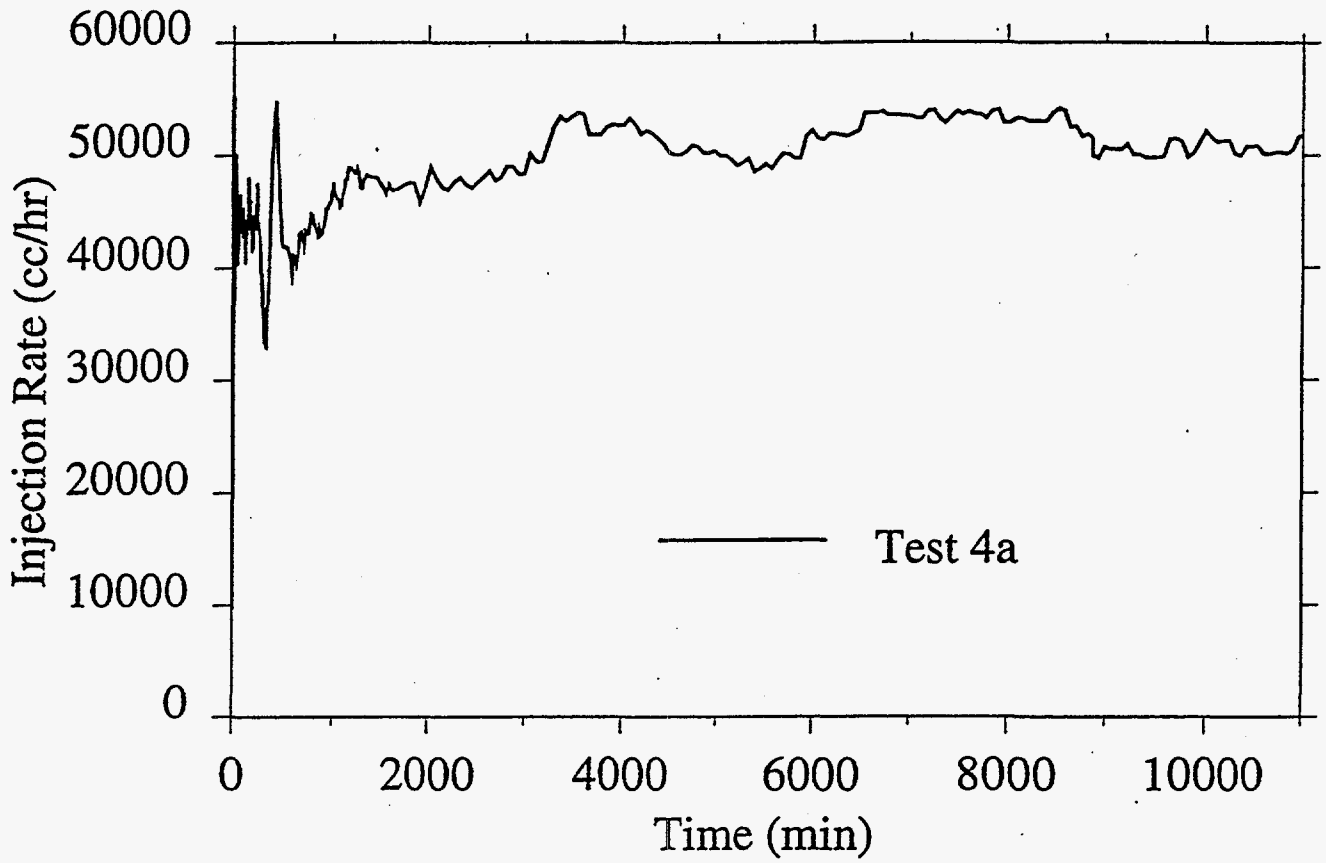


Figure 5: Injection rate data for Test 4a.

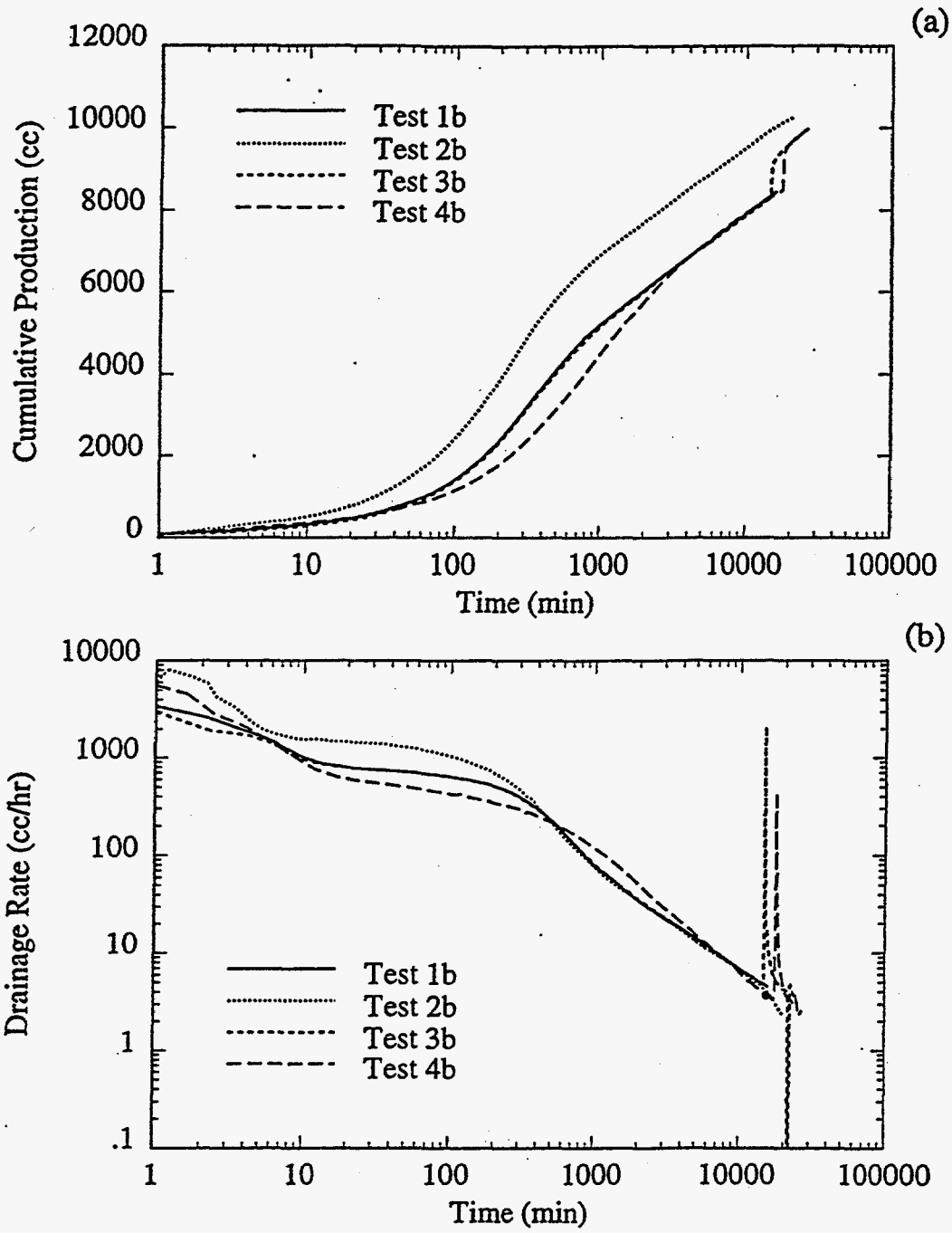


Figure 6: Comparison of cumulative production and rate data of configuration b.

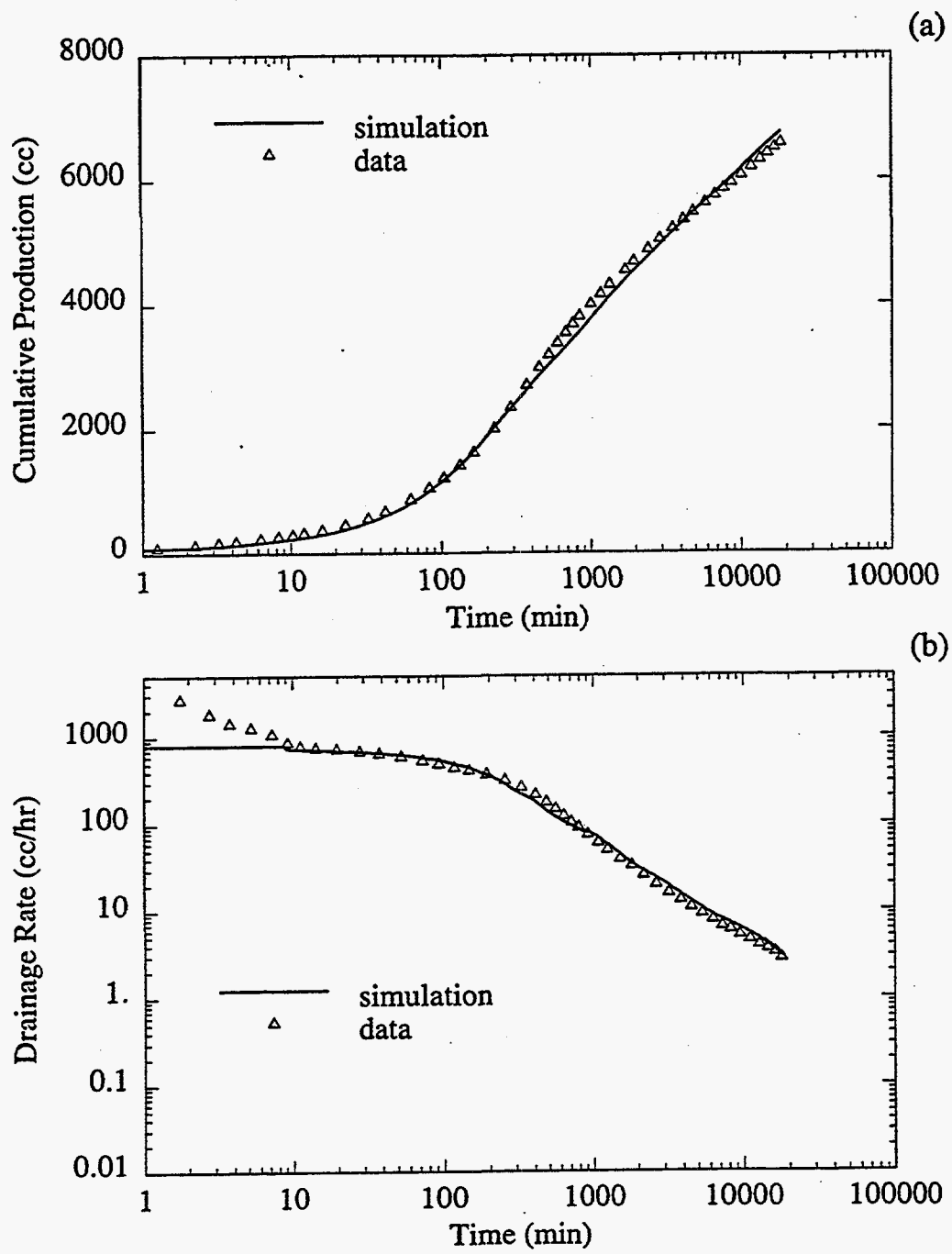


Figure 7: Cumulative production and rate data, and simulation results - Test 1a.

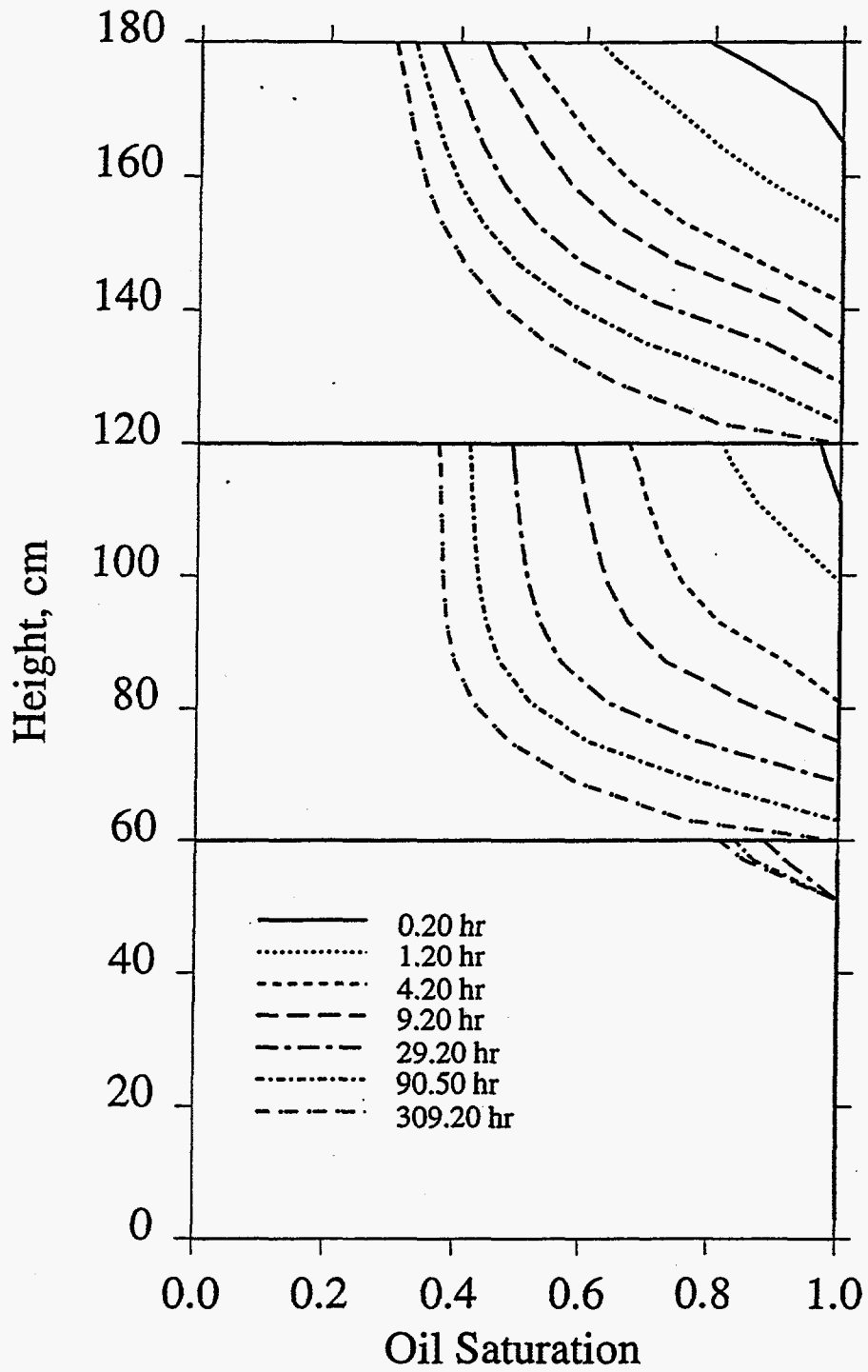


Figure 8: Calculated saturation profiles at different times - Test 1a

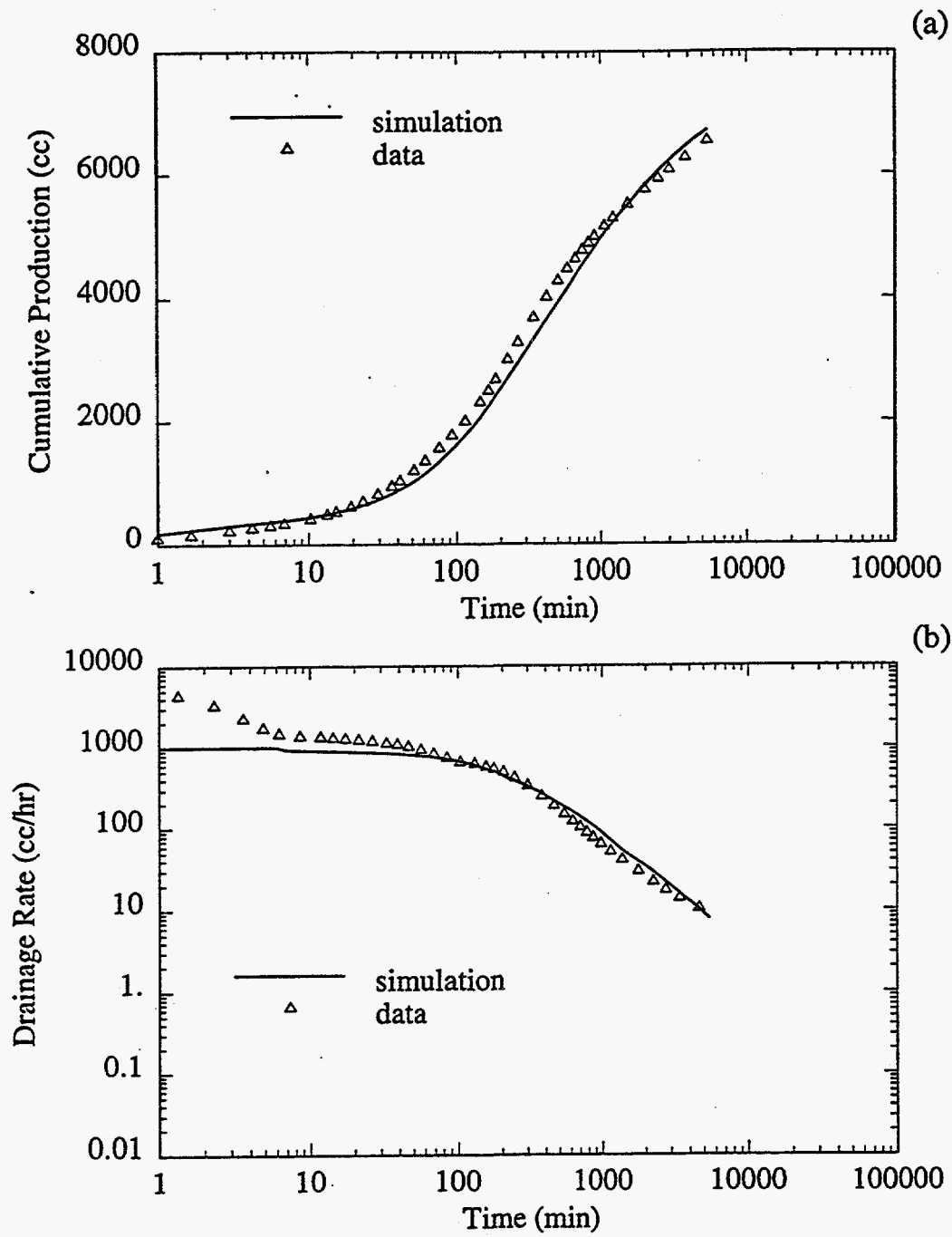
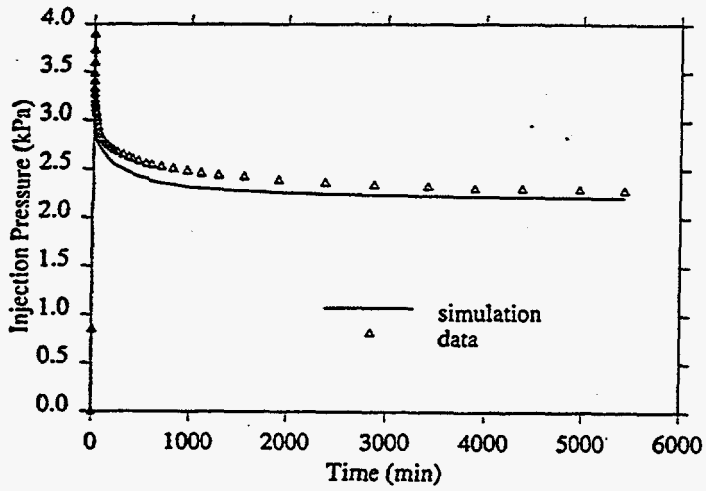
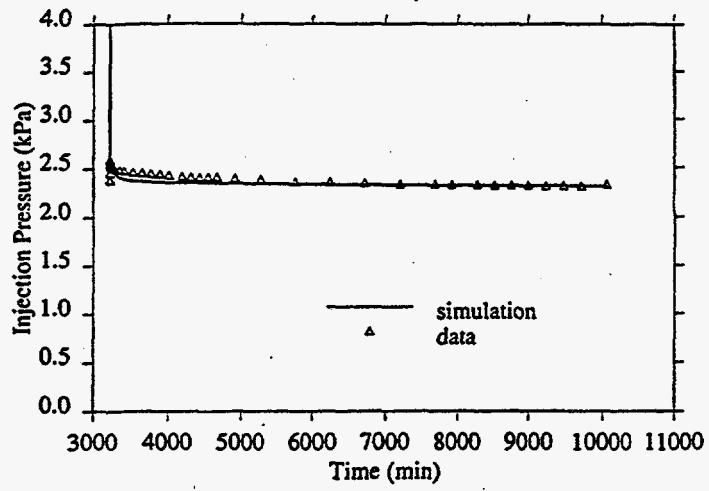


Figure 9: Cumulative production and rate data, and simulation results - Test 2a

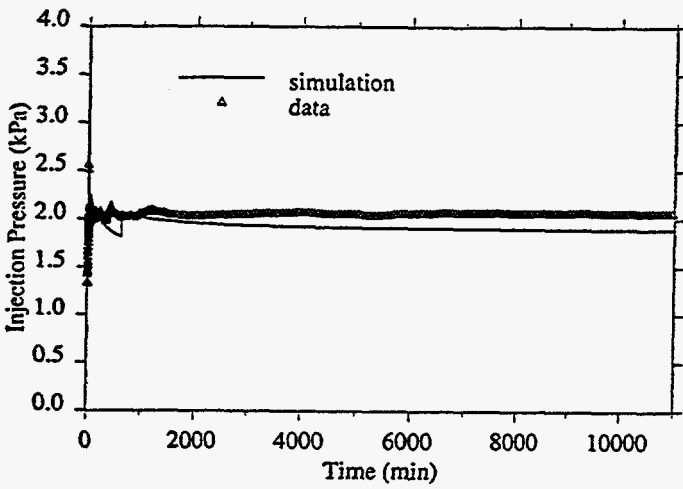
(a) Test 2a



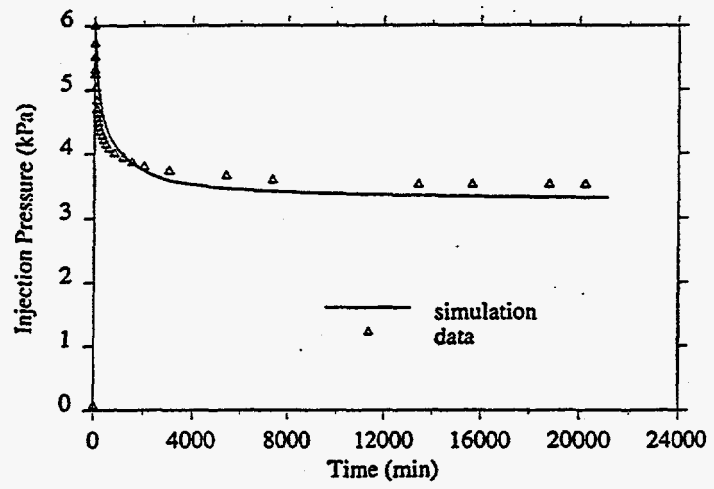
(b) Test 3a



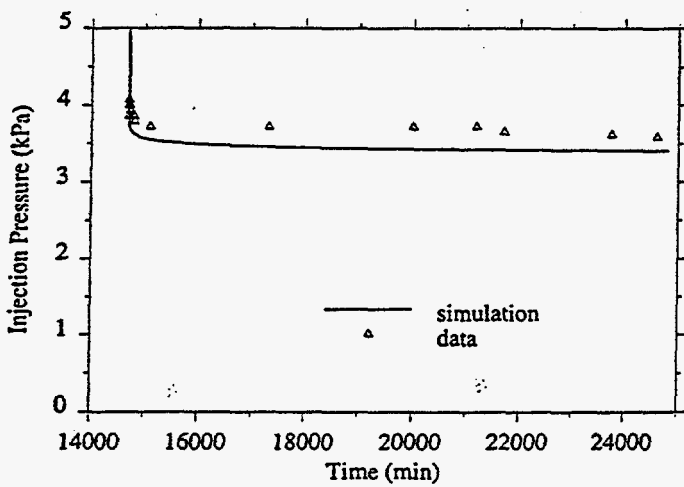
(c) Test 4a



(d) Test 2b



(e) Test 3b



(f) Test 4b

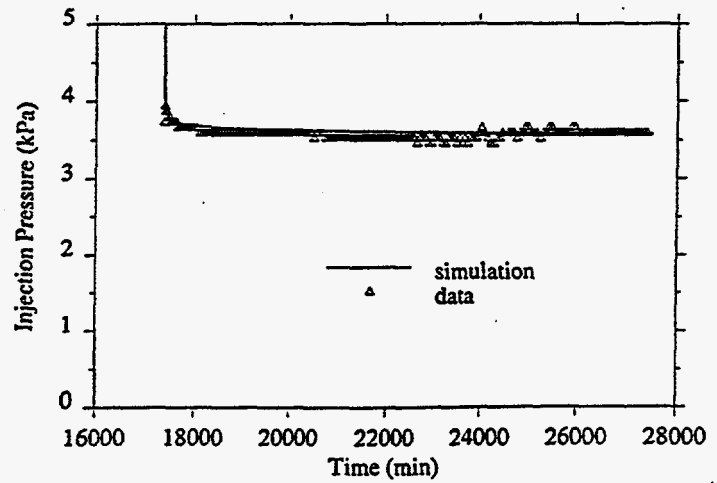


Figure 10: Injection pressure data and simulation results.

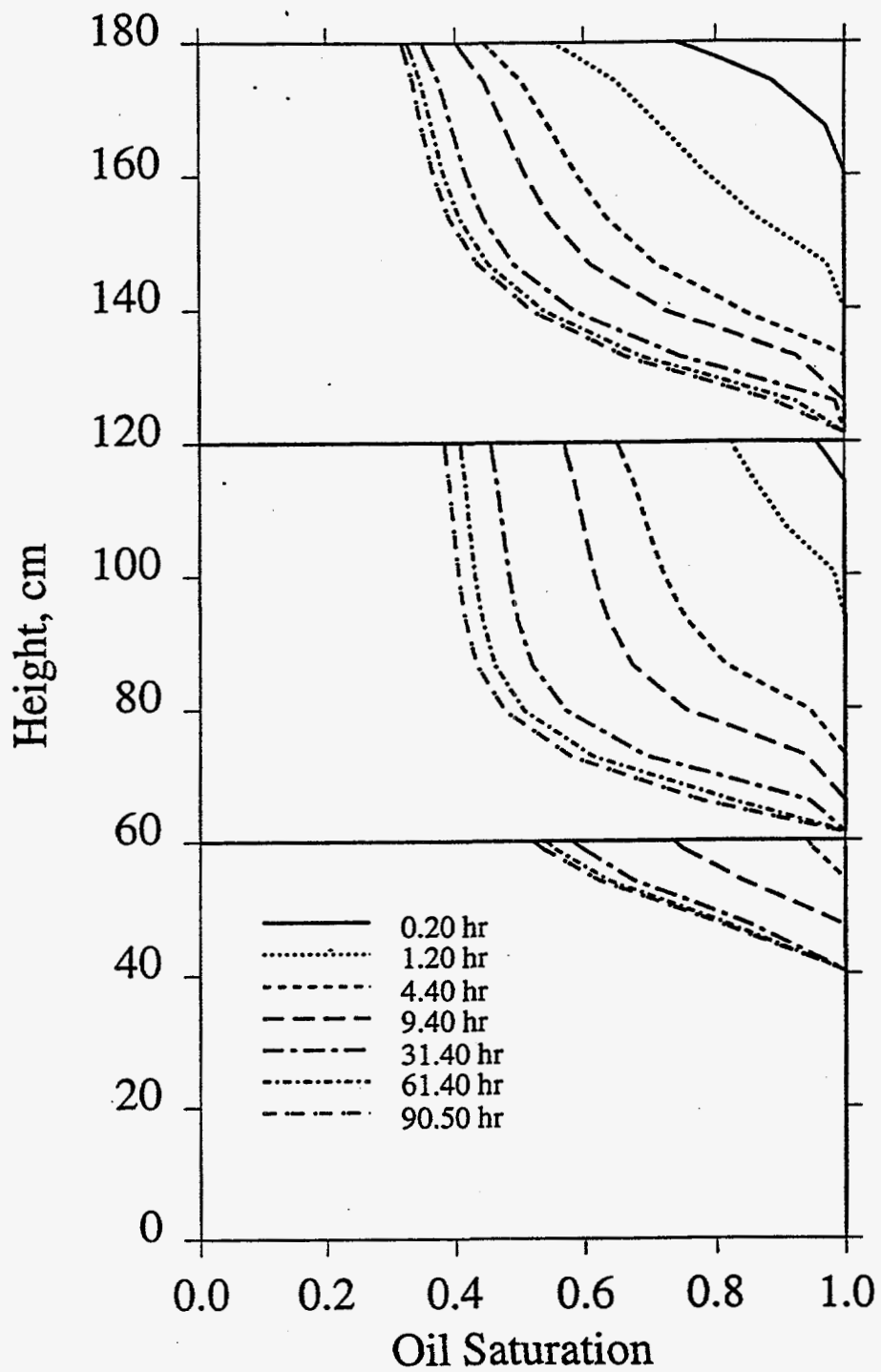


Figure 11: Calculated saturation profiles at different times - Test 2a.

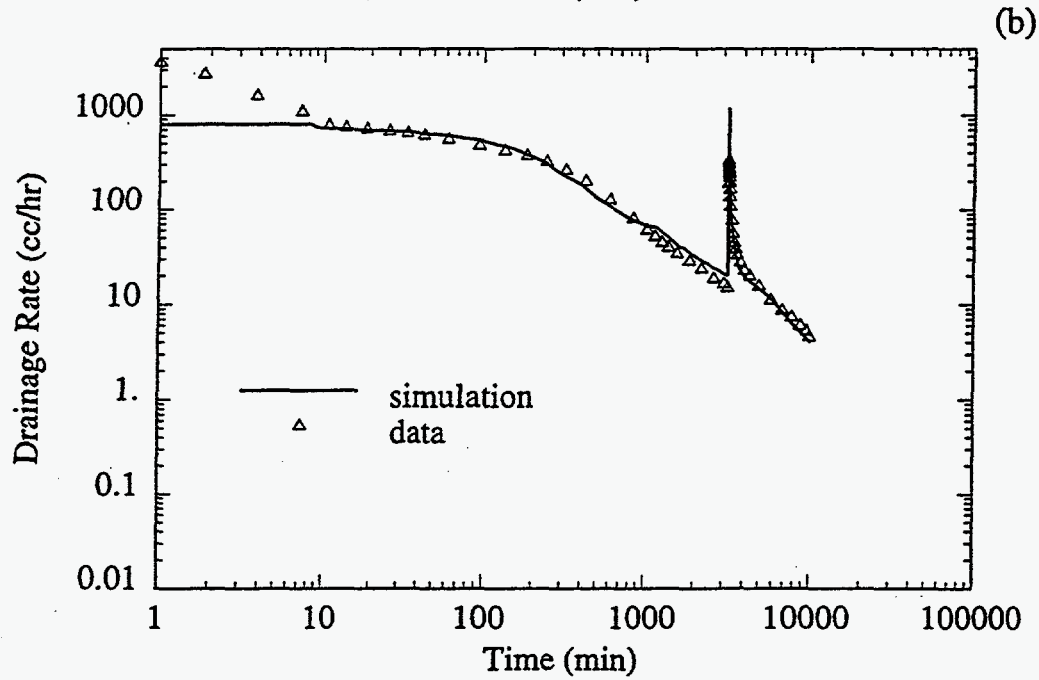
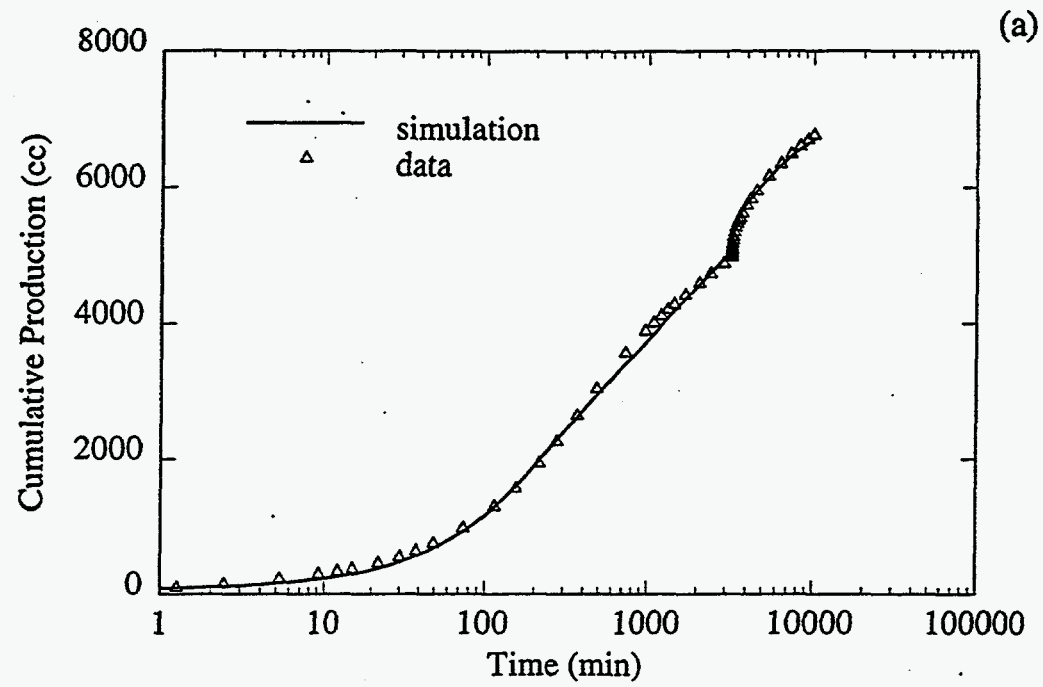


Figure 12: Cumulative production and rate data, and simulation results - Test 3a.

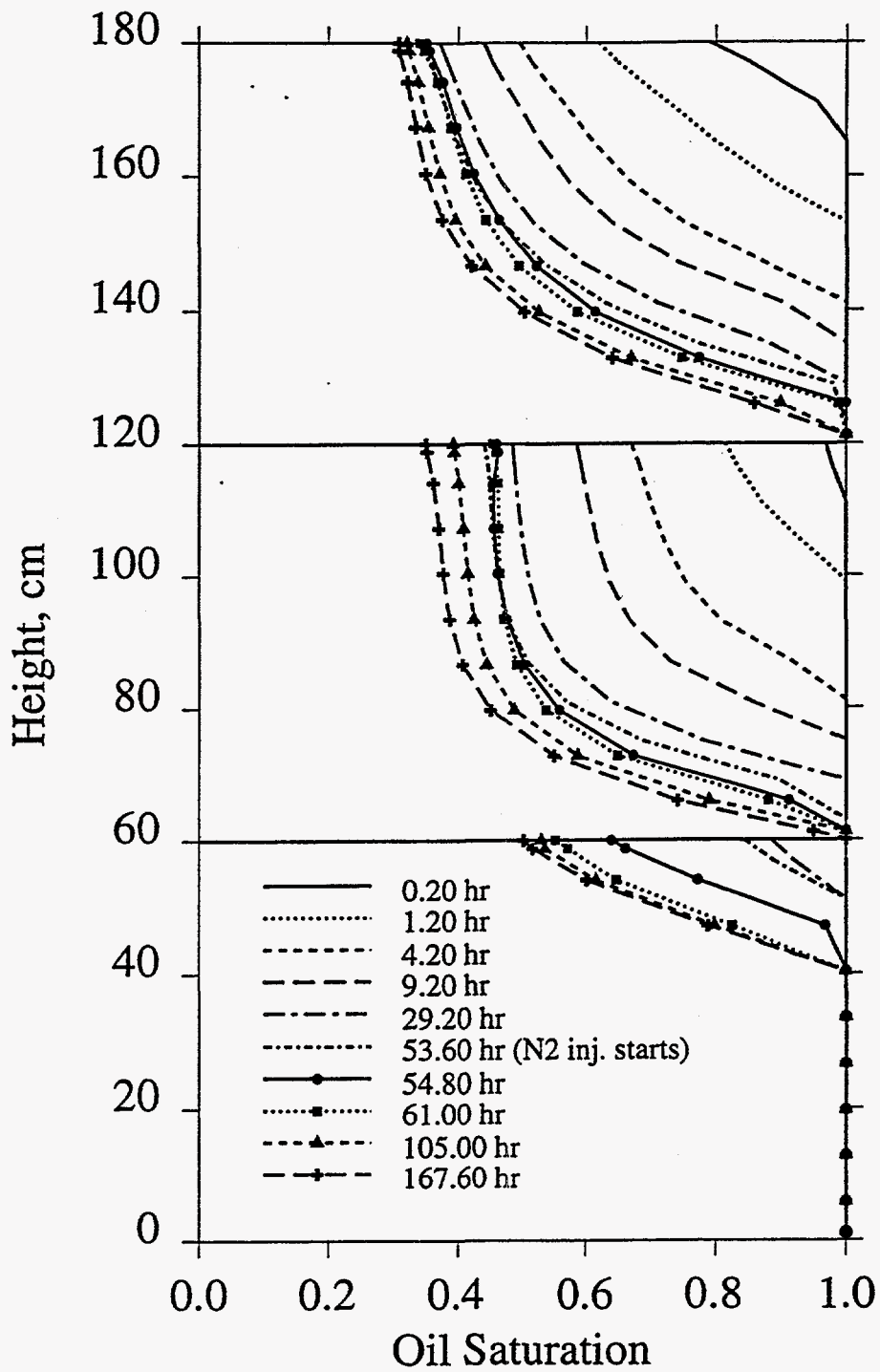


Figure 13: Calculated saturation profiles at different times - Test 3a.

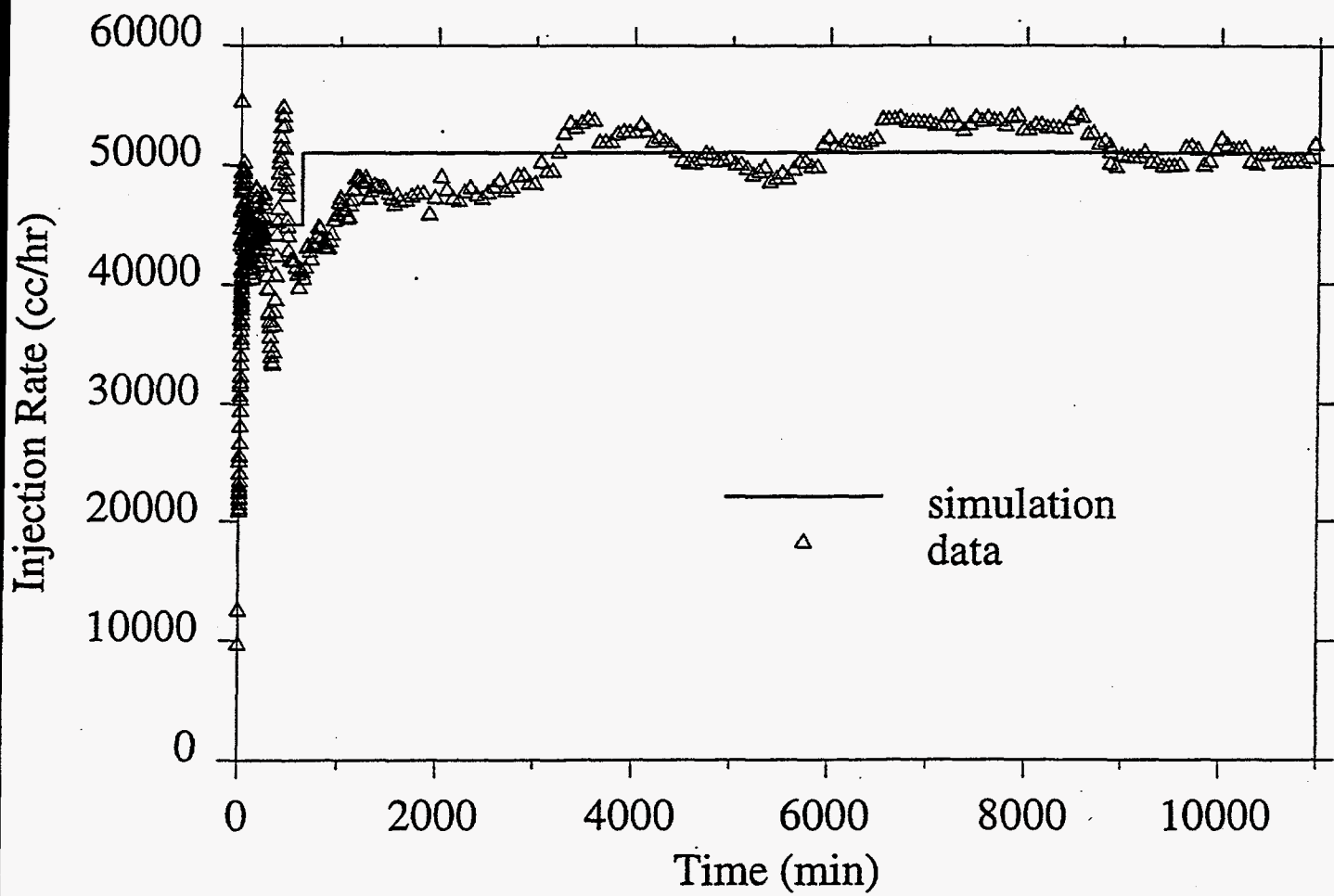


Figure 14: Injection rate data and input rate for simulation - Test 4a.

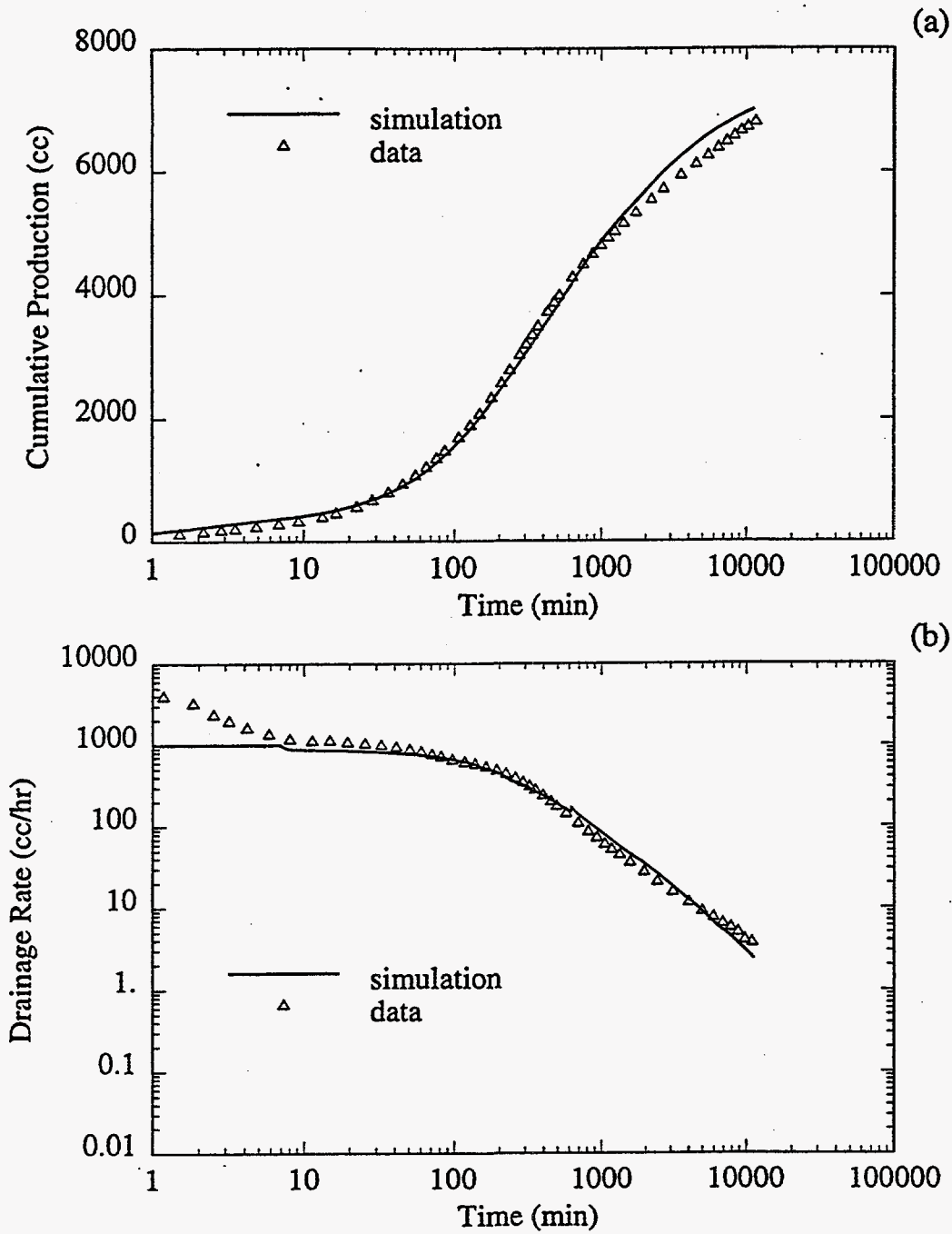


Figure 15: Cumulative production and rate data, and simulation results - Test 4a.

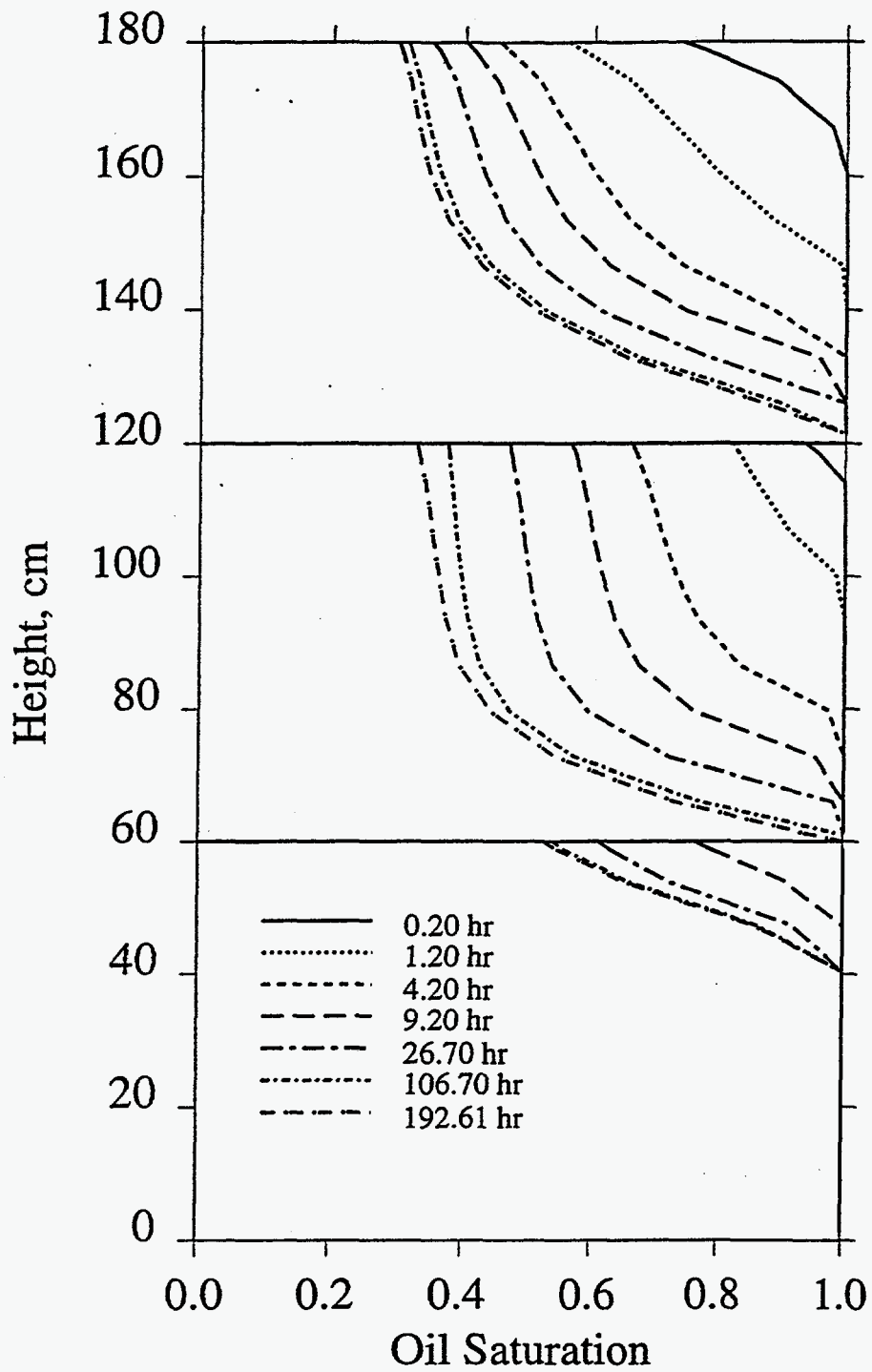


Figure 16: Calculated saturation profiles at different times - Test 4a.

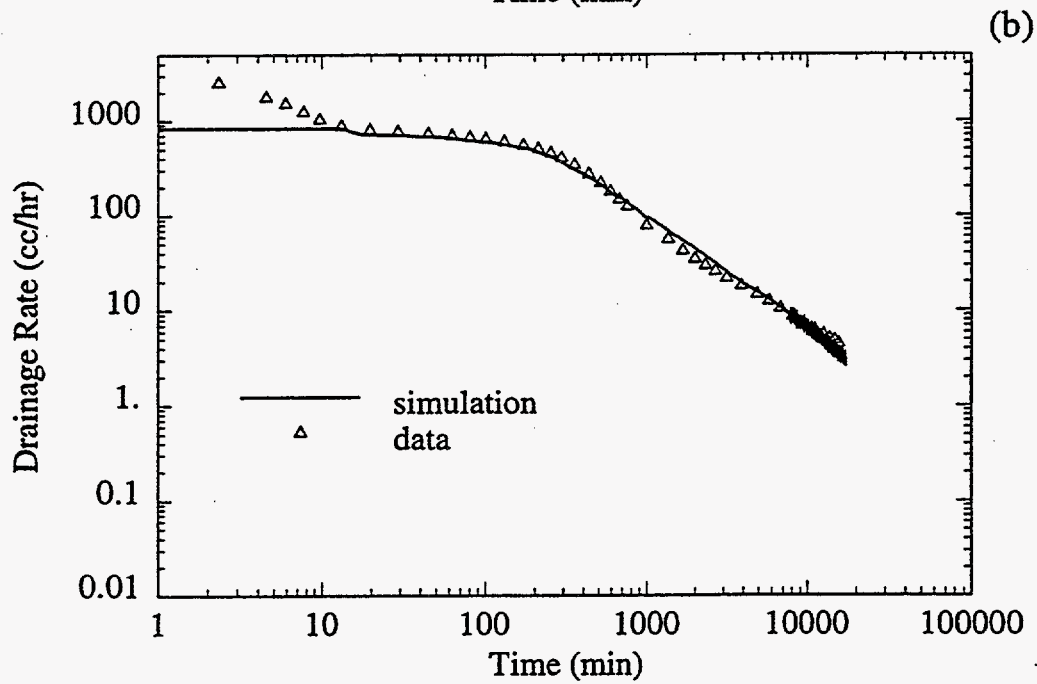
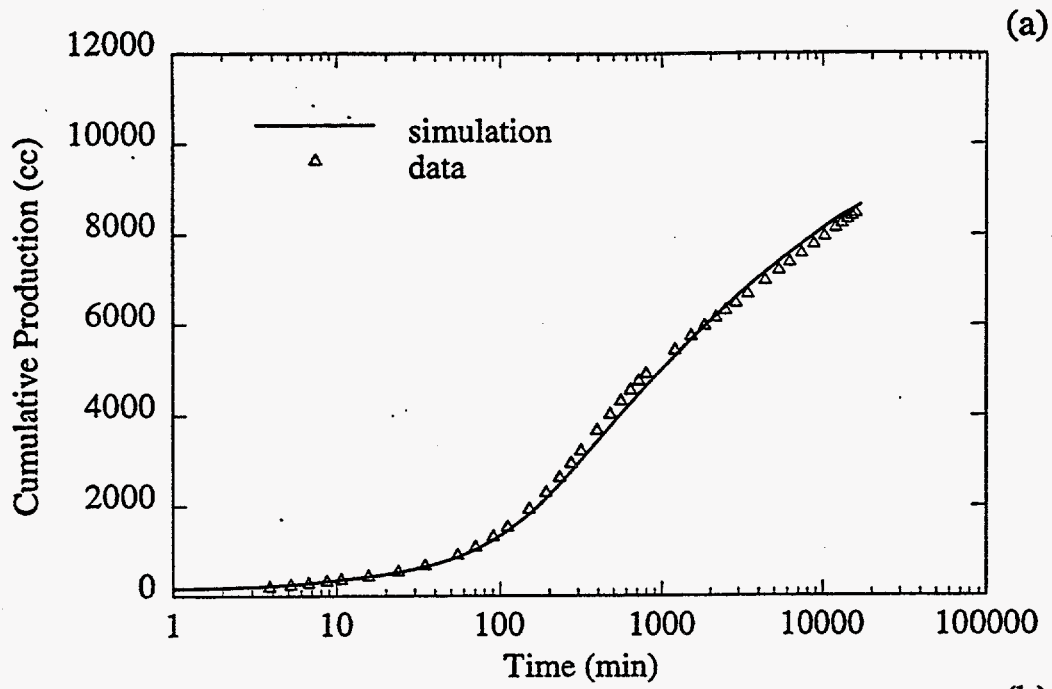


Figure 17: Cumulative production and rate data, and simulation results - Test 1b.

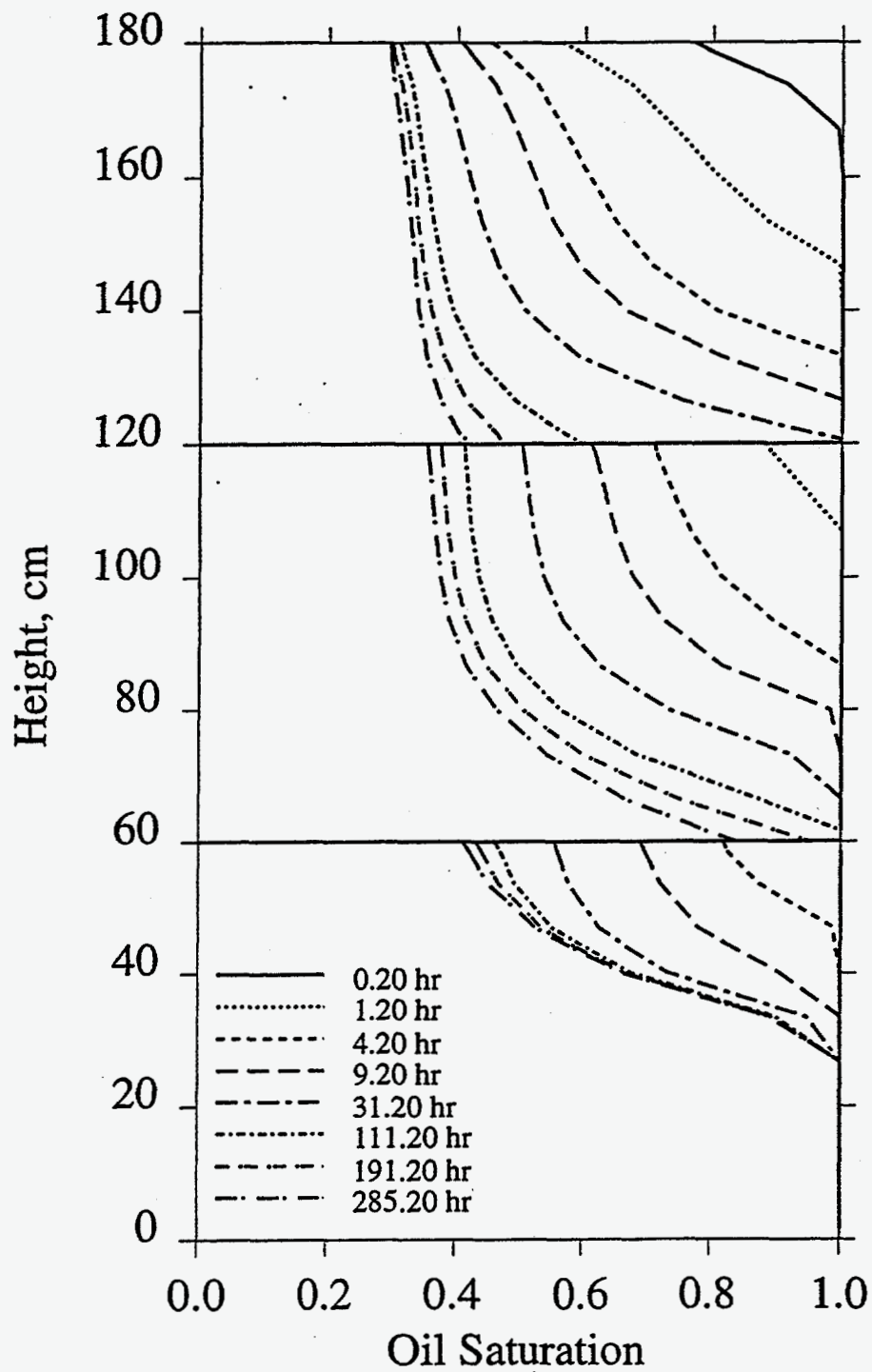


Figure 18: Calculated saturation profiles at different times - Test 1b.

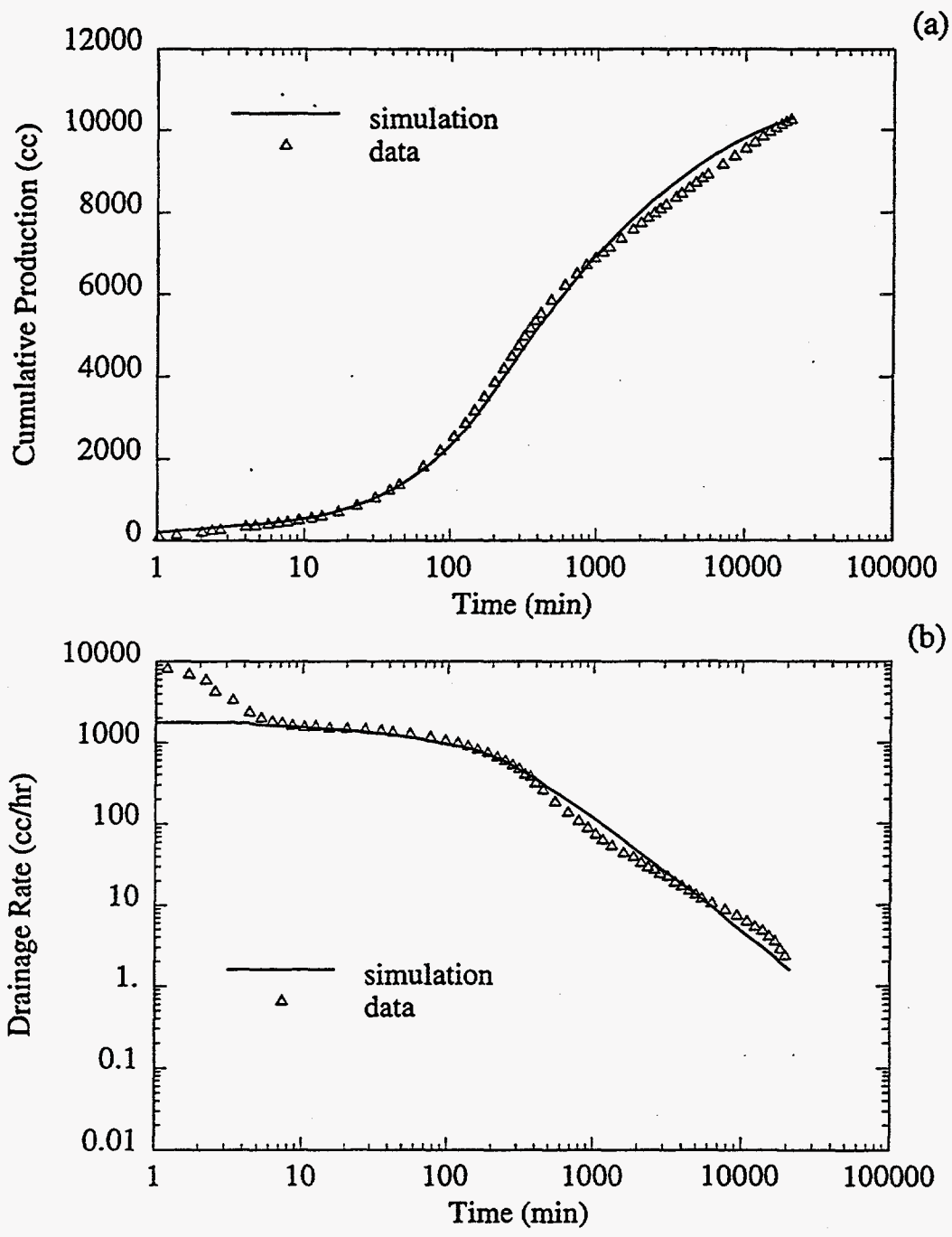


Figure 19: Cumulative production and rate data, and simulation results - Test 2b.

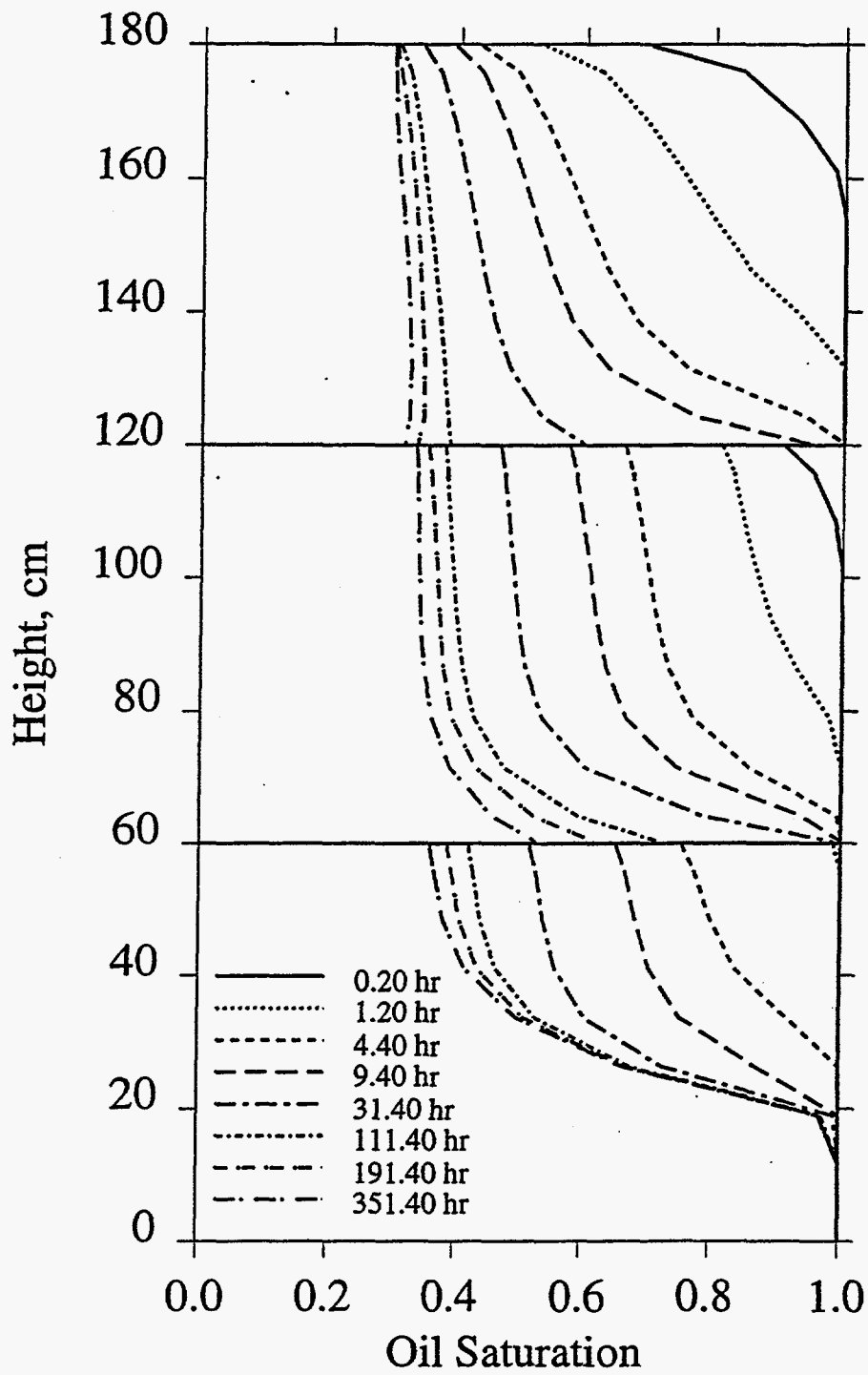


Figure 20: Calculated saturation profiles at different times - Test 2b.

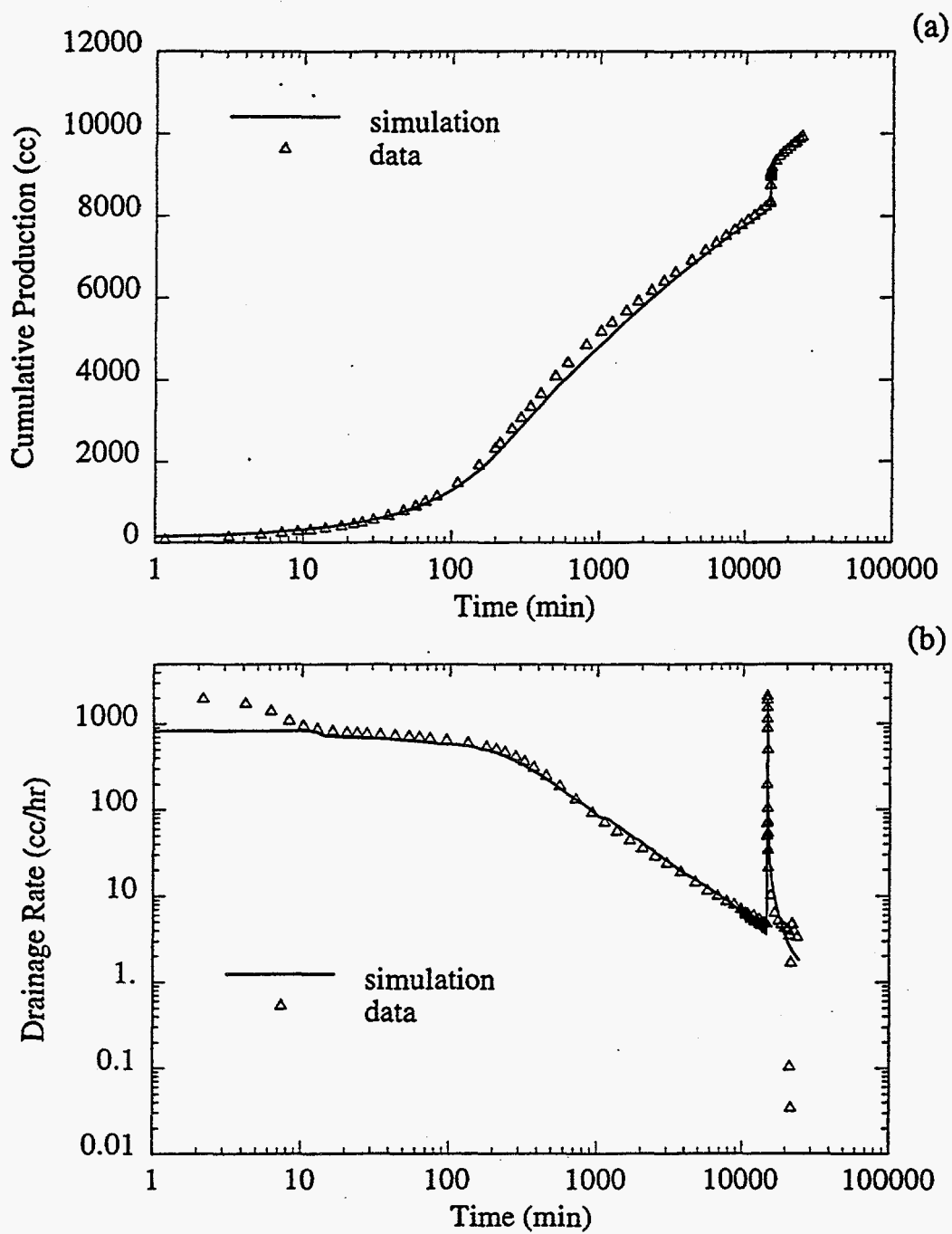


Figure 21: Cumulative production and rate data, and simulation results - Test 3b.

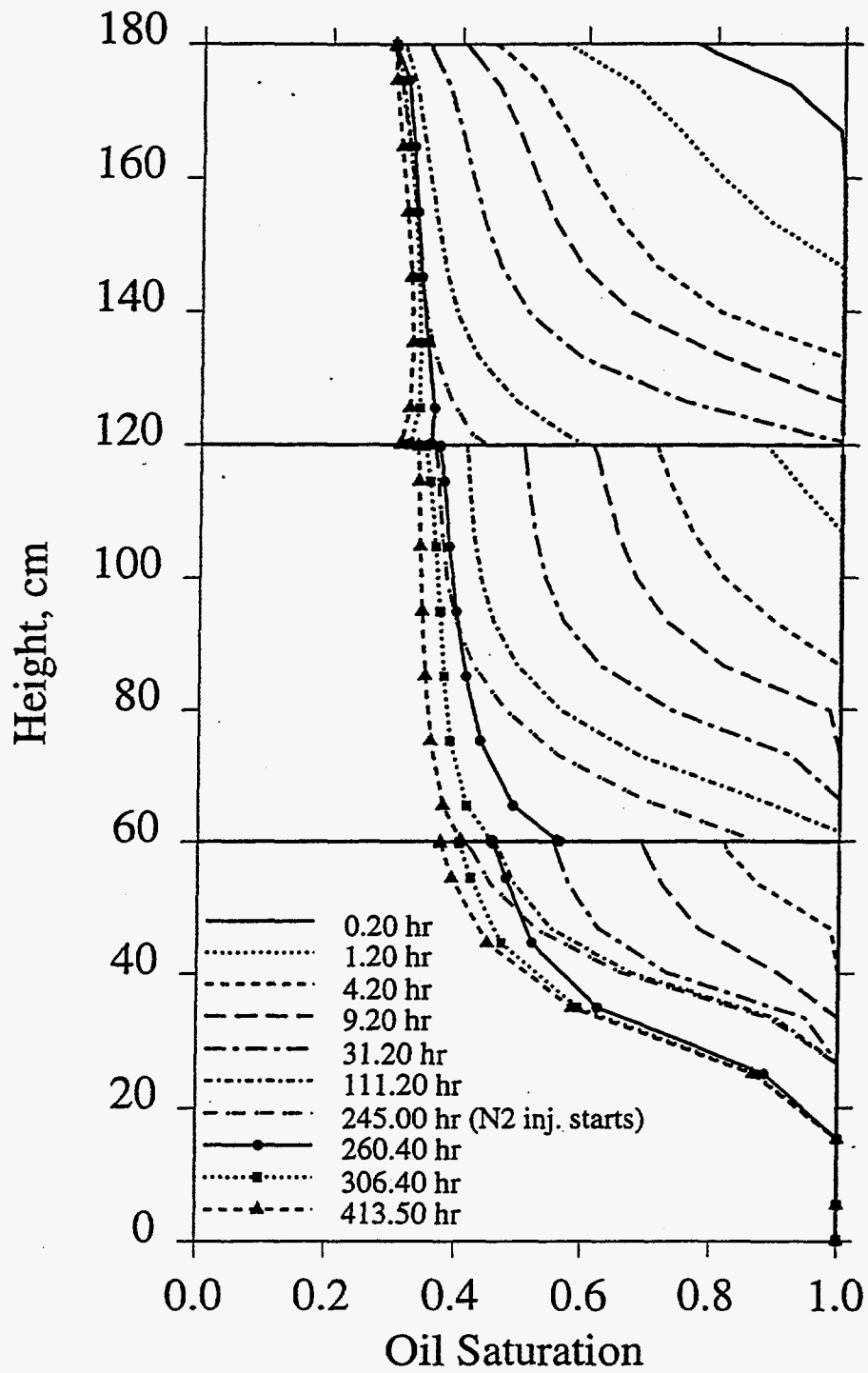


Figure 22: Calculated saturation profiles for Test 3b at different times.

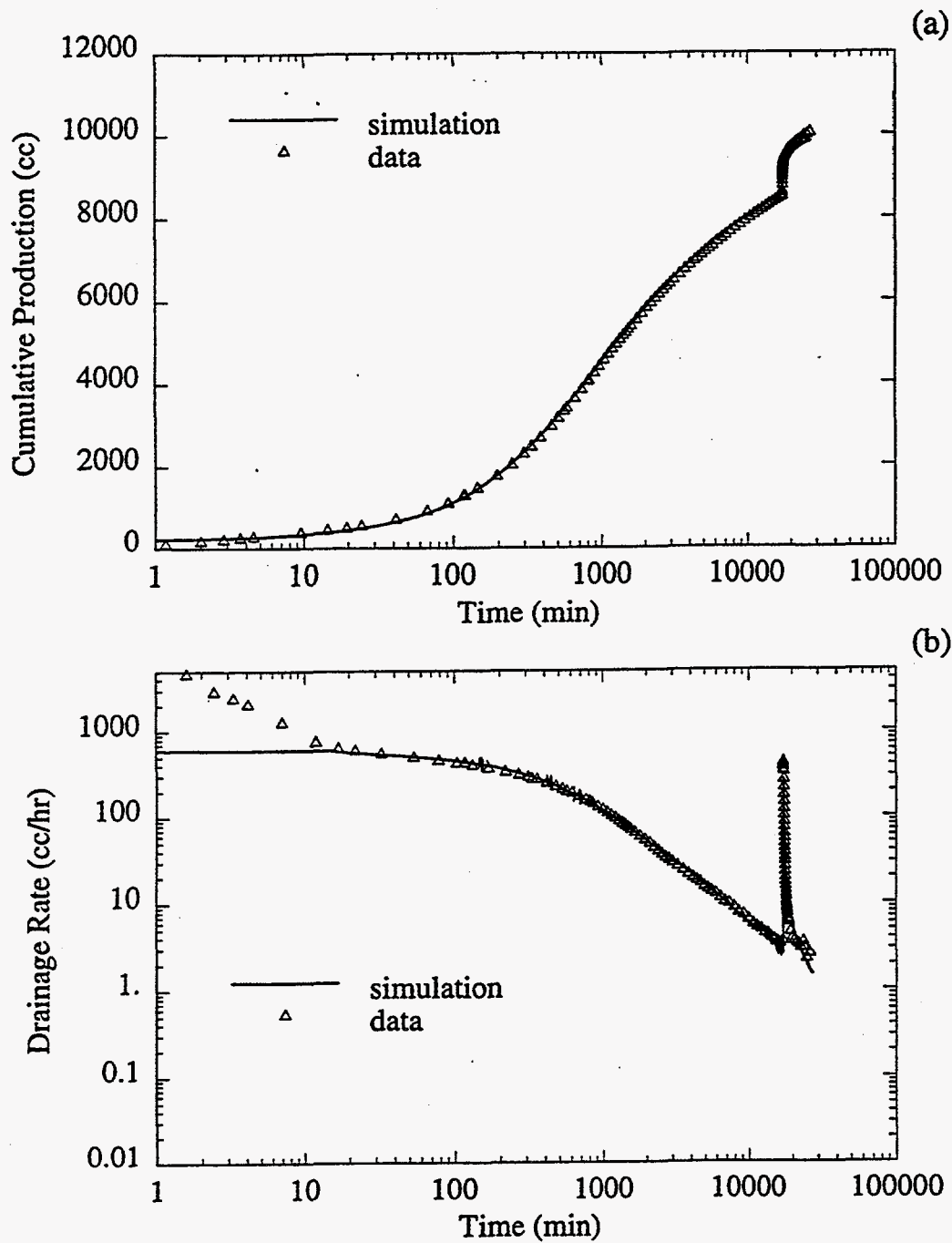


Figure 23: Cumulative production and rate data, and simulation results - Test 4b.

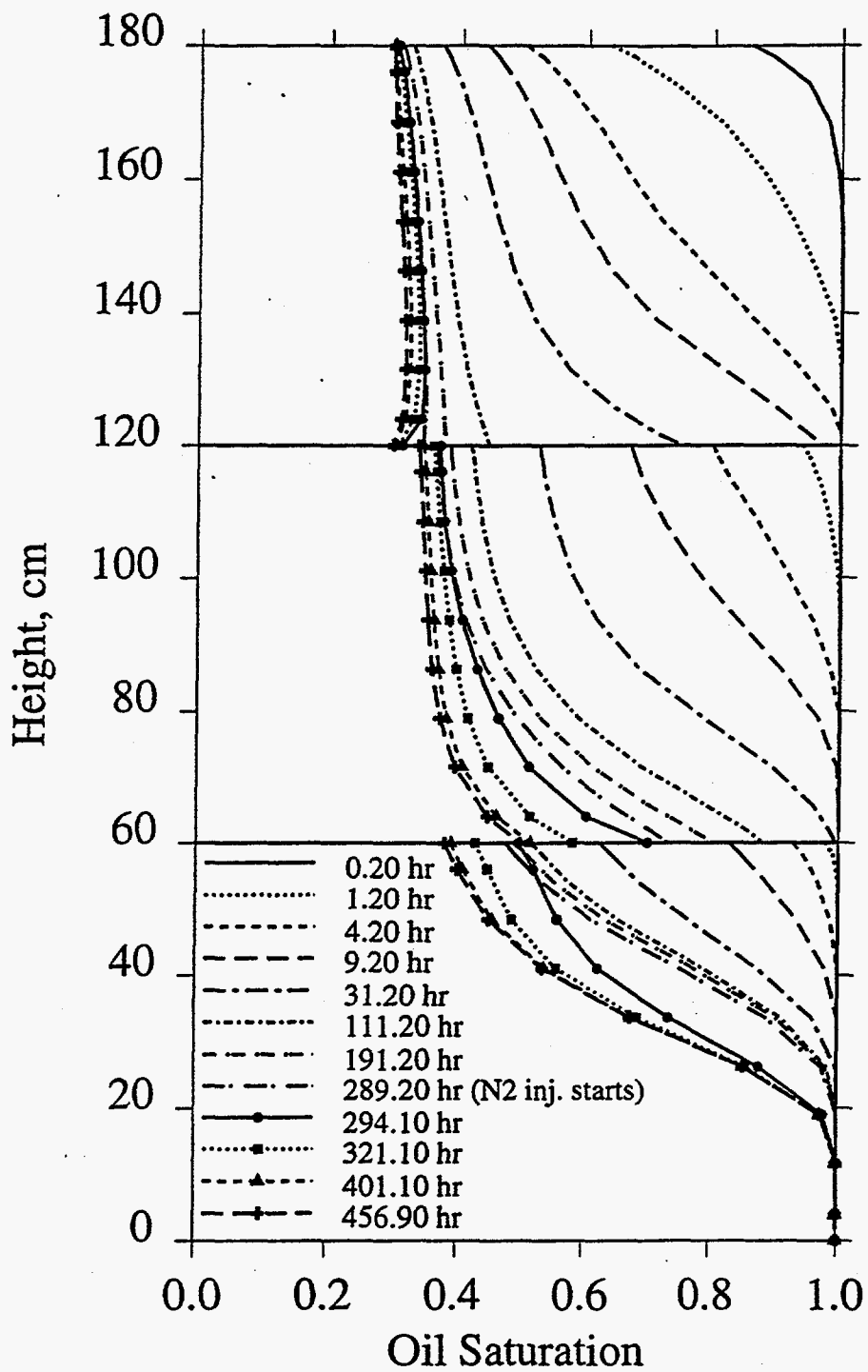


Figure 24: Calculated saturation profiles at different times - Test 4b.

Table 1: Dimensions of blocks and slabs, $L_x \times L_y \times L_z$.

SECTION	BLOCK or SLAB	L_x cm	L_y cm	L_z cm
A	BLOCK	15.00	30.00	60.00
B	SLABS	4×3.75	30.00	60.00
C	BLOCK	15.00	30.00	60.00
D	SLABS	4×3.75	30.00	60.00

Table 2: Matrix data.

VARIABLE	UNITS	BLOCK/SLAB			
		A	B	C	D
k_m	(μm^2)	0.883	0.883	0.883	0.883
σ_m	(kPa)	1.24	0.97	1.24	1.03
P_{cm}^o	(kPa)	2.69	2.34	3.79	2.21
h_m^o	(cm)	37.87	33.01	53.40	31.07
ϕ_m	(fraction)	0.222	0.222	0.210	0.222

Table 3: Fracture permeability and fracture capillary pressure parameters.

CASE	θ (Deg.)	k_f μm^2	S_{orf} (frac.)	σ_f (kPa)	P_{cf}^o (kPa)
Test 1a (30 μm)	0	2.159	0.01	-2.70	0.719
Test 2a (30 μm)	0	2.159	0.01	-2.70	0.719
Test 3a (30 μm)	0	2.159	0.01	-2.70	0.719
Test 4a (30 μm)	0	2.159	0.01	-2.70	0.719
Test 1b (26 μm)	0	1.620	0.01	-3.12	0.826
Test 2b (26 μm)	0	1.620	0.01	-3.12	0.826
Test 3b (26 μm)	0	1.620	0.01	-3.12	0.826
Test 4b (20 μm)	45	0.959	0.01	-4.05	1.078

Table 4: Measured and calculated final saturations for the matrix blocks and slabs of Test 4a, and Test 4b.

CASE	Time hrs	Calculated \bar{S}_o			Measured \bar{S}_o		
		TOP	MID.	BOT.	TOP	MID.	BOT.
Test 4a	192.61	0.490	0.465	0.923	0.508	0.450	0.900
Test 4b	456.93	0.307	0.368	0.733	0.293	0.440	0.678

CHAPTER II

Crossflow in Fractured/Layered Media Incorporating Gravity, Viscous, and Phase Behavior Effects

Birol Dindoruk

Abbas Firoozabadi

Reservoir Engineering Research Institute

SUMMARY

Crossflow across the interfaces of layered reservoirs, and between matrix blocks and fractures in fractured reservoirs may be very pronounced. The literature emphasizes viscous crossflow, however, crossflow due to gravity may be more significant.

In this paper, the crossflow due to various effects in layered and fractured media are presented. The examples selected for the layered media show that most of the oil is first transferred from the low permeability to the high permeability layer and then produced. The examples for fractured media reveal a significant contribution of crossflow to recovery performance. The fractured-media examples imply that a real challenge exists to perform compositional simulation of fractured reservoirs.

INTRODUCTION

Crossflow of fluids between a fracture network and rock matrix in fractured reservoirs, and between different layers in layered reservoirs can be very pronounced in displacement processes. The crossflow could be mainly due to: 1) gravity, 2) capillarity, 3) viscous, 4) phase behavior and compressibility, and 5) diffusion effects. As an example, for certain water injection processes in fractured porous media, due to capillary crossflow, the injected water at the water-oil interface in the fracture imbibes into the matrix and the oil is produced just above the interface. On the other hand, in certain high pressure gas injection processes, phase behavior effects reduce the surface tension significantly and, therefore, the capillary crossflow can be neglected.

In a recent work [1], we have demonstrated that the crossflow of the injected fluid from the fracture to the matrix and the crossflow of the matrix oil to the fracture strongly affect the recovery efficiency. Surprisingly, the crossflow due to gravity [2] is the dominant mechanism for high displacement efficiency for first contact miscible fluid injection in fractured porous media. The investigation of crossflow at conditions other than first contact miscibility is one major goal of this work.

Crossflow in both layered and fractured porous media can be a localized phenomena. With a substantial phase behavior effect between the injected gas and the in-place oil, sharp fronts may give amplified numerical dispersion. The numerical dispersion may mask qualitative and quantitative features of the solution and may make the interpretation difficult. The small fracture pore volume (PV) and the high contrast between the matrix and fracture permeability adds to the complexity of the use of a finite difference simulator. An analytical model would be an ideal tool for the study of flow and composition paths in layered and fractured media. In this work, we use the method of characteristics to solve for fluid flow problems by assuming that capillarity and diffusion are negligible. The assumption of negligible capillary pressure is justified for flow at high pressures and for near-miscible conditions where phase behavior effects are important and the surface tension is very low. The method of characteristics is mainly restricted to one-D and a small number of components, but provides a mechanistic understanding of the problem.

In an early paper, Zapata and Lake [3] studied viscous crossflow in layered media for immiscible fluid systems. Pande and Orr [4] also studied viscous crossflow in a two-layer system incorporating transfer of components between gas and liquid phases but neglected gravity and volume change due to mixing. In a recent study, Tan and Firoozabadi [2] included the effect of gravity in the study of crossflow between a matrix medium and a fracture medium. In all these studies, the effect of volume change on mixing was neglected. When an injected gas dissolves in the oil phase, the volume of the total system may reduce significantly. The subject of viscous crossflow has received considerable attention [3,4]. Crossflow due to viscous forces is generally not very significant. Gravity contribution to crossflow, on the other hand may be pronounced for fractured reservoirs, and for layered reservoirs with tilt angles in the range of 5-15°. Phase behavior effects which include component transfer and volume change due to mixing and incorporation of these effects in the crossflow term may also be important.

This study addresses a comprehensive examination of crossflow in fractured and layered media incorporating gravity, compressibility and phase behavior, and viscous effects. In the following, we will first present the problem formulation, and then outline the solution method. The examples of gas injection in two-layer and fractured media will be discussed, and at the end, conclusions will be drawn from the work.

PROBLEM FORMULATION

The introduction of volume change on mixing complicates considerably the evaluation of the crossflow term, since the sum of flow rates in the layers may change with position. In order to better understand this term, the problem formulation will be presented in two steps. First, flow formulation will be discussed for a homogeneous medium and then in a system with two distinct media consisting of a fracture and a matrix or two layers.

Homogeneous-Medium System. A homogeneous medium can be represented with one set of properties (permeability, porosity, relative permeability, etc.). The governing compo-

nent molar balance equations for one-dimensional multiphase multicomponent systems are given by,

$$A\phi \frac{\partial G_i}{\partial t} + \frac{\partial q_T F_i}{\partial x} = 0, \quad i = 1, \dots, n_c \quad (1)$$

where,

$$G_i = G_i(\vec{Z}) = \sum_{j=1}^{n_p} x_{ij} \rho_j S_j, \quad i = 1, \dots, n_c \quad (2)$$

and

$$F_i = F_i(\vec{Z}, q_T) = \sum_{j=1}^{n_p} x_{ij} \rho_j f_j, \quad i = 1, \dots, n_c. \quad (3)$$

G_i and $q_T F_i$ represent the number of moles of component i per unit pore volume and molar flow rate of component i , respectively. Other symbols are defined in the Nomenclature. The flow rate q_T (in Eq. 1) may not be constant due to volume change on mixing even when the total injection rate at the inlet is held constant. Note that the assumptions of, 1) chemical equilibrium, 2) isothermal flow, 3) negligible capillary and dispersion effect are made in the derivation of Eq. 1. Also note that the thermodynamic properties of the fluid are evaluated at a constant temperature and pressure; this is a good assumption as long as the pressure drop across the system is small.

The boundary and initial overall composition data are given by,

$$\vec{Z}(x, 0) = \begin{cases} \vec{Z}_{inj} & x \leq 0 \\ \vec{Z}_{ini} & x \geq 0 \end{cases} \quad (4)$$

The two constant compositions are injection composition, \vec{Z}_{inj} , and initial composition, \vec{Z}_{ini} .

The solution of the above Reimann problem with constant injection rate and constant injection and initial compositions is a function of a similarity variable, x/t [5,6]. The solution consists of continuous variations, shocks and constant states. The shock speed, Λ , is given by [5,6],

$$\Lambda = \frac{(q_T F_i)^{II} - (q_T F_i)^I}{A\phi(G_i^{II} - G_i^I)}, \quad i = 1, \dots, n_c \quad (5)$$

where the superscript I and II refer to opposite sides of the shock, downstream and upstream, respectively. Eq. 5 can be obtained by a material balance across the shock [5,6]. Dumoré, Hagoort and Risseuw [7] give a detailed account of the one-D analytical model for a three-component system for a homogeneous medium.

Two-Media System. Consider a two-media flow - one medium, low permeability and the other medium, high permeability. Each medium could represent a layer in layered-media or a fracture or a matrix in fractured media. Two cases are considered; one case in which the two media communicate (crossflow case), the other case in which there is no crossflow between the two media (no-crossflow case). In the following, both cases are discussed.

Crossflow Case. For this case, the problem becomes significantly simplified if we invoke the powerful crossflow equilibrium (CE) assumption between the two media [3,9,10]. Crossflow equilibrium means that the pressures in both media are equal along the displacement length. This is an appropriate assumption for geometries with $R_L = L/H\sqrt{k_v/k_h} > 10$, where k_v is thickness-weighted harmonic vertical permeability and, k_h is thickness-weighted average horizontal permeability [3]; L and H are the total system length and the total system thickness, respectively. Crossflow equilibrium is a key assumption and allows the elimination of the pressure dependency of the problem and solving the system of partial differential equations analytically. The validity of this assumption has been demonstrated in Ref. 10 for fractured media. In that work, the results from fine grid simulation and the analytical model for fractured media comprised of a vertical matrix block and a vertical fracture were compared at two different rates.

The material balance equations for the two-media system are obtained by including the crossflow (source/sink) term to the equations for the homogeneous system. The crossflow term represents the transverse communication of the two layers.

Crossflow Term. The molar flow equations for the two layers are given by

$$A^1 \phi^1 \frac{\partial G_i^1}{\partial t} + \frac{\partial (q_T^1 F_i^1)}{\partial x} + CR_{iM} = 0, \quad i = 1, \dots, n_c \quad (6)$$

$$A^2 \phi^2 \frac{\partial G_i^2}{\partial t} + \frac{\partial (q_T^2 F_i^2)}{\partial x} - CR_{iM} = 0, \quad i = 1, \dots, n_c \quad (7)$$

where $G_i^k = \sum_{j=1}^{n_p} x_{ij}^k \rho_j^k S_j^k$, $F_i^k = \sum_{j=1}^{n_p} x_{ij}^k \rho_j^k f_j^k$, CR_{iM} is the molar crossflow flux of component i from layer 1 to layer 2 (per length), and $k = 1, 2$ is the layer superscript; $k = 1$ is the more permeable medium and $k = 2$ is the less permeable medium. For crossflow from layer 2 to 1, the sign of the last term in Eqs. 6 and 7 is reversed. The relationship between molar crossflow flux of component i and volumetric crossflow flux, CR_{TV} , is given by

$$CR_{iM} = F_i^1 CR_{TV}, \quad i = 1, \dots, n_c, \quad (8)$$

when crossflow is from medium 1 to medium 2. Combining Eqs. 6 and 7 and summing over all the components yields,

$$CR_{TV} = \frac{-1}{\sum_{i=1}^{n_c} F_i^1} \sum_{i=1}^{n_c} \left[A^1 \phi^1 \frac{\partial G_i^1}{\partial t} + \frac{\partial (q_T^1 F_i^1)}{\partial x} \right]. \quad (9)$$

Note that the crossflow term given by Eq. 9 depends not only on $\partial q_T^1 / \partial x$ but also varies with $\partial G_i^1 / \partial t$ and $\partial F_i^1 / \partial x$. These last two terms are due to the volume change on mixing.

Rewriting the molar flow Eqs. 6 and 7 in dimensionless form with the expression of

crossflow from Eq. 9,

$$R^1 \frac{\partial G_i^1}{\partial t_D} + \frac{\partial (q_{TD}^1 F_i^1)}{\partial x_D} - \frac{F_i^1}{\sum_{i=1}^{n_c} F_i^1} \sum_{i=1}^{n_c} \left[R^1 \frac{\partial G_i^1}{\partial t_D} + \frac{\partial (q_{TD}^1 F_i^1)}{\partial x_D} \right] = 0, \quad i = 1, \dots, n_c - 1 \quad (10)$$

$$R^2 \frac{\partial G_i^2}{\partial t_D} + \frac{\partial (q_{TD}^2 F_i^2)}{\partial x_D} + \frac{F_i^1}{\sum_{i=1}^{n_c} F_i^1} \sum_{i=1}^{n_c} \left[R^1 \frac{\partial G_i^1}{\partial t_D} + \frac{\partial (q_{TD}^1 F_i^1)}{\partial x_D} \right] = 0, \quad i = 1, \dots, n_c \quad (11)$$

where

$$G_i^k = G_i^k(\vec{Z}^k) = \sum_{j=1}^{n_p} x_{ij}^k \rho_{jD}^k S_j^k, \quad i = 1, \dots, n_c, \quad k = 1, 2 \quad (12)$$

$$F_i^k = F_i^k(\vec{Z}^1, \vec{Z}^2, q_{TD}^k) = \sum_{j=1}^{n_p} x_{ij}^k \rho_{jD}^k f_j^k, \quad i = 1, \dots, n_c, \quad k = 1, 2. \quad (13)$$

Since the summation is used over all components in Eq. 6 to obtain the crossflow term, there will be only $n_c - 1$ independent equations in Eq. 10. The dimensionless variables and parameters are defined by

$$x_D = x/L, \quad t_D = \frac{q_{T,inj} t}{\phi A_T L}, \quad q_{TD}^k = \frac{q_T^k}{q_{T,inj}}, \quad \rho_{jD} = \rho_j / \rho_{ini}, \quad R^k = \frac{\phi^k A^k}{\bar{\phi} A_T}, \quad \bar{\phi} = \sum_{k=1}^2 \phi^k A^k / A_T, \quad A_T = \sum_{k=1}^2 A^k \quad (14)$$

where L is the system length.

The total mass balance for component i is the sum of Eqs. 10 and 11,

$$\frac{\partial G_i^T}{\partial t_D} + \frac{\partial F_i^T}{\partial x_D} = 0, \quad i = 1, \dots, n_c - 1 \quad (15)$$

where $G_i^T = R^1 G_i^1 + R^2 G_i^2$, and $F_i^T = q_{TD}^1 F_i^1 + q_{TD}^2 F_i^2$.

The total molar balance of all the components can be obtained by summing Eq. 15 from $i = 1$ to n_c ,

$$\frac{\partial G^T}{\partial t_D} + \frac{\partial F^T}{\partial x_D} = 0 \quad (16)$$

where $F^T = \sum_{i=1}^{n_c} F_i^T$, and $G^T = \sum_{i=1}^{n_c} G_i^T$. We then solve Eqs. 10, 15, and 16 instead of Eqs. 10 and 11. Similar to the homogeneous system, the initial and boundary conditions given by Eq. 4 apply to both media of the two-media system. The total flow rate in layer k , q_{TD}^k , can be related to the total flow rate in layer l , q_{TD}^l , \vec{Z}^k and \vec{Z}^l using the crossflow

equilibrium assumption, $dP^1/dx_D = dP^2/dx_D$. From the Darcy law, the pressure gradient of each medium is given by

$$\frac{dP^k}{dx_D} = -\frac{q_{TD}^k q_{T,inj} L}{A^k k^k \lambda_T^k} - \frac{gL \sin \theta}{\lambda_T^k} \sum_{j=1}^{n_p} \lambda_j^k M_j^k \rho_j^k, \quad k = 1, 2. \quad (17)$$

Using the crossflow equilibrium,

$$q_{TD}^k = C_R \frac{\lambda_T^k}{\lambda_T^l} \left[q_{TD}^l + \frac{A^l k^l g \sin \theta}{q_{T,inj}} \sum_{j=1}^{n_p} \lambda_j^l M_j^l \rho_j^l \right] - \frac{A^k k^k g \sin \theta}{q_{T,inj}} \sum_{j=1}^{n_p} \lambda_j^k M_j^k \rho_j^k, \quad k, l = 1, 2, \quad k \neq l \quad (18)$$

where the capacitance ratio, C_R , is defined as $C_R = A^k k^k / A^l k^l$. Eq. 18 can be used to calculate q_{TD}^k once q_{TD}^l ($l \neq k$), \bar{Z}^k , and \bar{Z}^l are known.

No-Crossflow Case. The flow equations for the no-crossflow (NC) case are similar to the equations for the CE case (Eqs. 10 and 11) without the crossflow term. In NC, the rates of the two media are related through the pressure drop boundary condition across the displacement length, $0 \leq x_D \leq 1$,

$$\Delta P^1 = \Delta P^2. \quad (19)$$

The pressure differences, ΔP^1 and ΔP^2 can be obtained by integrating the Darcy equation using Eq. 17.

$$\int_{x_D=0}^1 dP^k = -\frac{q_{TD,inj}^k L}{A^k k^k} \int_{x_D=0}^1 \frac{q_{TD}^k q_{T,inj}}{q_{TD,inj}^k \lambda_T^k} dx_D - gL \sin \theta \int_{x_D=0}^1 \frac{\sum_{j=1}^{n_p} \lambda_j^k M_j^k \rho_j^k}{\lambda_T^k} dx_D, \quad k = 1, 2. \quad (20)$$

Combining Eqs. 19 and 20 with the constant total injection rate condition at the inlet, $q_{TD,inj}^1 + q_{TD,inj}^2 = 1$, yields

$$q_{TD,inj}^1 = \left\{ \frac{A^1 k^1 g \sin \theta}{q_{T,inj}} \left[\int_{x_D=0}^1 \frac{\sum_{j=1}^{n_p} \lambda_j^2 M_j^2 \rho_j^2}{\lambda_T^2} dx_D - \int_{x_D=0}^1 \frac{\sum_{j=1}^{n_p} \lambda_j^1 M_j^1 \rho_j^1}{\lambda_T^1} dx_D \right] + \frac{A^1 k^1}{A^2 k^2} \int_{x_D=0}^1 \frac{q_{TD}^2}{q_{TD,inj}^2 \lambda_T^2} dx_D \right\} / \left\{ \int_{x_D=0}^1 \frac{q_{TD}^1}{q_{TD,inj}^1 \lambda_T^1} dx_D + \frac{A^1 k^1}{A^2 k^2} \int_{x_D=0}^1 \frac{q_{TD}^2}{q_{TD,inj}^2 \lambda_T^2} dx_D \right\}. \quad (21)$$

Eq. 21 indicates that the individual medium injection rate can vary as displacement process continues. Dependence of rate to other parameters (e.g. layer compositions) is implicit. However, Eq. 21 can be solved explicitly for $q_{TD,inj}^1$ over a time step. In the explicit scheme, the parameters at the right side of Eq. 21 are calculated from the old time step. Composition

profiles of each layer will still be similar to the profiles of a homogeneous system. Each layer is treated separately at a given time step, and solution is obtained using the same procedure as for the homogeneous systems. The details of the solution procedure for a homogeneous system will not be presented here, and can be found elsewhere [8].

SOLUTION TECHNIQUE

The method of characteristics is used to solve the one-dimensional flow equations with Riemann initial data [11]. We selected the system given by Eqs. 10, 15, and 16 with the initial data and boundary conditions of Eq. 4 and the crossflow equilibrium condition given by Eq. 18. Using the chain rule of differentiation for $G_i^k(\vec{Z}^k)$ and $F_i^k(\vec{Z}^k, \vec{Z}^l, q_{TD}^k)$, Eqs. 10, 15, and 16 can be written as

$$([F] - \lambda_D[G])\vec{X} = \vec{0} . \quad (22)$$

Eq. 22 is an eigenvalue problem where λ_D is the eigenvalue and \vec{X} is the eigenvector of the system. $[G]$ and $[F]$ contain the derivatives of the various terms. Explicit expressions for the entries of Eq. 22 for a binary mixture are presented later.

For a given point in the rate-composition space, continuous variations can be obtained by integrating along the eigenvectors of Eq. 22. The integration along an eigenvector requires a starting rate-composition vector, \vec{U}^0 . The solution procedure is as follows: 1) calculate all the eigenvalues, λ_{Dn} , and the associated eigenvectors, \vec{X}_n , 2) take sufficient small step, s , along a selected eigenvector to update the starting rate-composition, $\vec{U}^1 = \vec{U}^0 + s\vec{X}_k$. The full composition path (if permitted) can be obtained by using the same relationship recursively as $\vec{U}^m = \vec{U}^{m-1} + s\vec{X}_k$. Details for the case of no-volume change on mixing are given in Ref. 2.

Discontinuities. Eqs. 10, 15, and 16 or the system of equations given by Eq. 22 may yield multivalued solutions. When the material transport equations fail to describe physically correct single-valued flow, shocks (i.e., discontinuities) are introduced in the solution. Shocks do not satisfy Eq. 22, but they satisfy mass conservation across them. The shock balance equation with crossflow from medium 1 to medium 2 is derived in Appendix A; Eq. A-4 of that appendix corresponds to Eq. 10. The shock balances without the crossflow term corresponding to Eqs. 15 and 16 are [11,12],

$$\Lambda_{Di}^T = \frac{(F_i^T)^{II} - (F_i^T)^I}{(G_i^T)^{II} - (G_i^T)^I}, \quad i = 1, \dots, n_c - 1 \quad (23)$$

and,

$$\Lambda_D^T = \frac{(F^T)^{II} - (F^T)^I}{(G^T)^{II} - (G^T)^I}, \quad (24)$$

which are similar to the shock balances of the homogeneous systems, i.e., Eq. 5. Different symbols for the shock speeds are used to distinguish the right hand sides of the shock

balances. The shock speeds, $\Lambda_{D_i}^k$ (see Eq. A-4), $\Lambda_{D_i}^T$, and Λ_D^T are all equal to each other. In general, Eqs. A-4, 23, and 24 are coupled and their solution can only yield a maximum of $2n_c - 1$ unknowns. Depending on the information at the upstream and downstream of the shock, the shock equations could be coupled with other equations.

The above formulation along with method of characteristics solution procedure is for systems with any number of components. However, as the number of components increases, the degrees of freedom in the composition space also increase, and the solution construction becomes very complicated. In this paper, we restrict our study to binary systems. Even for a binary mixture, the solution usually includes more than two shocks and can become complicated as we will witness next. The shocks with intermediate speeds (intermediate shocks) are generally difficult to resolve, and require iterative schemes. As the qualitative features of the solution change, the solution construction algorithm needs to be modified. Solution of flow systems with volume change on mixing needs an extra level of trial and error procedure, because the total flow velocity in front of the fastest shock is also unknown.

BINARY FLOW AND EXAMPLES

The material balance equations given by Eqs. 11, 15, and 16 can be written for two components, $n_c = 2$. The associated eigenvalue problem and the solution procedure are presented in Appendix B.

The fractional flow equation for the gas phase without capillary pressure is given by,

$$f_g^k = \frac{1 - N_{gr}^k k_{rl}^k}{1 + \frac{\mu_g^k k_{rl}^k}{\mu_l^k k_{rg}^k}} \quad (25)$$

where N_{gr}^k is the gravity number defined by,

$$N_{gr}^k = \frac{k^k A^k (M_g^k \rho_g^k - M_l^k \rho_l^k) g \sin \theta}{\mu_l^k q_T^k} \quad (26)$$

Note that the fractional flow function of Eq. 25 depends on gravity and the total flow rate of the medium. Consequently, the crossflow (see Eq. 9) depends on gravity and the total flow rate of the medium. Due to this dependence, the fractional flow function becomes an implicit function of the composition of both media as can be seen from Eq. 13 and the definition of F_i^k . This results in the complication of the numerical computations. Gravity number defined by Eq. 26 is a function of time and position. However, gravity number at the inlet is constant (the medium injection rate is constant due to equal pressure gradients in the two media). The flow rate in medium 1 is $k^1 A^1 / (k^1 A^1 + k^2 A^2) q_{T, inj}$ and in medium 2 is $k^2 A^2 / (k^1 A^1 + k^2 A^2) q_{T, inj}$. At a given pressure and a fixed geometry, N_{gr} is proportional to $\sin \theta / q_T^k$; therefore, tilt angles as small as 5 to 15° could have a substantial effect on gravity number ($\sin 5^\circ \approx 0.09$, $\sin 15^\circ \approx 0.26$, and $\sin 90^\circ = 1$). Note that the inlet gravity number of both media are the same.

In Eqs. 25 and 26, phase viscosities can be calculated using equilibrium phase compositions from Lohrenz et al. [15] correlation, and the gas and liquid phase relative permeabilities can be obtained from,

$$k_{rg} = k_{rg}^o \left[\frac{S_g}{1 - S_{or}} \right]^{n_g}, \quad (27)$$

and

$$k_{rl} = k_{rl}^o \left[\frac{1 - S_g - S_{or}}{1 - s_{or}} \right]^{n_l}. \quad (28)$$

Relative permeabilities are a function of the gas saturation, S_g . For two-phase equilibrium conditions,

$$S_g = \frac{V}{V + (\rho_g/\rho_l)(1 - V)} \quad (29)$$

where V is the mole fraction of the gas phase given by,

$$V = \frac{Z_i - x_{il}}{x_{ig} - x_{il}}. \quad (30)$$

After establishing phase behavior and flow relations, the entries in the matrices of Eq. B-1 can be calculated. Partial derivatives are performed numerically due to implicitness of the phase behavior and flow relations. The numerical derivatives are calculated using the central difference formulation. For a generic function H ,

$$\frac{\partial H}{\partial Z_1^1} = \frac{H(Z_1^1 + \Delta Z_1^1, Z_2^1, Z_1^2, Z_2^2, q_{TD}^2) - H(Z_1^1 - \Delta Z_1^1, Z_2^1, Z_1^2, Z_2^2, q_{TD}^2)}{2\Delta Z_1^1} \quad (31)$$

To illustrate the significance of crossflow in layered and fractured media, we study gas injection in the following examples.

Layered Media Examples - For the layered media, a permeability contrast of 10 is chosen. Layer 1 has a permeability of 100 md (high permeability), and the permeability of layer 2 is 10 md (low permeability). Table 1 provides other relevant layer data and the parameters of the relative permeability. The porous media are initially saturated with normal decane (C_{10}) and methane (CH_4) is injected into the system. The temperature is fixed at 100°F. Flow at two pressures, 1000 and 4000 psia is investigated. At 1000 psi, the surface tension at the interface between the gas and liquid phases is high and the capillary pressure may not be negligible. Nevertheless, to use the model, we will assume that capillary pressure can be neglected. For a binary system according to the Gibbs phase rule, the composition in the two-phase region is fixed at specified temperature and pressure. The results for four examples are presented next.

Displacement at 1000 psi without gravity. We consider first horizontal displacement at 1000 psi. The fractional flow function for $\theta = 0$ (or $N_{gr}^k = 0$) is independent of rate (see

Eq. 25). The composition profiles are shown in Fig. 1a at $t_D = 0.25$ PV injection. Fig. 2 is the enlarged version of the Fig. 1a around the upstream edge of the composition profiles. Variation of flow rates in each layer is shown in Fig. 3a. Note that the sum of the flow rates of the two layers is significantly less than one, especially for $x_D > 0.58$. Figs. 4a and 5a show the saturation profiles and the recoveries of each layer, respectively. Two different types of recovery curves are plotted in Fig. 5. One is based on the remaining in-situ amount of C_{10} , and the other one is based on the layer effluent production. The total pore volume produced is the same for both plots. The two types of plots highlight the contribution of crossflow from one layer to the other layer. Fig. 5a shows that there is very little crossflow in the absence of gravity.

At the injection point (H), see Fig. 2, solution starts with a phase change shock into the two-phase region along the tie line. The slowest shock, trailing shock, is the one where the composition of the low permeability layer (layer 2) enters into the two-phase region (H→G shock - see Fig. 2). The upstream side of this shock is a single-phase gas (point H) and the downstream side is in two-phase (point G). Solution by a finite difference simulator revealed that the crossflow is from layer 2 to layer 1 at the trailing shock. The material balance equations for the trailing shock are given by Eqs. A-4, 23, and 24. In the shock balance equations, the upstream composition (superscript II) of the trailing shock is known from the injection condition (point H). The downstream side compositions, $Z_1^{1,G}$ and $Z_1^{2,G}$ and the rate, $q_{TD}^{2,G}$ are the only unknowns. However, the shock balances, Eqs. A-4, 23 and 24 constitute two independent equations, since $\Lambda_{D1}^{2,GH} = \Lambda_{D1}^{T,GH} = \Lambda_D^{T,GH}$. The trailing shock is a limit of continuous variation at which the downstream side of the shock moves with the speed of downstream composition. Therefore, the three independent equations are,

$$\Lambda_{D1}^{2,GH} = \Lambda_{D1}^{T,GH} = \Lambda_D^{T,GH} = \lambda_D^G \quad (32)$$

The above system of equations are nonlinear in unknowns, $Z_1^{1,G}$, $Z_1^{2,G}$ and $q_{TD}^{2,G}$. They can be solved using the multi-dimensional Newton-Raphson method. In Eq. 32, λ_D^G is the eigenvalue associated with layer 2 at point G. For flow without gravity, λ_D^G equals to the tie-line eigenvalue in layer 2,

$$\lambda_D^G = \frac{q_{TD}^{2,G} df_1^{2,G}}{R_2 dS_g^{2,G}} \quad (33)$$

At the downstream of trailing shock the solution path continues along the direction of the eigenvector associated with the slow eigenvalue (zone of continuous variation). The end point of this zone of continuous variation (point F) is not known a priori. Therefore, this zone of continuous variation is extended to a point that layer 1 enters into two-phase region (point E). At this stage, the location of this point is unknown. In layer 1, the shock that enters into two-phase region will be called the trailing (slow) intermediate shock. The trailing intermediate shock is defined by Eqs. A-4, 23 and 24, where point F is the upstream and point E is the downstream. From the finite difference solution, the crossflow is found to be from layer 1 to layer 2 at that shock. However, crossflow changes direction at the downstream of the trailing intermediate shock. The trailing intermediate shock is also a limit of continuous

variation such that,

$$\Lambda_{D1}^{1,EF} = \Lambda_{D1}^{T,EF} = \Lambda_D^{T,EF} = \lambda_D^E \quad (34)$$

where λ_D^E is obtained from Eq. 33. The nonlinear system of equations given by Eq. 34 yield the composition of the trailing intermediate shock (E→F shock). From the intermediate shock towards the downstream, there is an intermediate zone of continuous variation which terminates at the point that the low permeability layer (layer 2) enters into the single-phase liquid region via a shock (leading intermediate shock). The location and the composition of that shock are also unknown. In other words, the intermediate zone of continuous variation (DE) is bounded between two intermediate shocks which are unknown. We cannot guess the upstream composition of the leading intermediate shock on this intermediate zone of continuous variation (DE) which comes from a guessed point on the trailing intermediate shock. Therefore, we need to change the direction in our solution algorithm. The solution could also be initiated from the initial composition point (point A, see Fig 1a). The initial composition (single-phase liquid) is connected to the two-phase region via a phase change shock (A→B shock) similar to the trailing shock. Since that shock is the fastest, it will be called the leading shock. At the leading shock and the zone of continuous variation (leading), the crossflow is from layer 1 to layer 2. Only the shock balance equation with the crossflow term will be different for the leading shock. The shock balance equations are the same as Eq. 34 except that,

$$\lambda_D^B = \frac{q_{TD}^{1,B}}{R_1} \frac{df_1^{1,B}}{dS_1^{1,B}} \quad (35)$$

Solution of the systems in Eq. 34 with Eq. 35 for A→B shock is similar to the solution of trailing shock equations. The leading intermediate shock occurs due to change in the number of phases in layer 2. In systems with no crossflow, this shock corresponds to the leading shock in the slow layer. The details of the solution are given in Appendix C.

Figs. 1e, 6a, and 7a show the composition profiles, rate history, and recovery curves in the absence of crossflow (i.e., NC). Comparison of the composition profiles of solutions with and without crossflow (see Figs. 1a and 1e) reveals that there is a mild crossflow between the leading intermediate shock and the leading shock. The leading intermediate shock of CE solution corresponds to the fastest shock of NC solution in layer 2, and the leading shock of CE solution corresponds to the fastest shock of NC solution in layer 1. As can be seen in NC solutions (Fig. 1e), CH_4 is not present in layer 2 ahead of the leading shock, whereas due to crossflow there is some CH_4 present in the CE solution.

Displacement at 1000 psi with gravity. In this example, we consider the downward injection of CH_4 at a rate less than the maximum gravity drainage rate of layer 2. The maximum gravity drainage rate of layer 2 is calculated from $q_{gr}^2 = k^2 A^2 (M_g^2 \rho_g^2 - M_l^2 \rho_l^2) g \sin \theta / \mu_l^2$. We assign a gravity number (see Eq. 26) of 17.9 to this problem (gravity number is the same for both layers) which corresponds to an injection rate of $q_{T,inj}^2 = 0.614 q_{gr}^2$; at such a low injection rate (combination of large θ and low injection rate), the displacement becomes efficient due to effect of gravity on the fractional flow curve (Eq. 25). The composition profile at $t_D = 0.25$ PV is shown in Fig. 1b. Comparison of this plot with Fig. 1a reveals a drastic

influence of gravity on the displacement process. Figs. 3b, 4b, and 5b depict the rate, saturation and recoveries. The recovery data in Fig. 5b demonstrate a very pronounced effect of crossflow. The two layers contain nearly the same amount of oil (i.e., C_{10}) during the course of gas injection. However, bulk of the oil is produced from the more permeable layer (layer 1) due to crossflow from layer 2 to layer 1 (see Figs. 5a and 5b).

The features of the solution with and without gravity are quite different. The gravity dominant case has only two shocks since the two layers enter and exit the two-phase region with the same speed. One interesting feature of the solution with gravity is that there is a spreading segment in the single-phase region in layer 1 (see Fig. 1b, AB).

The trailing shock (E \rightarrow F) is calculated using Eqs. 23 and 24 and two eigenvalues of the downstream side of the shock. Therefore, at the trailing shock,

$$\Lambda_{D1}^{T,EF} = \Lambda_D^{T,EF} = \lambda_{D1}^E = \lambda_{D2}^E \quad (36)$$

where λ_{D1}^E and λ_{D2}^E are different from the definitions in Eqs. 33 and 35 due to effect of gravity. Both eigenvalues are directly obtained from Eq. B-7. Solution of the system in Eq. 36 yields downstream composition and rates of the trailing shock. In Eq. 36, the direction of crossflow is not given a priori, since both layers enter two-phase region simultaneously. The solution indicates that the crossflow is from layer 2 to layer 1 at the downstream of trailing shock and then, there is a zone of continuous variation (DE) where crossflow changes direction. At the leading edge of the continuous variation (D) crossflow is from layer 1 to 2. The change of crossflow direction shows itself as an extreme point in the rate profiles (see Fig. 3b).

The leading shock is constructed between the leading zone of continuous variation in single-phase region (AB) and the trailing zone of continuous variation (ED). From the solution of the shock balances, upstream and downstream compositions of the leading shock are obtained. Since the parametric representations of both continuous segments are known, one composition on each segment is sufficient to solve for the leading shock. Therefore, two balance equations are sufficient,

$$\Lambda_{D1}^{T,CD} = \Lambda_D^{T,CD} = \lambda_D^D \quad (37)$$

The AB segment of the solution is not fully known, since the total rate at point B is unknown. In order to calculate AB variation, total rate at point A in layer 2 is guessed and the full solution is obtained. The guessed rate of layer 2 at point A is varied until the overall material balance is satisfied.

The results without crossflow are shown in Figs. 1f, 6b, and 7b. The rate history in Fig. 6b shows that the amount of CH_4 entering layer 2 increases until $t_D = 0.84$ PV leading to a better sweep in the low permeability layer (layer 2). The total recovery and layer recovery plots (the recoveries based on in-situ amount of C_{10} for CE solution) are similar for solutions with and without crossflow (see Figs. 5b and 7b). The main differences between the cases with and without gravity are the length of the transition zone, leading shock strength (shock height), and the solution structure. For flow with no gravity (i.e. horizontal layers), breakthrough occurs at 0.43 PV injection (Fig. 5a), whereas the breakthrough time for the case with strong gravity is 0.66 PV (Fig. 5b). The speed of the leading shock for flow with

gravity is high. Furthermore, overall mole fraction of CH_4 at breakthrough at the outlet of layer 1 is 0.40 for no gravity case and zero (just at breakthrough) for the case with gravity. The leading shock for flow with gravity is stronger and slower than without gravity resulting in higher recovery. The main contribution of gravity is the enhancement of crossflow between the two layers resulting in a high recovery from the low permeability layer (Figs. 1a and 1b). The gravity effect is not very pronounced at the trailing shocks since those shocks are mainly affected by the solubility of C_{10} in CH_4 . This fact will be seen more clearly in the following two examples.

Displacement at 4000 psi without gravity. In order to investigate the effects of component partitioning, the injection of CH_4 at 4000 psi is considered and the solution is obtained in the absence of gravity. Solution profiles are shown in Figs. 1c, 3c, and 4c. The recovery curves in Fig. 5c reveal that the crossflow in the absence of gravity is insignificant.

The solution profiles include four distinct shocks, each is associated with phase change in a particular layer. At the inlet, solution starts with a shock across the phase boundary in layer 2 (F→G) shock (see Fig. 1c). This shock can be solved using the shock balance equations for crossflow from layer 2 to layer 1 (Eqs. 32 and 33), where λ_D is calculated at point F. The solution proceeds with a segment of continuous variation (EF) where layer 2 contains the two-phase fluid mixture and layer 1 contains only the gas phase. The continuous variation segment ends at an unknown point E which can be obtained from the intermediate shock balances. The intermediate shocks, C→D and D→E shocks are resolved at the last stage, since they are coupled shocks due to an unknown intermediate state, D. Therefore, we start solving for the leading shock, A→B shock, with a downstream flow rate guessed similar to the previous cases. Due to volume change on mixing, total flow rate in layer 2 at the downstream of the leading shock is unknown. The leading shock, A→B, is obtained using Eqs. 34 and 35 where λ_D is calculated at point B. The continuous solution segment, BC, is obtained from point B towards upstream by integration along the eigenvectors. Similar to point E, point C is also not known and can be obtained from the coupled intermediate shock balances. For the intermediate shocks, the following balance equations are used. For the trailing intermediate shock, E→D, where crossflow is from layer 2 to layer 1

$$\Lambda_{D1}^{2,DE} = \Lambda_{D1}^{T,DE} = \Lambda_D^{T,DE} = \lambda_D^D \quad (38)$$

and for the leading intermediate shock C → D, where crossflow is from layer 1 to layer 2,

$$\Lambda_{D1}^{1,CD} = \Lambda_{D1}^{T,CD} = \Lambda_D^{T,CD} = \lambda_D^C \quad (39)$$

The unknowns in Eqs. 38 and 39 are the compositions of layers at points C, E and D, and the rate of one of the layers at these locations. The rate of the other layer can be obtained from the crossflow equilibrium condition in Eq. 18. The unknowns of the coupled shock balances are $Z_1^{2,E}$, $Z_1^{1,C}$, $Z_1^{1,D}$, $Z_2^{2,D}$, and $q_{TD}^{2,D}$; $Z_1^{1,E}$ and $q_{TD}^{1,E}$ are not independent unknowns. Similarly, $Z_1^{2,C}$ and $q_{TD}^{1,C}$ can be calculated once $Z_1^{1,C}$ is known. Therefore, we have 6 equations and 5 unknowns. One extra equation is used to obtain the value for the total rate of layer 2 at the downstream of the leading shock. The correct solution is obtained when all the shock

balances and the overall material balance are satisfied. The details of the solution algorithm are given in Appendix C.

The solution without crossflow is presented in Figs. 1g, 6c, and 7c. Comparison of composition profiles of the cases with and without crossflow (Figs. 1c and 1g) shows that in layer 2, CH_4 presence in front of the C→D shock is due to crossflow from layer 1 to layer 2 (see Fig. 1c) which is similar to the corresponding low pressure case. This feature is missing in Fig. 1g due to the no-crossflow condition. Although, the overall recoveries of the two systems, with and without crossflow, show similar behavior (Figs. 5c, and 7c), layer 2 produces more in the crossflow case due to crossflow from layer 1.

Displacement at 4000 psi with gravity. This case is identical to the example at 1000 psi with gravity, except that the displacement pressure is 4000 psi. The gravity number for the system is 17.9 and, $q_{T,inj}/q_{gr}^2 = 0.614$; q_{gr}^2 is calculated based on the equilibrium phase compositions, phase densities and viscosities at 4000 psi. The qualitative aspect of the solution is the same as the 1000 psi case with gravity. Therefore, solution construction for this case is not repeated. The solution profiles and the recovery curves can be seen in Figs. 1d, 3d, 4d, and 5d.

The main difference between the solutions at 4000 psi and 1000 psi is due to phase behavior. The slow shock (D→E) for the 4000 psi case is better developed and much faster as compared to the low pressure case (1000 psi). The leading shock (B→C) is also stronger in both layers. Thus, almost 80 percent of the initial oil C_{10} is produced at the bulk breakthrough (arrival of the leading shock).

The solution without crossflow is presented in Figs. 1h, 6d, and 7d. The differences in the speeds of both shocks in the two layers can be viewed clearly. The trailing shock in layer 2 is about 3 times slower than the trailing shock in layer 1, and the leading shock in layer 1 is 2.6 times faster than the leading shock in layer 2. However, the corresponding shocks (trailing and leading shocks in the two layers) in the solutions with CE have the same speed. In other words, both layers enter and exit two-phase region via shocks of the same speed due to crossflow.

Fractured Media Examples - For the study of gas injection in fractured media, the matrix and fracture permeabilities are assumed 2 md and 34 darcy, respectively. The matrix block width is 30 cm, and the fracture aperture is 20 microns. Other parameters of the fracture and matrix are shown in Table 2. The fracture and the matrix are initially saturated with normal decane (C_{10}) and methane (CH_4) is injected into the system at 4000 psi. In the displacements at 1000 psi in the layered system, the phase behavior effects were not pronounced and therefore, gas injection in fractured media will be only studied at 4000 psi.

A total of four cases will be studied. The first example concerns with the dominant viscous forces, the second and the third examples are intermediate viscous-gravity cases, and the last example is the dominant gravity case. From the cross-sectional area and permeability of the fracture and the matrix given in Table 2, the dimensionless flow rates at the inlet of the

fracture and matrix are 0.526, and 0.474, respectively.

Dominant Viscous Crossflow. When the gravity number is zero or very small, i.e., N_{gr}^k is zero or small, the injected fluid, $q_{T,inj}$, mostly flows through the fracture. As a result, the recovery performance is very low. A special feature of low gravity number is a long two-phase transition zone. To study the features of low gravity number (i.e., dominant viscous crossflow) we have selected inlet $N_{gr} = 0.034$, i.e., $q_{T,inj} = 61.5q_{gr}^2$.

Composition profiles capturing the fronts in the fracture and the matrix are shown in Figs. 8a and 9a at $t_D = 0.00025$ PV and at $t_D = 0.5$ PV, respectively. The rate and saturation profiles are shown in Figs. 10a and 11a at $PV = 0.5$.

In this example, there are four shocks similar to the high pressure layered system with no gravity. We classify the shocks (fronts) arising in the solution based on their speeds relative to each other. The fastest shock which is associated with the fracture flow is called the leading shock; the slowest shock which is associated with the matrix flow is called the trailing shock; and the shock(s) between the leading and trailing shocks is called an intermediate shock(s). When there are more than one intermediate shock, they are classified according to their speeds. Each shock in the system corresponds to a phase change in either the fracture or the matrix. Although the breakthrough in the fracture is very fast compared to $t_D = 1$, the fronts in the fracture should still be resolved to obtain the full solution. The location of the shocks are especially important due to the localized nature of crossflow.

As expected, the flow with high CH_4 concentration in the fracture advances orders of magnitude faster than that in the matrix. The fronts in the matrix, where almost all the initial fluid (C_{10}) resides, move slower than those in the fracture leading to low recovery. Fig. 12a shows the recovery curves for both the crossflow and no crossflow cases. As can be seen, the case with crossflow leads to a slightly higher recovery than the case with no crossflow. However, the overall system recovery is very low due to the bypassed oil in the matrix; only about 4 percent of the total rate goes into the matrix for a long period of time as seen in Fig. 10a. Therefore, the low rate in the matrix combined with the CH_4 -filled fracture (in a very short time) results in such a low recovery.

Figs. 9a and 13a show the composition profile and the rate history, respectively, for the no-crossflow case. Again, most of the injected fluid passes through the fracture leading to a low overall recovery (Fig. 12a).

Moderate Viscous Crossflow. In order to highlight the effect of viscous and gravity crossflow, a moderate viscous crossflow is selected with $N_{gr} = 0.86$ and $q_{T,inj} = 2.46q_{gr}^2$. The qualitative features of this case are similar to the dominant viscous crossflow case, but there is an improvement in recovery performance. Figs. 8b and 9b show the composition profiles at $t_D = 0.00025$ and $t_D = 0.5$ PV, both in the fracture and in the matrix. Breakthrough in the fracture is almost instantaneous with a narrow two-phase region as the segment between the two shocks in Fig. 8b indicates (with respect to $N_{gr} = 0.034$ - Fig. 8a). Rate and saturation profiles are shown in Figs. 10b and 11b. As compared to the previous example, the crossflow reverses direction at the second shock front from the injection end of the displacement (Fig.

11b). The leading front in the matrix (Fig. 9b) advances faster than in the previous case. The recovery performance of this case is shown in Fig. 12b. The positive effect of gravity is clearly seen in the recovery plot. In the previous case ($q_{T,inj} = 61.5q_{gr}^2$), the total recovery is less than 5 percent at 1 PV (Fig. 12a) while the corresponding total recovery is about 21 percent for this case ($q_{T,inj} = 2.46q_{gr}^2$). The contribution of crossflow to recovery is, however, low (about 2 percent at 1 PV); the total recovery with crossflow is slightly higher than the total recovery without crossflow (Fig. 12b). The composition profile and rate history of the no-crossflow case are shown in Figs. 9f and 13b, respectively. The total inlet flow rates for the fracture and the matrix stay almost constant. The total fracture injection rate quickly (when both fast fronts in the fracture arrive to the production end) reaches to 77 percent of the total system rate and stays about the same for at least to 2 PV injection. The magnitude of the total recovery is about the same as the total rate share of the matrix (about 21 percent at 1 PV - see Fig. 12b).

As a supplement to the moderate viscous crossflow case, we lowered the total injection rate further for the third example ($N_{gr} = 1.43$ and $q_{T,inj} = 1.47q_{gr}^2$). The composition profile in the fracture is shown in Fig. 8c at 0.00025 PV. The transition zone between the two fronts becomes smaller as the two-phase transition shocks in the fracture approach each other (the trailing shock becomes faster and the leading shock becomes slower - see also Figs. 8a and 8b). At a certain gravity number ($N_{gr} \approx 1.5$), both fast shocks in the fracture converge resulting in a single shock. However, due to the negligible fracture volume, this increment in the recovery mainly comes from the matrix rate enhancement and the crossflow. The composition, rate and saturation profiles are shown in Figs. 9c, 10c, 11c, and 12c, respectively. Although the breakthrough in the fracture is almost instantaneous, more than 31 percent of C_{10} is recovered at 1 PV. The recovery curve for the no-crossflow case (see Fig. 12c) starts deviating from the case with the crossflow at later times ($t_D > 0.6$ PV) causing lower recovery than the crossflow case (28 percent at 1 PV). Composition profile at 0.5 PV and the rate history of no crossflow case are shown in Figs. 9g and 13c, respectively. Without crossflow, the rate share of the fracture increases as displacement progresses, leading to lower recovery than the corresponding crossflow case at later times (since most of CH_4 bypasses the matrix). But, the recovery performance of the no-crossflow case is still significantly higher than the previous no-crossflow cases with lower gravity numbers ($N_{gr} = 0.034$, and $N_{gr} = 0.859$).

Dominant Gravity Crossflow. For the dominant gravity crossflow case, the injection rate is lowered further to $q_{T,inj} = 0.614q_{gr}^2$; $N_{gr} = 3.43$. The qualitative aspects of this case are significantly different from the previous cases discussed above. As Fig. 8d reveals, the fast front in the fracture has a CH_4 mole fraction of 0.08. The leading edge of the fracture flow is in a single-phase liquid state due to a pronounced crossflow from the fracture to the matrix at the intermediate shock. Since the fracture pore volume is small, even a moderate amount of crossflow can eliminate two-phase flow in the fracture. At $t_D = 0.5$ PV, only single-phase gas is present in the fracture at the trailing edge of the displacement (Fig. 11d). The rate profiles of both the matrix and the fracture indicate that crossflow changes direction between the trailing shock and the intermediate shock. The change of crossflow direction shows itself

as an extreme point in the rate profiles (Fig. 10d). At the intermediate shock, the fluid in the fracture changes from the single-phase gas to the single-phase liquid without entering into the two-phase region (Fig. 11d), and the leading shock is coupled with the intermediate shock. This phenomenon occurs due to strong crossflow from the fracture to the matrix.

The efficiency of the displacement can be seen in Fig. 12d. Significant amount of C_{10} is produced at the bulk breakthrough (66 percent at 0.8 PV). The case without crossflow produces considerably less C_{10} (40 percent at 0.8 PV). The composition profile and inlet rate history for the no-crossflow case are shown in Figs. 9h and 13d, respectively. As the injection proceeds, the relative rate share of the fracture increases leading to low recovery at later times. Around $t_D = 1.25$ PV, the total inlet rate of the fracture exceeds the total inlet rate of the matrix (Fig. 13d).

DISCUSSION

Resolving the flow in the fracture and in the matrix is a difficult task both analytically and numerically, mainly due to the large contrast in the permeability and PV of the fracture and matrix media. The two distinct characteristic speeds (eigenvalues) of the system, one very large and the other very small cause complication. The large eigenvalue corresponds to the fracture flow and the small one corresponds to the matrix flow. Solution of the displacement problem in a composite fracture/matrix system involves resolving both characteristic speed scales accurately. The ratio of the characteristic speeds can be as high as $10^5:1$. This means that the speed of propagation in the fracture is about 10^5 times faster than the matrix. The solution of the shock balances is very sensitive to the initial guess. In the case of coupled intermediate shocks, the sensitivity becomes extreme, due to the inter-dependency of the two characteristic speed scales. This is basically due to the phase boundaries between CH_4 (injected gas) and C_{10} (initial fluid) and the equilibrium gas and liquid phases. Even a small amount of crossflow from the matrix to the fracture can cause a phase change to occur in the fracture. Because the shock balances are solved using the Newton-Raphson technique, the set of unknowns may fluctuate until convergence is achieved. This type of underestimation or overestimation can have significant effect on the fracture flow, and can cause divergence. One main reason of divergence is the discontinuity of eigenvalues across phase boundaries. The unphysical phase change in the fracture, therefore, can cause discontinuities in the characteristic speeds and divergence. As a practical step, the governing parameters of the problem are changed slowly, while the answer of the previous solution is used as the initial guess for the new problem. In the examples considered here for the fractured media, the gravity number is increased gradually to obtain the solutions with pronounced gravity.

In general, some of the qualitative features of the solution are known a priori. For instance, phase boundaries are crossed via shocks, and the solution is divided into different segments by those shocks. However, due to the pronounced effect of gravity, the direction reversal in the crossflow can alter the qualitative features of the solution. For example, fracture flow can skip the two-phase region with a direct jump from the single-phase gas to the single-phase liquid. This kind of behavior along with the unknown downstream rates due to volume

change on mixing can make it difficult to obtain the proper solution.

Comparison of the results of all the cases indicate that the recovery enhancement may occur at a high gravity number (see Fig. 12). By increasing gravity, more fluid goes into the matrix yielding a higher overall sweep of the initial oil, C_{10} . This type of recovery improvement occurs in both solutions, with and without crossflow (Fig. 12). At low to moderate gravity numbers, the recovery plots for both crossflow and no-crossflow solutions exhibit similar responses. But for the dominant gravity crossflow, the difference between the crossflow and no-crossflow solutions becomes significant. At very high gravity numbers (very low rate of injection as compared to the initial free gravity drainage rate of the matrix), the crossflow and no-crossflow solutions approach each other. At the limit when the rate goes to zero, high displacement efficiency in both crossflow and no-crossflow cases is achieved.

CONCLUSIONS

1. An analytical one-D model based on the method of characteristics is used to study the effect of crossflow on the recovery. In this work, the effects of gravity and volume change on crossflow are taken into account on the performance of a two media system. For a two-layer media, in spite of very pronounced crossflow due to gravity, the total recovery with and without crossflow is surprisingly close for the examples that we have studied. However, with crossflow, bulk of the oil is transferred from the less permeable to the more permeable layer and then produced from the more permeable layer. In this respect, layered and fractured media behave the same.
2. For recovery performance of a fractured media comprised of a matrix block and a fracture, the crossflow between the matrix and the fracture often changes direction. In one of the examples, the recoveries at 1 PV injection are 68 percent with crossflow and 47 percent without crossflow. The effect of crossflow in a multiblock system may be even more pronounced (10).

NOMENCLATURE

A	=	flow area
A^k	=	flow area of layer k
A_T	=	total flow area (Eq. 14)
C_R	=	capacitance ratio
f_j	=	fractional flow function of phase j
F_i^k	=	molar fractional flow of component i in layer k (Eq. 13)
g	=	acceleration of gravity
G_i^k	=	number of moles of component i per unit volume in layer k (Eq. 12)
k	=	absolute permeability
k_{ro}	=	relative permeability of liquid phase (oil)
k_{ro}^o	=	relative permeability coefficient of liquid phase (oil)

k_{rg}	=	relative permeability of vapor phase (gas)
k_{rg}^o	=	relative permeability coefficient of vapor phase (gas)
L	=	system length
M_g^k	=	molecular weight of gas phase
M_l^k	=	molecular weight of liquid phase
n_o	=	relative permeability exponent of liquid phase (oil)
n_g	=	relative permeability exponent of vapor phase (gas)
n_p	=	number of phases
n_c	=	number of components
P	=	pressure
q_{gr}^k	=	gravity drainage rate of layer k , $q_{gr}^k = k^k A^k (M_g^k \rho_g^k - M_l^k \rho_l^k) g \sin \theta / \mu_l^k$
q_T	=	total rate of injection
$q_{T,inj}^k$	=	total rate of injection in layer k at the inlet
$q_{TD,inj}^k$	=	total dimensionless rate of injection in layer k at the inlet
q_T^k	=	total rate of injection in layer k
q_{TD}^k	=	total dimensionless rate of injection in layer k
R^k	=	fractional pore volume of layer k
S_j	=	saturation of phase j , fraction
S_o	=	liquid phase (oil) saturation, fraction
S_g	=	gas phase (vapor) saturation, fraction
S_{or}	=	residual saturation of liquid phase (oil), fraction
t	=	time
t_D	=	dimensionless time, (Eq. 14)
x	=	spatial dimension
x_D	=	dimensionless distance, (Eq. 14)
x_{ij}	=	mole fraction of component i in phase j
\bar{X}	=	eigenvector
Z_i	=	overall mole fraction of component i
\bar{Z}	=	composition vector

Greek Symbols

ϕ	=	porosity
ϕ^k	=	porosity of layer k
$\bar{\phi}$	=	volume averaged porosity (Eq. 14)
μ_j	=	viscosity of phase j
ρ_j	=	molar density phase j
ρ_{jD}	=	dimensionless molar density of phase j
θ	=	tilt angle
Λ	=	shock speed
Λ_D	=	dimensionless shock speed
λ	=	eigenvalue (characteristic velocity)
λ_D	=	dimensionless eigenvalue (dimensionless characteristic velocity)

$$\lambda_j^k = \text{mobility of phase } j \text{ in layer } k, \lambda_j^k = k_{rj}^k / \mu_j^k$$

$$\lambda_T^k = \text{total fluid mobility in layer } k, \lambda_T^k = \sum_{j=1}^{n_p} k_{rj}^k / \mu_j^k$$

Abbreviations

CE	:	crossflow equilibrium
NC	:	no crossflow
VE	:	vertical equilibrium

ACKNOWLEDGMENTS

This work is supported by the U.S. Department of Energy (Contract No. DE-FG22-93BC14875), and by the members of the Research Consortium on Fractured/Layered Reservoirs of the Reservoir Engineering Research Institute. Their support is greatly appreciated.

References

1. Tan, J.C-T. and Firoozabadi, A.: "Miscible Displacement in Fractured Porous Media: Part II - Analysis," paper SPE 27837 presented at the SPE/DOE Ninth symposium on Improved Oil Recovery, Tulsa, OK, April 17-20, 1994.
2. Tan, J.C-T. and Firoozabadi, A.: "Theoretical Analysis of Miscible Displacement in Fractured Porous Media by a One-Dimensional Model: Part I - Theory," *Journal of Canadian Petroleum Technology* (February 1995) 17-27.
3. Zapata, V.J. and Lake, L.W.: "A Theoretical Analysis of Viscous Crossflow," paper SPE 10111 presented at the 56th Annual Fall Technical Conference and Exhibition of the SPE, San Antonio, TX, October 1981.
4. Pande, K.K., and Orr, F.M., Jr.: "Composition Paths in Binary CO_2 - C_{10} Displacements: Effects of Reservoir Heterogeneity and Crossflow on Displacements with Limited Solubility," presented at the Second European Conference on the Mathematics of Oil Recovery, France, September 1990.
5. Lax, P.D.: "Hyperbolic Conservation Laws II," *Communications on Pure and Applied Mathematics* (1957) 10, 537-566.
6. Rhee, H., Aris, R. and Amundson, N.R.: *First-Order Partial Differential Equations: Volume I*, Prentice-Hall, Englewood Cliffs, N.J. (1986).
7. Dumoré, J.M., Hagoort, J., and Risseeuw, A.S.: "An Analytical Model for One-Dimensional, Three-Component Condensing and Vaporizing Gas Drives," *Society of Petroleum Engineers Journal* (April 1984) 24, 169-179.

8. Dindourk, B.: *Analytical Theory of Multiphase Multicomponent Flow in Porous Media*, PhD dissertation, Stanford University, Stanford, CA (June 1992).
9. Coats, K.H., Dempsey, J.R., and Henderson, J.H.: "The Use of Vertical Equilibrium in Two-Dimensional Simulation of Three-Dimensional Reservoir Performance," *Trans. AIME* (1971) **251**, 63-71.
10. Tan, J.C-T, and Firoozabadi, A.: "Theoretical Analysis of Miscible Displacement in Fractured Porous Media by a One-Dimensional Model: Part II - Features," *Journal of Canadian Petroleum Technology* (February 1995) 28-35.
11. Rhee, H., Aris, R. and Amundson, N.R.: *First-Order Partial Differential Equations: Volume II*, Prentice-Hall, Englewood Cliffs, N.J. (1989).
12. Smoller, J.: *Shock Waves and Reaction-Diffusion Equations*, First Edition, Springer-Verlag, New York, N.Y. 10010 (1983).
13. Myint-U, T., and Debnath, L.: *Partial Differential Equations for Scientists and Engineers*, Third Edition, North Holland, New York (1987).
14. Peng, D.Y. and Robinson, D.B.: "A New Two-Constant Equation of State," *Ind. Eng. chem. Fund.* (1976) **15**, 59-64.
15. Lohrenz, J., Bray, B.C. and Clark, C.R.: "The Viscosity of Pure Substances in Dense Gaseous and Liquid Phases," *Journal of Petroleum Technology* (1964) 1171-1176.

Appendix A—Shock Balances with Crossflow

Discontinuities or shocks are required in solution construction when continuous variations are not possible (i.e., faster upstream compositions than the downstream compositions - multivaluedness). We define a shock with two sets of parameters, upstream and downstream, across which the parameters change discontinuously. In the following, II and I indicate upstream and downstream values, respectively. Consider a control volume of length Δx where a shock passes across. At time t (just before shock passes the control volume), the amount of component i present in the control volume is $\phi^k A^k \Delta x (G_i^k)^I$. At time $t + \Delta t$ (just after the shock passes the control volume), the amount of component i present in the control volume is $\phi^k A^k \Delta x (G_i^k)^{II}$. As shock passes through the control volume, inflow of component i is $(q_T^k F_i^k)^{II} \Delta t$, and outflow of component i is $(q_T^k F_i^k)^I \Delta t$. If there was no crossflow, the change in the amount of component i in the control volume would be equal to the difference between inflow and outflow. However, crossflow will emerge from the difference of change in total material in the control volume and the net total flow. Hence, total crossflow is defined by,

$$\phi^k A^k \Delta x \sum_i^{n_c} [(G_i^k)^{II} - (G_i^k)^I] - \Delta t \sum_i^{n_c} [(q_T^k F_i^k)^{II} - (q_T^k F_i^k)^I] \quad (A - 1)$$

For component i , the crossflow term becomes

$$\frac{F_i^k}{\sum_i^{n_c} F_i^k} \Big|_{\text{shock}} \left\{ \phi^k A^k \Delta x \sum_i^{n_c} [(G_i^k)^{II} - (G_i^k)^I] - \Delta t \sum_i^{n_c} [(q_T^k F_i^k)^{II} - (q_T^k F_i^k)^I] \right\} \quad (\text{A} - 2)$$

and the shock balance for component i including the crossflow term is,

$$\phi^k A^k \Delta x (G_i^k)^{II} - \phi^k A^k \Delta x (G_i^k)^I = (q_T^k F_i^k)^{II} \Delta t - (q_T^k F_i^k)^I \Delta t + \frac{F_i^k}{\sum_i^{n_c} F_i^k} \Big|_{\text{shock}} \left\{ \phi^k A^k \Delta x \sum_i^{n_c} [(G_i^k)^{II} - (G_i^k)^I] - \Delta t \sum_i^{n_c} [(q_T^k F_i^k)^{II} - (q_T^k F_i^k)^I] \right\} \quad (\text{A} - 3)$$

or,

$$\Lambda = \frac{\Delta x}{\Delta t} = \left\{ (q_T^k F_i^k)^{II} - (q_T^k F_i^k)^I - \frac{F_i^k}{\sum_i^{n_c} F_i^k} \Big|_{\text{shock}} \left[\sum_{i=1}^{n_c} (q_T^k F_i^k)^{II} - \sum_{i=1}^{n_c} (q_T^k F_i^k)^I \right] \right\} / \left\{ A^k \phi^k \left\{ (G_i^k)^{II} - (G_i^k)^I - \frac{F_i^k}{\sum_i^{n_c} F_i^k} \Big|_{\text{shock}} \left[\sum_{i=1}^{n_c} (G_i^k)^{II} - \sum_{i=1}^{n_c} (G_i^k)^I \right] \right\} \right\}, \quad i = 1, n_c - 1 \quad (\text{A} - 4)$$

The main issue in Eq. A-4 is to calculate the term $F_i^k / \sum_i^{n_c} F_i^k \Big|_{\text{shock}}$ which is discontinuous across a shock. For $F_i^k / \sum_i^{n_c} F_i^k \Big|_{\text{shock}}$, a rate-weighted form similar to Zapata and Lake [3], and Pande and Orr [4] is adopted. Thus,

$$\frac{F_i^k}{\sum_i^{n_c} F_i^k} \Big|_{\text{shock}} = \alpha_i^k = \frac{q_{TD}^{k,II} \left(\frac{F_i^k}{\sum_{i=1}^{n_c} F_i^k} \right)^{II} + q_{TD}^{k,I} \left(\frac{F_i^k}{\sum_{i=1}^{n_c} F_i^k} \right)^I}{q_{TD}^{k,II} + q_{TD}^{k,I}}, \quad i = 1, \dots, n_c - 1 \quad (\text{A} - 5)$$

For $\alpha_i^k = 0$, Eq. A-4 is equivalent to the shock balance for the homogeneous system. The shock balances without the crossflow term are given by Eqs. 23 and 24 of the text.

Appendix B—Eigenvalue Problem and Solution Procedure

The eigenvalue problem for a two-component mixture based on Eqs. 11, 15 and 16 of the text is,

$$\left\{ \begin{bmatrix} a & b & c \\ \frac{\partial F^T}{\partial Z_1^1} & \frac{\partial F^T}{\partial Z_1^2} & \frac{\partial F^T}{\partial q_{TD}^2} \\ \frac{\partial F_1^T}{\partial Z_1^1} & \frac{\partial F_1^T}{\partial Z_1^2} & \frac{\partial F_1^T}{\partial q_{TD}^2} \end{bmatrix} - \lambda_D \begin{bmatrix} d & 0 & 0 \\ \frac{\partial G^T}{\partial Z_1^1} & \frac{\partial G^T}{\partial Z_1^2} & 0 \\ \frac{\partial G_1^T}{\partial Z_1^1} & \frac{\partial G_1^T}{\partial Z_1^2} & 0 \end{bmatrix} \right\} \begin{bmatrix} \frac{dZ_1^1}{d\eta} \\ \frac{dZ_1^2}{d\eta} \\ \frac{dq_{TD}^2}{d\eta} \end{bmatrix} = \begin{bmatrix} 0 \\ 0 \\ 0 \end{bmatrix} \quad (\text{B-1})$$

where the eigenvectors are defined by,

$$\vec{X} = \left[\frac{dZ_1^1}{d\eta} \quad \frac{dZ_1^2}{d\eta} \quad \frac{dq_{TD}^2}{d\eta} \right]^T \quad (\text{B-2})$$

The top row elements are,

$$a = \frac{\partial q_{TD}^1 F_1^1}{\partial Z_1^1} - \frac{F_1^1}{\sum_{i=1}^2 F_i^1} \frac{\partial \sum_{i=1}^2 q_{TD}^1 F_i^1}{\partial Z_1^1} \quad (\text{B-3})$$

$$b = \frac{\partial q_{TD}^1 F_1^1}{\partial Z_1^2} - \frac{F_1^1}{\sum_{i=1}^2 F_i^1} \frac{\partial \sum_{i=1}^2 q_{TD}^1 F_i^1}{\partial Z_1^2} \quad (\text{B-4})$$

$$c = \frac{\partial q_{TD}^1 F_1^1}{\partial q_{TD}^2} - \frac{F_1^1}{\sum_{i=1}^2 F_i^1} \frac{\partial \sum_{i=1}^2 q_{TD}^1 F_i^1}{\partial q_{TD}^2} \quad (\text{B-5})$$

$$d = R^1 \left(\frac{\partial G_1^1}{\partial Z_1^1} - \frac{F_1^1}{\sum_{i=1}^2 F_i^1} \frac{\partial \sum_{i=1}^2 G_i^1}{\partial Z_1^1} \right) \quad (\text{B-6})$$

The eigenvalues, λ_{D1} and λ_{D2} , are the roots of the equation,

$$\begin{vmatrix} (a - \lambda_D d) & b & c \\ \left(\frac{\partial F^T}{\partial Z_1^1} - \lambda_D \frac{\partial G^T}{\partial Z_1^1} \right) & \left(\frac{\partial F^T}{\partial Z_1^2} - \lambda_D \frac{\partial G^T}{\partial Z_1^2} \right) & \frac{\partial F^T}{\partial q_{TD}^2} \\ \left(\frac{\partial F_1^T}{\partial Z_1^1} - \lambda_D \frac{\partial G_1^T}{\partial Z_1^1} \right) & \left(\frac{\partial F_1^T}{\partial Z_1^2} - \lambda_D \frac{\partial G_1^T}{\partial Z_1^2} \right) & \frac{\partial F_1^T}{\partial q_{TD}^2} \end{vmatrix} = 0 \quad (\text{B-7})$$

Eq. B-7 has two roots, λ_{D1} and λ_{D2} . Each eigenvalue, λ_{Dn} , has an associated eigenvector, \vec{X}_n (Eq. B-2) which describes the direction in the composition-rate space. Each eigenvalue yields one potential composition path. The first and second rows of the eigenvector, Eq. B-2 provide the changes in the compositions of medium 1 and medium 2, respectively. The last row in Eq. B-2, $dq_{TD}^2/d\eta$, provides the changes in q_{TD}^2 along a selected eigenvector direction. The rate in layer 1, q_{TD}^1 , can be updated from the crossflow equilibrium condition stated in Eq. 18 once the changes in Z_1^1 , Z_1^2 , and q_{TD}^2 are known.

Solution Construction. A correct physical solution consists of compatible waves where velocity constraint is satisfied. The velocity constraint requires monotonic wave velocities which increase from upstream to downstream. Shocks are included in the solution when the

condition of monotonicity is violated. In addition, the phase boundaries are crossed via the shocks.

The shocks in binary flow are always associated with phase appearance and disappearance in one or both of the media. In other words, the shocks appear in the solution when the phase boundaries are crossed in at least one of the media. In the solutions, the path switch is allowed as long as the velocity constraint is satisfied. The solution is constructed combining separate segments (zone of constant states, shocks, and zone of continuous variations) satisfying both the material balance and the velocity constraint.

Computation of Eigenvalues and Eigenvectors. Computation of eigenvalues and eigenvectors entails calculation of the entries in Eq. B-7. Each entry of this determinant is coupled with the phase equilibrium calculations. Therefore, a phase behavior model must be used in the calculations. In this study, we have selected the Peng-Robinson [14] equation of state to perform the phase equilibrium calculations.

Appendix C—Solution Steps

Displacement at 1000 psi without gravity. There are two key composition points that correspond to both intermediate shocks and are obtained through a trial and error procedure. We have used a procedure similar to the one by Pande and Orr [4] for low permeability contrast displacements. The iteration steps are (see Fig. 2):

1. Calculate the trailing shock composition (G).
2. Compute the trailing continuous variation (GF).
3. Guess a point on the trailing continuous variation. This point constitutes the upstream composition of the trailing intermediate shock (F).
4. Calculate the trailing intermediate shock composition (E) using Eqs. A-4, 23, and 24.
5. Compute the intermediate continuous variation (ED) based on the guess in step 3.
6. Calculate the leading shock composition (B) using Eqs. A-4, 23, and 24.
7. Compute the leading zone of continuous variation (BC).
8. Guess a point on the leading zone of continuous variation (C). This point will be downstream composition of the leading intermediate shock.
9. Calculate the composition of the leading intermediate shock (CD) using Eqs. 33 and 34.
10. Compute the intermediate zone of continuous variation (DE) based on the guess in step 8.

11. The intermediate zone of continuous variation segments in steps 5 and 10 must be the same if both of the guesses in steps 3 and 8 are right. Both guesses are varied until the area between the two solution curves (steps 5 and 10) is negligible.

The solution procedure becomes more complicated when the volume change on mixing is considered. The total flow velocity in medium 2 at the downstream of the leading shock must also be obtained through an iterative procedure. From the crossflow equilibrium condition, the total rate in medium 1 is determined. However, with the inclusion of volume change on mixing, the above iteration scheme is not sufficient to obtain the solution. Overall material balance with the steps above should also be used. Therefore, even when step 11 is satisfied, overall material balance error should be checked to ensure that the estimated rate value at the downstream of the leading shock is correct. If the overall material balance is not satisfied, the estimated rate in medium 2 in front of the leading shock has to be modified and steps 3 to 11 should be repeated. The convergence will be achieved when both step 11 and overall material balance are satisfied.

Displacement at 4000 psi without gravity. The solution steps are as follows:

1. Calculate the trailing shock (F→G shock) composition and rate.
2. Compute the continuous variation, FE.
3. Calculate the leading shock (A→B shock) composition and rate with a guessed total rate in medium 2 at point A.
4. Compute the continuous variation, BC.
5. Solve for E→D, and C→D shocks simultaneously.
6. Check the overall material balance to validate the estimated downstream rate in step 3. If the overall material balance and one of the remaining shock balances do not hold, then we go back to step 3 until the total material balance and all the shock balances are satisfied.

Table 1: ROCK AND FLUID PROPERTIES - LAYERED MEDIA

PARAMETER	Layer 1	Layer 2
ϕ (fraction)	0.25	0.25
A (cm ²)	7432	7432
k (Darcy)	0.1	0.01
k_{rg}^o	1.0	1.0
k_{rl}^o	1.0	1.0
S_{or}	0.25	0.25
n_g	3	3
n_l	3	3

Table 2: ROCK AND FLUID PROPERTIES - FRACTURED MEDIA

PARAMETER	Fracture (Medium 1)	Matrix (Medium 2)
ϕ (fraction)	1	0.25
A (cm ²)	0.12	1860
k (Darcy)	34	0.002
k_{rg}^o	1.0	1.0
k_{rl}^o	1.0	1.0
S_{or}	0	0.25
n_g	1.2	4.5
n_l	1.2	4.5

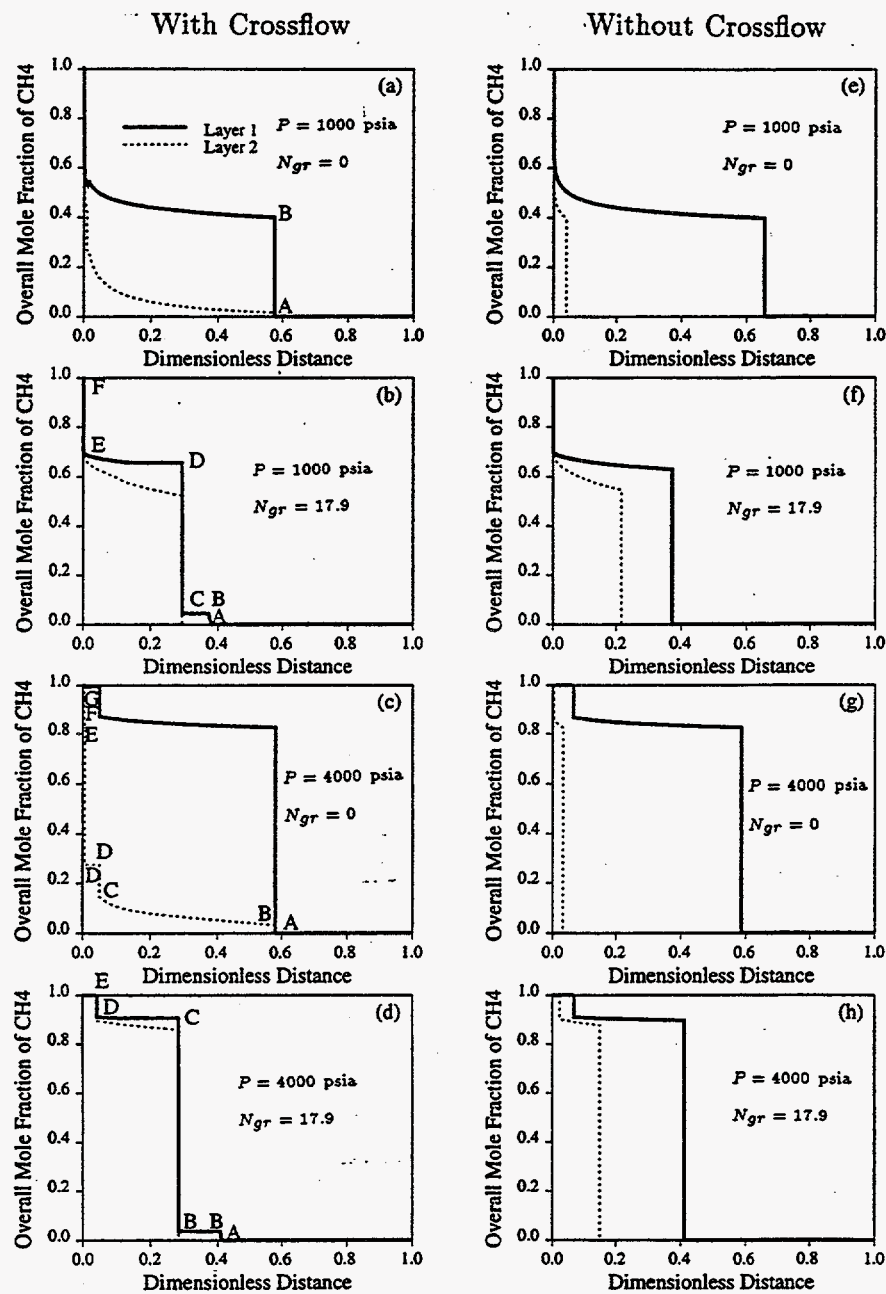


Figure 1: Composition profiles at $t_D = 0.25$ PV injection (with and without crossflow) at different pressures and inlet gravity numbers; the right column is without crossflow and the left column is with crossflow—layered media.

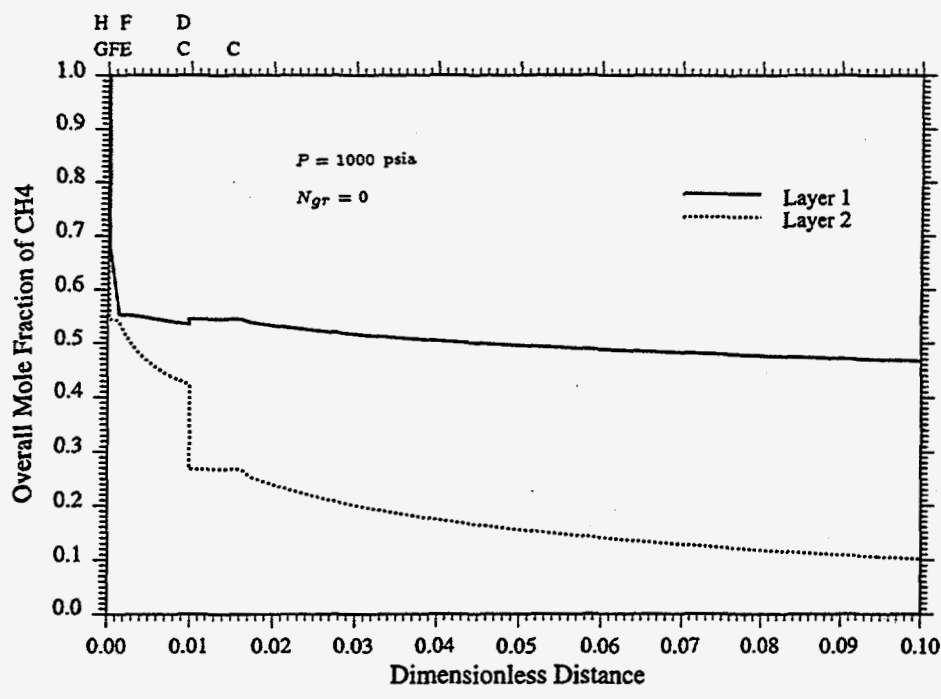


Figure 2: Close look at the composition profiles at $t_D = 0.25$ PV for CH_4-C_{10} displacement (with crossflow) at 1000 psia and $N_{gr} = 0$ —layered media.

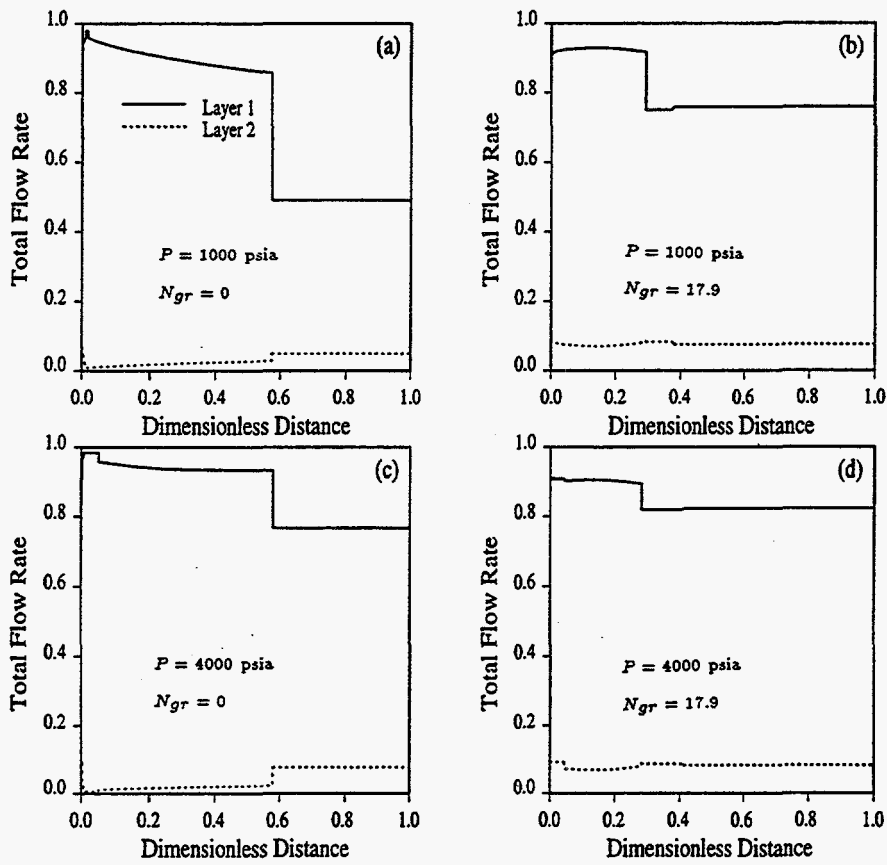


Figure 3: Flow rate profiles at $t_D = 0.25$ PV injection (with crossflow) at different pressures and inlet gravity numbers—layered media.

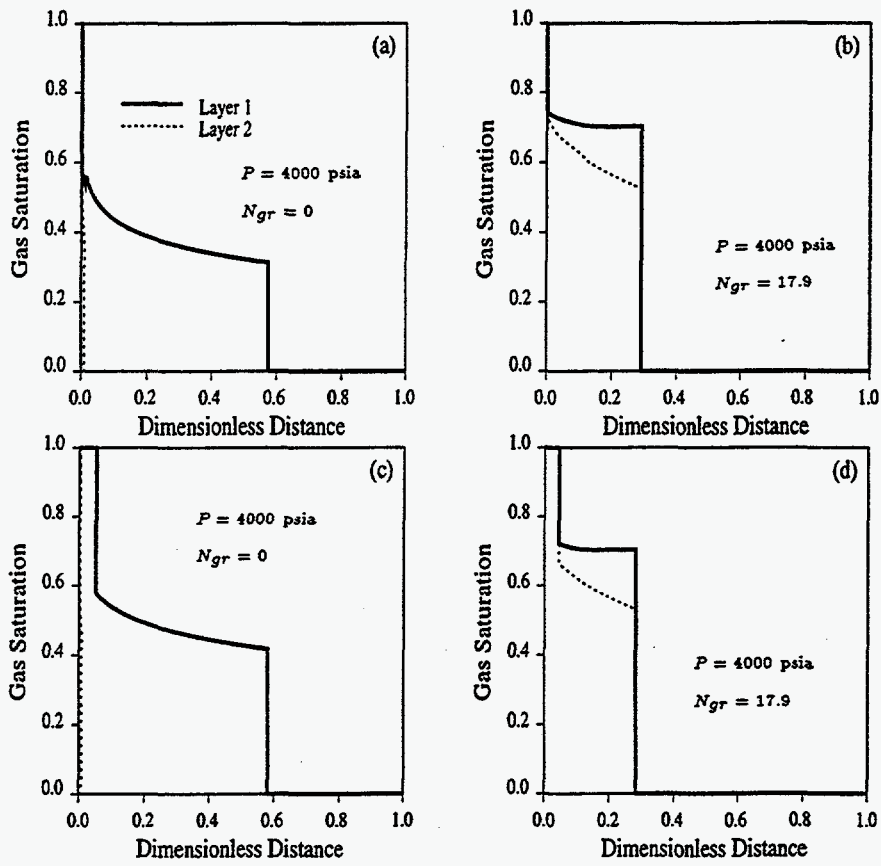


Figure 4: Saturation profiles at $t_D = 0.25$ PV injection (with crossflow) at different pressures and inlet gravity numbers—layered media.

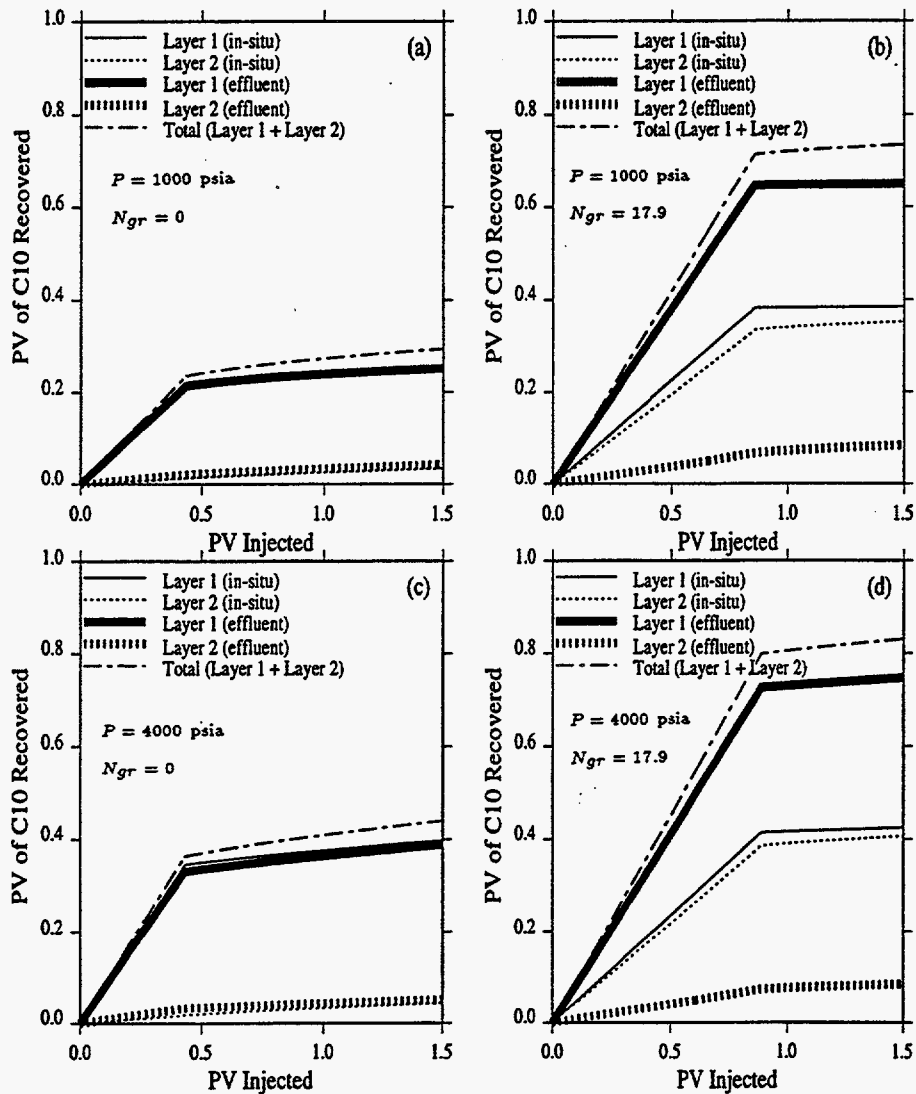


Figure 5: Recovery plots (with crossflow) at different pressures and inlet gravity numbers—layered media.

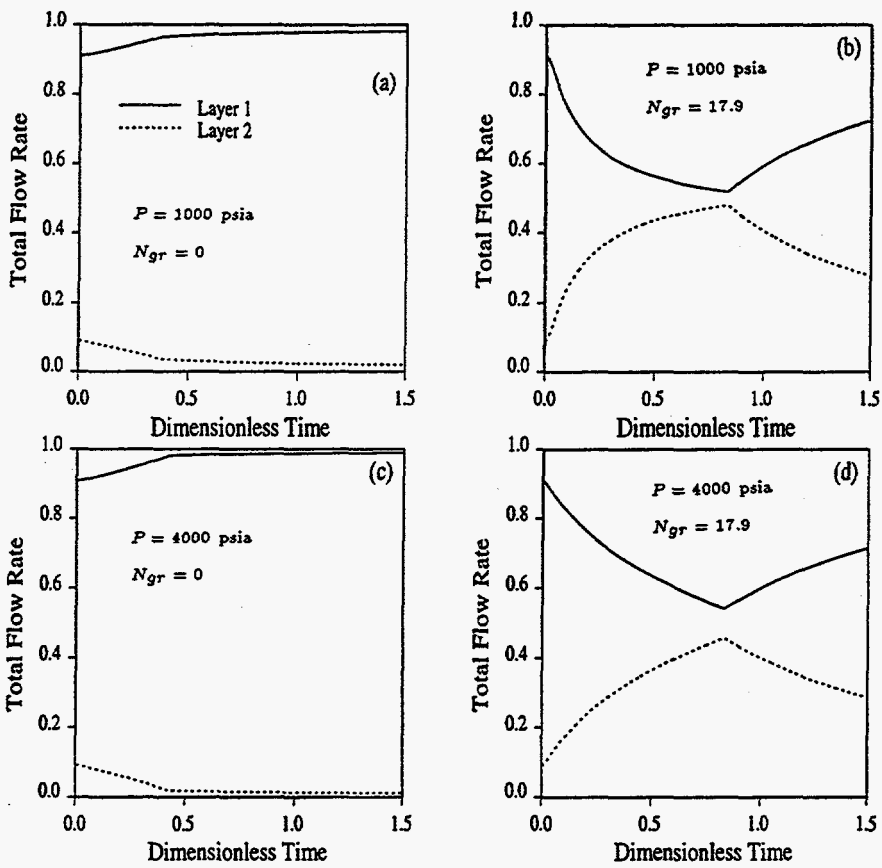


Figure 6: Inlet rate history (without crossflow) at different pressures and inlet gravity numbers—layered media.

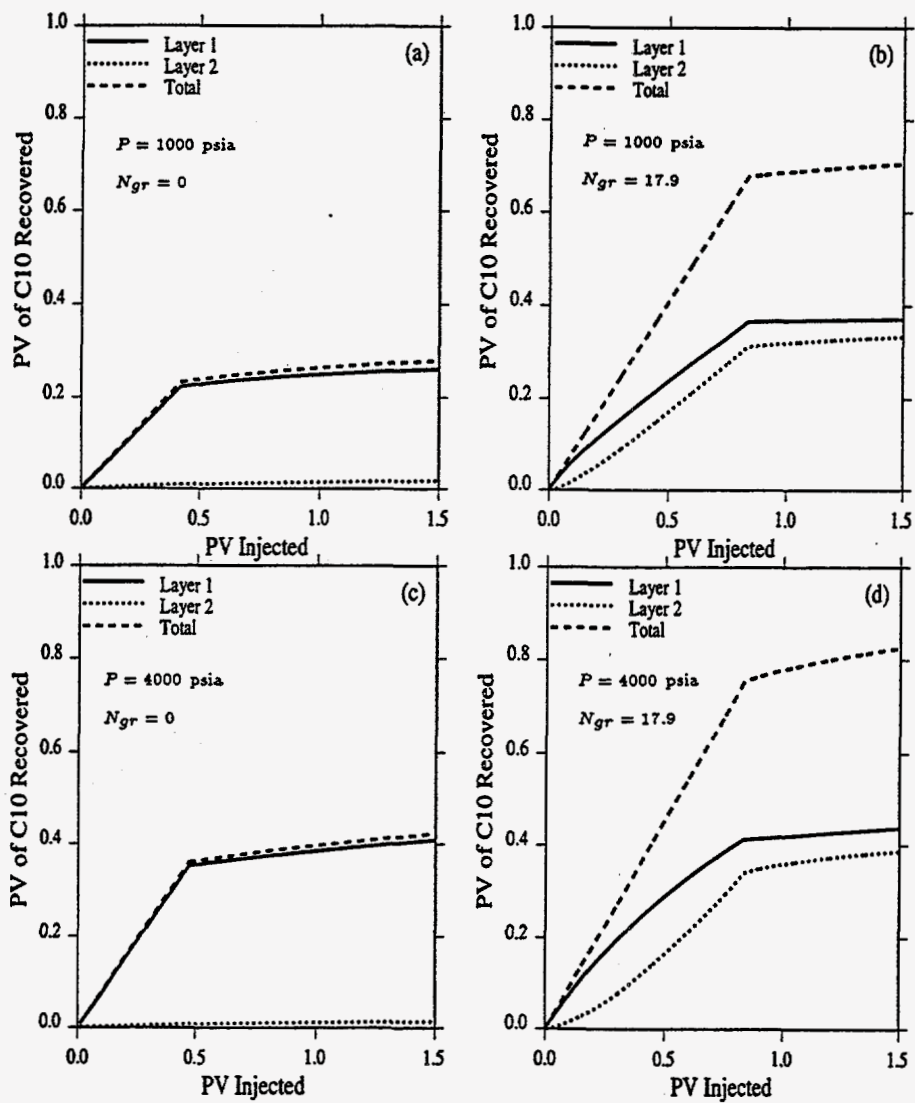


Figure 7: Recovery plots (without crossflow) at different pressures and gravity numbers—layered media.

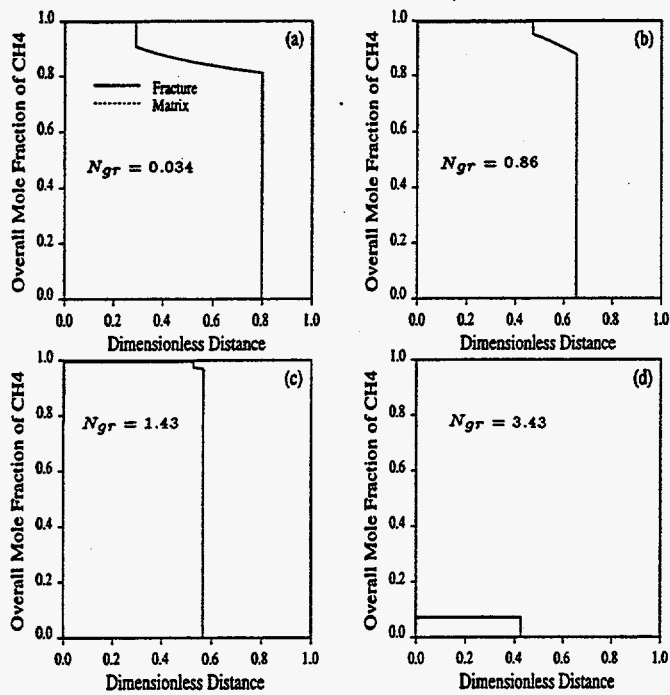


Figure 8: Composition profiles at $t_D = 0.00025$ PV injection (with crossflow) for different inlet gravity numbers at 4000 psia—fractured media.

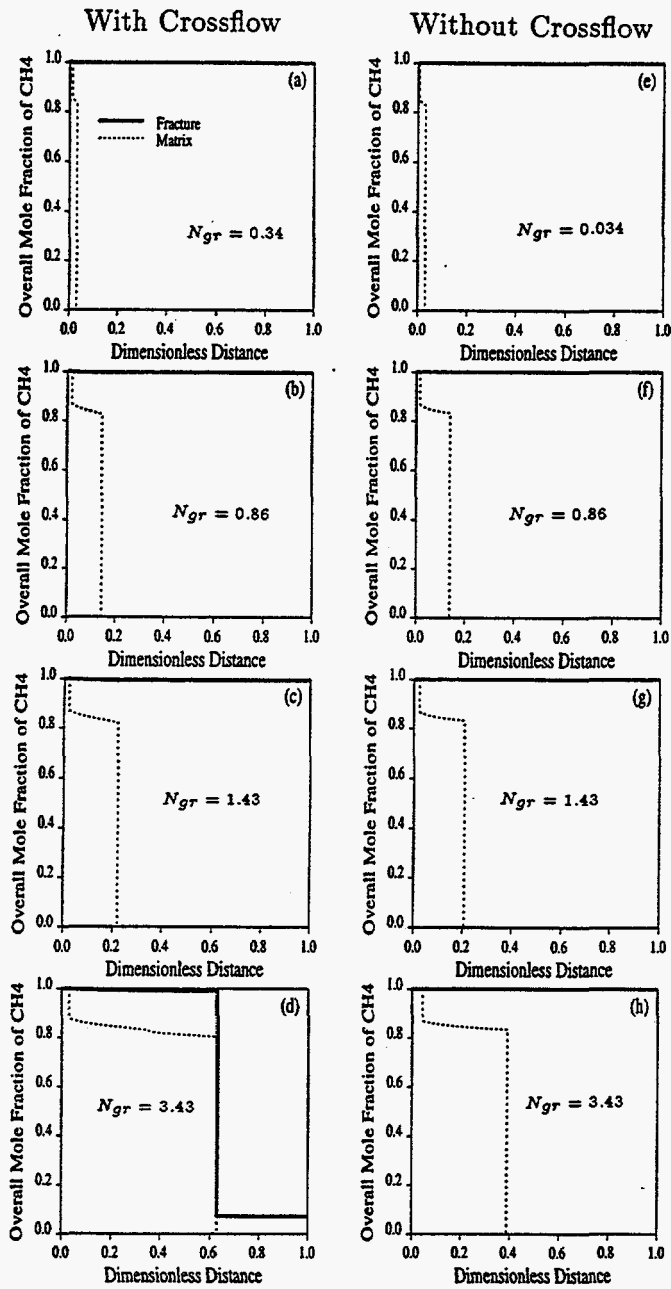


Figure 9: Composition profiles at $t_D = 0.5$ PV injection (with and without crossflow) for different inlet gravity numbers at 4000 psia; the right column is without crossflow and the left column is with crossflow—fractured media.

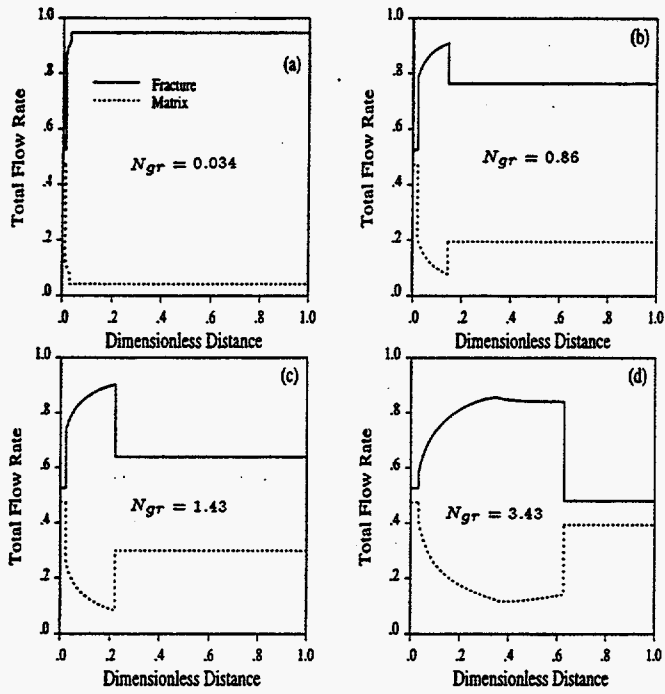


Figure 10: Flow rate profiles at $t_D = 0.5$ PV injection (with crossflow) for different inlet gravity numbers at 4000 psia—fractured media.

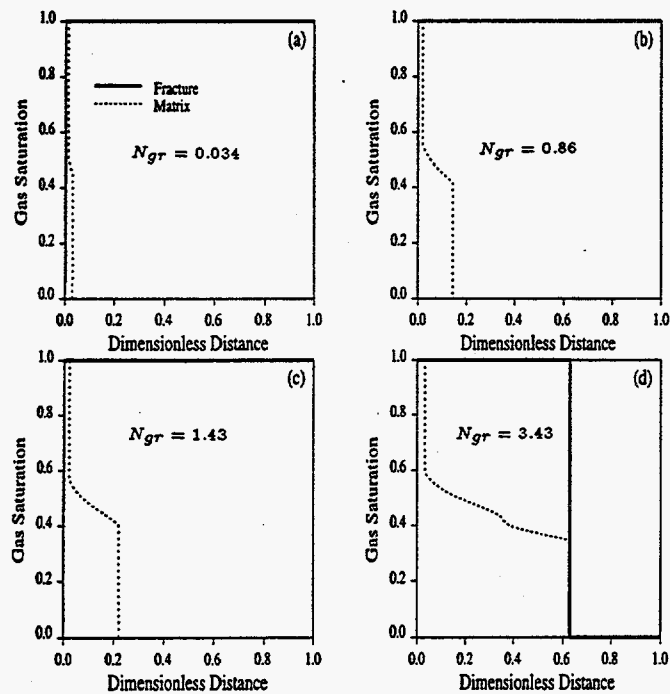


Figure 11: Saturation profiles at $t_D = 0.5$ PV injection (with crossflow) at different inlet gravity numbers at 4000 psia—fractured media.

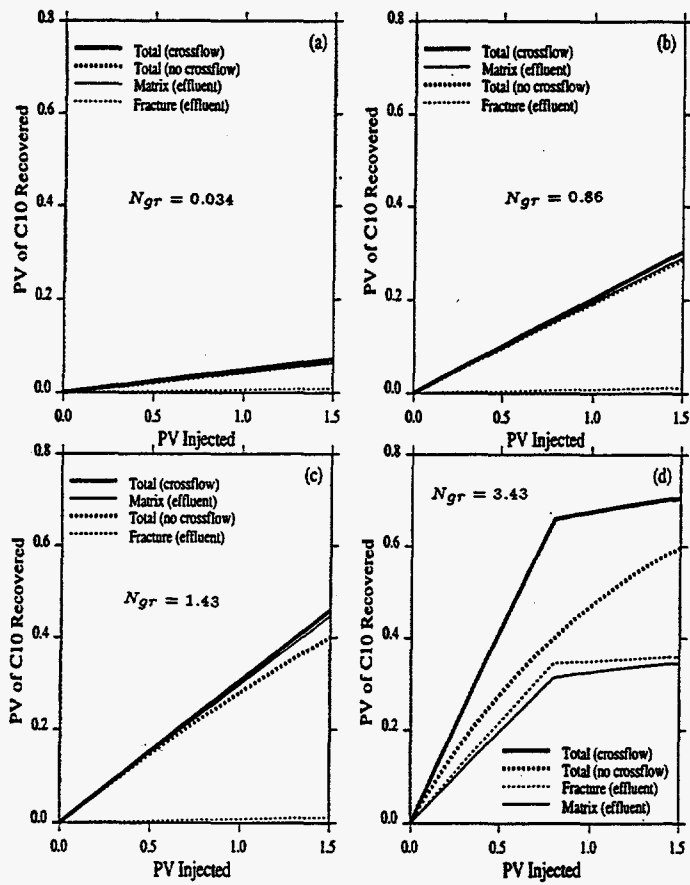


Figure 12: Recovery plots for (with and without crossflow) for different gravity numbers at 4000 psia—fractured media.

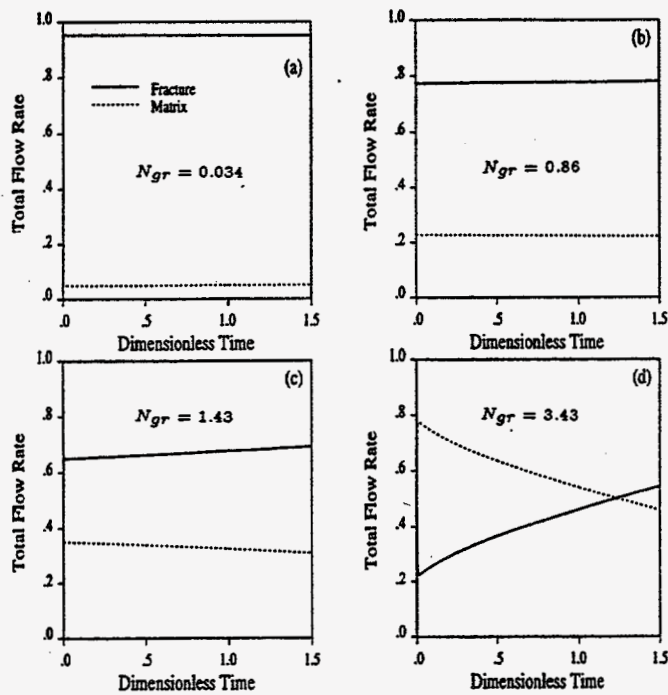


Figure 13: Inlet rate history (without crossflow) for different gravity numbers at 4000 psia—fractured media.

CHAPTER III

Co-Current and Counter-Current Imbibition in a Water-Wet Matrix Block

Mehran Pooladi-Darvish
Abbas Firoozabadi
Reservoir Engineering Research Institute

SUMMARY

The imbibition in water-wet matrix blocks of fractured porous media is commonly considered to be counter-current. Despite this general belief, our theoretical and experimental studies indicate that co-current imbibition may be the dominant mechanism. Using numerical simulation of the imbibition process it is found that oil is predominantly recovered by co-current imbibition; the time for a specified recovery is only a fraction of that required for counter-current imbibition. In counter-current imbibition, oil is forced to flow in the two-phase region; in co-current imbibition, oil can flow in the single phase. This study reveals that co-current imbibition is much more efficient than counter-current imbibition. Consequently, use of the imbibition data by immersing a single block in water and its scale-up provide pessimistic recovery information.

INTRODUCTION

Fractured porous media are idealized as an aggregate of matrix blocks and a fracture network. In order to understand two-phase flow in such a system, there is a need to understand first the recovery performance of a single matrix block (Firoozabadi, 1994). For gas-oil flow, due to the effect of fracture capillary pressure and fracture flow, the flow performance of an aggregate of matrix blocks may be very different from the single matrix block. For water-oil flow, when the rock is water-wet, the performance of a single matrix block and fractured porous media are believed to be closely related.

It is generally believed that matrix oil recovery due to water displacement in a water-wet fractured porous media is dominated by counter-current imbibition. However, our recent experimental observations reveal that co-current and not the counter-current imbibition is the main mechanism of oil recovery by water injection in water-wet fractured media. Since the oil recovery efficiency of co-current and counter-current imbibition might be very different, it is of significant practical interest to understand these two processes.

Counter-current imbibition has received considerable attention in the literature. The mathematical formulation of counter-current imbibition is of the form of a nonlinear diffusion equation [Marle 1981], and is simpler than co-current imbibition. Analytical and semi-

analytical solutions of counter-current imbibition have been recently emphasized. Chen [1988] reviewed the self-similar solutions of incompressible two-phase flow problems in linear systems. He presented the solution for a 1-D horizontal medium, when the total velocity (summation of oil and water velocities,) is assumed to be inversely proportional to square-root of time. The 1-D counter-current imbibition problem is a special case of the above, with the proportionality constant equal to zero. The solution involves trial and error and numerical integration of an ordinary differential equation, which is valid only for $S_{wi} \leq S_{iw}$ [Chen et al. 1990], where S_{wi} is the initial water saturation, and S_{iw} is the irreducible water saturation. Barenblatt et al. [1990] showed that for $S_{wi} \leq S_{iw}$, and for realistic capillary pressure and relative permeability functions, the velocity of the saturation front is finite; saturation drops to the initial value at a finite length which increases with time. Under the above condition, the solution obtained for a semi-infinite system is valid for a finite medium before the saturation front reaches the far boundary.

Using an iterative integral method, McWhorter and Sunada [1990] have also presented an analytical solution for the 1-D counter-current problem. The iterative procedure has been found to converge and to be fast. Chen et al. [1990] used this method when the initial water saturation was higher than the irreducible water saturation. The integral solution satisfactorily predicts the saturation distribution and imbibition rate before the saturation front reaches the far boundary. General analytical solutions for the 1-D, two-phase co-current imbibition problem are not available.

Much experimental work on counter-current imbibition has been reported. In these experiments, the oil-saturated cores are either immersed in water, or sealed such that water in-flow, and oil out-flow occur through the same faces [Mattax and Kyte 1962, Iffly et al. 1972, du Prey 1978, Hamon and Vidal 1986, Cuiec et al. 1994, Zhang et al. 1995]. Some studies on co-current imbibition have reported oil production from a face not covered with water (i.e., co-current imbibition) [Parsons and Chaney 1964, Iffly et al. 1972, Kleppe and Morse 1976, Hamon and Vidal 1986, Bourbiaux and Kalaydjian 1990]. No conclusive comparison between co-current and counter-current imbibition were presented by these authors, except Bourbiaux and Kalaydjian, who in a detailed experimental study examined the co-current and counter-current imbibition processes on a laterally coated core. When the two opposing faces were open to flow, and water was in contact with one face, oil was mostly produced by co-current imbibition from the face in contact with oil; oil production from the water-contacted face was very small—about 3%. It is not clear if this small amount was produced from the rock, or was the oil from the dead volume. The counter-current experiment had a slower recovery than the co-current experiment; the half-recovery time for co-current imbibition was 7.1 hrs and that for counter-current imbibition was 22.2 hrs, for one set of experiments. The measured saturation profiles for the two processes were different, also.

In order to appreciate the difference between co- and counter-current imbibition processes, consider imbibition in a cylindrical core, initially at irreducible water saturation. The surface area around the core is coated with an impermeable material, and one (or two) end-face(s) is (are) open to flow. First, consider counter-current imbibition, in which the open-end is initially in contact with oil at ambient pressure, say zero pressure. The water pressure in the

core is fixed by the capillary pressure relationship, $p_w = -P_c(S_{wi})$. The imbibition begins when the oil outside the core in the open-end is replaced by water at ambient pressure. If we assume $P_c = 0$ at this face, both the oil and water pressure will be zero at the inlet, from $t = 0^+$. (This boundary condition is experimentally verified, as will be discussed later). Water will imbibe into the core due to the low water pressure in the core, and oil flows out of the core from the same face (the fluids are assumed incompressible). Oil flows because oil pressure within the rock is higher than that at the inlet. Figure 1 shows the oil and water pressures in 1-D counter-current imbibition at various times for an example which we will discuss later. At $t = 0^+$, the oil pressure inside the core is high. As time progresses, oil pressure decreases, approaching zero at very long times. Water pressure at $t = 0^+$ is low and increases with time; it approaches zero at very long times. Now, for co-current imbibition, consider a situation in which the oil pressure at both ends of the core is initially fixed at zero, for example by exposing it to oil at ambient pressure. Water at ambient pressure is then introduced at one end. Since oil pressure at both ends is zero, oil pressure within the core goes through a maximum, as shown in Figure 2. This suggests that oil may flow from both ends. We will demonstrate later that most of the recoverable oil is produced by the co-current process from the end-face exposed to oil at the ambient pressure. In an early paper, Rakhimkulov and Shvidler [1962] showed that for a certain class of 1-D, two-phase incompressible flow problems, when the total velocity is assumed to be inversely proportional to square-root of time, oil flow at the end-face in contact with water can be counter-current to water flow, whereas at the other end-face is co-current.

With the above introduction to co-current and counter-current imbibition, in the following we will first examine the mathematical formulation of these two processes. Since one main goal is to examine the efficiency of these two processes, scaling studies will be used to draw general conclusions. Towards the end, the results from an experiment is presented to confirm the superiority of co-current over counter-current imbibition.

MATHEMATICAL INVESTIGATION

Many studies of the imbibition process have assumed that the pressure gradient in the displaced oil phase may be negligible [Beckner et al. 1987, Dutra and Aziz 1992]. This assumption was based on the common practice in hydrology, where the mathematical formulation of unsaturated water flow ignores the air pressure gradient (see Morel-Seytoux [1973] for an account of this assumption). Under the above assumption, the imbibition process can be described by a nonlinear diffusion equation [Handy 1960] of the form of,

$$\frac{\partial}{\partial x} \left(D(S_w) \frac{\partial S_w}{\partial x} \right) = \frac{\partial S_w}{\partial t}, \quad (1)$$

where,

$$D(S_w) = -\frac{k k_{rw}}{\phi \mu_w} \frac{dP_c}{dS_w}. \quad (2)$$

The initial and boundary conditions are,

$$S_w = S_{wi}, t = 0, 0 \leq x \leq L, \quad (3)$$

$$S_w = 1 - S_{or}, t > 0, x = 0, \quad (4)$$

$$q_w = 0, t > 0, x = L. \quad (5)$$

Equation 1, assumes that the fluids are incompressible, and the effect of gravity is neglected. Equation 4 states the continuity of capillary pressure at the inlet-face, and Equation 5 implies that the imbibition continues so long as the water pressure inside the core is less than that outside. Note that the above formulation applies to both co- and counter-current imbibition.

Equations 1 to 5 may be good approximations for the unsaturated flow problem, where viscosity of the displaced nonwetting phase is much smaller than water viscosity (i.e., air). We will show later that for the water-oil system, where oil and water viscosities can be of the same order, the oil pressure gradient may not be neglected. If we include the oil pressure gradient, Equation 1 with initial and boundary conditions 3 to 5 can describe the counter-current imbibition process [Marle 1981]. The corresponding diffusion coefficient, however, will be of the form,

$$D(S_w) = -\frac{k k_{ro}}{\phi \mu_o} f(S_w) \frac{dP_c}{dS_w}, \quad (6)$$

where,

$$f(S_w) = \frac{1}{1 + \frac{k_{ro}\mu_w}{k_{rw}\mu_o}}. \quad (7)$$

Co-current imbibition, when the oil phase pressure gradient is included, cannot be formulated as Equation 1. In this case, the water saturation equation is given by (see McWhorter and Sunada [1990]),

$$\frac{\partial}{\partial x} \left(D(S_w) \frac{\partial S_w}{\partial x} - q_t f(S_w) \right) = \frac{\partial S_w}{\partial t}, \quad (8)$$

where D and f functions are given by Equations 6 and 7, respectively. In Equation 8, $q_t = q_o + q_w$ is unknown, and an additional equation, i.e., the pressure equation with its own initial and boundary conditions is required to complete the formulation. For co-current imbibition the saturation and pressure equations are coupled and must be solved simultaneously. For counter-current imbibition, the two equations are decoupled.

A review of Figures 1 and 2 highlights the difference between the two processes. In counter-current imbibition, oil and water pressures ahead of the saturation front are constant and are neither a function of time nor position (see Figure 1). In co-current imbibition, however, water and oil pressures ahead of the saturation front vary with time and position (see Figure 2). Co-current imbibition takes advantage of a pressure gradient ahead of the front. This improves the process, especially because it is acting in the single phase region. Heuristically, there is a contribution of a convective term for co-current imbibition, which is in addition to the diffusive term of Equation 1. As we will see later, at a very early time, the magnitude of the convective term with respect to the diffusive term is small, and

the co-current imbibition rate is very close to counter-current imbibition. Beyond the very early time, the effect of the convective term increases, such that most oil recovery from an imbibition process with both ends open is obtained by co-current flow, making co-current imbibition much more efficient than counter-current imbibition.

NUMERICAL MODEL

It was mentioned earlier that the analytical solution of the problem is limited to an infinite-acting period for counter-current imbibition. Therefore, we need to use a numerical model to study co- and counter-current imbibition at early and late time in finite porous media. We used the method of Douglas, Peaceman and Rachford [1959], discussed by Peaceman [1967, 1977], to develop 1-D and 2-D finite difference models. In this method, the continuity equation is coupled with the Darcy law for oil and water phases,

$$\nabla \cdot \left(k \frac{k_{ro}}{\mu_o} \nabla p_o \right) = -\phi \frac{dS_w}{dP_c} \left(\frac{\partial p_o}{\partial t} - \frac{\partial p_w}{\partial t} \right) \quad (9)$$

$$\nabla \cdot \left(k \frac{k_{rw}}{\mu_w} \nabla p_w \right) = \phi \frac{dS_w}{dP_c} \left(\frac{\partial p_o}{\partial t} - \frac{\partial p_w}{\partial t} \right) \quad (10)$$

The above two equations are solved simultaneously. The initial and the inlet boundary conditions for co- and counter-current imbibition are the same. The outlet boundary condition for the oil phase is different for the two processes. For the 1-D problem, the initial and boundary conditions are given by,

$$p_o = 0, t = 0, 0 \leq x \leq L \quad (11)$$

$$p_w = -P_c(S_{wi}), t = 0, 0 \leq x \leq L \quad (12)$$

$$p_o = 0, t > 0, x = 0 \quad (13)$$

$$p_w = 0, t > 0, x = 0 \quad (14)$$

$$q_w = 0, t > 0, x = L \quad (15)$$

for counter-current imbibition

$$q_o = 0, t > 0, x = L \quad (16)$$

and for co-current imbibition

$$p_o = 0, t > 0, x = L \quad (17)$$

In the Appendix, we briefly discuss some choices in regards to the treatment of the nonlinear terms and the boundary conditions.

For numerical calculations of this study, and to illustrate the differences between co- and counter-current imbibition, a 1-D matrix block with absolute permeability of 20 *md* and length of 20 *cm* is considered. Oil and water viscosities are 1 *cp*. The relative permeability and imbibition capillary pressure functions are expressed as,

$$k_{ro} = A_o(1 - S)^{n_o}, k_{rw} = A_w S^{n_w} \quad (18)$$

$$P_c(S) = -B \ln(S), \quad (19)$$

where,

$$S = \frac{S_w - S_{iw}}{1 - S_{or} - S_{iw}} \quad (20)$$

The parameters A_o, A_w, n_o, n_w, B are constant. Table 1 gives the values considered for the base case example. Sensitivity studies will be performed to study the effect of different parameters on the two imbibition processes.

Next, the results of the numerical solution of the base case example for the counter-current imbibition is validated against the analytical solution during the infinite-acting period.

Validation: We used the analytical solution of counter-current imbibition by McWhorter and Sunada [1990]. The saturation and pressure profiles and the recovery curve¹ are shown in Figures 1, 3 and 4, and are compared with the numerical solution with 300 grid blocks. The analytical solution can be used for the infinite-acting period only. In all the figures, a close match is observed. For comparison, the recovery curve with 50 grid blocks is shown in Figure 4. The recovery at the early time is overestimated somewhat by the coarser grid, and the saturation plots (not shown) indicate a limited numerical dispersion. All the 1-D results presented in this work are performed using 300 grid blocks and the 2-D calculations with 50×50 grid blocks. A small effect of numerical dispersion was observed in the 2-D calculations due to the coarse grids.

1-D RESULTS

In this section, the behavior of the counter-current and co-current imbibition are illustrated using the numerical model described above.

Counter-Current and Co-Current Imbibition: Pressure and saturation profiles of counter-current imbibition are shown in Figures 1 and 3. Figure 1 indicates that oil and water phase pressure drops across the two phase region are constant before the saturation front reaches the far boundary; oil and water pressures are constant beyond the saturation front, and are independent of the length. It can be concluded that counter-current imbibition exhibits an infinite-acting behavior, and the solution does not depend on the length of the formation before saturation front reaches the far boundary. This does not hold for co-current imbibition, as we will see soon. Note that, oil and water exhibit very sharp pressure gradients, at the inlet end and at the front, respectively, where their corresponding relative permeabilities are small. Figure 1 indicates that oil phase pressure drop is smaller than the water phase, but the steep oil pressure gradient at the inlet suggests that its neglect, as assumed by Beckner et al. [1987] and others, may not be appropriate. Figure 4 shows the recovery curve when the oil phase pressure gradient is neglected.

Figure 3 reveals that before the saturation front reaches the far boundary, sharp saturation gradients are observed at the inlet and at the front. This is caused by the small value

¹The recovery curves are based on the total recoverable oil in place.

of the diffusion coefficient at high and low saturations which restricts flow unless high saturation gradients are established. The saturation profile at 40 days depicts steep gradients at the inlet which are due to low values of diffusion coefficient, corresponding to saturation values that are present at the inlet only.

The pressure and saturation profiles for 1-D co-current imbibition are depicted in Figures 2 and 5. Clear differences with counter-current imbibition can be noticed. Oil and water pressures ahead of the saturation front are not constant; they vary with time and position, i.e., co-current imbibition does not show an infinite-acting behavior, because oil pressure *feels* the effect of the far boundary from the beginning of imbibition. Moreover, oil pressure is not monotonic; it passes through a maximum in the two-phase region. Behind the maximum, oil flows in the opposite direction of water. Saturation profiles advance more in co-current imbibition compared with that in counter-current imbibition (compare Figures 3 and 5). The latter shows the superiority of co-current over counter-current imbibition.

Figure 6 shows the recovery curve for co- and counter-current imbibition. If the residual oil saturation for co- and counter-current imbibition is equal, as assumed here, recovery curves at very late times approach the same value. At earlier times, however, especially before the saturation front reaches the far boundary, there is a substantial difference between the two curves. For example, the half-recovery time for counter-current imbibition is more than five times that of co-current imbibition. As we will demonstrate later, the above difference is not limited to the base case example.

We used the same relative permeability curves for co- and counter-current imbibition. Recent studies suggest that relative permeability curves for the two processes could be different [Bourbiaux and Kalaydjian 1990, Bentsen and Manai 1991]. The difference between the two relative permeabilities is commonly attributed to viscous coupling. Bourbiaux and Kalaydjian [1990] reduced the co-current relative permeabilities by 30% to use them for counter-current imbibition. Figure 6 depicts the recovery curve for counter-current imbibition when relative permeabilities are reduced by 30%. Half-recovery time for counter-current imbibition is then 32 days, compared with 4.5 days for co-current imbibition. Figure 6 also shows the contribution of oil recovery from the face in contact with water (the other face is in contact with oil). The contribution of the back-flow production at a recovery of 80% is less than 5%, a large portion of the back-flow recovery is obtained at a very early time. Very fine grid studies with small time-steps indicate the early high back-flow is a characteristic of the process.

As mentioned above, oil flow behind the maximum oil pressure is in the opposite direction to water flow. If co- and counter-current relative permeabilities are different, appropriate relative permeabilities should be used in different regions. We did not incorporate this modification.

The results presented above show that the oil recovery by co-current imbibition is much more efficient than counter-current imbibition. The scaling studies of the following section will show that, this conclusion is not limited to the data used for the base case example.

Scaling Studies: Rapoport [1955] presented the scaling criteria for two-phase incompress-

ible flow through porous media. Using inspectional analysis of the differential equations of water-oil flow through porous media, he found that saturation distribution is a function of dimensionless time provided: 1) geometric similarity is preserved, 2) initial and boundary conditions are the same, 3) relative permeability functions and water-oil viscosity ratio are the same, and 4) capillary pressure functions are related through direct proportionality. Rapoport's dimensionless time is given by,

$$t_D = \frac{kt}{\phi\mu_w L^2} \frac{dP_c}{dS_w} \quad (21)$$

We varied the value of absolute permeability, length, derivative of the capillary pressure curve with respect to water saturation, and water viscosity (at a constant viscosity ratio). Figure 7 shows that the above scaling law applies to both co- and counter-current imbibition. Rapoport [1955] presented the above scaling criterion for water-oil systems. In the literature, however, its validity has been demonstrated for counter-current imbibition, only. Figure 7 suggests that if the above four conditions hold, the Rapoport scaling is also valid for the co-current imbibition, as expected. The dimensionless time ratio (defined as the time ratio of the two processes to achieve a specific recovery) vs. recovery for co- and counter-current imbibition of Figure 7 is shown in Figure 8 by the solid line. At the very early time, the recovery performance of co- and counter-current imbibition is similar, and the time ratio is equal to one. The time ratio increases rapidly such that, half-recovery time for counter-current imbibition is more than 5 times of that of co-current imbibition. After the saturation front reaches the far boundary, at about 50% recovery for counter-current imbibition, recovery rate decreases drastically (see Figure 7). For co-current imbibition, however, the saturation front does not reach the far boundary until about 70% recovery. Hence, the time ratio between the two processes increases sharply in this interval. Beyond this time, the recovery rate for co-current imbibition drops, and the time ratio decreases. Figure 8 indicates that for the most part, oil recovery for co-current imbibition is more than four times faster than the counter-current imbibition. Note that the data labeled as base case in Figure 8 encompasses all the variations shown in Figure 7.

Sensitivity Studies: In the following, the numerical model is used to investigate the effect of some of the variables on the imbibition process, which are not included in the Rapoport scaling law [1955].

We varied the oil and water relative permeability exponents, viscosity ratio, and initial water saturation. The effect of these parameters is most obvious on the saturation and pressure profiles (not shown here). When the water exponent was reduced to 2, the sharp saturation gradient at the front was absent. Water reached the far boundary much faster than for the base case example. Reduction of oil exponent to 2, reduced the saturation gradient at the inlet. By the time saturation front reached the far boundary, a larger recovery was obtained. Reduction of oil viscosity to 0.2 *cp*, had similar effects to the latter case, but to a lesser degree. When the initial water saturation was increased to $S_i = 0.2$, a tongue was observed at the leading edge of the saturation front. This behavior in counter-current

imbibition was previously studied by Barenblatt et al. [1990]. The scaling study of the previous section indicates that a pair of recovery curves, similar to those of Figure 7, can be presented for each of the above cases. These, of course, will be independent of the parameters included in Equation 21. From such recovery calculations, co- and counter-current imbibition are compared and the results are also shown in Figure 8. Again, a large difference between the two processes are observed. Among the parameters varied, the exponent of oil relative permeability has the largest effect (see the thin-dashed line in Figure 8).

It is interesting to note that the time ratio at large recoveries approaches 4. All parameters being the same, a four-time permeability increase is required for co- and counter-current imbibition to behave similarly at high recoveries. The high recoveries shown in Figure 8 are at extremely low rates.

Now, let us consider a 1-D core open from both ends, once immersed in water, and another time, one face exposed to water and the other face exposed to oil, both at the same constant pressure. In the former case, because both end faces are in contact with water, water has to move half of the distance of the latter. Hence, at a given time, the dimensionless time of the counter-current imbibition is four times of the co-current imbibition (See Equation 21). Figure 8 indicates that with the properties of the base case example, co-current imbibition works faster after about 20% recovery is obtained. Experimental data of Bourbiaux and Kalaydjian [1990] show that the co-current process takes over counter-current imbibition with immersed end faces after 5% recovery. Reduction of the relative permeability curves for the counter-current imbibition is not included in the calculations of Figure 8.

Co- and Counter-Current Imbibition at the Early Times: Figure 7 implies that the superiority of co-current over counter-current imbibition does not depend on the length of the porous medium. On the other hand, Figure 2 suggests that the oil pressure gradient in the single phase region depends on the length of the core. Figure 9 shows the total oil produced for co- and counter-current imbibition for lengths of 20, 100, and 1000 *cm*. This figure indicates that as the length of the core increases, oil production for co-current imbibition decreases, and approaches that of counter-current imbibition. In fact, for the time considered in Figure 9, most of the oil is produced due to back-flow when the core is 1000 *cm* long. For a semi-infinite medium co- and counter-current imbibition recoveries become the same. Although Figure 9 shows a small difference between oil production of co- and counter-current imbibition from the 1000 *cm* sample, large differences between recoveries will be observed at later times. This shows that there were no errors in the early time calculations. Moreover, the superiority of co-current vs. counter-current imbibition for specific rock and fluid properties, is a function of dimensionless time only, as shown in Figure 8.

2-D RESULTS

In the previous section, co- and counter-current imbibition were studied for a 1-D geometry, where oil is either produced from the inlet or has to flow the length of the core to be produced from the other end. In this section, we examine co- and counter-current imbibition in 2-D

media. The properties of the base case example are used for a square porous medium (the dimensions are 20×20 cm and very long). The left and bottom faces are in contact with water at ambient pressure, and the top and right faces are either closed or in contact with oil at ambient pressure.

Counter-Current and Co-Current Imbibition: Figure 10 displays the recovery curve for the two processes. Similar to the 1-D case, co-current imbibition is much more efficient than counter-current imbibition. At $t = 4$ days, oil recoveries for co- and counter-current imbibition are 70% and 37%, respectively. Recovery due to back-flow production for the co-current imbibition is about 5%. Figure 11 depicts the time ratio for the two imbibition processes. The calculations are performed to about 6 years. Figures 10 and 11 for 2-D imbibition are similar to Figures 6 and 8 for 1-D imbibition with minor differences.

By varying the parameters in Equation 21 we can test the scaling law of Rapoport [1955] in a 2-D geometry. Similar results to the 1-D case are obtained (not shown here). Thus, Figures 10 and 11 can be used for other 2-D systems, if the four requirements of scaling, mentioned earlier, are met. (Time in Figures 10 and 11 should then be replaced by the corresponding dimensionless values.)

In order to study further the similarities and the differences between 1-D and 2-D imbibition, the saturation, pressure and velocity profiles of the 2-D imbibition are examined. Figures 12 and 13 show the water saturation, oil velocity, and oil and water pressure distributions for counter-current imbibition. The corresponding graphs for co-current imbibition are shown in Figures 14 and 15. (The arrows below the graphs on the right side of Figures 12 and 14 show the velocity magnitude.) Similar to 1-D case, the saturation profiles have high gradients at the inlet and at the front. Water and oil pressures, have high gradients at the front, and at the inlet, respectively. Oil velocity profiles, especially for the co-current process indicate that oil rates are higher where there is small distance between the water front and the open face. As the saturation front moves from the bottom to the top, oil is mostly produced from the right face. In contrast with the 1-D case, the effect of the outlet end is felt on the saturation profiles from a very early time.

Superposition: Experimental and mathematical studies of 1-D imbibition cannot be used for multi-dimensional predictions due to lack of geometric similarity, a requirement from the scaling law of Rapoport [1955]. Superposition of 1-D solutions to 2- and 3-D has been suggested to address this point, although superposition does not hold for nonlinear problems. Dutra and Aziz [1992] used superposition of approximate 1-D solutions to describe a 2-D imbibition process. Recently, Zhang et al. [1995] proposed that, for counter-current imbibition, L in Equation 21 can be replaced by a characteristic length, L_c . The definition of L_c resembles superposition of 1-D solutions in Cartesian coordinates. Figures 16 and 17 show the comparison between the recovery obtained from the superposition of 1-D solutions to 2-D with the results of 2-D calculations for co- and counter-current imbibition. The 1-D and 2-D calculations are performed using 50 grid blocks. These figures indicate that a good approximation is obtained at early times, however the late-time behavior is significantly

overpredicted by the superposition solution.

EXPERIMENTAL

In a visual coreholder, where the matrix rock is surrounded by the fractures, we observed that the injection of water does not result in the counter-current production of oil, unless the fractures are flooded with water in a very short time. The oil was produced from the matrix above the water-oil contact in the fractures. With this simple experimental observation we then embarked on an experimental study with a two-fold purpose: 1) to verify the inlet boundary condition of $P_c = 0$ (see Equations 13 and 14), and 2) to confirm the enhanced efficiency of co-current imbibition over counter-current imbibition.

A brief description of the apparatus and the experimental results follow.

Apparatus: Figure 18 shows the schematic of the apparatus. The central part is the epoxy-coated core which is laid horizontally to reduce the effect of the gravity force. The core is connected to two acrylic caps, and the inlet/outlet connections and the inlet fluid collection are mounted on the caps. The core rests on a frame which can rotate 90 degrees.

Rock and Fluid Properties: We used a sandstone of 100 md permeability and porosity of 18.5 %. The dimensions of the core are 61 cm (2 ft) in length and 7.6 cm (3 in) in diameter. The aqueous and oleic phases were solution of 1 w % NaCl in distilled water and normal decane, respectively.

Test Procedure: We first removed the in-situ fluid and adsorbed material on the pore surface by exerting a high vacuum on the core-holder. The drying period took about one to two weeks. The core was then saturated with normal decane, and a period of two days was allowed for complete saturation. The volume of nC_{10} was recorded for pore volume measurement. Gravity-driven single phase flow of nC_{10} was then performed for permeability measurement. While the core was in vertical position with the inlet down, brine was introduced into the inlet cap to displace nC_{10} . Before the brine solution touched the surface of the rock, the core was turned to a horizontal position. The excess nC_{10} was immediately collected at the top of the inlet collector and recorded (density of nC_{10} is 0.724). This was the start of the counter-current imbibition experiment with the outlet valve closed. Later in the experiment, the outlet valve was opened and the level of the outlet collector was adjusted so that the inlet water pressure was equal to the outlet oil pressure.

In the experiment which is reported next, the outlet pressure was kept constant. The inlet pressure, however, decreased by a few inches of water, before it was adjusted again. The adjustment was done five times during the course of the co-current experiment. The change in inlet pressure seems to have negligible effect on oil recovery as indicated by the smooth production data.

Verification of the Inlet Boundary Condition: The counter-current imbibition exper-

iment started with the appearance of oil drops on the rock surface which is similar to oil production behavior of counter-current imbibition with immersion boundary condition [Zhu et al. 1995]. Since the diameter of the oil drops are much larger than the pore diameter, the zero-capillary pressure assumption is valid [Barrenblatt et al. 1990]. Oil production into the water-filled inlet cap continued after the outlet valve was opened. It is shown in the following that at this stage, most of the oil was produced from the outlet, i.e., co-current imbibition. The production of limited oil from inlet, is in line with the modeling results and verifies the zero-capillary pressure boundary condition at the inlet.

Counter-Current vs. Co-Current Imbibition: Figure 19 shows the oil production data; for the first 17 days the outlet valve was closed and oil production by counter-current imbibition was 40 cm^3 . A significant increase in the oil production rate is observed when the outlet valve was opened at 17 days. The production data in Figure 19 correspond to summation of inlet and outlet production, while the contribution of inlet production is less than 5%.

Figure 19 clearly demonstrates that when one face of the rock is in contact with water and the other face with oil at the same pressure, the dominant displacement is co-current imbibition. While it took 17 days for 40 cm^3 oil production by counter-current imbibition, the same amount of oil was produced in less than 3 days, when the process was changed to co-current.

The above findings have strong implications for the experimental studies of water injection in fractured reservoirs, in that, the scaling experiment of counter-current imbibition which is commonly used to evaluate water injection in fractured reservoirs may lead to very pessimistic results.

CONCLUSIONS

1. Experimental and modeling studies reveal that, when a water-wet porous media is partially in contact with water, oil recovery is dominated by co-current imbibition, not counter-current. Moreover, co-current imbibition is much more efficient than counter-current imbibition; the time for a specific recovery by co-current imbibition is a fraction of that by counter-current imbibition.
2. The scaling criterion of Rapoport [1955] is valid for both co- and counter-current imbibition. However, oil recovery calculations based on scaling studies of counter-current imbibition, when used for a co-current process lead to very pessimistic predictions.
3. In modeling the imbibition process, the oil pressure gradient may not be neglected. Therefore, the diffusion equation may be inappropriate for the description of the co-current imbibition process.

ACKNOWLEDGMENTS

This research project was supported by the US DOE grant DE-FG22-96BC14850 and the members of the Research Consortium on the Fractured/Layered Reservoirs of the Reservoir Engineering Research Institute. This support is greatly appreciated. We are thankful to Mr. R. Jahanian for the design and construction of the experimental apparatus.

NOMENCLATURE

Latin Letters

<i>A</i>	Relative permeability constant
<i>B</i>	Capillary pressure constant
<i>D</i>	Diffusion coefficient, cm^2/s
<i>L</i>	Length, cm
<i>P_c</i>	Capillary pressure, psi
<i>S</i>	Normalized saturation
<i>S_i</i>	Normalized water saturation
<i>S_w</i>	Water saturation
<i>S_{wi}</i>	Initial water saturation
<i>S_{iw}</i>	Irreducible water saturation
<i>f</i>	Fractional Flow
<i>h</i>	Fracture Aperture, cm
<i>k</i>	Permeability, D
<i>n</i>	Relative permeability exponent
<i>q</i>	Velocity, cm/s
<i>t</i>	time, s

Greek Letters

ϕ	Porosity
μ	Viscosity, cp

Subscripts

<i>D</i>	Dimensionless
<i>o</i>	Oil
<i>or</i>	Residual Oil
<i>r</i>	Relative
<i>w</i>	Water

REFERENCES

Barenblatt, G.I., Entov, V.M., and Ryzhik, V.M.: *Theory of Fluid Flows Through Porous Media*, Kluwer Academic, Dordrecht, The Netherlands (1990) P. 279-281.

Beckner, B.L., Ishimoto, K., Yamaguchi, S., Firoozabadi, A., and Aziz, K.: "Imbibition Dominated Matrix Fracture Transfer in Dual Porosity Simulators," paper SPE 16981 presented at the 1987 SPE Annual Technical Conference and Exhibition, Dallas, Sept. 27-30.

Bentsen, R.G. and Manai, A.A.: "Measurement of Co-Current and Counter-Current Relative Permeability Curves Using the Steady State Method," *AOSTRA J. of Research* 7 (1994) 169-181-208.

Blair, P.M.: "Calculation of Oil Displacement by Counter-Current Water Imbibition," *Trans. AIME* (1964) 231, 195-202.

Brand, C.W., Heinemann, J.E., and Aziz, K.: "The Grid Orientation Effect in Reservoir Simulation," paper SPE 21228 presented at the 1991 SPE Symposium on Reservoir Simulation, Anaheim, CA, Feb. 17-21.

Bourbiaux, B. and Kalaydjian, F.: "Experimental Study of Cocurrent and Countercurrent Flow in Natural Porous Media," *SPE* (Aug. 1990) 361-368, *Trans. AIME*, 289.

Chen, Z.-X.: "Some Invariant Solutions of Two-Phase Fluid Displacement Problems Including Capillary Effect," *SPE* (May 1988) 691-700.

Chen, Z.-X., Bodvarsson, G.S., and Whitherspoon, P.A.: "An Integral Equation Formulation for Two-Phase Flow and Other Nonlinear Flow Problems Through Porous Media," paper SPE 20517 presented at the 1990 SPE Annual Technical Conference and Exhibition, New Orleans, LA, Sept. 23-26.

Cuiec, L.E., Bourbiaux, B.J., and Kalaydjian, F.J.: "Oil Recovery by Imbibition in Low-Permeability Chalk," *SPE* (Sept. 1994) 200-208.

Douglas, J.Jr., Peaceman, D.W., and Rachford, H.H.Jr.: "A Method for Calculating Multi-Dimensional Immiscible Displacement," *Trans. AIME* (1959) 216, 297-308.

Dutra, T.V. and Aziz, K.: "A New Double-Porosity Reservoir Model for Oil/Water Flow Problems," *SPE* (Nov. 1992) 419-25.

Firoozabadi, A.: "Recovery Issues of Immiscible and Miscible Gas-Oil Flow in Fractured Reservoirs: Laboratory Observations and Theoretical Analysis," (ed. U Kimura), Proceedings of the First JNOC-TRC International Symposium on Carbonate Rocks - Hydrocarbon Exploration and Reservoir Characterization, Chiba, Japan, March 1-5, 1993.

Handy, L.L.: "Determination of Effective Capillary Pressure for Porous Media from Imbibition Data," *Trans. AIME* (1960) 219, 75-80.

Hamon, G. and Vidal, J.: "Scaling-Up the Capillary Imbibition Process from Labora-

tory Experiments on Homogeneous Samples," paper SPE 15852 presented at the 1986 SPE European Petroleum Conference, London, Oct. 22-25.

Iffy, R., Rousselet, D.C., and Vermeulen, J.L.: "Fundamental Study of Imbibition in Fissure Oil Fields," paper SPE 4102 presented at the 1972 Annual Fall Meeting, San Antonio, TX Oct. 6-9.

Kleppe, J. and Morse, R.A.: "Oil Production From Fractured Reservoirs by Water Displacement," paper SPE 5084 presented at the 1974 SPE Annual Fall Technical Conference and Exhibition, Houston, Oct. 6-9.

Lefebvre du Prey, E.: "Gravity and Capillary Effects on Imbibition in Porous Media," *SPEJ* (June 1978) 195-200.

Marle, C.M.: *Multiphase Flow in Porous Media*, Gulf Pub. Co. Editions Technip, Paris 1981.

Mattax, C.C. and Kyte, J.R.: "Imbibition Oil Recovery From Fractured Water Drive Reservoirs," *SPEJ* (June 1962) 177-184, *Trans. AIME* 225.

McWhorter, D.B. and Sunada, K.D.: "Exact Integral Solution for Two Phase Flow," *Water Resources Research* (1990) 26, 339-413.

McWhorter, D.B. and Sunada, K.D.: "Reply to Comment on Exact Integral Solution for Two Phase Flow," *Water Resources Research* (1992) 28, 1479.

Morel-Seytoux, H.J.: "Two-Phase Flow in Porous Media," in *Advances in Hydroscience*, 9 ed. Dewiest, R.J.M., Academic Press, San Diego, CA. (1973).

Parsons, R.W. and Chaney, R.R.: "Imbibition Model Studies on Water-Wet Carbonate Rocks," *SPEJ* (March 1966) 26-34, *Trans. AIME* 237.

Patankar, S.V.: *Numerical Heat Transfer and Fluid Flow*, Hemisphere Pub. Co, Washington D.C. (1980).

Peaceman, D.W.: "Numerical Solution of the Nonlinear Equations for Two-Phase Flow through Porous Media," in *Nonlinear Partial Differential Equations - Methods of Solutions*, ed. Ames, W.F., Academic Press, New York (1967) 71-91.

Peaceman, D.W.: *Fundamentals of Numerical Reservoir Simulation*, Elsevier Scientific Pub. Co., Amsterdam (1977).

Rakhimkulov, I.F. and Shvidler, M.I.: "Self-Similar Problem of Simultaneous Flow of Oil and Water," *Izv. Nauk, USSR, Mekh. i Mash.* (1962) 136-37 (in Russian).

Rapoport, L.A.: "Scaling Laws for Use in Design and Operation of Water-Oil Flow Models," *Trans. AIME* (1955) 204, 143-150.

Settari, A. and Aziz, K.: "Treatment of Nonlinear Terms in Numerical Solution of Parabolic Differential Equations of Multi-Phase Flow in Porous Media," *Int. J. Multiphase Flow* (1975) 1, 817-44.

Shen, C. and Ruth, D.W.: "Impact of Inlet Boundary Conditions on the Numerical Solution of One-Dimensional Coreflooding," *J. Can. Pet. Tech.* (Jan. 1996) 19-24.

Zhang, X., Morrow, N.R., and Ma, S.: "Experimental Verification of Modified Scaling Group for Spontaneous Imbibition," *SPEFE* (Nov. 1996) 280-85.

Zhu, X., Torsaeter, O., Xie, X., and Morrow, N.R.: "The Effect of Crude-Oil Aging Time and Temperature on Rate of Water-Imbibition and Long-Term Recovery by Imbibition," *SPEFE* (Dec. 1995) 259-264.

Appendix: Simultaneous Solution of Oil and Water Equations

The time discretization of Equations (9) and (10) in the text is performed according to that suggested by Douglas, Peaceman, and Rachford [1959]. In this method, the transmissibilities are treated explicitly, and the oil and water pressures implicitly. For the treatment of the nonlinear term $\frac{dS_w}{dP_c}$, we incorporated the two methods proposed by Peaceman [1967] and chose the method which had a better rate of convergence. Mid-point weighting technique was used for the evaluation of transmissibilities. Settari and Aziz [1975] showed through an example that when capillarity is small, the mid-point technique may lead to a wrong solution. Our numerical experimentation showed that for small enough time-steps, mid-point technique gave better results than the commonly used up-stream weighting technique. We used the analytical solution of the counter-current problem for the comparison.

Space discretization was performed in accordance to the control volume method of Patankar [1980] on equally spaced point distributed grids. The application of control volume method enabled us to incorporate the boundary conditions directly and the use of reflection point technique for the no-flow boundaries was avoided [Patankar, 1980]. In all the calculations automatic time-stepping was implemented. Although not tested, little or no grid orientation effect is expected in the 2-D problem, since the mobility ratio in our examples is small [Brand et al., 1991].

Table 1. Data for the base case example

L	20 cm	n_o	4.0
k	20 md	n_w	4.0
μ_o	1 cp	A_o	0.75
μ_w	1 cp	A_w	0.20
ϕ	0.3	B	1.45 psi
S_i	0.001		

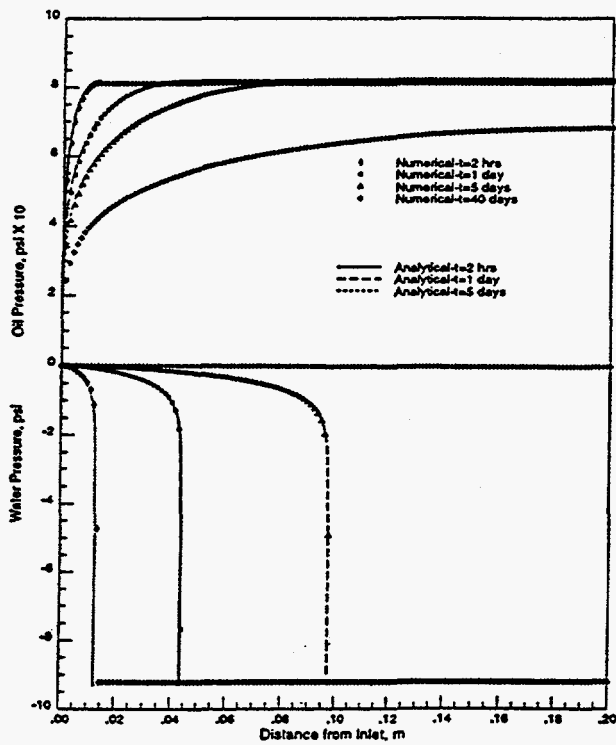


Figure 1. Oil and water pressure distribution for 1-D counter-current imbibition

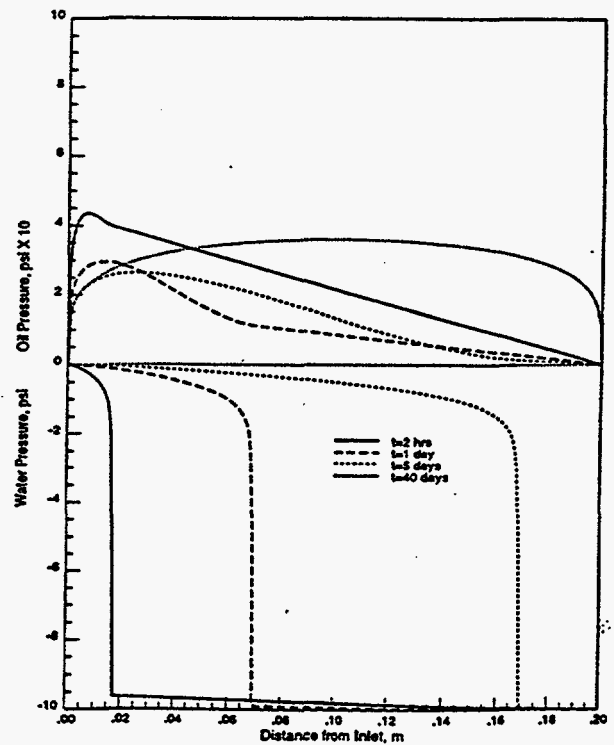


Figure 2. Oil and water pressure distribution for 1-D co-current imbibition

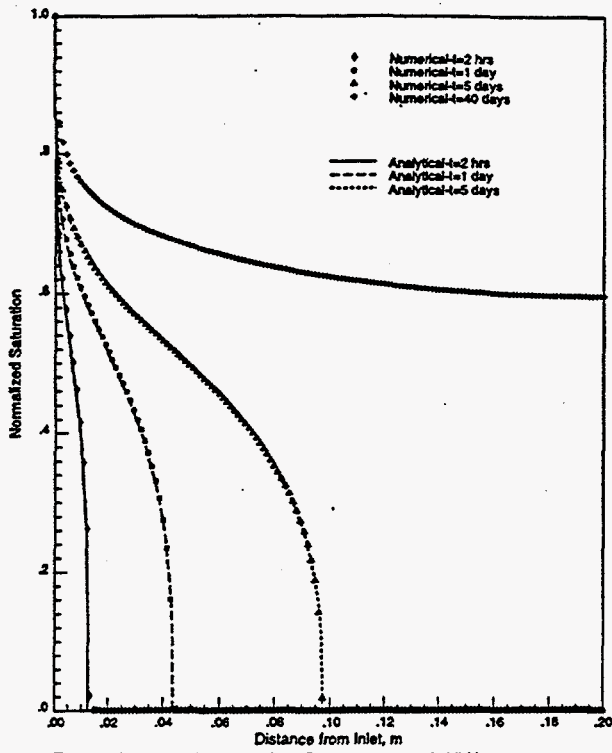


Figure 3. Saturation distribution for 1-D counter-current imbibition

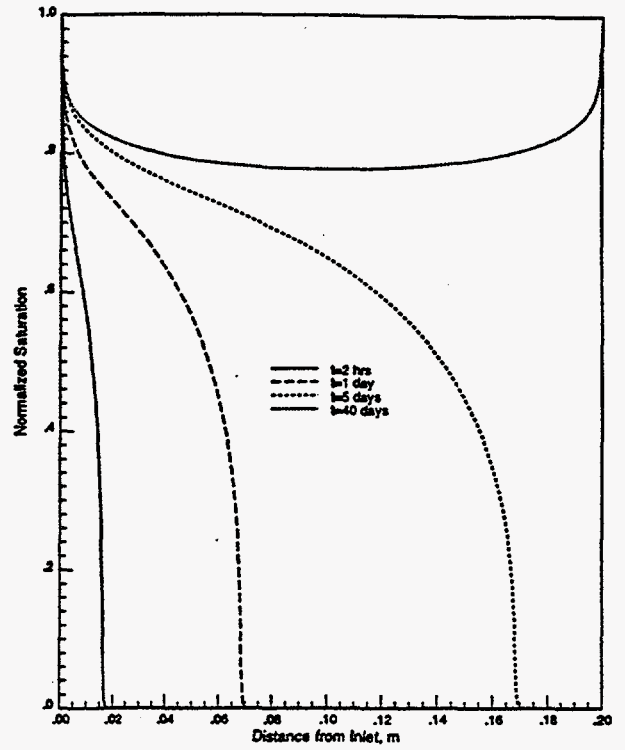


Figure 5. Saturation distribution for 1-D co-current imbibition

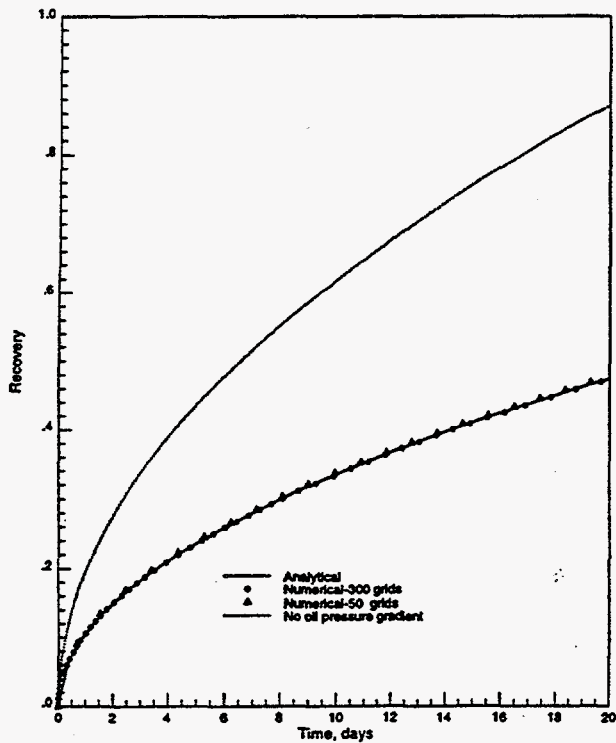


Figure 4. Recovery for 1-D counter-current imbibition

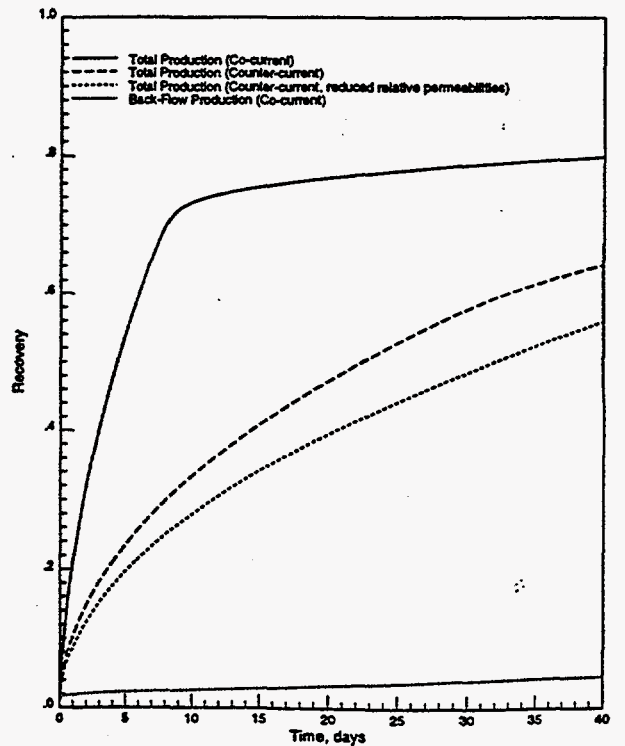


Figure 6. Recovery for 1-D co- and counter-current imbibition

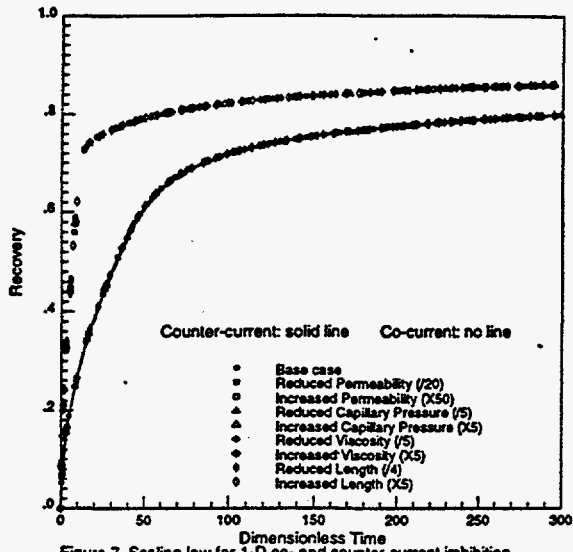


Figure 7. Scaling law for 1-D co- and counter-current imbibition

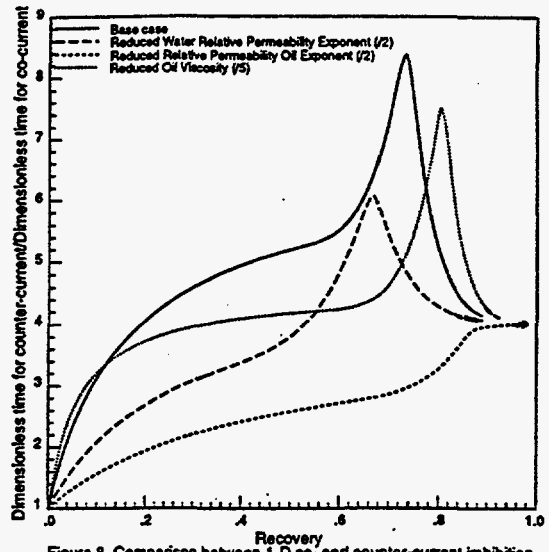


Figure 8. Comparison between 1-D co- and counter-current imbibition

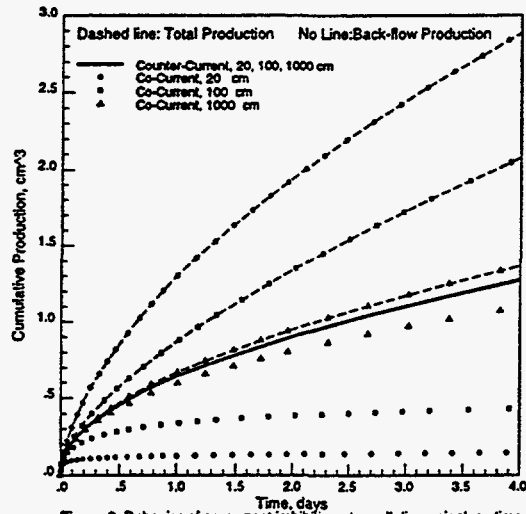


Figure 9. Behavior of co-current imbibition at small dimensionless time

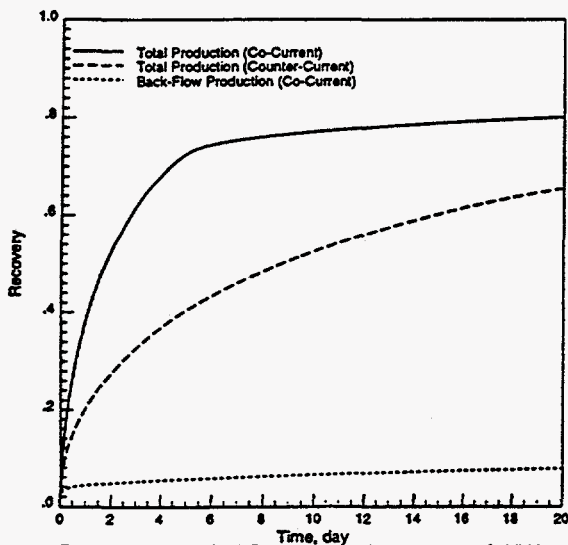


Figure 10. Recovery for 2-D co-current and counter-current imbibition

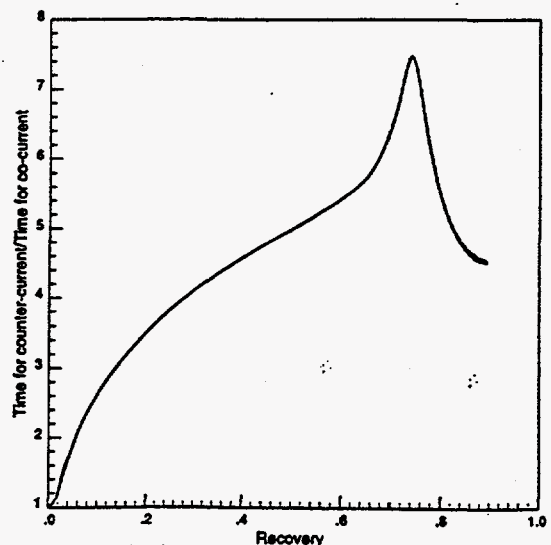
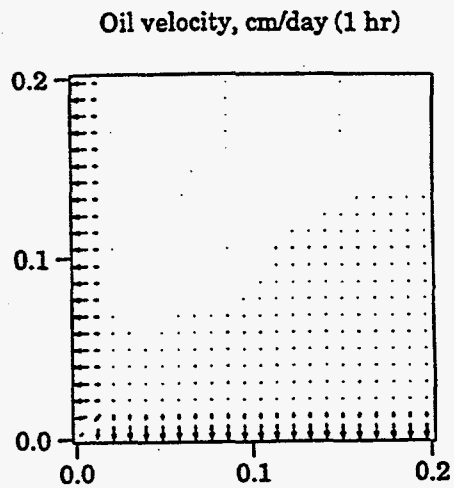
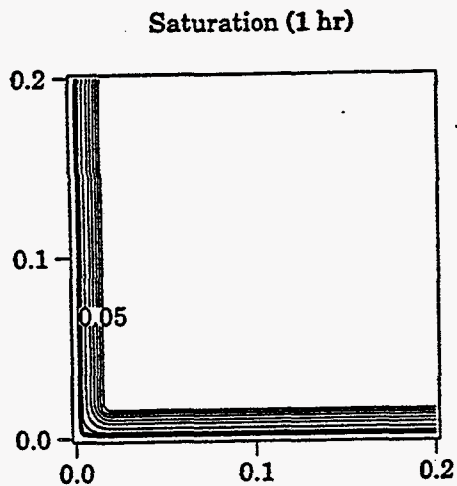
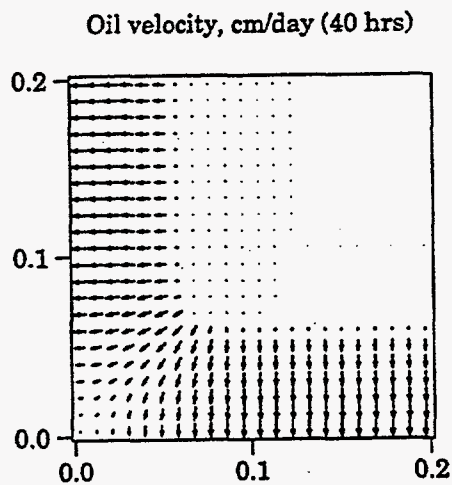
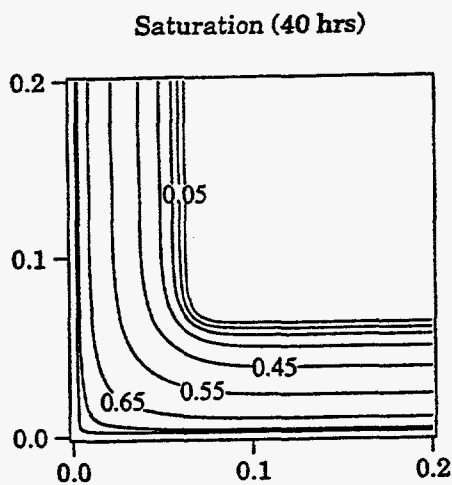


Figure 11. Comparison between 2-D co- and counter-current imbibition (base case)



$\tau = 1.60$



$\tau = 0.24$

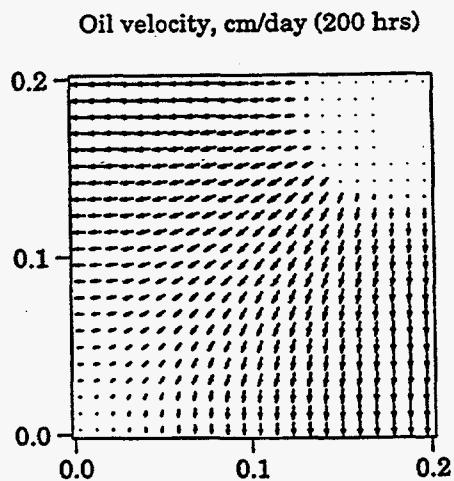
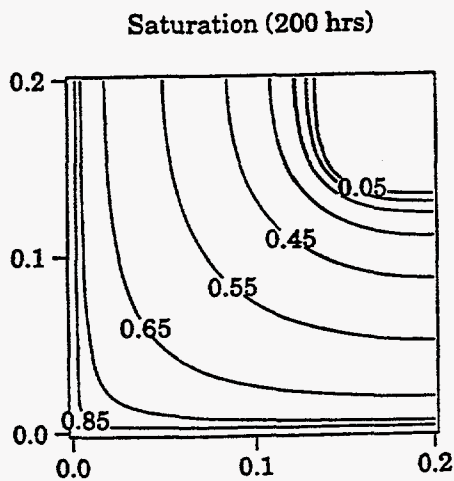


Figure 12. Saturation and oil velocity profiles for 2-D counter-current imbibition. $\tau = 0.10$

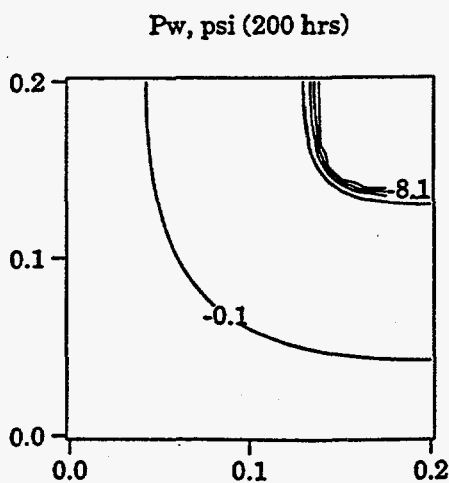
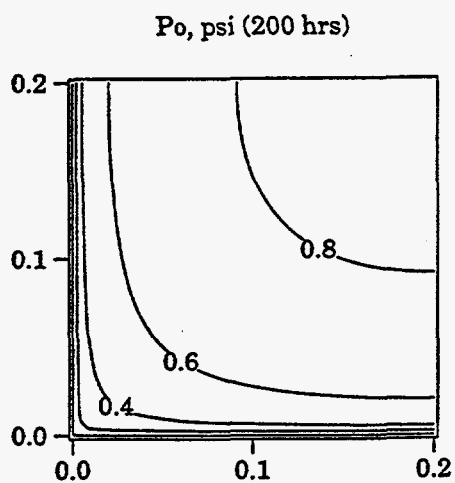
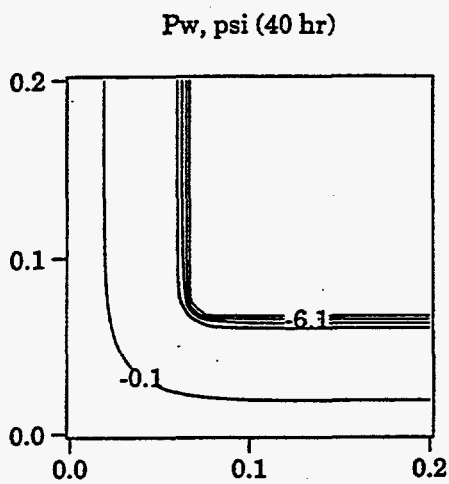
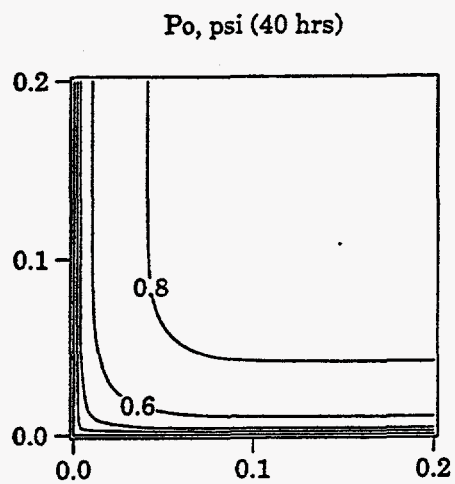
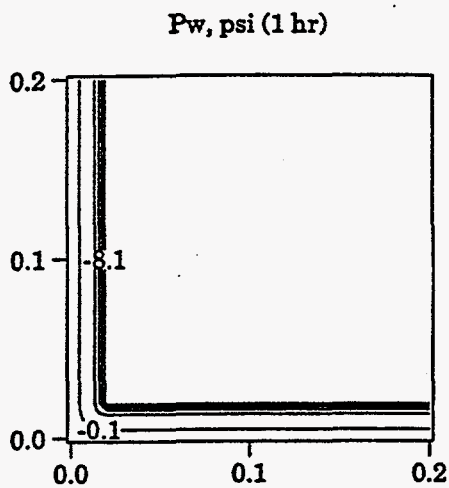
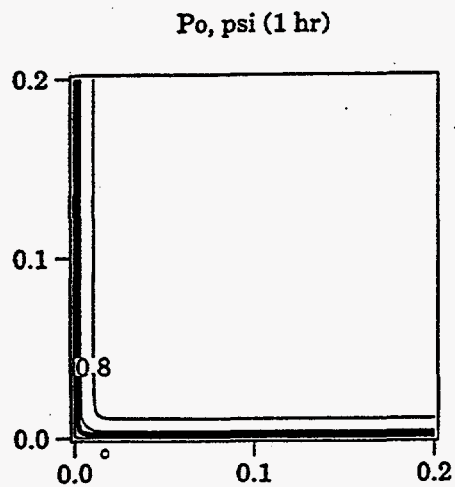
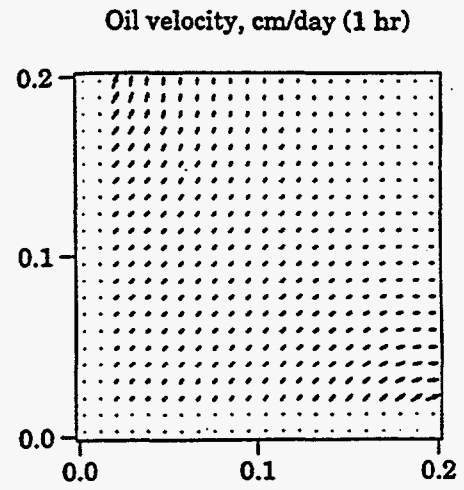
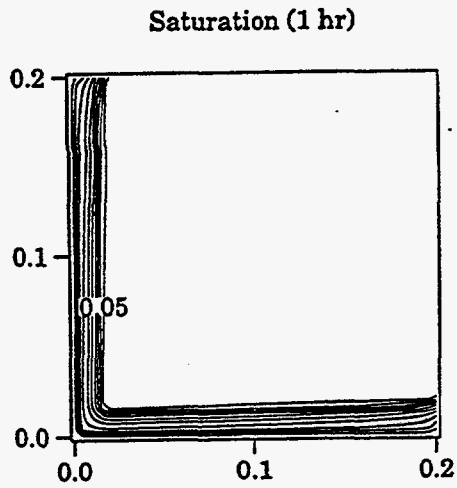
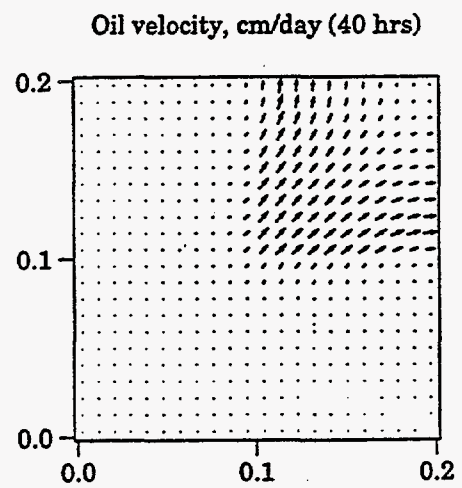
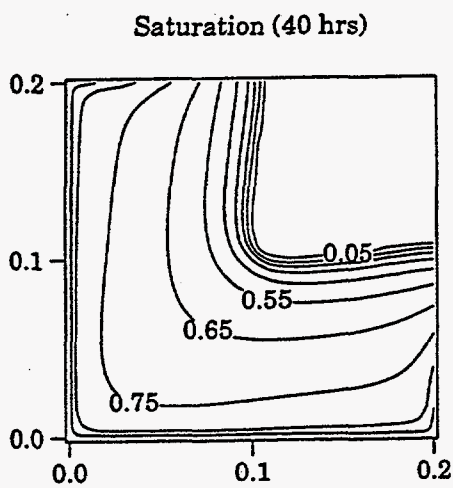


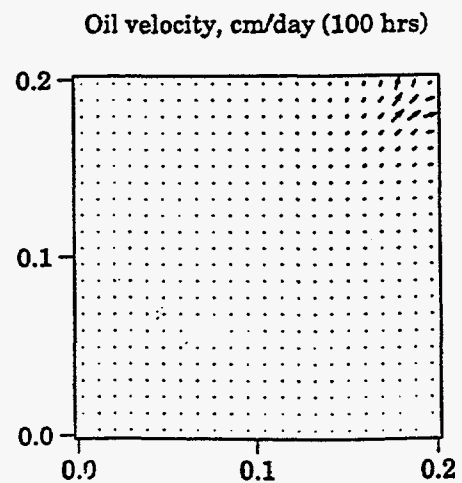
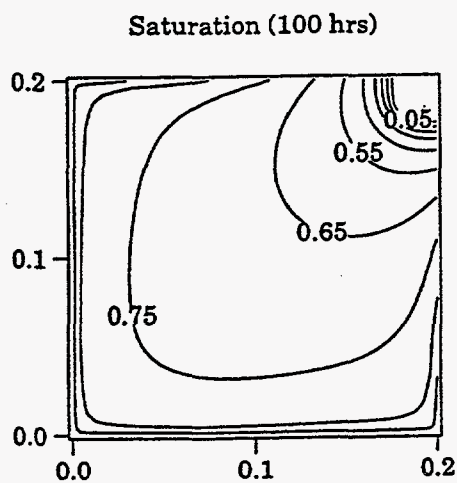
Figure 13. Oil and water pressure profiles for 2-D counter-current imbibition.



$\bar{v} = 9.37$



$\bar{v} = 1.40$



$\bar{v} = 0.84$

Figure 14. Saturation and oil velocity profiles for 2-D co-current imbibition.

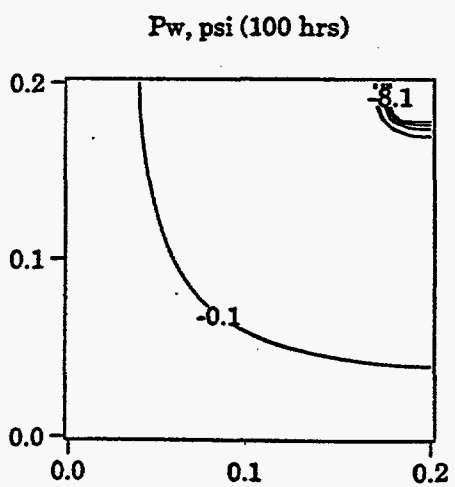
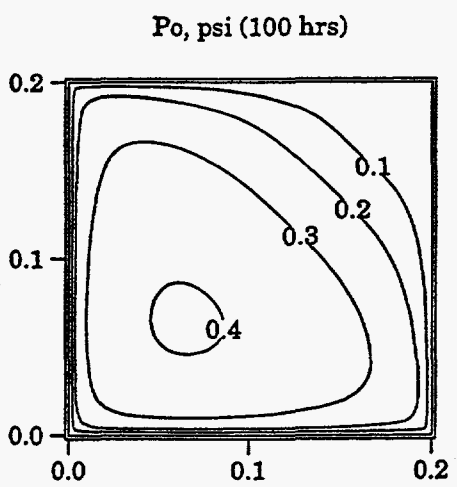
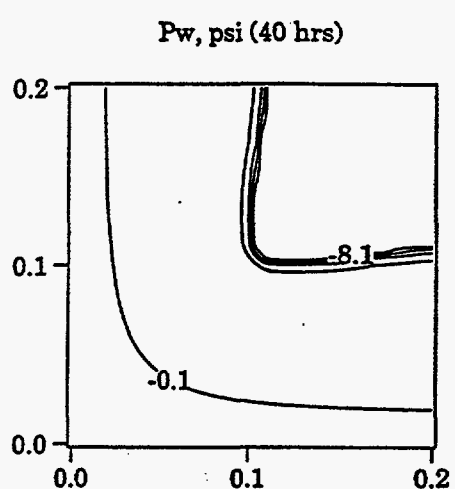
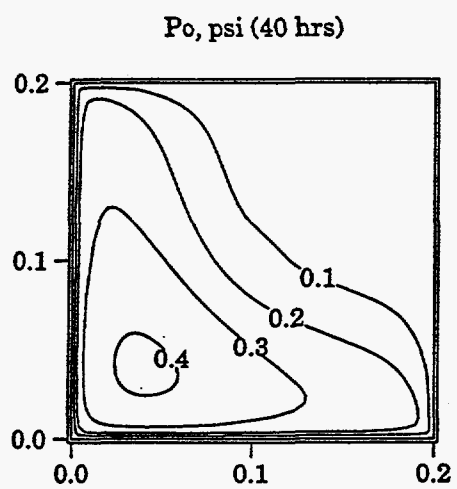
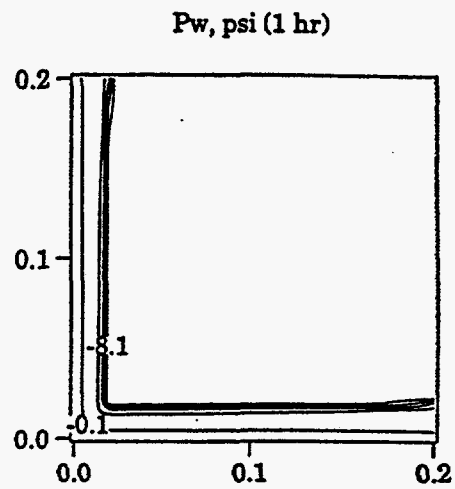
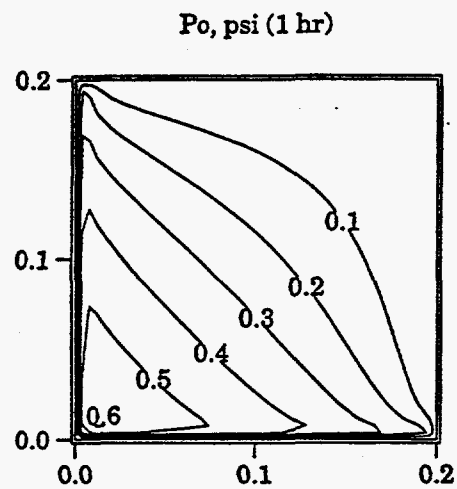


Figure 15. Oil and water pressure profiles for 2-D co-current imbibition.

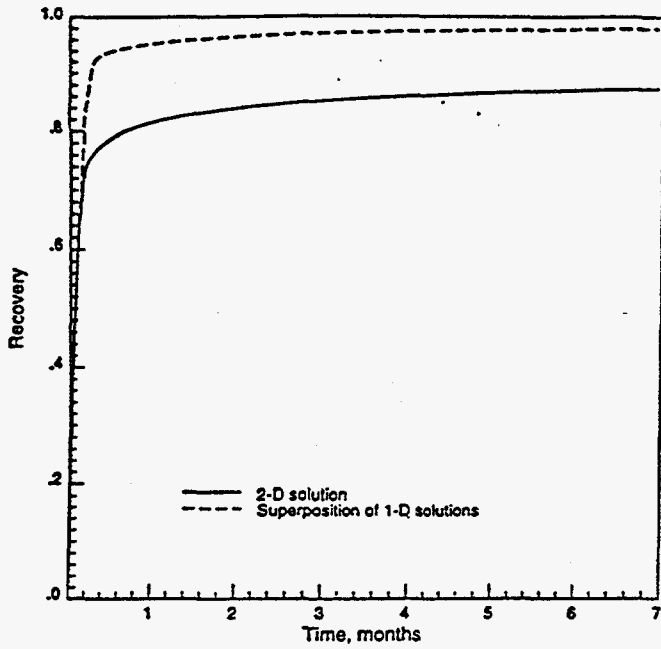


Figure 16. Superposition for co-current imbibition

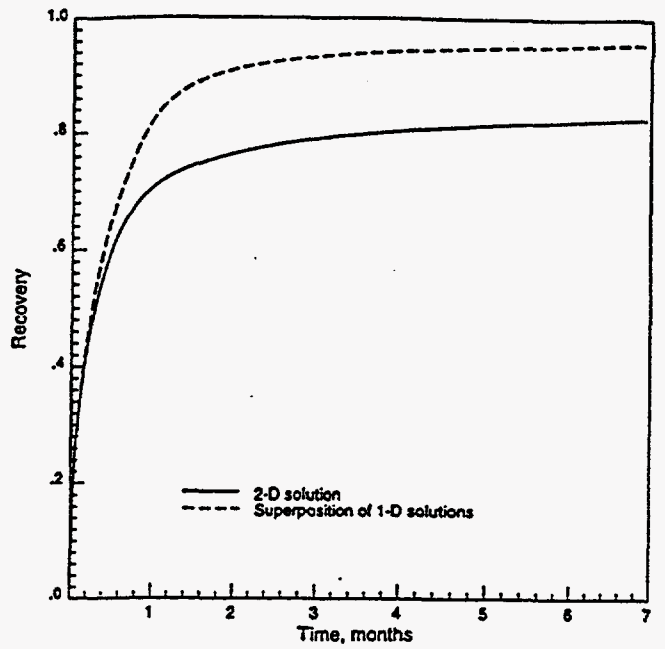


Figure 17. Superposition for counter-current imbibition

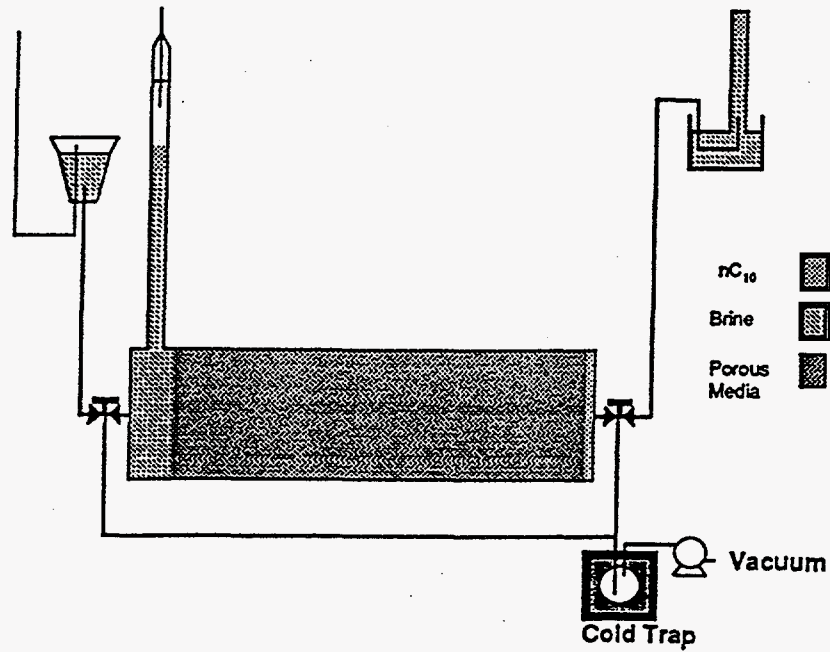


Figure 18. Schematic diagram of apparatus during a run.

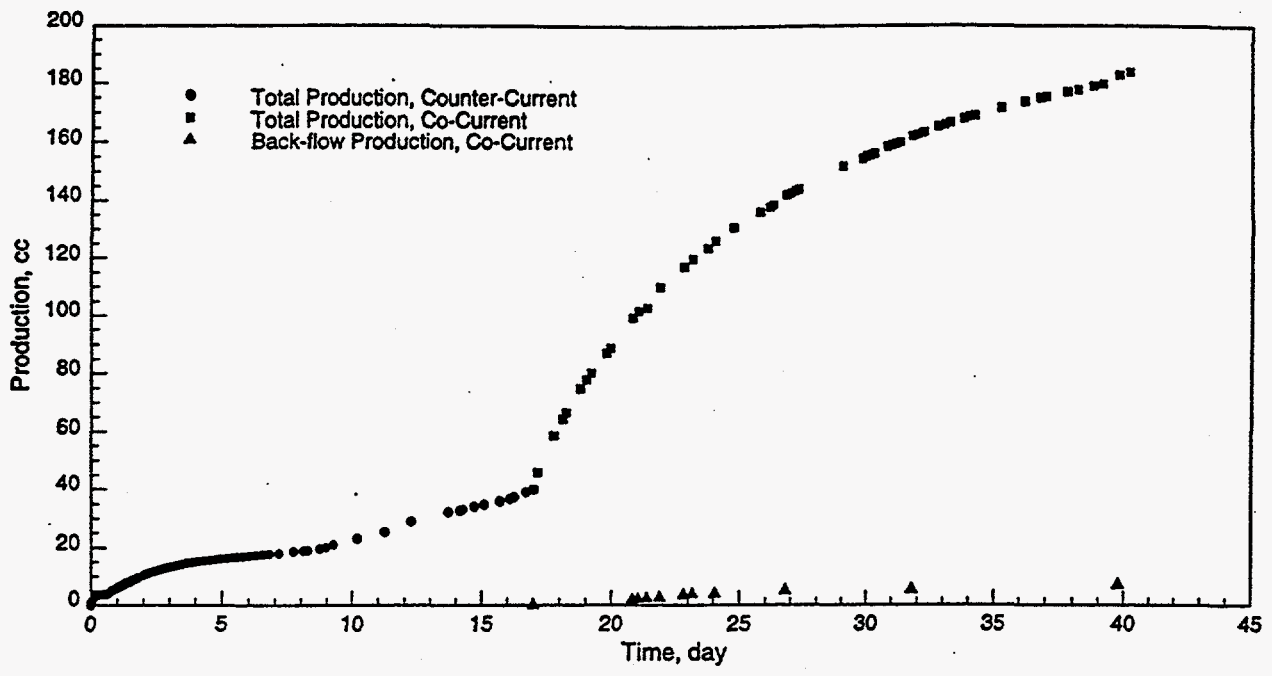


Figure 19. Oil production data for co- and counter-current imbibition

CHAPTER IV

Gravity Drainage in Layered Media: Experimental Data and Analysis

Abbas Firoozabadi

Tore Markeset

Reservoir Engineering Research Institute

SUMMARY

Gas-oil gravity drainage in layered media has important features that are different from drainage in homogeneous media. The experiments presented in this paper confirm the validity of features that were introduced in an earlier theoretical work. Based on the analysis of a number of experiments, it is concluded that unlike homogeneous media, where drainage characteristics are often weakly related to gas relative permeability and gas mobility, drainage in layered media can be sensitive to these parameters.

INTRODUCTION

Layered reservoirs provide a large share of oil production. Gas-oil gravity drainage in these reservoirs could have certain features which are not generally recognized. In a recent theoretical study,¹ we have demonstrated that in a two-layer media with a low permeability layer on top and a high permeability layer below, gas could finger downward through the less permeable top layer to reach the more permeable bottom layer. This type of fingering can only occur when the top layer is the less permeable layer. It cannot occur when the top layer is the more permeable layer. If the gas mobility is assumed to be infinity, gas would finger through the less permeable top layer instantaneously. The occurrence of downward gas fingering is related to the layers' permeability ratio, the threshold capillary pressure of the less permeable layer, and the thickness of the more permeable layer.¹ Downward gas fingering can occur if $k_2/k_1 > (1 - h_2^\circ/h_1)$, where k_2 and h_2° are the permeability and threshold height of the top layer, and k_1 and h_1 are the permeability and thickness of the bottom layer.¹ Capillary pressure is a key parameter in downward gas fingering of layered media, whereas in downward viscous fingering, capillary pressure is neglected.² In order to appreciate the concept, the schematic diagram shown in Fig. 1 will be useful.

Through the use of Fig. 1, we wish to show when to expect downward gas fingering in a two-layered media. Let us assume initially both layers are saturated with a liquid. At time, $t=0+$, liquid starts to drain and the gas enters from the top to replace the drained liquid. The gas can enter the top layer provided the liquid pressure at the top of this layer, P_l , is equal to $-(P_c^\circ + P_ggh)$. The dotted line in Fig. 1, AO represents the gas phase pressure profile, and the dashed line represents the final equilibrium pressure when gravity/capillary equilibrium is established. The solid thick line, BO connects the initial flowing liquid phase pressure at the top

to the origin at point O. It is assumed that both the liquid and gas phase pressures are equal to zero at the outlet, and therefore $P_c=0$. If $k_2/k_1 < 1$, the liquid phase pressure profile should be to the left side of the line BO. Now, let us draw from point B, line BC parallel to line AO, and connect point C to the origin. The shaded area between lines BO, BC, and CO, and the region to the left of BCO have an important characteristic. If the initial flowing liquid pressure profile is within the shaded area, downward gas fingering will not occur. However, if the initial flowing liquid pressure profile is to the left of BCO, gas will instantaneously finger through the top layer to reach the more permeable bottom layer provided gas mobility is infinite and the liquid is incompressible.¹ This type of gas fingering can affect the production performance significantly; GOR may fluctuate and sweep efficiency may decrease. In addition to the above unstable flow behavior, another important feature of gas-oil drainage in layered reservoirs with distinct permeabilities is the recovery sensitivity of less permeable layers to capillary pressure. Due to capillary pressure contrast between layers, the liquid drainage in the less permeable layer becomes very slow. This characteristic of layered reservoirs is similar to fractured reservoirs.³

The work on gravity drainage in layered systems presented in Refs. 1 and 3 is based on the assumption of infinite gas mobility, which may be appropriate for gas-oil drainage for homogeneous media. It may not be an appropriate assumption for layered media. There is no literature data on gas-oil gravity drainage in layered media. We, therefore, carried out a number of experiments to confirm the concepts presented in Ref. 1. The experimental work carried out in this work is expected to improve over insight and can be used as a basis for further understanding of drainage in layered media.

In this paper, we will first describe the experimental setup. Then the results will follow. Analysis of the experiments will help to examine the importance of gas mobility in layered systems.

EXPERIMENTAL

Fig. 2 shows the apparatus schematic. A 60 cm long Berea core, of 7.62 cm (3") diameter sits on the top of a 68.6 cm long sand layer. The transparent coreholder which houses the sand, has an internal diameter of 9.65 cm (3.8") at the top, 8.89 cm (3.5") at the middle and then reduces to 7.62 cm (3.0"). The length of the 3.8", 3.5", and 3.0" diameter segments are 5.2, 2.5, and 60.4 cm, respectively. Details are shown on the right hand side of Fig. 2. The Berea is covered with a layer of polyester casting resin (1/4" thick). The entire coreholder setup is transparent. But the gas-oil front can be distinguished only in the sand layer. The piston-like setup shown in Fig. 2 allows capillary continuity between the Berea sandstone and the sand grains at all times.

Permeability of the Berea sandstone, and the sandlayer are 950 md, and 46 darcy, respectively. The porosity of the Berea is 21.0%. The porosity of the sand is around 38%, and changes slightly from one test to the next, due to compaction. For each test, the pore volume (PV) of the sandlayer is measured to account for PV change. The PV of the Berea is 574 cm³ and its capillary threshold height for air/nC₁₀ system is 36 cm. The threshold height of the sand is 13 cm.

At the end of each test, by weighing both the Berea and sandpack core holders, liquid saturations are established. In all the tests, the two-layer porous media was saturated with liquid normal decane. Atmospheric air from the top provided the gas phase to drain the liquid.

In the following, prior to discussing test results in the two-layer system, the measured capillary pressure and liquid relative permeability of the Berea and the sand will be presented.

P_c and k_{rl} Data - The capillary pressure of the sand and the Berea were measured using the technique described in Ref. 4. Capillary pressures are given by:

$$P_c = P_c^\circ - \sigma \ln [(S_0 - S_{\alpha}) / (1 - S_{\alpha})] \quad (1)$$

For the Berea, $P_c^\circ=0.37$ psi, $\sigma=0.145$ psi, and $S_{\alpha}=0.26$. The parameters for the sand capillary pressure are: $P_c^\circ=0.128$ psi, $\sigma=0.067$, and $S_{\alpha}=0.085$. The capillary pressure curves were measured for normal decane/air fluid system at a room temperature of 76°F. Figure 3 shows a plot of the data. We also performed drainage experiments for single columns of the sand and the Berea to estimate the liquid phase relative permeability curve. The procedure for liquid phase relative permeability calculations from drainage data are also presented in Ref. 4. The liquid relative permeability of both Berea and sand are well represented by $k_{rl}=S_1^{*3}$, where S_1^* is the normalized liquid saturation defined by $S_1^*=(S_0-S_{\alpha})/(1-S_{\alpha})$. For a homogeneous medium, the drainage is not sensitive to gas phase mobility and the liquid phase relative permeability describes the process.

RESULTS

In the tests to be described in the following, the position of the production outlet valve was varied along the vertical direction to change the length of the system. All the tests, except tests 15 and 16, were conducted under the condition of free flow of liquid. In tests 15 and 16, the rate of liquid production was controlled at a specified value.

Tests 2, 3, 15, and 16 - In all these four tests, the production outlet was fixed 1 cm above the bottom face of the sand layer (i.e., 67.1 cm below the Berea/sand interface). In duplicate tests 2 and 3, gravity drainage was allowed to occur by opening the outlet valve fully and the top of the sand layer (i.e. the interface between the two layers) was watched carefully. After about 12 minutes, gas appeared at the interface for both tests 2 and 3. From then on, the gas-liquid front in the sand layer moved downward; which implies production from both layers from $t=12$ min. Fig. 4 shows the cumulative production and rate data for tests 2 and 3. Prior to the arrival of the gas finger to the interface, the production rate is constant -- around 192 cm³/hr, then increases gradually to 220 cm³/hr at $t=50$ min. A sharp rate increase to 280 cm³/hr at $t<80$ min then follows. Fig. 5 shows the position of the gas-liquid front in the sandlayer for test 3 (solid curve). The same figure also shows the gas-liquid front when only the sandlayer is drained (dashed curve). The dashed curve is the drainage of the sand when there is no Berea layer on top. Note that if the gas mobility was infinite the drainage from the sandlayer would have been much higher when gas had arrived at the interface for test 3. At the termination of this test, we removed the Berea layer on top, and the sand was allowed to produce to equilibrium. A total of 136 cm³ of liquid was produced in about 280 minutes, where still production rate was 2.5 cm³/hr. The production of this large quantity of liquid from the sandlayer implies that the assumption of infinite gas mobility, while is appropriate for drainage in homogeneous media, may not be

appropriate for drainage in layered media. This important point will be discussed when we analyze the tests.

Fig. 4 reveals that although the conditions of duplicate tests 2 and 3 were the same, the cumulative production data are not reproduced, due to unstable behavior.

Tests 15 and 16 (duplicate tests) are different from tests 2 and 3, with respect to the outlet boundary conditions. In tests 2 and 3, as mentioned above, $P_c=0$ at the outlet. In tests 15 and 16, the production rate was fixed at a value of $60 \text{ cm}^3/\text{hr}$ by the manual adjustment of a needle valve. At this rate, gas should not finger through the top less permeable layer as we will see later. Fig. 6 graphs the production and rate data for these two duplicate tests. After 700 minutes, the production rate drops to less than $60 \text{ cm}^3/\text{hr}$ and the outlet valve is opened fully. The production and rate data for these two tests reveal very similar behavior; the difference is a reflection of the manual rate adjustment. In both tests, the gas front reached the interface at around 220 minutes, where total production was about 220 cm^3 . Fig. 7 shows the gas-liquid front position at various times. Note that in tests 2 and 3, due to unstable flow conditions, gas appears at the interface after production of only 30 cm^3 .

Table 1 gives the final liquid saturation of the Berea and sand layers at the end of the tests. This table provides other data such as test duration, and gas arrival time at the interface. The saturation data of Table 1 reveal that the bulk of the production for tests 2 and 3 is a result of simultaneous production from the Berea and sand layers.

Test 5 and 6 - In these duplicate runs, the production outlet was fixed 33.6 cm below the interface. According to the criterion established in Ref. 1, the gravity drainage should be stable for the condition of duplicate tests 5 and 6. The drainage data are nearly the same (see Fig. 8) and there is no early gas arrival to the interface. Table 1 gives the saturation of the two layers at test termination for these two tests. Capillary pressure contrast between the two layers slows down the establishment of gravity/capillary equilibrium, similar to tests 2, 3, 15, and 16.

Test 7 and 9 - In these two tests, the outlet valve was held at 44.6 cm below the interface. According to the criterion of Ref. 1, the gas oil gravity drainage should be unstable. For both tests, the gas front reached the interface at $t < 105 \text{ min}$ implying that a quick gas fingering did not occur. However, production data (see Fig. 9) imply an unstable gravity drainage process. From Table 1, it is seen that at the end of these two tests, the liquid saturations of the Berea layer is close to the previous tests. The gas-liquid front position is shown in Fig. 10. At the end of tests 7 and 9, after removal of the top Berea layer, the sand layer was allowed to drain; 13.8 and 53.0 cm^3 of liquid were produced. It took 80, and 50 minutes to produce these volumes where production rates were still 0.4 and $0.1 \text{ cm}^3/\text{hr}$, respectively, at the end.

Tests 10, 11, and 12 - In these three tests, the production level was fixed at 78.1 cm below the interface. Fig. 11 shows the production and rate data. For all three tests, the rate is about $230 \text{ cm}^3/\text{hr}$ in the first ten minutes (decreases very slowly) and the gas arrives at the interface at about $t=10 \text{ min}$. The production rate increases gradually to about $300 \text{ cm}^3/\text{hr}$ at $t=40 \text{ min}$. There is a sharp rate increase at this time. Around $t=50 \text{ min}$, the production rate reaches $350 \text{ cm}^3/\text{hr}$ for test 12. Similar to other unstable tests, there is a difference in production data which is believed to be due to unstable flow conditions. Note that the liquid saturations of the Berea layer is about the

same as all other tests. Fig. 12 shows that the gas-oil front position in the sand layer moves slowly due to finite gas mobility.

Test 13 - In this test, the production level outlet was fixed at 98.1 cm below the interface. Since $h_1^0=13$ cm, the gas could flow out of the sand bottom face. The initial production rate was around 260 cm³/hr, but began to increase from $t<3$ min. At time $t=60$ min, the production rate reached maximum value of 535 cm³/hr, and then a decreasing trend began (see Fig. 13). The run was terminated when gas breakthrough occurred at the sand outlet. Gas appeared at the interface in about 10 minutes which signifies gas fingering through the top Berea layer. It is likely that gas arrival at the interface was earlier since we could only see the appearance of gas at the interface from the circumference.

ANALYSIS

Fine grid simulations were performed to analyze the above experiments by using measured capillary pressure, liquid phase relative permeability, absolute permeability of both layers, and fluid density and viscosity data. Eclipse simulator⁵ was used in this work and the drainage performance are compared with the simulation results. Let us consider the drainage performance of tests 2 and 3 shown in Fig. 4. A very large gas phase mobility by assuming viscosity of gas to be very close to zero, i.e., $\mu_g=0.0001$ cp and $k_{rg}=(1-S_1^*)^3$ will result in instantaneous gas fingering from the Berea layer to the sand layer and significant overprediction of production. However, with proper value of gas viscosity (air at atmospheric pressure and at room temperature, $\mu_g=0.01$ cp), and different gas phase relative permeabilities, we can study the drainage performance of the layered system. As a first attempt, let us assume $k_{rg}=(1-S_1^*)^3$. Fig. 4 depicts the simulation results (designated by simulation k_{rg3}) and the data for tests 2 and 3. From the simulation results, it is revealed that the gas reaches the interface at $t=20$ min, compared to the observed value of $t=10$ min. The simulation gives a peak drainage rate of 350 cm³/hr which is higher than the experimental value of 275 cm³/hr (see Fig. 4). With few trials, a gas phase relative permeability was found to give the same arrival time of the gas phase to the interface, and the same peak production rate as the experimental values. Simulation results for the modified gas phase relative permeability is labeled as "simulation k_{rga} " in Fig. 4. One may further readjust the gas phase relative permeability to obtain a better match between the measured drainage rate and the simulation results. Fig. 14 shows the two gas relative permeability curves.

We have also plotted the simulation results for the liquid production of the top Berea layer of the two-layer system, and the top 60 cm portion of a homogeneous Berea column of length=127.1 cm and diameter=7.62 cm (see Fig. 15). The plot clearly shows that due to capillary contrast between the two layers in the two-layer system, the drainage performance of the Berea layer when located on top of a more permeable layer is less efficient than a homogeneous system. For the Berea top layer in the layered system, after 11 1/2 days, the recovery is 60.3 percent, whereas in the homogeneous system, the corresponding portion produces 70 percent. At capillary/gravity equilibrium, the recovery of the two will, of course, be the same.

Gravity/capillary equilibrium in a layered system may take a very long time and may be beyond the economic life of a reservoir at reservoir conditions. The capillary pressure curves provide a

liquid saturation of about 30 percent for the Berea layer whereas all the measured values of the liquid saturation of the Berea layer in Table 1 are more than 45 percent.

The criterion for stable downward displacement for the capillary and gravity forces when gas phase mobility is assumed to be infinity is $k_2/k_1 > (1-h_2^0/h_1)$ (see Ref. 1). The parameter h_2^0 of the Berea layer is 36 cm, and $h_1=67.1$ cm for tests 2 and 3; which gives $k_2/k_1 > 0.46$ for stable drainage in two-layer system. The permeability ratio k_2/k_1 of the Berea-sand layers is 0.022, and therefore gas fingering should occur.

The analysis of the other experiments are given in the following.

Tests 15 and 16 - As was mentioned in the Results section, the outlet valve for tests 15 and 16, similar to tests 2 and 3, was held at 67.1 cm below the interface. The production rate was, however, kept at a constant rate of 1 cm³/min, until the rate of drainage decreased below this value. The criterion for stable gravity drainage in a two-layer system with infinite gas mobility, is that production rate should be kept less than $k_2 A \Delta \rho / \mu_o$, where A is the cross-sectional area, $\Delta \rho$ is the density difference between gas and liquid phases, and μ_o is the oil phase density (Ref. 1). Since $k_2 A \Delta \rho / \mu_o = 2.0$ cm³/min, and the production is kept at 1 cm³/min, the gas-oil gravity drainage should be stable. The gas front in tests 15 and 16 arrived at the interface at $t=220$ min; at this time, the liquid saturation of the Berea layer was 62 percent. The experiments are in line with theory showing stable gravity drainage. Simulation results are also in line with experiments (results not shown).

Tests 5 and 6 - To further examine the validity of the theoretical criterion, the production outlet valve in these two tests was fixed 33.6 cm below the interface; $h_2^0=36$ cm, and $h_1=33.6$ cm, and therefore $(1-h_2^0/h_1)=-0.07$, which satisfies the stability criterion of Ref. 1.

Fig. 8 shows the simulation results and the data. In the simulation, the adjusted gas phase relative permeability of Fig. 14 was used. The agreement between the simulation results and data is fair. In the duplicate tests 5 and 6, there was no production from the sand layer ($h_2^0=36$ cm).

Tests 7 and 9 - In these two tests, the production outlet valve was fixed at 44.6 cm below the interface. According to the criterion of Ref. 1, the gas-oil gravity drainage should be unstable. For both tests, the gas front arrived at the interface at $t=105$ min, implying that a quick gas fingering did not occur. Fig. 9 depicts the measured data and simulation results; the agreement between the two is good. From the simulation, the gas front reaches the interface at $t=70$ min, which is less than the measured value of $t=105$ min. The gas phase relative permeability from $k_{rg}=(1-S_1^*)^3$ gives the arrival of the gas front at the interface at $t=130$ min and overestimates the production in the 180 to 500 min period significantly (results not shown). Note that lack of reproducibility of production data for tests 7 and 9 may imply unstable behavior.

Tests 10, 11, and 12 - In these three tests, $h_1=78.1$ cm (the production outlet valve was kept 78.1 cm below the interface), and therefore, the gravity drainage is unstable according to criterion of Ref. 1. The arrival of the gas phase at the interface is at around 10 minutes, indicating unstable behavior.

The data and the simulation results are shown in Fig. 11. The arrival of the gas phase to the interface from the simulation is at $t=10$ min, which is the same as in the experiments. Except in the 30-70 min period, the simulation results and the data are in good agreement. We also

performed simulation with $k_{rg}=(1-S_1)^3$. The arrival time of gas at the interface was at $t=35$ min and a maximum drainage rate of $450 \text{ cm}^3/\text{min}$ at $t=85$ min were obtained for this gas phase relative permeability. These results are substantially different from the data.

Test 13 - In this test, the production outlet was fixed at 98.1 cm below the interface. As expected, this test should be an unstable drainage. Fig. 13 shows the data and simulation results. The simulation results from $k_{rg}=(1-S_1)^3$ give a longer time for the gas arrival at the interface and a higher peak production rate than the experimental data. The simulation results from the adjusted relative permeability are in good agreement with data.

DISCUSSION AND CONCLUSIONS

Gravity drainage performance in homogeneous media for gas-oil systems is not generally sensitive to gas phase mobility. However, for layered-media, gas phase mobility may strongly influence the drainage performance. An infinite gas mobility could lead to substantial overprediction of rate of drainage. The analysis of various experiments described in this work reveals that the shape of the gas relative permeability governs the arrival of the gas phase at the interface between the layers when the drainage is unstable.

Numerical simulation of layered reservoirs is often carried out by either ignoring capillary pressure or assigning an average capillary pressure to various layers. Since there is no average for capillary pressure of layered media, assigning proper capillary pressure curves to various layers becomes important when gas-oil gravity drainage is studied. The sensitivity of simulation results to the capillary pressure curves of various layers is expected to depend on the thickness of layers.

The main conclusions from this work are:

1. It has been established experimentally that gas-oil gravity drainage in layered media can be unstable.
2. Gas-oil gravity drainage in layered media, unlike homogeneous media, can be strongly dependent on gas phase mobility.
3. Gas phase mobility affects both the nature of unstable behavior as well as the rate of drainage.

NOMENCLATURE

A - crosssectional area
h - column thickness, $h_1 + h_2$
 h^o - threshold height
 k_{rl} - liquid phase relative permeability
 k_{rg} - gas phase relative permeability
 P_c - capillary pressure
 P_c^o - threshold capillary
 S_1 - liquid saturation

S_l^* - normalized liquid saturation, $S_l^*=(S-S_{or})/(1-S_{or})$

S_{or} - residual liquid saturation

σ - parameter of capillary pressure model

ρ - density

$\Delta\rho$ - density difference between gas and oil phase

μ - viscosity

Subscripts

1 - bottom sand layer

2- top Berea layer pressure

g- gas phase

l - liquid phase

ACKNOWLEDGMENTS

This research project was supported by the US Department of Energy, contract No. DE-AC22-91 BC 14835, and by the members of the Research Consortium on Fractured/Layered Reservoirs of the Reservoir Engineering Research Institute. Their support is greatly appreciated.

REFERENCES

1. Correa, A.C., and Firoozabadi, A.: "Concept of Gas-Oil Gravity Drainage in Layered Porous Media," SPE Journal (March 1996) 101-111.
2. Slobod, R.L., and Howlett, W.E.: "The Effect of Gravity Segregation in Studies of Miscible Displacement in Vertical Unconsolidated Porous Media," SPEJ (March 1964) 1-8.
3. Firoozabadi, A., "Recovery Issues of Immiscible and Miscible Gas-Oil Flow in Fractured Reservoirs: Laboratory Data and Theoretical Analysis," Proceedings of the First JNOC-TRC International Symposium on Carbonate Rocks-Hydrocarbon Exploration and Reservoir Characterization, Chiba, Japan, March 1-5, 1993 (ed. K. Kimura).
4. Firoozabadi, A., and Markeset, T.: "Laboratory studies in Fractured Porous Media: Part I - Reinfiltration for Gas-Liquid Systems," In Situ (1995) Vol. 19, No. 1, 1-21.
5. Eclipse Reference Manual, Version 92A, Exploration Consultants Limited (1992).

Table 1 - Summary of Test Results

Test	2	3	15	16	5	6	7	9	10	11	12	13
Level from interface, cm	67.1	67.1	67.1	67.1	33.6	33.6	44.6	44.6	78.1	78.1	78.1	98.1
Test duraratin, min	7263	2628	7211	5743	4167	4110	9702	1407	1327	1776	5747	222
Final Rate, cm3/hr	0.34	3.07	0.17	0.18	0.41	0.21	0.15	6.53	4.35	1.93	0.19	132.6
PV, Sand, cm3	1304	1305	1241	1234	1285	1275	1258	1244	1260	1222	1234	1246
So, Berea, %	47.3	48.6	45.8	45.9	47.4	48.2	46.2	49.4	49.6	47.8	48.1	55.4
So, Sand, %	30.5	39.4	30.9	31.2	100	100	59.8	64.9	28.7	26.4	18.2	22.8
Gas arrival at interface, min.	12	12	220	220	-	-	105	105	9	10	10	<10

Fig. 1 - Stable and unstable regions of gravity drainage in layered media.

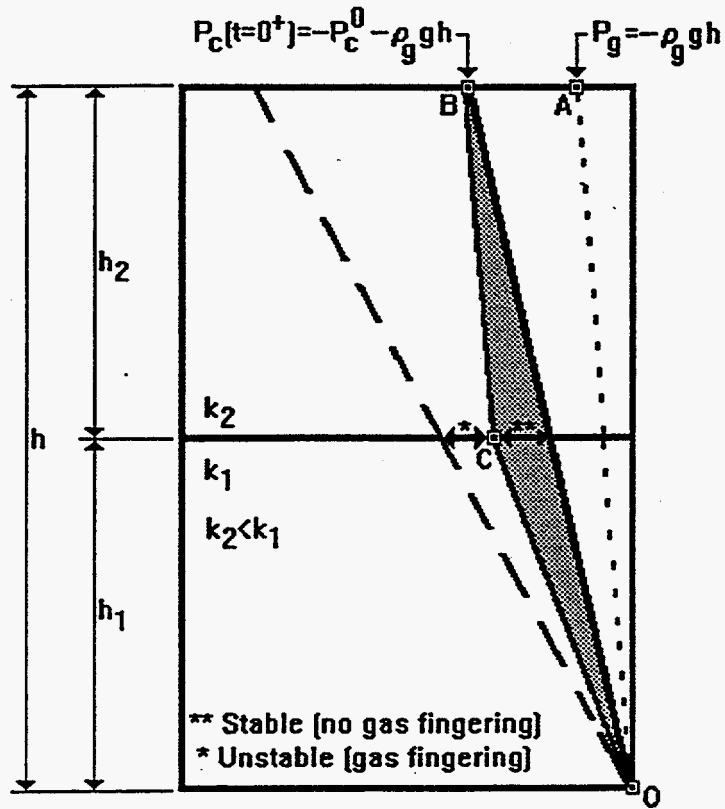


Fig. 2 - Schematic of layered-media apparatus.

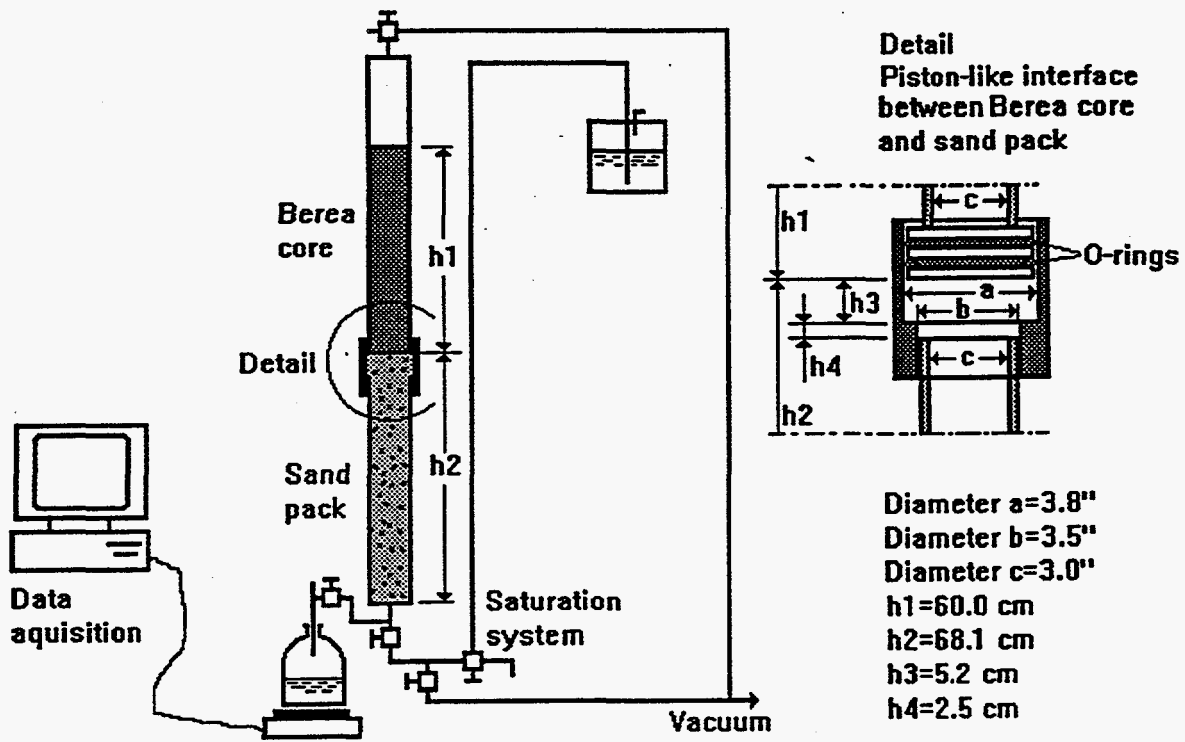


Fig 3 - Measured Capillary Pressures of Berea and Sand

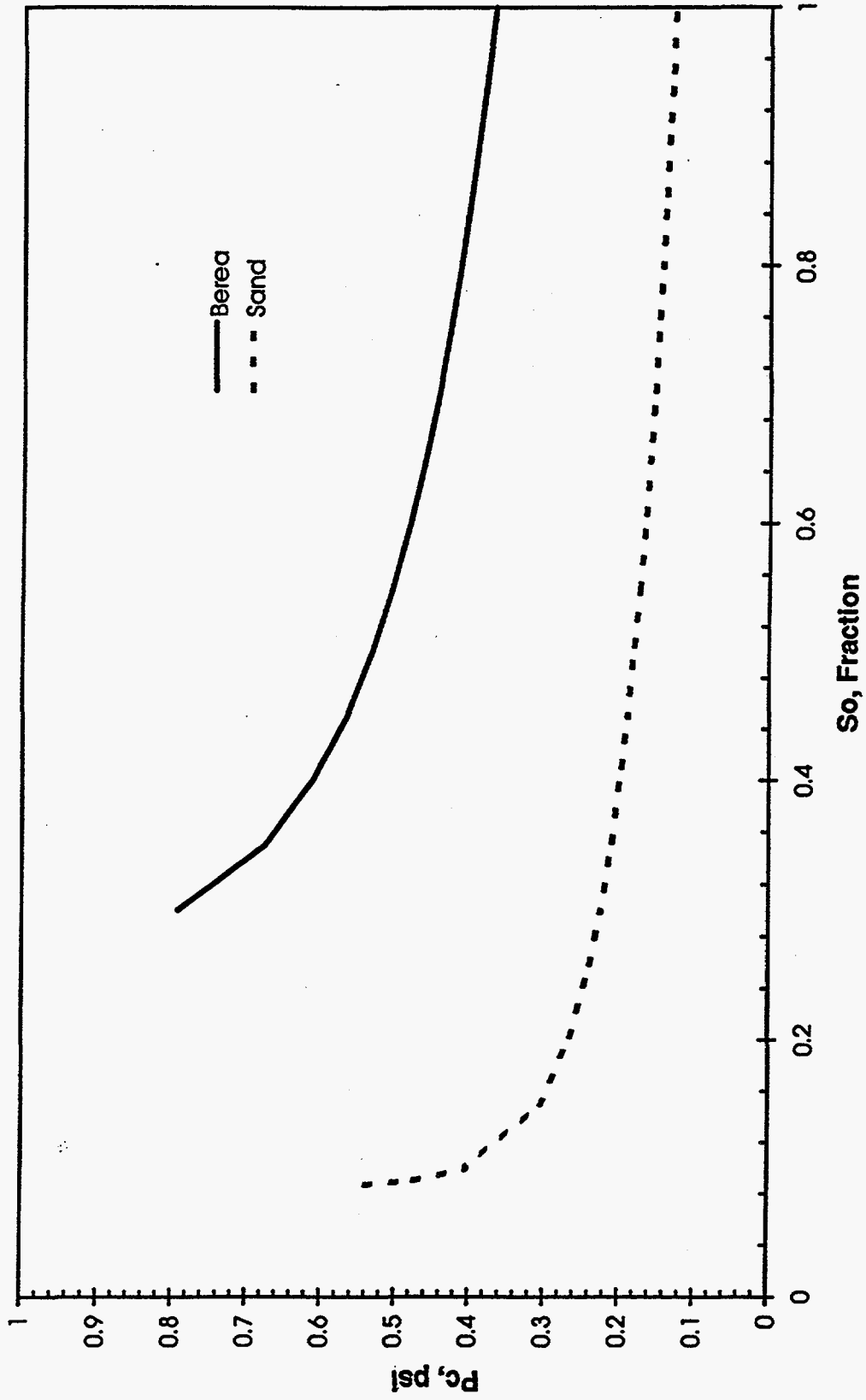
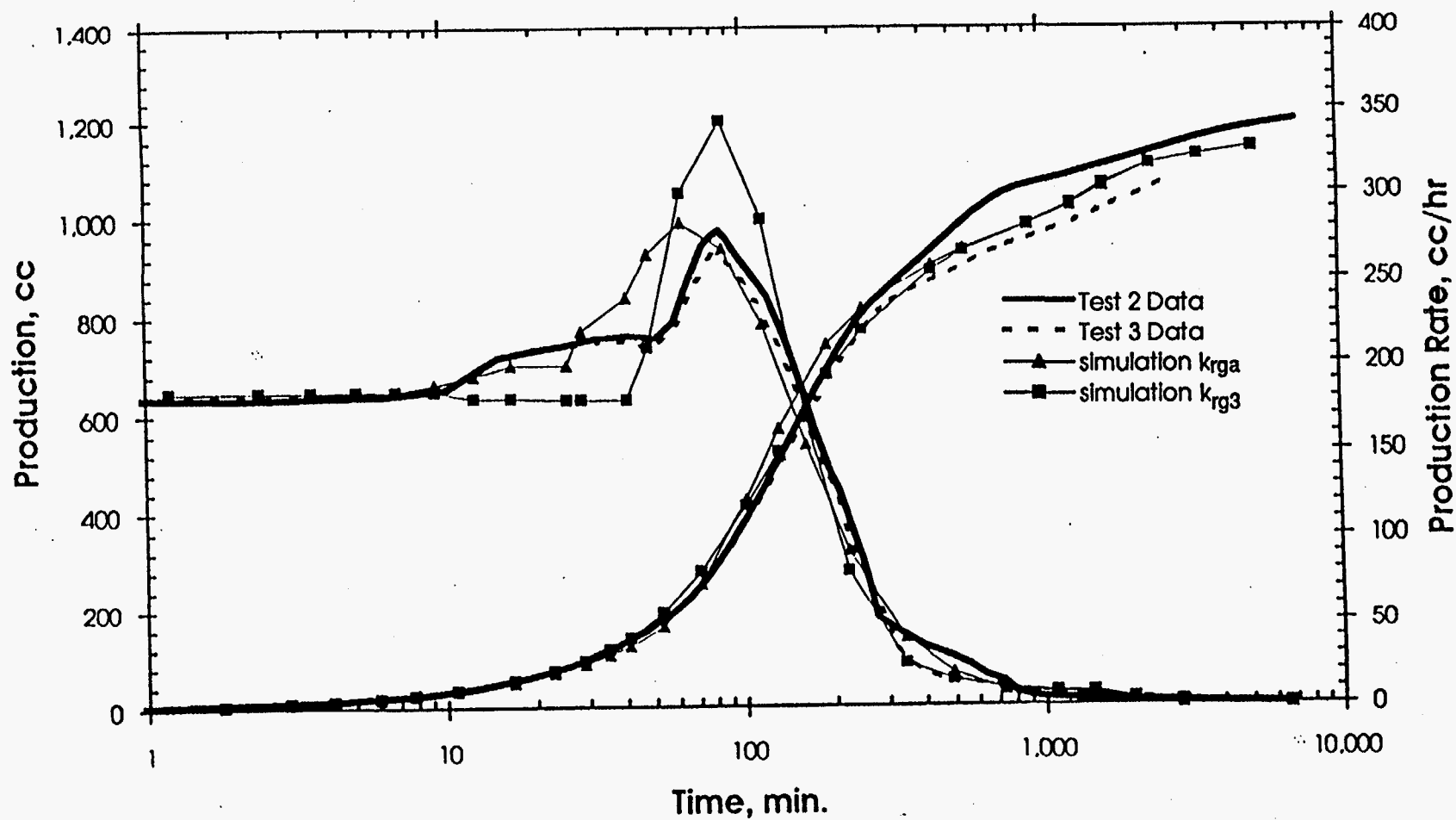


Fig. 4 - Measured and simulated production and rate for tests 2 and 3.



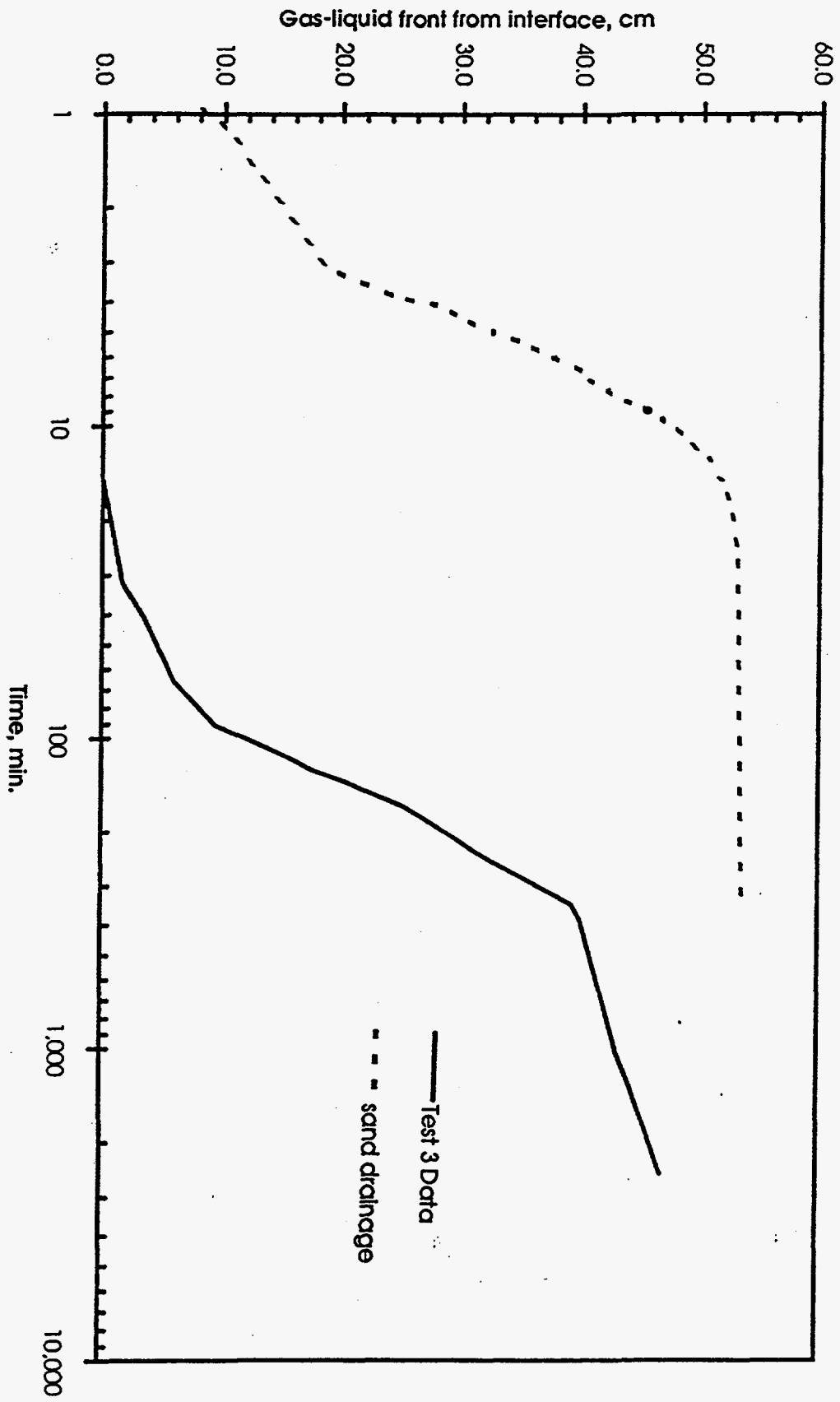


Fig. 5 - Position of gas-liquid front in the sand layer.

Fig. 6 - Production and rate data of tests 15 and 16.

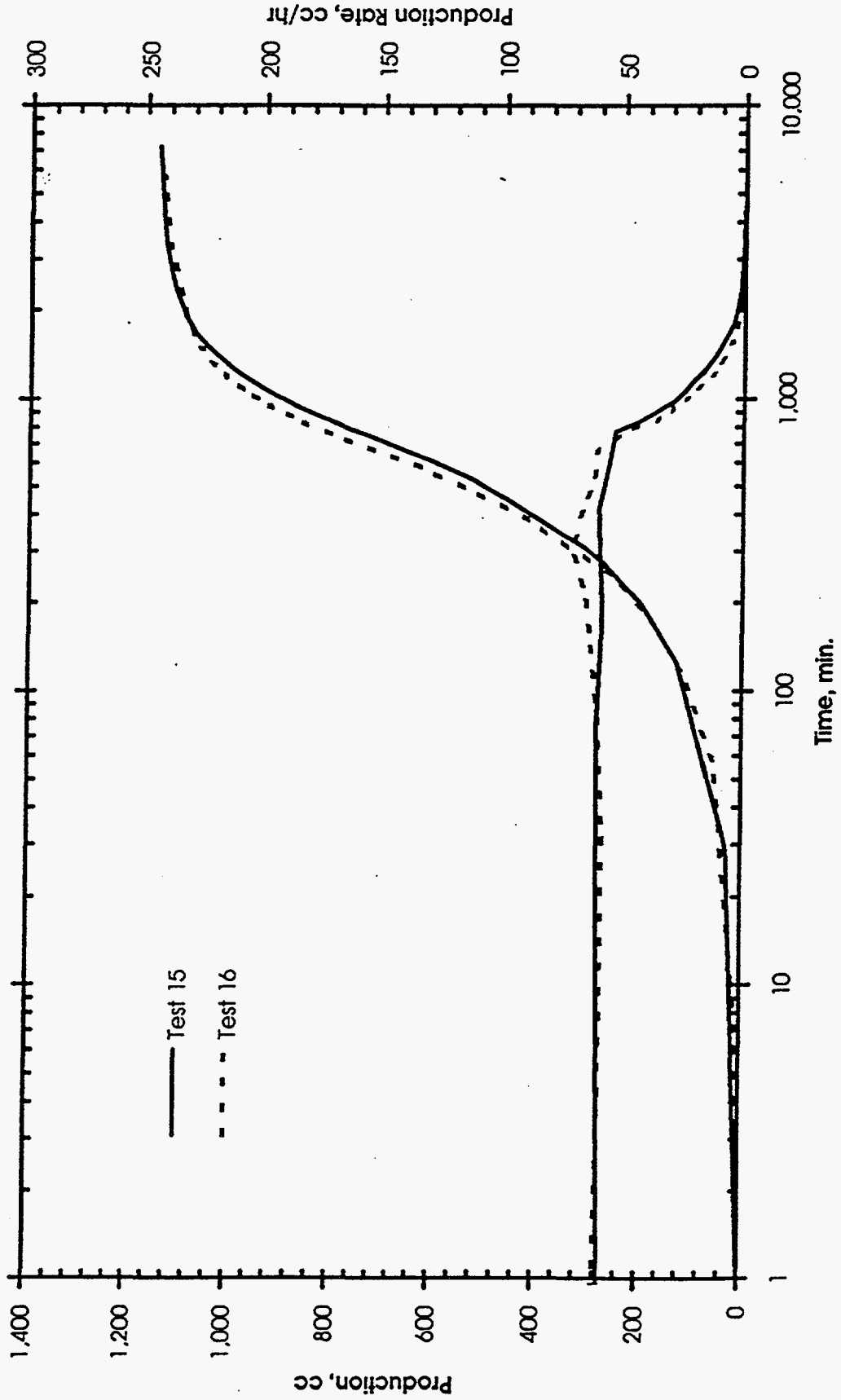


Fig. 7 - Gas-liquid front from interface for test 15.

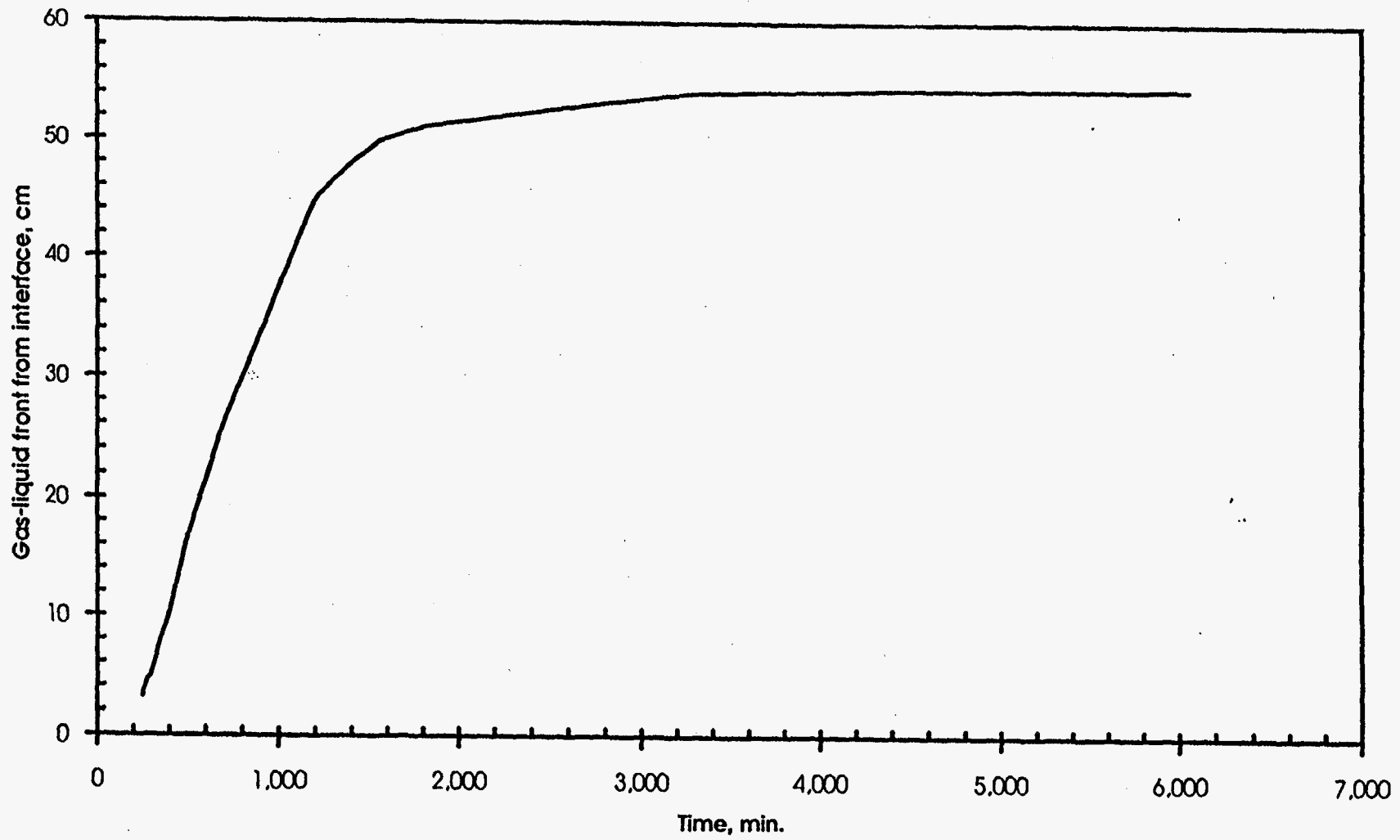


Fig. 8 - Measured and simulated production and rate for tests 5 and 6.

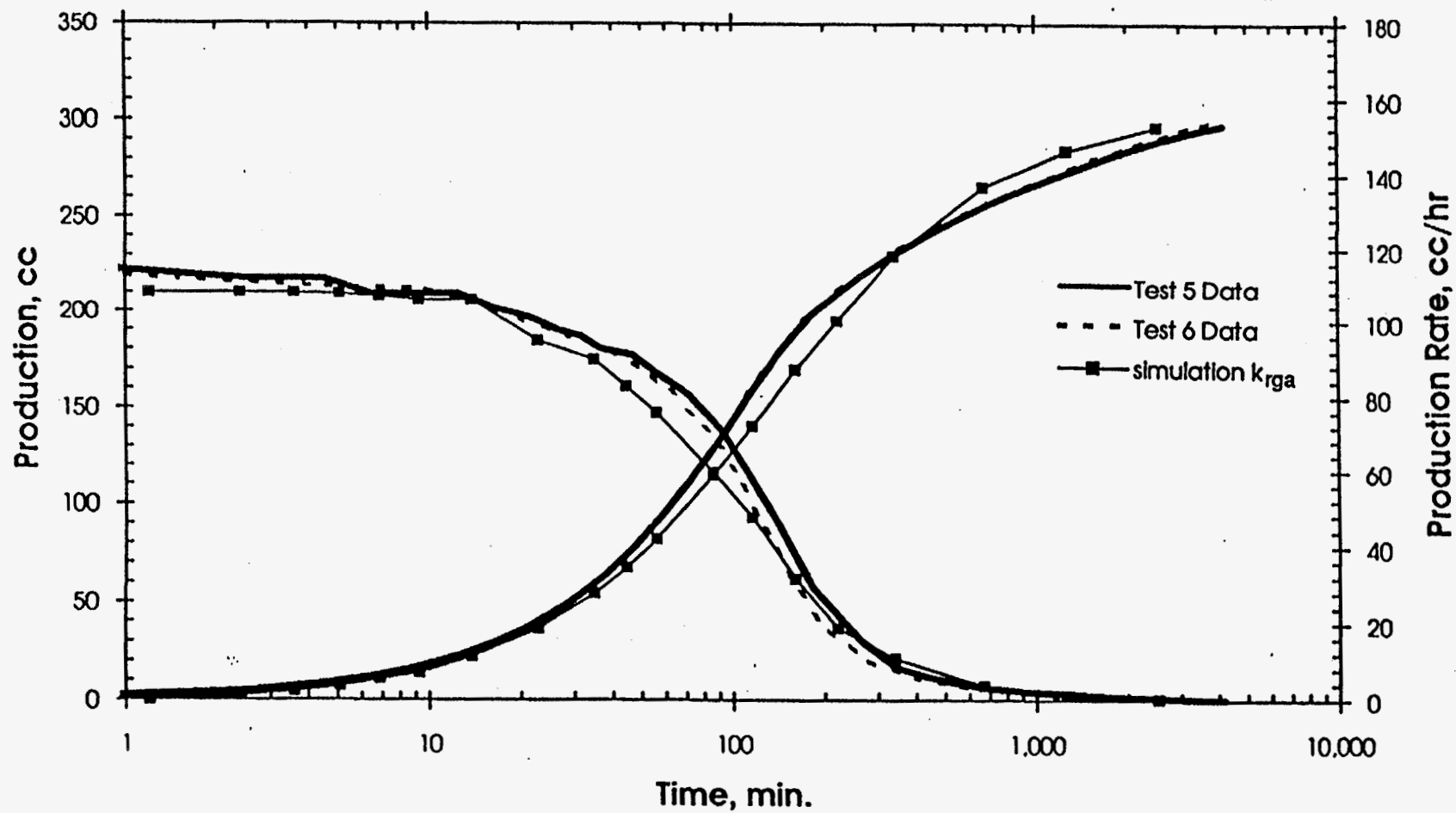


Fig. 9 - Measured and simulated production and rate for tests 7 and 9.

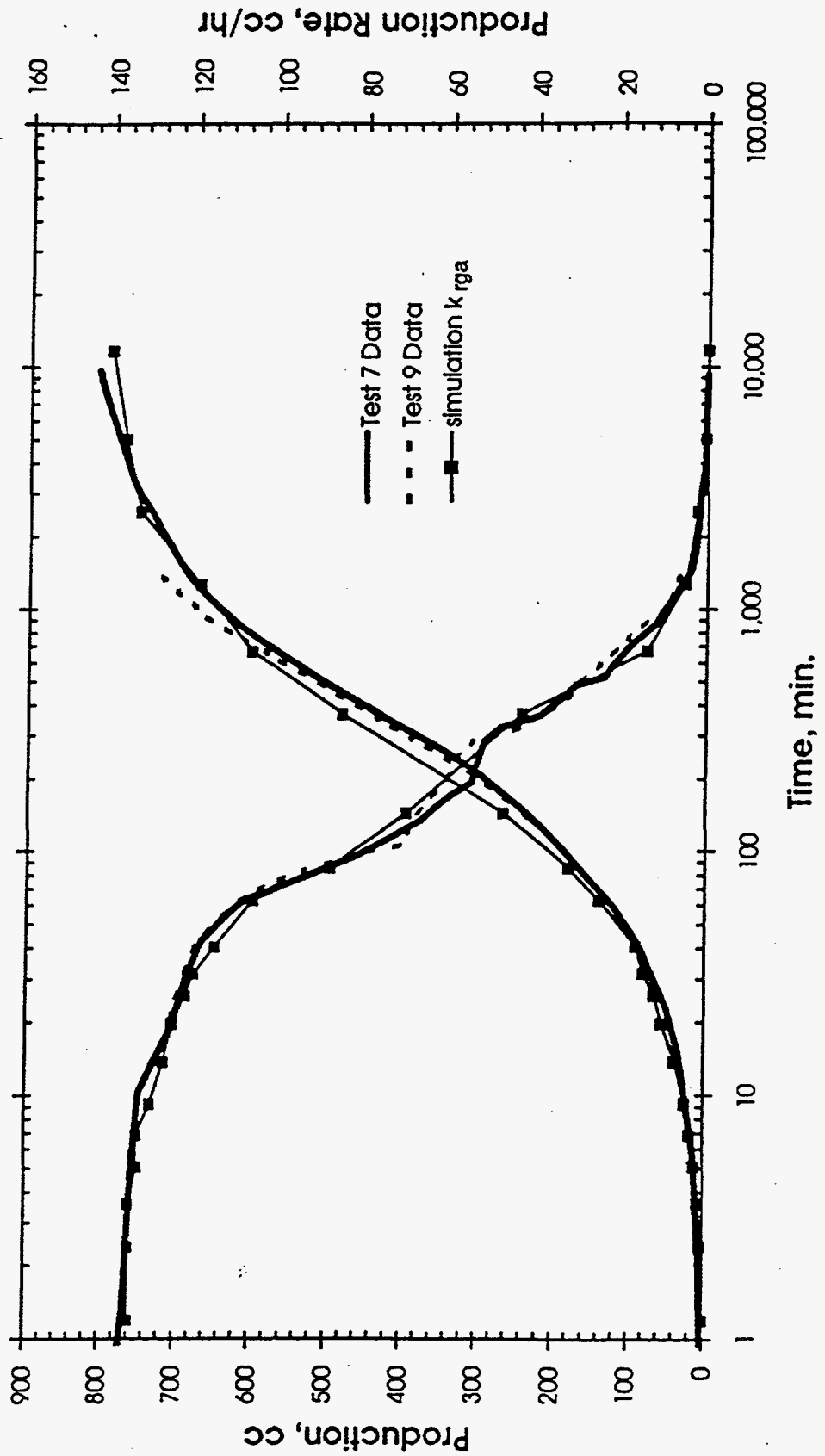


Fig.10 - Gas-liquid front from interface for tests 7 and 9.

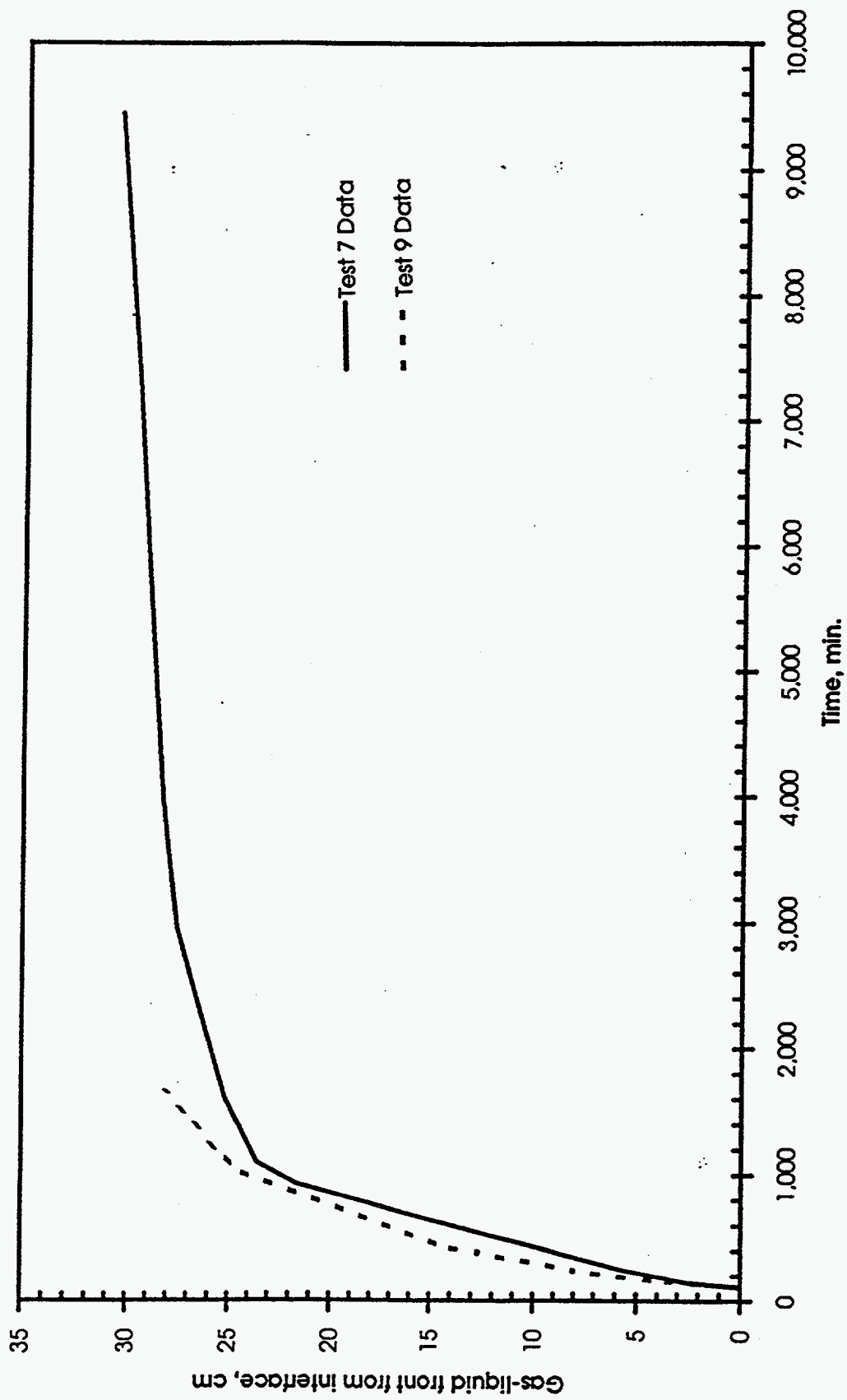


Fig. 11 - Measured and simulated production and rate for tests 10, 11, and 12.

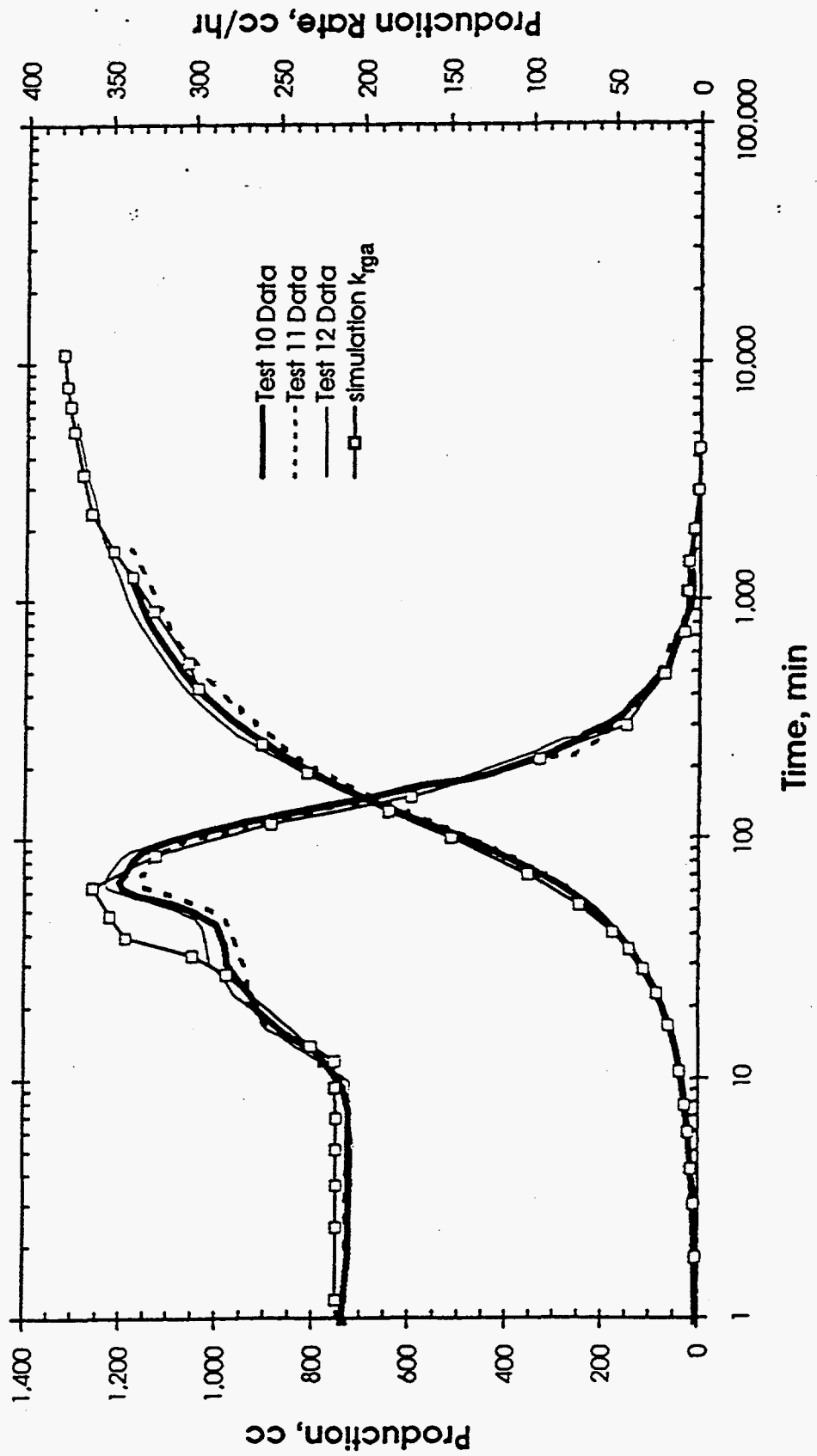


Fig. 12 - Gas-liquid front from interface for tests 10, 11, and 12.

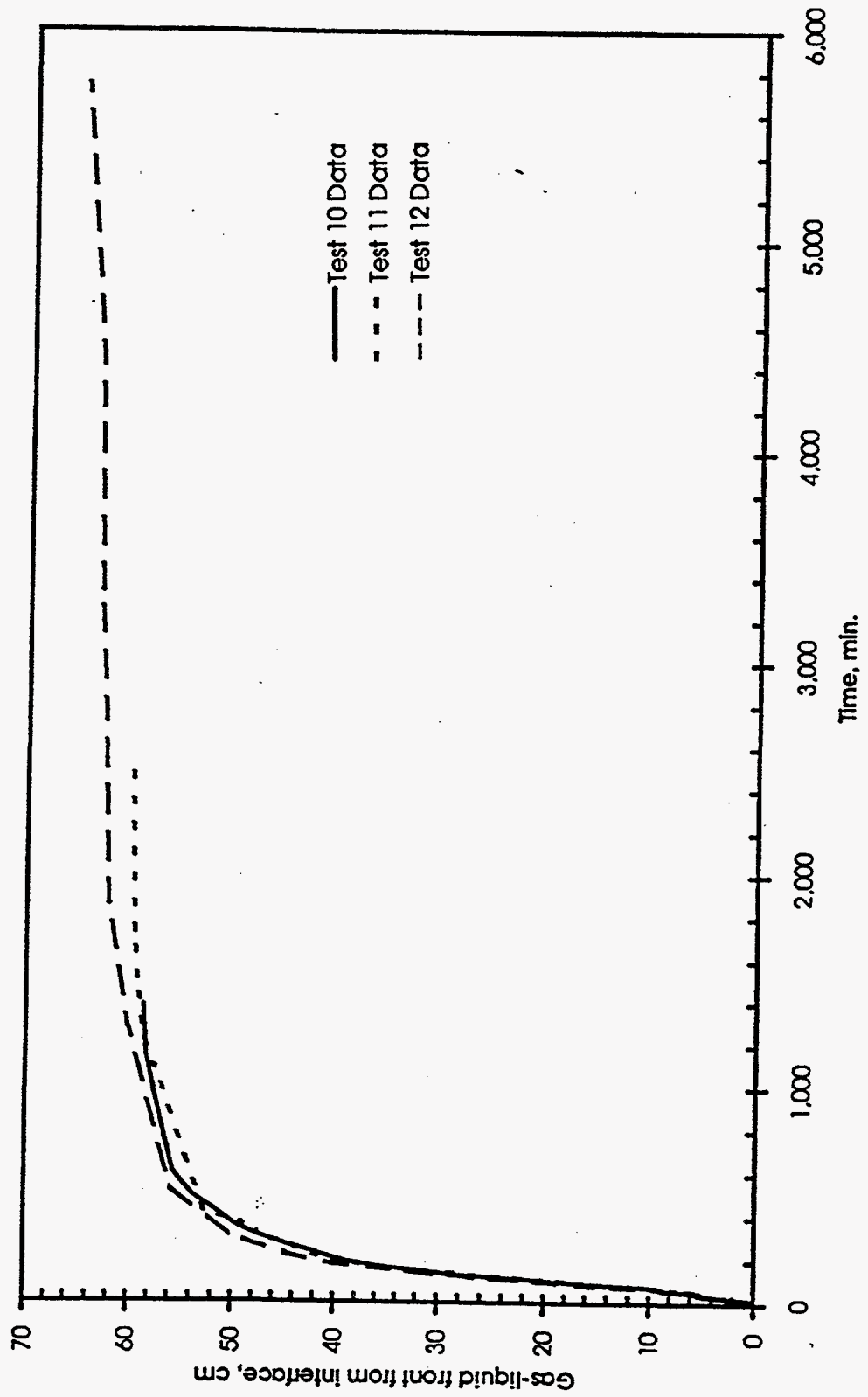


Fig. 13 - Measured and simulated production and rate for test 13.

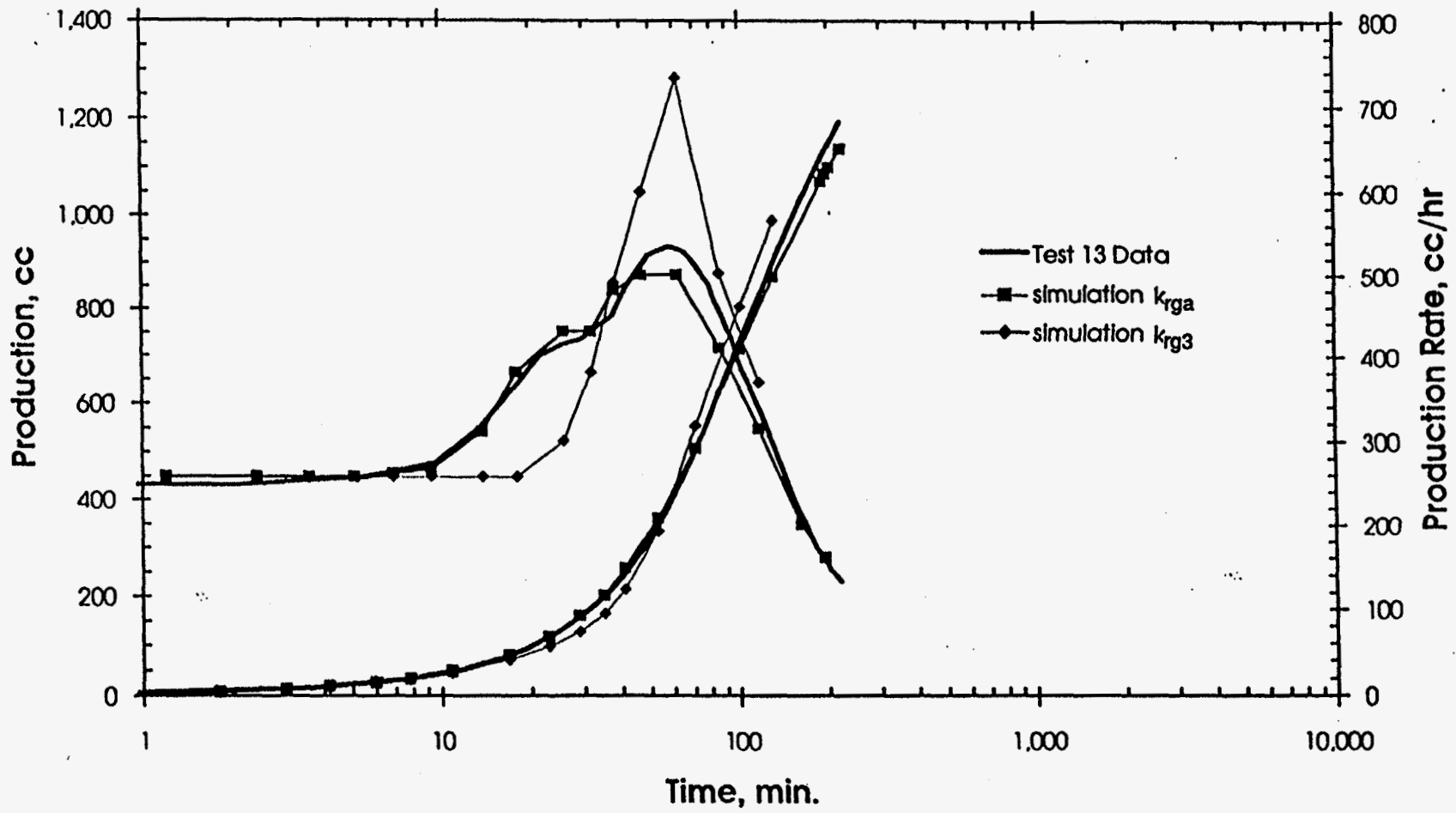


Fig. 14 - Gas relative permeabilities.

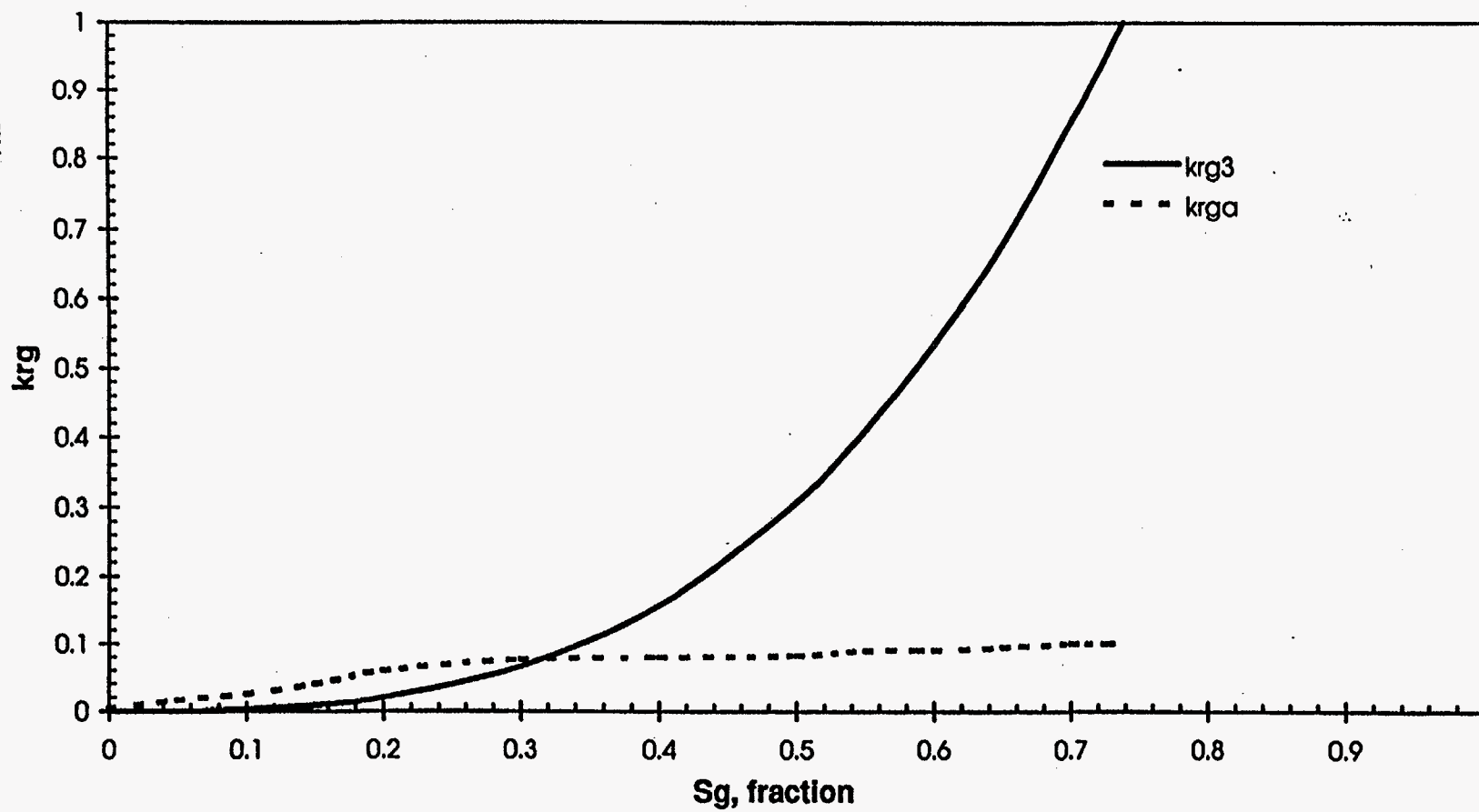
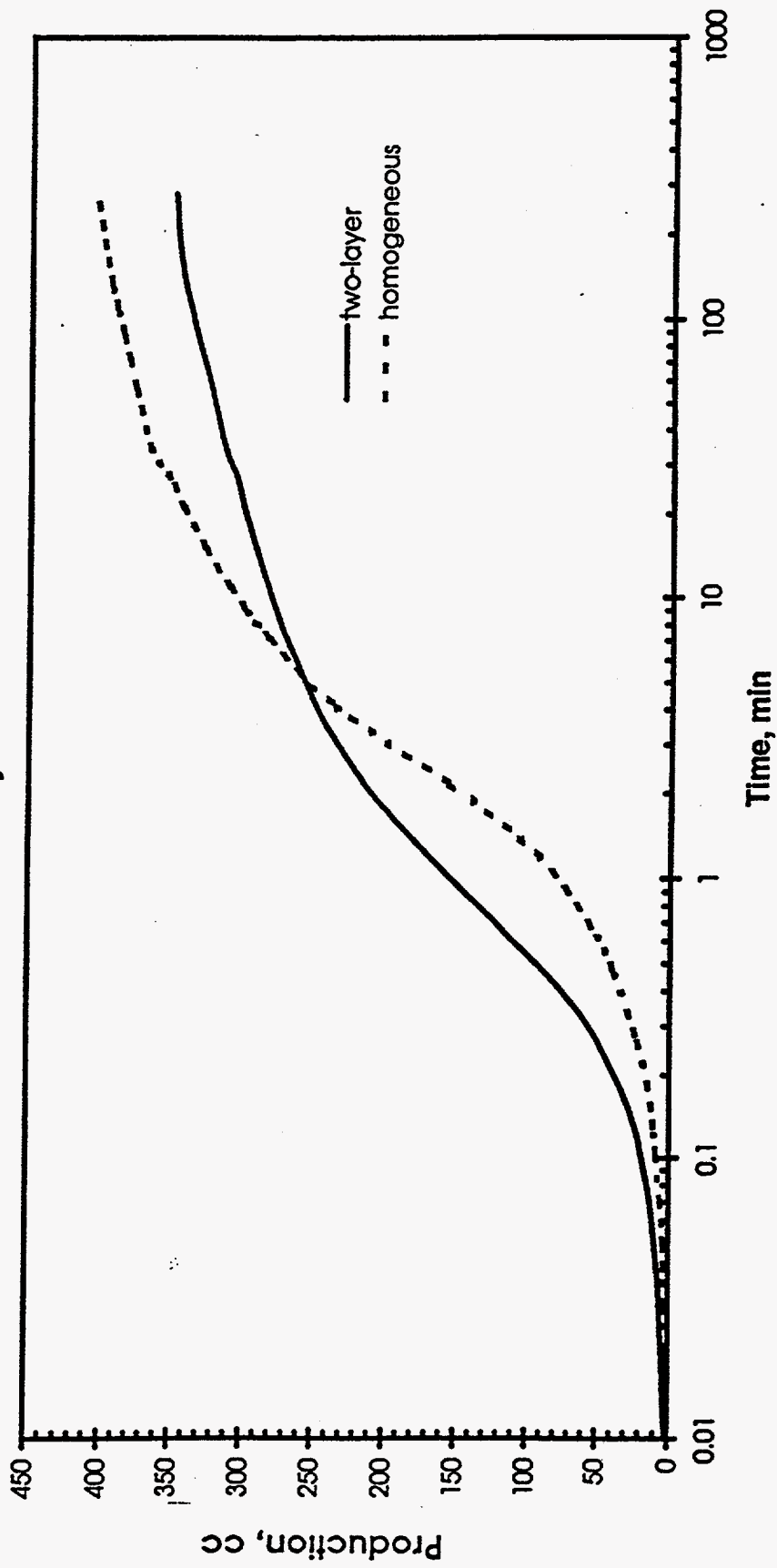


Fig. 15 - Production for the Berea layer in a two-layer and in a homogeneous system.



CHAPTER V

Dual-Porosity Simulation Incorporating Reinfiltration and Capillary Continuity Concepts Part I: Single Gridcell

J.C.T. Tan

Abbas Firoozabadi

Reservoir Engineering Research Institute

SUMMARY

We have developed a method to account for reinfiltration and capillary continuity effects in the simulation of fractured reservoirs. The proposed method requires fine grid simulation of a three-block stack (two-block stack if it is assumed that there is no capillary continuity). The information is then used to construct the drainage curves of different gridcells that may contain a large number of matrix blocks. Variation of capillary pressure, block height, and permeability of various matrix blocks within a gridcell are accounted for without the need for fine grid simulation.

INTRODUCTION

It is generally recognized that in fractured porous media, the reinfiltration of drained oil from some matrix blocks to the neighboring blocks in the gas-oil two-phase region could have an important effect on the drainage performance¹⁻⁴. It has also been demonstrated that capillary continuity (i.e., oil phase pressure continuity) between matrix blocks (with fractures between them) has a significant effect on oil recovery performance and GOR behavior^{5,6}. Reinfiltration is due to the capillary and gravity forces⁷, and capillary continuity is related to the fracture capillary pressure⁶. The understanding of both processes has set the stage for their incorporation in dual-porosity fractured models. Two recent papers discuss the modification of dual-porosity/dual permeability models to account for reinfiltration and capillary continuity. We will first review these two papers. Fung⁸ included reinfiltration in a computational gridcell of a dual-porosity reservoir simulation that contains a stack of matrix blocks. He first refined the grid into the level of individual matrix blocks, then adopted a dual-porosity approach to calculate the drainage performance of the entire stack (computational gridcell). In this model, the reinfiltration effect is taken into account by allowing the communication between each fracture and the matrix block below. The amount of reinfiltration is characterized by a fractional reinfiltration parameter, β . Once the drainage rate versus the average stack saturation is obtained, the information is then used to construct a pseudo-capillary pressure curve for the full scale reservoir simulation. Fung showed a reasonable agreement between his model and the fine grid simulation results. The deficiencies in such a model are: 1) the assumption that the drainage rate of every matrix block in the stack is a simple function of the average matrix block saturation (this assumption may not be valid as we will observe later in this paper), 2) when $\beta < 1$, one has to perform fine grid simulation

to obtain this parameter, 3) the model may not be valid for a stack of blocks with non-uniform matrix block properties, 4) the model does not "dynamically" take into account the change of drainage rate with capillary pressure change; one has to obtain the pseudo-capillary pressure curves at various pressures (interfacial tension effect) for every gridcell by using fine grid simulation, and 5) dual-permeability concept is used to account for capillary continuity which may not be a proper approach.

Por, et al.⁹ applied a different approach. To account for the effect of reinfiltration, they introduced additional connections between matrix and fracture nodes. Connection-dependent relative permeabilities were used to prohibit flow in the fractures when fracture oil saturation is below a certain threshold. Similar to Fung, Por, et al. used the dual-permeability approach to account for capillary continuity. Deficiencies associated with this model are: 1) the reinfiltration is taken into account only between the computational gridcells but not within the grid block, unless each computational grid represents a single matrix block, 2) it is not clear how matrix-fracture relative permeabilities were obtained, probably through fine grid simulation, and 3) reinfiltration is assumed to be entirely driven by the gravity potential, which neglects the capillary pressure driving force.

Based on the above brief review, it is clear that the state-of-the-art fractured simulation models need further improvement to account for reinfiltration and capillary continuity processes.

The objective of this work is to provide a simple method to model the reinfiltration and capillary continuity processes in the simulation of gas-oil drainage in fractured porous media. In part I of the study, the reinfiltration and capillary continuity effects are modelled in a single computational gridcell; a computational cell is usually comprised of a large number of matrix blocks. In Part II, capillary and reinfiltration interactions between gridcells in a dual-porosity model are presented.

In the following, we will first present modeling of reinfiltration, and then capillary continuity representation in a computational gridcell will be discussed.

REINFILTRATION IN A COMPUTATIONAL GRIDCELL

Through the examination of saturation behavior of various matrix blocks in a stacked-block system, we have found that there is a correlation between the drainage rate and the individual matrix average saturation. For the purpose of illustration, the analytical model of Firoozabadi and Ishimoto³ will be used to investigate the variation of drainage rate versus average saturation of individual matrix blocks in a stack. In this example, all matrix blocks are assumed to be 60 cm in height, have a permeability of 0.7 darcy, porosity of 22%, and cross-sectional area of 225 cm². Fracture permeability is assumed to be 100 darcy. The density difference between the oil and gas phases is assumed 0.724 g/cm³, and the oil viscosity is assigned a value of 0.866 cp. The analytical model of Ref. 3 is based on, 1) infinite gas mobility, 2) incompressible gas and oil phases, and 3) zero fracture capillary pressure. The oil relative permeability and the gas-oil capillary pressure are expressed by $k_{ro}=C_o(1-S_g)$, and $P_c=-P_{co}\ln(1-S_g)$, respectively. In this illustration, we assign $C_o=1$, and $P_{co}=0.15$ psi. The symbols are defined in the Nomenclature.

Both the fine grid simulation and the concepts advanced in Ref. 3 reveal that oil drained from the upper matrix blocks will completely reinfiltrate into the lower blocks, provided the stack is surrounded by gas. The rate of drainage of each matrix block in a stack of N identical blocks (the

case of non-identical blocks will be considered later) is given by,

$$\begin{aligned}
 q_1 &= -\phi Ah \left(\frac{d\bar{S}_{g1}}{dt} \right) \\
 q_2 &= -\phi Ah \left(\frac{d\bar{S}_{g2}}{dt} \right) + q_1 \\
 q_N &= -\phi Ah \left(\frac{d\bar{S}_{gN}}{dt} \right) + q_{N-1}
 \end{aligned}
 \tag{1}$$

In the above equation, S_{gi} is the average gas saturation and q_i is the drainage rate of block i . Both S_{gi} and q_i are function of time, t , and maybe different for different blocks.

The solution techniques of Ref. 3 were used to calculate S_{gi} analytically. Then Eq. 1 was employed to calculate q_i . The normalized drainage rate, $q_i/\phi Ah$, versus S_{gi} is plotted in Fig. 1 for $N=10$. Note that ϕAh is the pore volume (PV) of each matrix block. The figure reveals that each matrix block in a stack has a drainage behavior that is different from the others. The difference is particularly large between the first block and the rest. However, we observe that drainage behavior for blocks $i \geq 2$ is generally similar. Therefore, we may approximate the drainage rate for all the matrix blocks in a stack by using only two drainage curves 1) the drainage curve for the first block where reinfiltration is absent, and 2) the drainage curve for the rest of the blocks (represented by the drainage curve of the second block) where reinfiltration can take place. Such an approach requires that the drainage rate versus average saturation behavior for blocks 2 to N be the same. It will be demonstrated next that by using the two drainage curves one can accurately obtain the drainage performance of the entire stack of N matrix blocks.

The relationship between the drainage rate and the block average gas saturation for the two cases (without and with reinfiltration of oil) are defined by $F_1(S_{gi})$ and $F_2(S_{gi})$. We use F_1 to calculate the drainage rate of the first block and F_2 for the rest of the blocks; then Eq. 1 becomes,

$$\begin{aligned}
 \frac{d\bar{S}_{g1}}{dt} &= \frac{-1}{\phi Ah} F_1(\bar{S}_{g1}) \\
 \frac{d\bar{S}_{g2}}{dt} &= \frac{-1}{\phi Ah} F_2(\bar{S}_{g2}) + \frac{d\bar{S}_{g1}}{dt} \\
 \frac{d\bar{S}_{gN}}{dt} &= \frac{-1}{\phi Ah} F_N(\bar{S}_{gN}) + \frac{d\bar{S}_{g(N-1)}}{dt}
 \end{aligned}
 \tag{2}$$

where $F_i = F_2$ for $i \geq 2$. By integrating Eq. 2 the average saturation versus time for all the matrix blocks and thus the drainage rate of the entire stack can be computed.

Fig. 2 shows the cumulative production (normalized by the total PV) calculated from the analytical solution of Ref. 3 and our proposed model using the first and second drainage curves of Fig. 1. For all three cases — $N=3, 5$, and 10 (Figs. 2a, 2b, and 2c), the agreement between the analytical solution and our proposed model is excellent. The results for average gas saturation versus the time for individual blocks of the 10 block-stack are depicted in Fig. 3. The saturation of the individual matrix blocks is also reasonably predicted by the model.

Proposed Model

Based on the above numerical experiment, we propose the following procedure to model reinfiltration for a stack of matrix blocks:

- a) From fine grid simulation of a stack of two blocks, drainage rate versus S_g relationships— F_1 , and F_2 curves are established. These two curves, F_1 , and F_2 represent zero reinfiltration and reinfiltration, respectively.
- b) Eq. 2 is integrated to calculate S_{gi} versus time, using the F_1 curve for the top and the F_2 curve for the blocks below.
- c) From the total material balance, the drainage rate versus S_g for the stack of N matrix blocks is obtained. The information in this step provides the drainage behavior of a gridcell in a dual-porosity simulation model.

Numerical Examples

A number of examples are considered in comparing fine grid simulation results with the proposed model. Unless stated otherwise, a stack of ten matrix blocks comprises a single numerical gridcell. Fluid properties, matrix porosity and permeability, and areal dimensions are the same as those used in our illustrative example. The oil relative permeability and the gas-oil capillary pressure for the matrix are,

$$k_{rom} = \left(\frac{S_{om} - S_{orm}}{1 - S_{orm}} \right)^{3.5} \quad (3)$$

$$P_{cm} = P_{cm}^o - \sigma_m \ln \left(\frac{S_{om} - S_{orm}}{1 - S_{orm}} \right) \quad (4)$$

with $S_{orm}=0.26$. Gas is assumed to have an infinite mobility. For the fracture, we assume k_{rof} changes linearly with S_{of} , and the fracture capillary pressure is zero. In Eq. 4, P_{cm}^o is the threshold capillary pressure of the matrix. All numerical simulations were conducted using the Eclipse¹⁰ reservoir simulator. We used ten grids for each matrix block for $h=60$ cm and twenty grids for $h : 180$ cm. These grid numbers per matrix block are adequate to correctly describe the saturation profile and drainage rate.

Case 1: Identical Blocks ($h=60$ cm)-For this case, $h=60$ cm, $P_{cm}^o=0.4$ psi, and $\sigma_m=0.17$ psi. A matrix threshold capillary pressure of 0.4 psi is equivalent to a 38.8 cm gravity head ($\Delta\rho=0.724$ g/cm³). The average equilibrium gas saturation S_{ge} (average block gas saturation at $t ; T$) is 0.114 for all the matrix blocks.

Fig. 4 shows the normalized drainage rate ($q_i/\phi Ah$) versus S_{gi} for the first four blocks. It is interesting to note that except for the first block, all other blocks have a very similar drainage behavior. We used the drainage curves for the first and second blocks in Fig. 4 (which are similar in this case), and applied Eq. 2 to calculate the gas saturation for each block.

Comparison of S_g from the model prediction and the numerical simulation is shown in Fig. 5; results indicate that there is an excellent agreement between the two. In Fig. 5b, the saturation history under the condition of zero reinfiltration is also plotted; the difference is significant.

Case 2: Identical Blocks (h=180 cm)-The difference between Case 2 and Case 1 is the increase in block height from 60 to 180 cm. The average equilibrium gas saturation for the 180-cm-blocks is equal to 0.513.

Fig. 6 shows the computed drainage rate for the individual matrix blocks using fine grid simulation, which reveals that unlike Case 1, the drainage curve for the first matrix block is very different from the rest. It also demonstrates the importance of using the second drainage curve for our model. In Fig. 7, we compare the results from model predictions with fine grid numerical simulation; a good agreement is evident. Notice that for Case 2 (see Fig. 7b), the effect of neglecting oil reinfiltration is more pronounced than that of Case 1 (see Fig. 5b), indicating the influence of matrix block height.

Block-Stack with Non-Uniform Matrix Properties

When matrix blocks in a stack have different properties (i.e., different permeabilities, heights, etc.), the assumption of complete reinfiltration may no longer be valid, and the more general form of Eq. 1 becomes,

$$\begin{aligned} q_1 &= -\phi_1 A h_1 \left(\frac{d\bar{S}_{g1}}{dt} \right) \\ q_2 &= -\phi_2 A h_2 \left(\frac{d\bar{S}_{g2}}{dt} \right) + R_1 \\ q_N &= -\phi_N A h_N \left(\frac{d\bar{S}_{gN}}{dt} \right) + R_{N-1} \end{aligned} \quad (5)$$

In the above equation, R_i is the oil reinfiltration rate to matrix block (i+1). We scale the drainage rate linearly to the permeability k , so that

$$q_i = \frac{k_i}{k^*} q_i^* \quad (6)$$

where q_i^* is the drainage rate of matrix block i in a homogeneous stack with a permeability k^* ; therefore q_i^* is the same as F_i . Combining Eqs. 5 and 6,

$$\begin{aligned} \frac{d\bar{S}_{g1}}{dt} &= \left(\frac{-1}{\phi_1 A h_1} \right) \frac{k_1}{k^*} F_1 (\bar{S}_{g1}) \\ \frac{d\bar{S}_{g2}}{dt} &= \left(\frac{-1}{\phi_2 A h_2} \right) \left[\frac{k_2}{k^*} F_2 (\bar{S}_{g2}) - R_1 \right] \\ \frac{d\bar{S}_{gN}}{dt} &= \left(\frac{-1}{\phi_N A h_N} \right) \left[\frac{k_N}{k^*} F_N (\bar{S}_{gN}) - R_{N-1} \right] \end{aligned} \quad (7)$$

The next step is to determine the reinfiltration rate, R_i in Eq. 7. A conservative approach to include reinfiltration in our model would be to assume that the rate of reinfiltration to any matrix block is always equal to the initial (i.e., maximum) drainage rate for that particular block³. Let us define,

$$r_{i+1} = \sum_{j=1}^i (q_j - R_j) \quad (8)$$

where r_{i+1} is the oil rate bypassing matrix block (i+1) which could be zero. Then we can write,

$$\begin{aligned} R_i &= q_i + r_i, \text{ if } (q_i + r_i) \leq q_{i+1}^o \\ R_i &= q_{i+1}^o, \text{ if } (q_i + r_i) > q_{i+1}^o \end{aligned} \quad (9)$$

In Eq. 9, q_{i+1}^o is the initial (maximum) rate of drainage of block (i+1). Eqs. 7 through 9 complete the formulation. The following two examples for non-uniform matrix blocks demonstrate the validity of the above expressions.

Case 3: Non-Uniform Blocks (Permeability and Block Height Variation)-The six-block stack shown in Fig. 8 has different permeabilities and heights. Other properties are similar to Case 2. Matrix capillary pressure is the same for all the blocks. The drainage curves from the fine grid simulation of homogeneous stacked blocks for Case 1 (second curve) and Case 2 (first and second curves) are used, and then Equations 7 to 9 are applied to solve the saturation history. Results shown in Fig. 9 indicate that our model not only matches the drainage performance of the whole stack, but the saturation history of the individual blocks as well.

Scaling

So far it has been assumed that gas-oil capillary pressure does not vary with pressure and that all the matrix blocks have the same capillary pressure. Matrix capillary pressure is generally a function of both permeability and the reservoir pressure. We thus wish to find a proper scale for the drainage rate so that the number of the fine grid simulations required for our model can be reduced. Coats¹³ proposed that for the drainage of a single matrix block, since the initial drainage rate is proportional to $(\Delta\rho g - P_{cm}^o/h)$ and the average gas saturation of the block approaches S_{ge} at an infinite time, one may scale the drainage rate and the matrix block saturation with $(\Delta\rho g - P_{cm}^o/h)$ and S_{ge} to obtain a similar form of solution for the block saturation history. To verify Coats' proposal, fine grid simulations were performed to obtain the drainage of, 1) a single block, and 2) four stacked-block systems. Block heights and coefficients of capillary pressure expression in Eq. 4 were varied. Let us define,

$$S_g^+ = \frac{\bar{S}_g}{\bar{S}_{ge}} \quad (10)$$

and,

$$t^+ = t \frac{(\Delta\rho gh - P_{cm}^o)^*}{(\Delta\rho gh - P_{cm}^o)} \quad (11)$$

Superscript "*" refers to the data of the reference matrix block. Fig. 10 depicts S_g^+ versus t^+ of a single matrix block where its height and capillary pressure are varied. The reference matrix properties are those of the matrix block of Case 2. The figure reveals that except for the two cases that have relatively large values of $P_{cm}^o/\Delta\rho gh$, other results are fairly close to each other. These two cases can be identified as the cases that have low equilibrium average gas saturation. The equilibrium gas saturation values for all the cases are listed in Table 1. Considering such a wide variation in S_{ge} , the scaling expressions given by Eqs. 10 and 11 provide a satisfactory approximation for the drainage performance of a matrix block system. We next examined the drainage performance of a stack of four blocks. The reference state is also the single block of Case 2. Since there is no fracture capillary pressure, the equilibrium average gas saturation for the stack is the same as that of the individual blocks (see Table 1). In Fig. 11, a similar behavior to Fig. 11 is observed; S_g^+ versus t^+ of the total stack approximately falls on one curve provided $P_{cm}^o/\Delta\rho gh$ is small. We therefore postulate that, under the condition that there is no fracture capillary pressure, if the matrix blocks are tall or the threshold pressure is small, we can obtain a single relationship between S_g^+ and t^+ to approximate the drainage rate when matrix capillary pressure (due to reservoir pressure) and block heights vary. This approach significantly reduces the number of fine grid simulations required for each computational gridcell in dual-porosity models.

The next example illustrates how we can use the above scaling to calculate the drainage performance of a stack of blocks of non-uniform properties.

Case 4: Non-Uniform Blocks (Permeability, Block Height and Capillary Pressure Variation)—The schematic of Case 4 is shown in Fig 8. For this complicated example, matrix blocks have different heights and permeabilities. The matrix capillary pressure is assumed to be inversely proportional to the square root of its permeability, and fracture capillary pressure is assumed zero. The following expression is employed to approximate the drainage rate of each block,

$$q_i = \frac{k_i (\Delta\rho gh - P_{cm}^o)_i^* h_i}{k^* (\Delta\rho gh - P_{cm}^o)_i h^*} q_i^*(S_g^+) \quad (12)$$

Eq. 12 is substituted into Eq. 5 to perform saturation calculations. Here, we choose the properties of the matrix block of Case 2 as reference; $q_1^*(S_{g1}^+) = F_1$, and $q_2^*(S_{g2}^+) = F_2$,

where F_1 and F_2 are the drainage functions for 0.7 darcy matrix blocks of the first and second blocks of Case 2, respectively. Fig. 12 shows the results from our model and the fine grid simulation. The overall agreement between the model and the simulation results is excellent.

In the next section, the incorporation of both capillary continuity and reinfiltration in a computational gridcell will be discussed.

CAPILLARY CONTINUITY IN A COMPUTATIONAL GRIDCELL

In the study of the drainage behavior of a stack of matrix blocks with zero fracture capillary pressure, we found that the drainage rate of the individual matrix blocks is influenced by reinfiltration, and the drainage rate could be approximated as a function of the matrix block average gas saturation. Only two drainage curves (drainage rate versus the average block gas saturation) are adequate to obtain the drainage performance of the entire stack. These curves are: 1) the drainage curve for the top block where reinfiltration does not take place, and 2) the drainage curve for the rest of blocks where oil drained from one block could reinfiltrate to the blocks below. The analysis becomes more complicated when capillary continuity exists between matrix blocks. Due to capillary continuity, the equilibrium average gas saturation, S_{ge} , is different for different matrix blocks. With the additional complexity of capillary continuity, we desire to find a general drainage behavior for all the blocks so that there is no need to obtain drainage curves of all the individual blocks. In the following, we will discuss how capillary continuity could be accounted for in a computational gridcell.

Fine grid simulations were conducted to examine the effects of reinfiltration and capillary continuity on drainage performance of a stack of ten matrix blocks. The fluid and matrix block properties are the same as those used in the preceding section. The matrix relative permeability and the gas-oil capillary pressure are given in Eqs. 3 and 4, with $P_{cm}^o=0.4$ psi and $\sigma_m=0.17$ psi. For the fracture,

$$k_{rof} = \left(\frac{S_{of} - S_{orf}}{1 - S_{orf}} \right) \quad (13)$$

$$P_{cf} = P_{cf}^o - \sigma_f \left[\ln \left(\frac{S_{of} - S_{orf}}{1 - S_{orf}} \right) \right]^2 \quad (14)$$

with $S_{orf}=0$. In this study, we assumed $P_{cf}^o=0.0088$ psi and $\sigma_f=0.0023$ psi. Dindoruk and Firoozabadi¹¹ have found that the expression for the fracture capillary pressure is an important parameter for gas-oil flow in fractured porous media. Fracture capillary pressure increases with the decrease of the fracture aperture; as a result, the rate of drainage across the stack increases¹². They used the above capillary pressure and relative permeability expressions to successfully simulate the experimental data for the gas-oil gravity drainage across a stack of three blocks¹¹. We adopted the same equations for the relative permeability and capillary pressure.

The drainage rate versus the average block gas saturation of the individual matrix blocks was examined first. Figs. 13 and 14 show results for block heights of $h=60$ and 180 cm, respectively. Notice that although some blocks have a different equilibrium gas saturation (see Table 1), due to capillary continuity effect, we observe that there are three distinct drainage characteristic curves for each case. Those are: 1) the first curve belongs to the drainage of the top block where the matrix block is not subject to reinfiltration, but it is in capillary contact with the second block, 2) the second series of curves represent the drainage performance of blocks 2 to $N-1$ where both reinfiltration and capillary continuity processes take place, and 3) the third curve belongs to the drainage of the bottom matrix block where reinfiltration exists, but fracture capillary pressure is zero at the bottom face. The drainage characteristic of the middle blocks, 2 to $N-1$, can be approximated by a single curve. The first and middle drainage

curves exhibit a long tail at high S_g , suggesting that due to fracture capillary pressure, the upper matrix blocks will drain continuously until the average gas saturation of the three blocks reaches S_{gei} (S_{gei} is the equilibrium average gas saturation for block i). The equilibrium process may realize at time infinity and may not happen during field life. The results presented in Figs 13 and 14 suggest that the fine grid simulation of a stack of three matrix blocks may suffice from which one can obtain the drainage performance of an N stacked-block system. To resolve the issue of different S_{gei} for different blocks in a stack, we propose to linearly interpolate the drainage rate from S_{ga} to S_{gei} , where S_{ga} is the average block saturation at which the drainage rate is small. Our experience suggests that the choice of S_{ga} has little effect on the results. S_{gei} is evaluated from the integration of the matrix capillary pressure curve in the stack.

Proposed Model

Our procedure for the calculation of the drainage performance of a stack of N blocks where both reinfiltration and capillary continuity processes take place include:

- a) From the fine grid simulation of a stack of three blocks, drainage rate versus S_{gi} is established. The three curves represent the drainage rate of, 1) the top block with fracture capillary pressure and with zero reinfiltration, 2) the middle block with both reinfiltration and fracture capillary pressure, and 3) the bottom matrix block with reinfiltration and zero fracture capillary pressure, respectively.
- b) The end point of each drainage curve for different blocks is modified to account for variation of S_{gei} within the stack.
- c) Eq. 2 is then used to calculate S_{gi} versus time. In this equation, we assume complete reinfiltration from upper to lower matrix blocks.
- d) From the total material balance, the drainage rate versus S_g for the stack of N matrix blocks is computed. The information in step (d) is then used to calculate the drainage behavior of a computational gridcell in a dual-porosity simulation model which contains a stack of N blocks.

Numerical Examples

Two examples were studied to incorporate the combined effects of reinfiltration and capillary continuity. Both examples comprise a stack of 10 matrix blocks, and block height are 60 cm and 180 cm, respectively.

Case 5: Identical Blocks ($h=60$ cm)-Dindoruk and Firoozabadi¹¹ matched the experimental data of Ref. 12 for a three-block stack with fine grid simulation. We used the same data that they used but increased the number of matrix blocks to ten. We first performed a fine grid simulation of a three stacked-block to obtain the three basic drainage curves. The end point for those curves were modified according to S_{gei} ; the value for each matrix block is listed in Table 2. These three drainage curves were used to obtain the gas saturation history for each block

and the entire stack. The results from the model are compared with the fine grid simulation of the ten stacked-block. Fig. 15 shows that our model prediction is in excellent agreement with the simulation results. Fig. 15b also shows the recovery performance predicted from the fine grid simulation based on zero reinfiltration and zero fracture capillary pressure assumptions. The error is significant.

Case 6: Identical Blocks (h=180 cm)-This case is similar to Case 5, except block heights are 180 cm. The equilibrium gas saturation for each block is listed in Table 2. Note that the equilibrium average gas saturation for blocks 1 to 9 is the same.

We adopted the same procedures as those used in Case 5 to obtain the saturation history. Results shown in Fig. 16 demonstrate the strength of our proposed model. The error from neglecting the reinfiltration and capillary continuity effects is less in this case than in Case 5, but is still significant at early times. Notice that if the fracture capillary pressure is zero, we only need to consider the reinfiltration, and two drainage curves are adequate to obtain the drainage performance.

Next, results for the non-uniform stacked block systems will be presented.

Stacked block with Non-Uniform Matrix Properties

As we stated previously, the assumption of complete reinfiltration when matrix blocks in a stack have different properties (i.e., different heights and permeabilities, etc.) may not be valid. In such a case Eqs. 7 through 9 are used to calculate the drainage of non-uniform blocks. The following examples reveal that our model is also suitable for non-uniform matrix blocks.

Case 7: Non-Uniform Blocks (Permeability and Block Height Variation) For this case, different heights and permeabilities are assigned for each of the matrix blocks in the stack (see Fig. 8), but a single matrix capillary pressure curve is used. The drainage curves from the simulation of homogeneous stacked-blocks in Cases 5 and 6 were used to obtain the saturation history. Results shown in Fig. 17 indicate that the match of the saturation history for the entire stack is very good, but only fair for the individual blocks. This could be due to the fact that drainage rate is not only a function of the average matrix gas saturation as proposed by our model, but that it is also affected by the fracture capillary pressure (fracture gas saturation). However, any attempt to include the effect of the fracture gas saturation in the model will significantly increase the complexity of the approach and may make it impractical to apply to a dual-porosity reservoir simulation model. We have also run other examples similar to Case 7 and found that our model performs well (results are not presented).

Scaling

The scaling approach presented earlier has to be modified to include the effect of fracture capillary pressure. There may not be a simple procedure to include both matrix and fracture capillary pressures in the scaling groups. We have adopted Eq. 10 and modified Eq. 11, to,

$$t^+ = t \frac{(\Delta\rho gh - P_{cm}^o + P_{cf}^o)^*}{(\Delta\rho gh - P_{cm}^o + P_{cf}^o)} \quad (15)$$

In Eq. 15, the superscript "*" refers to the data of the reference matrix block. Fig. 18 shows the fine grid simulation results of S_g^+ vs. t^+ for the drainage of a four-block stack for various capillary pressures and block heights. The figure indicates that results are more scattered than that of the zero fracture capillary pressure case shown in Fig. 11, mainly because different blocks in a stack have different S_{ge} values and thus different scales. However, we still observe that most data exhibit a similar trend provided, $P_{cm}^o/\Delta\rho gh$ is small. (The results in Fig. 18 are based on both matrix and fracture capillary pressure variation.)

CONCLUDING REMARKS

The reinfiltration and capillary continuity processes are incorporated in a simple way in the simulation of a gridcell which may contain a large number of matrix blocks. The variation of matrix block height, and permeability within the gridcell are accurately accounted for in the proposed method. The change of capillary pressure and its variation within the gridcell may not be modelled with the same accuracy as the matrix block height and permeability variation. Nevertheless the results for capillary pressure variation are also promising. In part II of this study¹⁴ the incorporation of reinfiltration and capillary continuity effects between gridcells in a dual-porosity model is presented.

ACKNOWLEDGMENTS

This research project is supported by the U.S. Dept. of Energy (Contract No: DE-FG22-93BC14875), and by the members of the Research Consortium on Fractured Petroleum Reservoirs of the Reservoir Engineering Research Institute. Their support is greatly appreciate. We thank Dr. M. NIKRAVESH for his help in the preparation of this paper

NOMENCLATURE

- A = cross sectional area
- g = gravity
- h = matrix block height
- k = permeability
- k_r = relative permeability
- N = total number of matrix blocks in a stack
- P_c = capillary pressure
- P_c^o = threshold capillary pressure
- q = drainage rate
- R = reinfiltration rate
- r = oil flow rate bypassing a matrix block
- S = saturation
- S_{ge} = equilibrium gas saturation
- S_{or} = residual oil saturation

\bar{s} = average saturation
t = time
x = x direction
y = y direction
z = z direction
 β = fractional reinfiltration factor
 μ = viscosity
 ϕ = porosity
 ρ = density
 σ_f = coefficient of fracture capillary pressure curve defined by Eq. 14
 σ_m = coefficient of matrix capillary pressure curve defined by Eq. 4

Subscripts

f = fracture
g = gas
i = matrix block index (from top)
m = matrix
n = phase
o = oil

Superscripts

* = reference state
+ = scaled variable
o = initial rate

REFERENCES

1. du Prey, E. L., "Cascade Drainage of Blocks in a Fissured Reservoir," *Rev. Inst. Francais du Petrole* (Jan.-Feb. 1976) 173-78.
2. Saidi, A. M., Tehrani, D.H., and Wit, K., "Mathematical Simulation of Fractured Reservoirs Performance Based on Physical Model Experiments," *Proc. 10th World Petroleum Congress, Bucharest (1979) paper PD10 (3) 225-33.*
3. Firoozabadi, A. and Ishimoto, K., "Reinfiltration in Fractured Porous Media - Part 1: One Dimensional Model", *SPE Advanced Technology Series* (April 1994) vol.2, No.2, 35-44.
4. Firoozabadi, A. and Ishimoto, K., and Dindoruk, B., "Reinfiltration in Fractured Porous Media - Part 2: Two Dimensional Model", *SPE Advanced Technology Series* (April 1994) vol.2, No.2, 45-51.
5. Firoozabadi, A., and Thomas, L.K.:" Sixth SPE Comparative Solution Project: Comparison of Dual-Porosity Simulators," *J. of Petroleum Technology*, (June 1990) 710-715, 762-763.
6. Firoozabadi, A, and Hauge, J., "Capillary Pressure in Fractured Porous Media," *JPT* (June 1990) 784-791.

7. Barkve, T., and Firoozabadi, A., "Analysis of Reinfiltration in Fractured Porous Media," paper SPE 24900, presented at the 1992 SPE Annual Technical Conference and Exhibition, Washington, DC, Oct. 4-7.
8. Fung, L. S.-K., "Simulation of Block-to-Block Processes in Naturally Fractured Reservoirs", SPE Reservoir Engineering J. (Nov. 1991) 477-484
9. Por, G. J., Boerrigter, P., Maas, J. G., and de Vries, A., "A Fractured Reservoir Simulator Capable of Modeling Block-Block Interaction", paper SPE 19807, presented at the 1989 Annual Technical Conference and Exhibition, San Antonio, TX, Oct. 8-11,1989.
10. Eclipse Reference Manual, Version 92A, Exploration Consultants Ltd. (1992).
11. Dindoruk, B., and Firoozabadi, A., "Computation of Gas-Liquid Drainage in Fractured Porous Media Recognizing Fracture Liquid Flow," paper No. 94-23, presented at the 45th annual technical meeting of the Petroleum Society of CIM, Calgary, June 12-15, 1994.
12. Firoozabadi, A., and Markeset, T., "Fracture Liquid Transmissibility in Fractured Porous Media," SPE Reservoir Engineering J. (Aug. 1994) 201-207.
13. Coats, K. H., "Implicit Compositional Simulation of Single-Porosity and Dual-Porosity Reservoirs", paper SPE 18427 presented at the 1989 SPE Symposium on Reservoir Simulation, Houston, TX., Feb. 6-8, 1989.
14. Tan, J.C.T., and Firoozabadi, A.: "Dual-Porosity Simulation incorporating Reinfiltration and Capillary Continuity Concept: Part II- Gridcells Interaction," paper to be submitted to SPE.

Table 1. S_{ge} values for single blocks.

h, cm	1/2 Pc	Pc	2 Pc
60	0.399	0.114	0.00
180	.626	0.513	0.291
360	0.683	0.626	0.513

Table 2. S_{ge} values for individuals matrix blocks in the stack.

Block No.	N=10, h=60 cm	N=10, h=18 cm
1-7	0.740	0.740
8	0.739	0.740
9	0.685	0.739
10	0.114	0.513

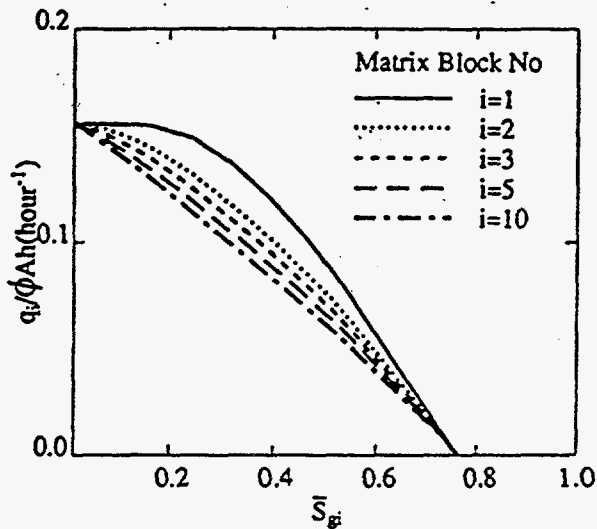


Fig. 1- Drainage rate vs. \bar{S}_{gi} for various matrix blocks in a 10-block stack.

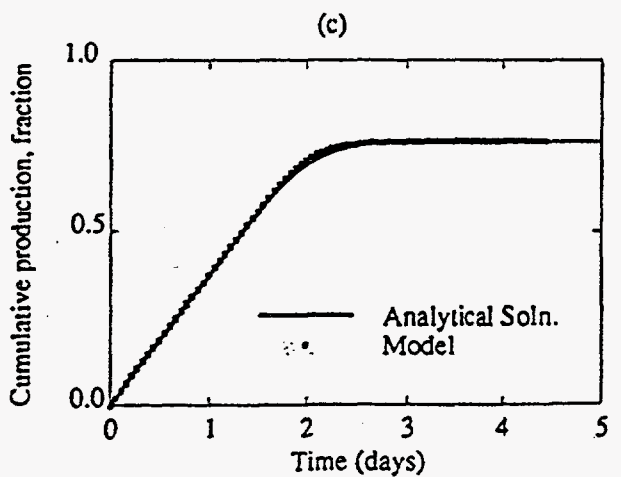
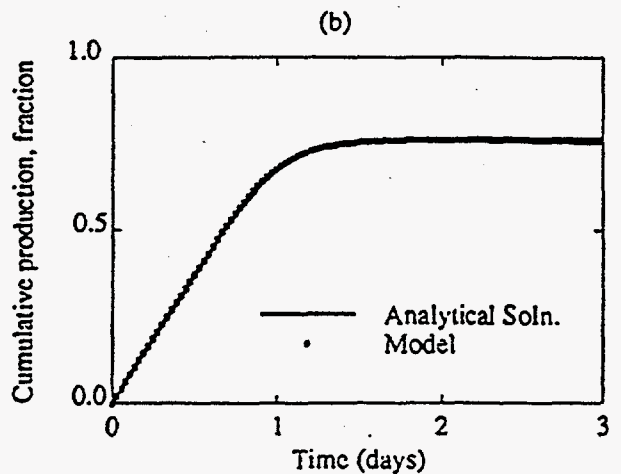
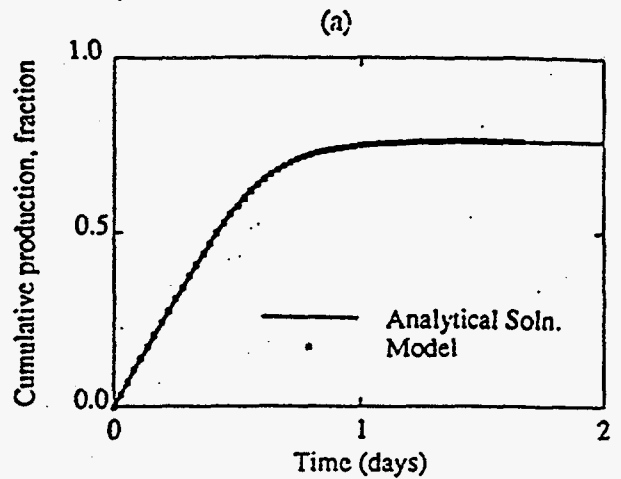


Fig. 2- Cumulative production vs. time for a (a) 3, (b) 5, and (c) 10-block stack.

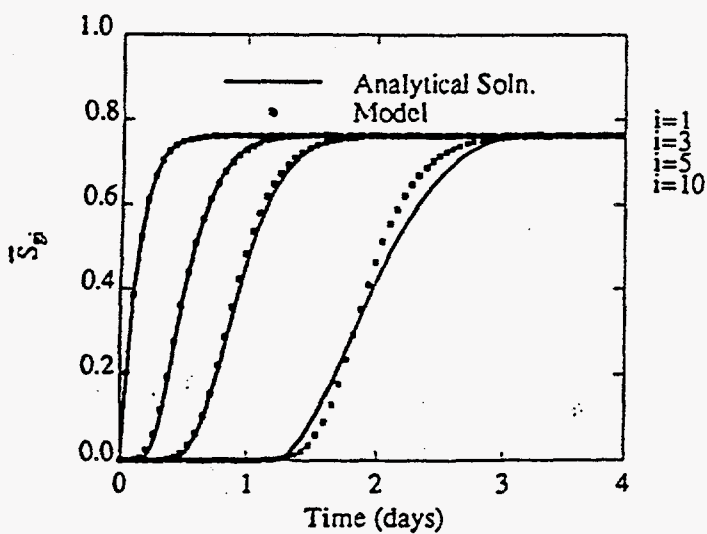


Fig. 3- Saturation history for various matrix blocks in a 10-block stack.

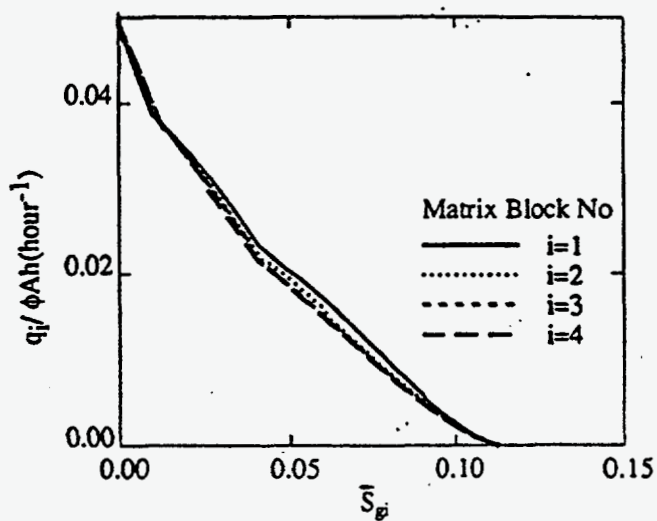


Fig. 4- Drainage rate vs. \bar{S}_{gi} — Case 1.

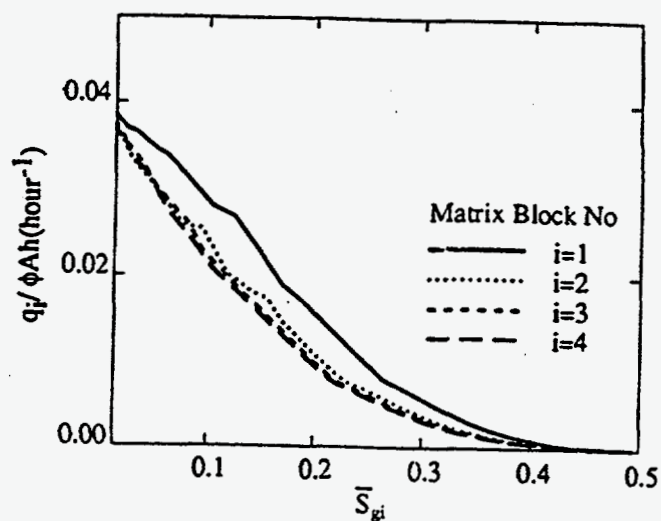


Fig. 6- Drainage rate vs. \bar{S}_{gi} — Case 2.

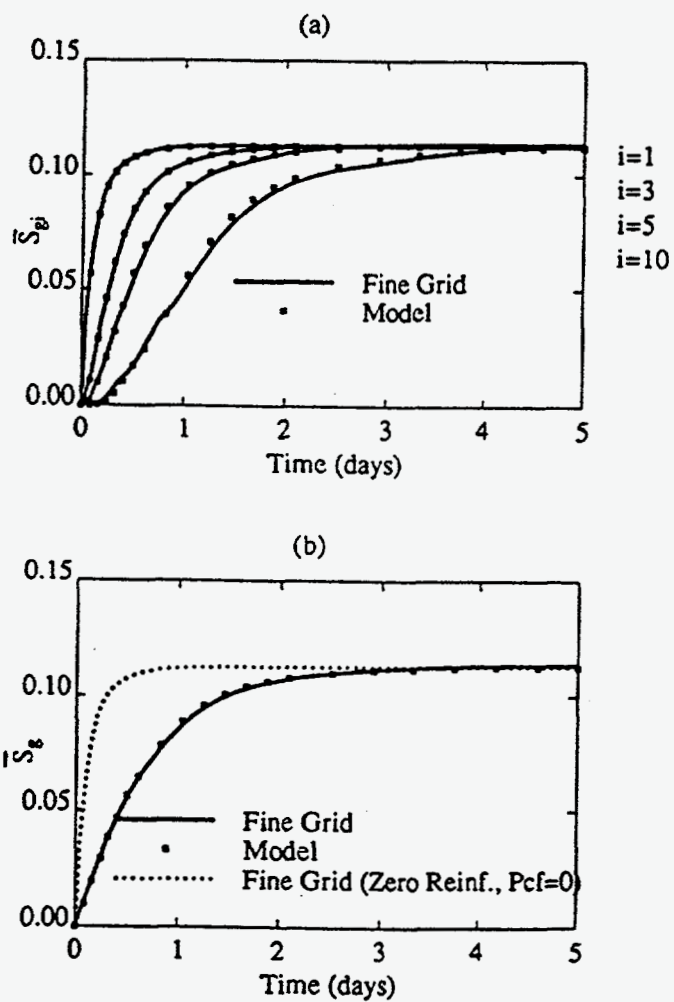


Fig. 5- Saturation history: (a) individual blocks, and (b) entire stack — Case 1.

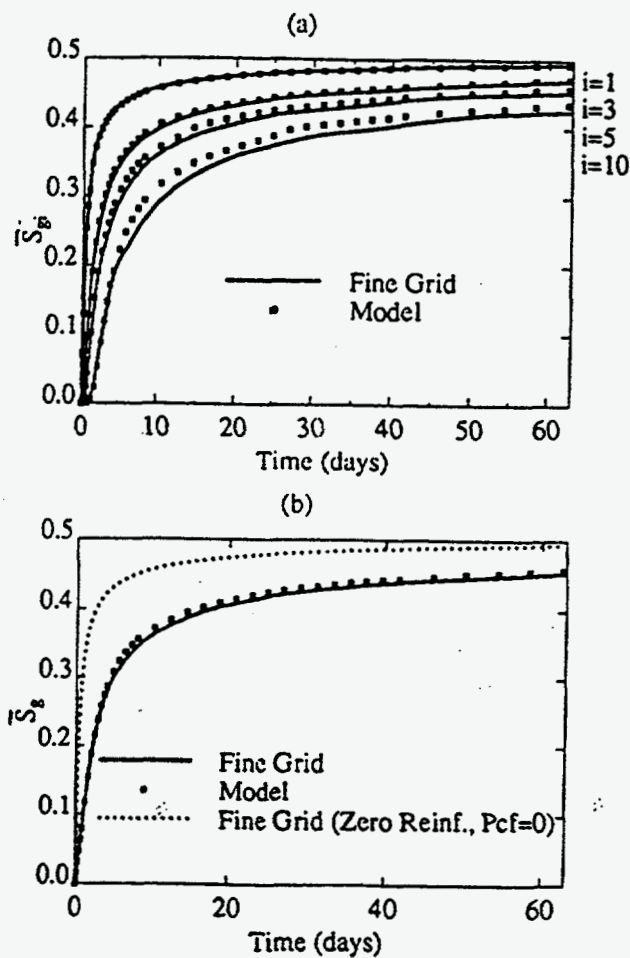


Fig. 7- Saturation history: (a) individual blocks, and (b) entire stack — Case 2.

h=180 cm	k= 0.5 darcy	h=150 cm	k=1.0 darcy
h=60 cm	k= 0.7 darcy	h=250 cm	k=0.7 darcy
h=180 cm	k= 0.1 darcy	h=200 cm	k=1.0 darcy
h=60 cm	k= 0.4 darcy	h=100 cm	k=1.5 darcy
h=180 cm	k= 0.2 darcy	h=250 cm	k=0.5 darcy
h=180 cm	k= 0.3 darcy	h=180 cm	k=0.7 darcy

CASES 3 and 7

CASE 4

Fig. 8- Schematic of stacked blocks Cases 3, 4, and 7.

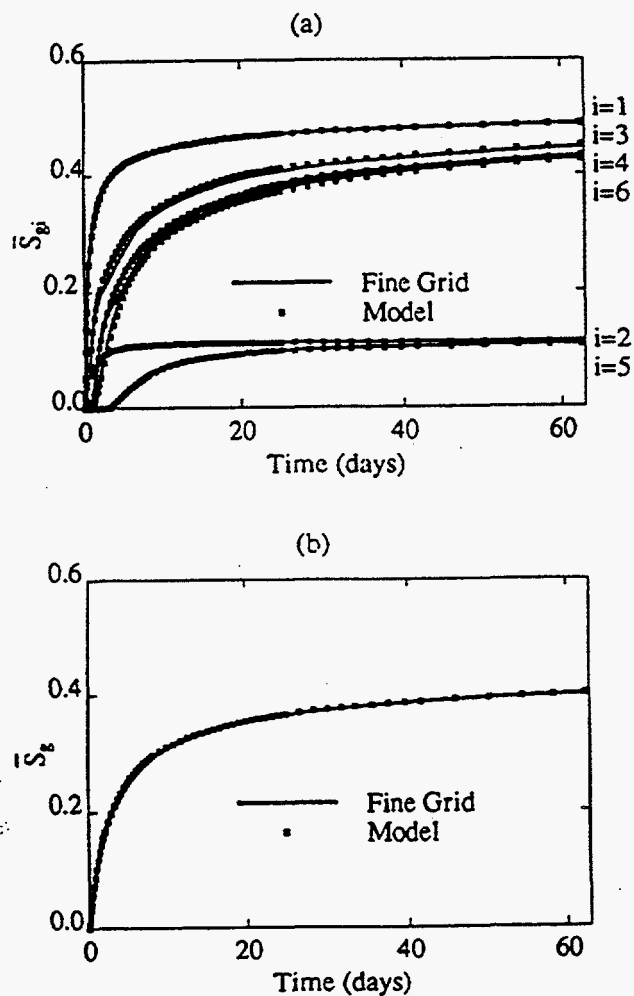


Fig. 9- Saturation history: (a) individual blocks, and (b) entire stack — Case 3.

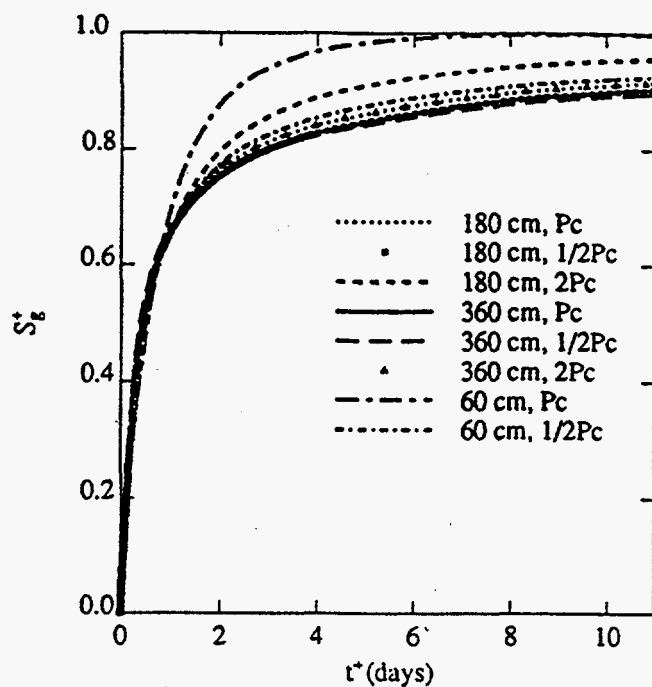


Fig. 10- Drainage performance of a single matrix block.

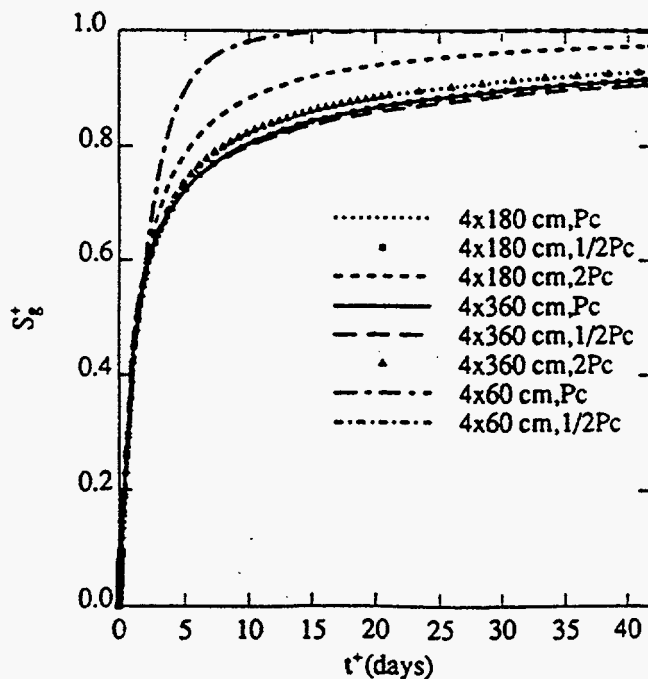


Fig. 11- Drainage performance of a four-block stack, $P_{cf} = 0$.

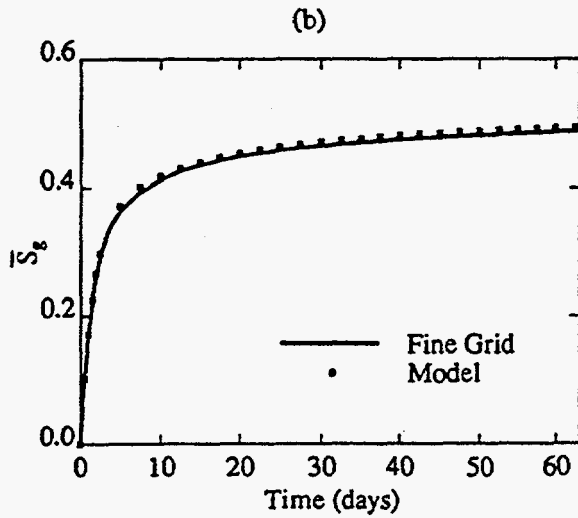
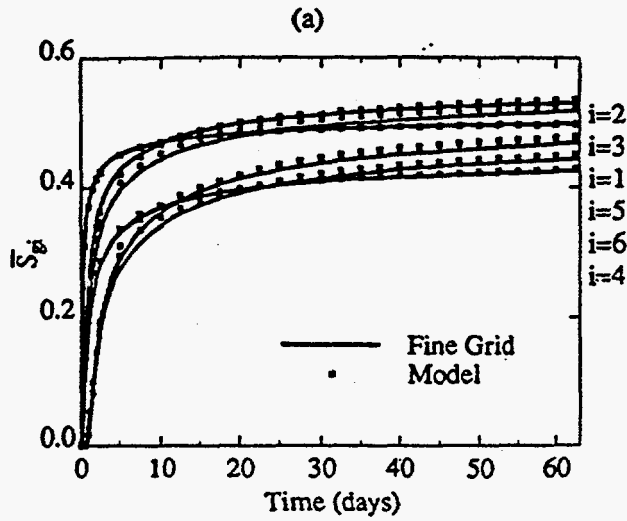


Fig. 12- Saturation history: (a) individual blocks, and (b) entire stack — Case 4.

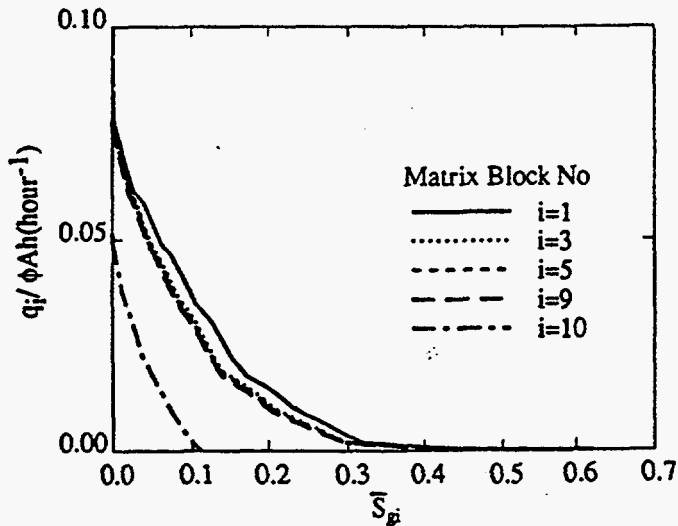


Fig. 13- Drainage rate vs. \bar{S}_{gi} for various blocks in a 10-block stack, $h=60$ cm.

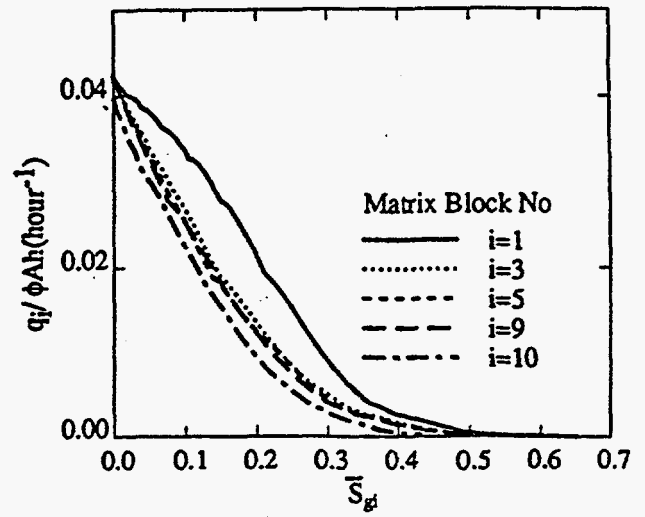


Fig. 14- Drainage rate vs. \bar{S}_{gi} for various blocks in a 10-block stack, $h=180$ cm.

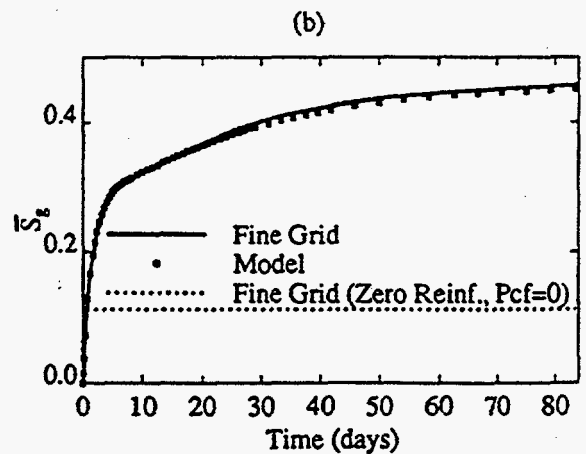
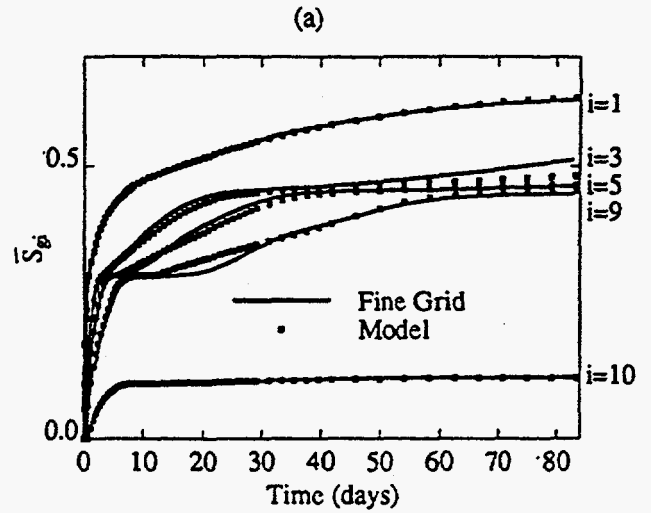


Fig. 15- Saturation history: (a) individual blocks, and (b) entire stack — Case 5.

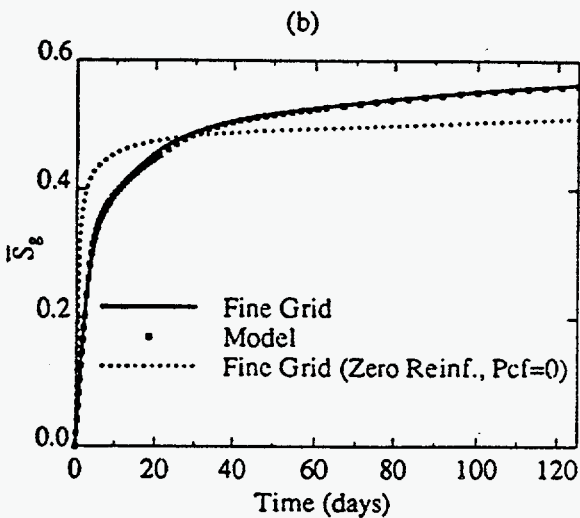
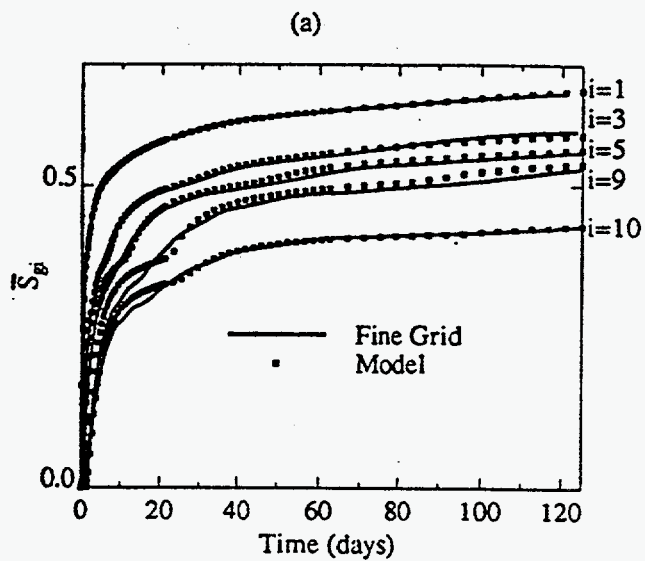


Fig. 16- Saturation history: (a) individual blocks, and (b) entire stack — Case 6.

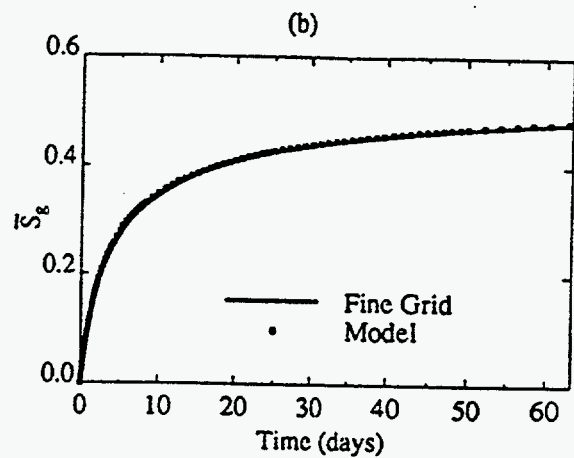
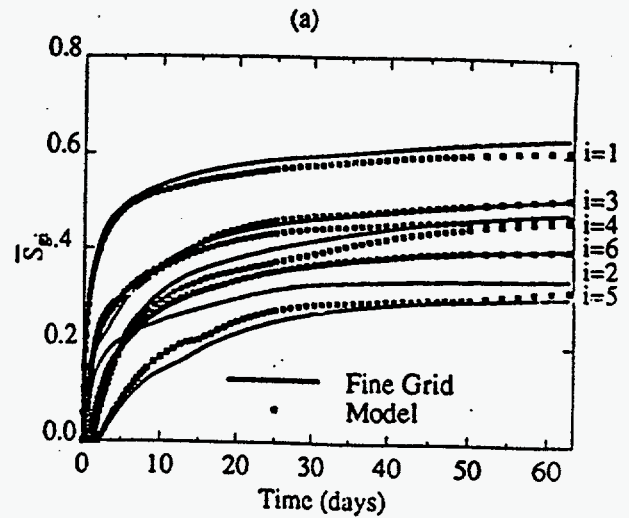


Fig. 17- Saturation history: (a) individual blocks, and (b) entire stack — Case 7.

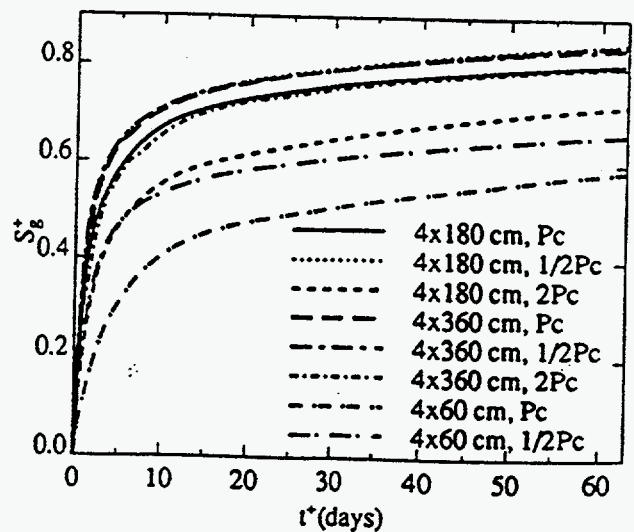


Fig. 18- Drainage performance of a four-block stack, $P_{cf} \neq 0$.

CHAPTER VI

Areal and Vertical Composition Variation in Hydrocarbon Reservoirs: Formulation and One-D Binary Results

Abbas Firoozabadi

Birol Dindoruk

Reservoir Engineering Research Institute

Eric Chang

Arco Exploration and Production Technology

SUMMARY

Very large compositional variation both areally and vertically has been observed in some hydrocarbon reservoirs. Several mechanisms are believed to contribute to such variations. These include: 1) gravitational segregation, 2) molecular diffusion, 3) thermal diffusion, and 4) thermal convection. At isothermal conditions only gravitational segregation and molecular diffusion contribute to vertical compositional grading. The Gibbs segregation concept can properly account for this process. Under nonisothermal conditions, which is often the case, the process is thermodynamically irreversible and, therefore, Gibbs criteria of equilibrium cannot be invoked.

The current literature often combines the Gibbs segregation concept and the natural convection process to formulate the interaction of convection and gravity segregation for multicomponent systems at nonisothermal conditions. The Darcy law is also used without the modification of the velocity weighting for multicomponent systems. Such a formulation may not describe the process properly. In this paper, we formulate compositional variation in hydrocarbon reservoirs at nonisothermal conditions and present the results for the special case of gravity and thermal diffusion in one dimension. The results reveal that thermal diffusion can either enhance or weaken the segregation.

INTRODUCTION

In some hydrocarbon reservoirs, very large compositional variation has been observed both areally and vertically. As an example, the areal variation of composition of H_2S in a reservoir in Abu Dhabi varies from less than one percent on one side to more than 12 percent on the other side of the reservoir (the pressure communication is excellent indicating that compartmentalization is not a possible explanation of this variation (Hamoodi, Abed, and

Firoozabadi, 1996)). In the vertical direction, the variation of composition may be even more pronounced (Lira-Galeana, Firoozabadi, and Prausnitz, 1994).

A number of papers have addressed the subject of compositional variation in hydrocarbon reservoirs. Those papers which focus on gravitational equilibrium demonstrate a fair degree of success.

There is generally a temperature gradient in hydrocarbon reservoirs in the vertical direction. In some reservoirs, there may also be a small temperature gradient in the horizontal direction (say 0.5 to 1 °C/km). Temperature gradients as small as 0.5 °C/km may have significant effects on areal composition variation. The horizontal temperature gradient always induces both thermal convection and thermal diffusion. The vertical temperature gradient causes thermal diffusion but may or may not induce thermal convection. To our knowledge, Jacqmin's work (1990) is the main investigation that integrates gravity segregation and thermal convection in oil and gas reservoirs. He assumed that with thermal convection, the criterion of Gibbs gravity equilibrium, $d\mu_i = -M_i g dz$ (z is the vertical distance and is assumed to be positive upward, μ is the chemical potential, and M is the molecular weight) is valid. At nonisothermal conditions, the Gibbs criterion of gravity equilibrium cannot be invoked because of nonzero entropy production. Apparently, Jacqmin also assumed that the velocity in the Darcy equation and the diffusion equation are the same for multicomponent systems.

There are a number of studies on the interaction of gravity segregation and thermal diffusion. Examples include the work of Holt, et al., 1983, Belery and da Silva 1990, and the recent work by Faissat, et al, 1994. These authors basically begin their formulation with the thermodynamics of irreversible processes. Based on a numerical example, Holt, et al. conclude that thermal diffusion significantly enhances the composition gradient in the vertical direction. The results by Belery and da Silva also reveal that thermal diffusion enhances the vertical variation of composition. Contrary to these conclusions, the data on binary hydrocarbons, as we will discuss in this paper, reveal that thermal diffusion can both enhance and weaken compositional variation in the vertical direction. The study by Faissat et al. provides a background on thermal diffusion and gravity segregation processes. The above brief review reveals that the interaction between thermal convection, thermal diffusion, and gravity segregation has yet to be studied. There is also a need for a simple problem formulation with clear physical meaning for the contribution of various mechanisms

The purpose of our work is the study of the variation of composition in oil and gas reservoirs and the investigation of the major mechanisms that affect such a variation. The first step towards this end, is a simple problem formulation with clear physical insight, using a two-component model fluid. The second step is a comprehensive understanding of the interaction between all the mechanisms including thermal diffusion, thermal convection, and segregation using appropriate mathematical techniques. In this paper, the problem formulation is presented, and one-dimensional results are discussed. Subsequent publications will discuss other aspects of the work.

PROBLEM FORMULATION

The continuity equation for each component may be written as,

$$\nabla \cdot \bar{m}_i = -\phi \frac{\partial}{\partial t}(\rho \omega_i) \quad i = 1, 2 \quad (1)$$

where \bar{m}_i is the mass flux of component i , ϕ is the porosity, ρ is the mass density, and ω_i is the mass fraction of component i . In this paper, the formulation will be limited to a two-component system in order to avoid complications which arise from diffusion coefficients in higher component systems. (In binary systems $D_{12} = D_{21}$, where D is the diffusion coefficient, and 1 and 2 are component indices; in ternary and higher component systems D_{ij} and D_{ji} are not in general equal).

The mass flux \bar{m}_i is given by,

$$\bar{m}_i = \rho \omega_i \bar{v} + \bar{J}_i^{(i)} \quad i = 1, 2 \quad (2)$$

where \bar{v} is the mass-average velocity, and $\bar{J}_i^{(i)}$ is the total diffusion mass flux (non-convective) of component i . In Eq. 2 the first term is the convective mass flux. The Darcy equation provides the velocity,

$$\bar{v}_d = -\frac{k}{\mu}(\nabla P + \rho g \nabla z) \quad (3)$$

where k is the permeability, μ is the viscosity and P is the pressure. In the above equation, \bar{v}_d is the overall volumetric velocity (in our judgment, overall-volumetric velocity is the same as the volume-average velocity). According to Bird, Stewart, and Lightfoot (1960), volume-average and mass-average velocities are related by,

$$\bar{v}_d = \bar{v} - \left(\frac{\bar{V}_2}{M_2} - \frac{\bar{V}_1}{M_1} \right) \bar{J}_1^{(1)} \quad (4)$$

In Eq. 4, M is the molecular weight and \bar{V} is the partial molar volume. We question the validity of the above equation (see the derivation and discussion in Appendix A).

Combining Eqs. 1 and 2, and substituting for $\omega_i = x_i n M_i / \rho \omega$,

$$\nabla \cdot (x_i n \bar{v} + \bar{J}_i^{(i)} / M_i) = -\phi \frac{\partial}{\partial t} (x_i n) \quad i = 1, 2 \quad (5)$$

where x_i is the mole fraction and n is total molar density.

The expression for the total diffusive mass flux in a binary system for component 1 is given by (see Bird, Stewart, and Lightfoot, 1960),

$$\bar{J}_1^{(1)} = -(n^2 / \rho) M_1 M_2 D_{12} \left[\left(\frac{\partial \ln f_1}{\partial \ln x_1} \right)_{T,P} \nabla x_1 + \frac{M_1 x_1}{RT} \left(\frac{\bar{V}_1}{M_1} - \frac{1}{r} \right) \nabla P + k_T \nabla \ln T \right] \quad (6)$$

where D_{12} is the molecular diffusion coefficient of components 1 and 2, f is the fugacity, T is the temperature, and k_T is the thermal diffusion ratio of components 1 and 2. The evaluation of k_T is a major task and will be later discussed separately. We assign the positive sign to k_T when component "1" moves to the colder region. This sign convention is the same as used by Bird, Stewart, and Lightfoot.

Three diffusion processes are included in Eq. 6; the first term represents the molecular diffusion, the second term is for pressure diffusion which under the influence of gravity leads to gravity segregation, and the last term represents thermal diffusion. A very interesting feature of Eq. 6 is that in the absence of a temperature gradient, it simplifies to the Gibbs segregation equation (see Appendix B). As was stated before, with thermal diffusion and even without convection, the segregation equation, $d\mu_i = -M_i g dz$, does not hold.

Combining Eqs 5 and 6, one obtains,

$$\nabla \cdot x_1 n \bar{v} - \nabla \cdot \left\{ (n^2 / \rho) M_2 D_{12} \left[\left(\frac{\partial \ln f_1}{\partial \ln x_1} \right)_{T,P} \nabla x_1 + \frac{M_1 x_1}{RT} \left(\frac{\bar{V}_1}{M_1} - \frac{1}{\rho} \right) \nabla P + k_T \nabla \ln T \right] \right\} = -\phi \frac{\partial}{\partial t} (x_1 n) \quad (7)$$

Eq. 7 can be written for component 2, but it is simpler to write Eq. 7 for components 1 and 2 and then by adding them and using the relationship $\bar{J}_1^{(v)} + \bar{J}_2^{(v)} = 0$, one obtains,

$$\nabla \cdot \rho \bar{v} = -\phi \frac{\partial \rho}{\partial t} \quad (8)$$

The following constraint equation,

$$x_1 + x_2 = 1 \quad (9)$$

and the equation of state (EOS),

$$n = P / ZRT \quad (10)$$

complete the formation. We use the Peng-Robinson EOS (Peng and Robinson, 1976) to calculate fugacity derivatives, partial molar volumes, and the density.

In this work, the temperature is assumed to be known. Therefore, there is no need to solve the energy equation. In fact, in hydrocarbon reservoirs the vertical temperature distribution is often available.

For a two - D space (x, z) with two components, there are two unknowns at each point; x_1 and P . There are also two equations; Eqs. 7 and 8. In the event that there is no bulk fluid motion, the equations become first order. For this case, one can write Eq. 7 for components 1 and 2 to obtain both x_1 and P . A simpler alternative is to use $\bar{J}_1^{(v)} + \bar{J}_2^{(v)} = 0$, and the Gibbs-Duhem relationship to obtain $\nabla P = -\rho g \nabla z$ which is valid for both isothermal and nonisothermal conditions. Note that Eq. 3 with $\bar{v}_a = 0$ gives $\nabla P = -\rho g \nabla z$. Use of Eq. 7 and $\nabla P = -\rho g \nabla z$ also provides P and x_1 .

Boundary and Initial Conditions - The boundary conditions in the general case are:

$$J_{1z} = 0 \quad \text{and} \quad v_z = 0 \quad @ \quad z = 0, \quad 0 \leq x \leq l_x \quad (11)$$

$$J_{1z} = 0 \quad \text{and} \quad v_z = 0 \quad @ \quad z = l_z, \quad 0 \leq x \leq l_x \quad (12)$$

$$J_{1x} = 0 \quad \text{and} \quad v_x = 0 \quad @ \quad x = 0, \quad 0 \leq z \leq l_z \quad (13)$$

$$J_{1x} = 0 \quad \text{and} \quad v_x = 0 \quad @ \quad x = l_x, \quad 0 \leq z \leq l_z \quad (14)$$

The above boundary conditions state that the normal velocity and the normal mass flux are zero.

For unsteady state, the initial conditions may be specified as,

$$x_1(t=0, x, z) = x_1^0(x, z) \quad (15)$$

$$P(t=0, x, z) = P^0(x, z) \quad (16)$$

THERMAL DIFFUSION AND GRAVITY SEGREGATION IN ONE-D

We can study the combined effect of thermal diffusion and gravity segregation in one-dimensional vertical direction at steady state by writing $J_{1z}^{(0)} = 0$ and,

$$dP/dz = -\rho g \quad (17)$$

From Eq. 6, one can derive,

$$\frac{dx_1}{dz} = \left(\frac{\partial \ln x_1}{\partial \ln f_1} \right)_{T,P} \left[\frac{M_2/\bar{V}_2 - M_1/\bar{V}_1}{1/(x_1\bar{V}_1) + 1/(x_2\bar{V}_2)} \frac{g}{RT} - k_T \frac{d \ln T}{dz} \right] \quad (18)$$

by using $\rho = \left(\sum_{i=1}^2 x_i M_i \right) / \left(\sum_{i=1}^2 x_i \bar{V}_i \right)$. These two equations provide x_1 and P by employing a numerical scheme, say Euler's scheme. Only pressure and composition at a given depth should be specified. Vertical temperature gradient has also to be specified. The PR-EOS can be used to calculate $(\partial \ln x_1 / \partial \ln f_1)_{T,P}$, \bar{V}_1 , \bar{V}_2 , and ρ . In the following, the results of several numerical examples will be presented. These examples will illustrate the contribution of gravity and thermal diffusion to vertical composition variation.

C₁-C₃ Column

Figs. 1, 2, and 3 provide the composition vs. depth for the C₁/C₃ binary system in the single phase state. The temperature gradient in this and subsequent examples is 1 °C/30.5 m.

Fig. 1 shows the composition variation for methane along the length of a liquid column of 610 m. The composition, pressure, and temperature at zero depth are fixed at 30 percent methane, 7.24 MPa, and 72.8 °C, respectively. The calculated results presented in the figure reveal that gravity segregation at isothermal conditions is pronounced (when gravity alone is considered, temperature is held constant.) The thermal diffusion at nonisothermal conditions causes a further increase in the variation of composition with depth. Fig. 2 presents the composition variation vs. the depth for a fluid in a gas state away from the critical point. The composition, pressure and temperature at depth=0 are 33.5 percent methane, 4.05 MPa, and 7.28 °C, respectively. This figure reveals that thermal diffusion has a very significant effect on the composition change with depth. Fig. 3 depicts the variation of composition with depth for a binary liquid mixture away from the critical point. In this case, gravity exerts only mild effect. The combination of thermal diffusion and gravity results in a weak change of composition with depth. Note that thermal diffusion reduces the compositional variation.

For the fluid system of Fig. 1, the calculated thermal diffusion factor, $\alpha(k_T = \alpha x_1 x_2)$, at depth=0 is 16.5 and decreases rapidly to 0.5 at depth=152 m, and remains nearly constant at this value for depth>152 m. For the fluid system of Fig. 2, the calculated $\alpha = 6$ at depth=0; it

increases very slowly to $\alpha \approx 6.7$ at depth= 600 m. For the fluid system of Fig. 3, at depth= 0, the calculated $\alpha \approx -2$ and increases gradually to zero at depth= 600 m.

C₁-C₄ Column

Fig. 5 provides the variation of methane composition vs. depth for a liquid mixture of C₁/nC₄. The composition, pressure, and temperature at depth= 0 are 49 mole percent C₁, 19.3 MPa, and 71.1°C, respectively. Measured α data are available for this system. As we will discuss later, the calculated α 's are adjusted for the C₁/nC₄ system to decrease the difference between the calculated results and measured data. The composition at the top, depth= 0, is selected such that the system is away from the critical region. Fig. 5 shows that the gravity results in segregation, as expected. However, thermal diffusion weakens the segregation to the extent that methane concentration increases with depth. The thermal diffusion factor used in the calculations varies from $\alpha = -3$ at depth= 0 to $\alpha = -2.1$ at depth= 600 m in an almost linear fashion.

C₁-C₁₀ Column

Fig. 6 presents the result for a binary liquid mixture of C₁/nC₁₀ away from the critical point. Gravity results in segregation, but thermal diffusion in combination with gravity provides an increase of the light component, methane, with depth. The composition, pressure, and temperature at depth= 0 are chosen as 50 mole percent methane, 20.7 MPa, and 71.1 °C, respectively. Fig. 7 provides the pressure composition profile as well as the C₁/nC₁₀ phase diagram at 71.1 °C. At depth= 0, the calculated $\alpha = -3.9$; it increases gradually to about -3.2 at depth= 600 m.

C₇-C₁₆ Column

Several binary mixtures of two heavy hydrocarbons are also studied. For all of those systems, gravity may cause a weak segregation. The thermal diffusion effect is also weak. Fig. 8 provides the results for the nC₇-nC₁₆ binary liquid mixture. At depth=0, nC₇ is 75 mole percent, pressure=13.8 MPa, and temperature=35 °C. The combined effect of gravity and thermal diffusion provides a mild decrease of C₇ with depth. Note that for the gravity mechanism, the mole fraction of the lighter component (i.e., C₇) does increase with depth which suggests that molecular weight alone may not cause segregation; the partial molar volume is also important. Thermal diffusion factor, $\alpha \approx 0.9$, at depth=0, and decreases to $\alpha = 0.7$ at depth =600 m.

In addition to the results presented in Figs. 1-8, calculation for other hydrocarbon binary systems revealed that as the critical region is approached both the gravity and thermal diffusion strongly affect composition variation. For thermal diffusion, one could expect either an increase or a decrease of the lighter component with depth.

ESTIMATION OF THERMAL DIFFUSION RATIO

In this section, we will, in some detail, review the work on the estimation of thermal diffusion ratio, k_T . Experimental measurements of the thermal diffusion ratio are somewhat sparse, even for binary mixtures. This is especially the case for typical reservoir conditions of elevated temperature and pressure. Furthermore, due to the relatively recent application of

this theory to hydrocarbon reservoir fluids, a corresponding database of measurements has not yet been accumulated. Finally, such measurements are difficult to make, due to the small magnitude of the phenomena as well as the possible obscuring effect of thermal convection, and are thus subject to uncertainty. Even the sign of k_T is uncertain, since it can be difficult to predict *a priori* based on molecular structure, even for binary systems, whether a component will drift with or against the thermal gradient (Jones and Foreman (1953), Jones and Milberger (1955)). It is necessary, therefore, to rely on theoretical calculations for k_T . While these formulas are subject to uncertainty, especially in the absence of corroborating experimental measurements, they represent the only estimates of k_T for some systems under reservoir conditions. The models described in the literature appear to fall into two major groups. The first is based on Dougherty and Drickamer's early work and attempts to find a value for the thermal diffusion factor, $\alpha = k_T/(x_1x_2)$ in terms of the specific heats of transport of the two components in a binary mixture. These, in turn, are estimated from the "activation energy of molecular motion" which can be obtained from the viscosity behavior of the mixture. Similar approaches have been followed later by other investigators (Tichachek, Kmack and Drickamer (1956), Whittaker and Pigford (1958)). The second main line of investigation considers the maximization of the partition function of an idealized two-bulb thermal diffusion apparatus (Haase (1969), Kempers (1989)). This yields an expression for α in terms of either the enthalpy difference from the standard state of the components along with a value of α at low densities (which may be obtained from kinetic theory) in the case of Haase's work, or the absolute enthalpies only (Kempers). Holt et al., and Belery and da Silva have employed the first method. It is difficult to obtain experimental values for derivatives of viscosity with respect to temperature and pressure, but they may be calculated in a straightforward manner from a viscosity model, although existing viscosity models may not be reliable.

The Dougherty and Drickamer formula, as mentioned previously, expresses α in terms of the specific heats of transport ΔU_1^* and ΔU_2^* , for components 1 and 2 respectively, as follows,

$$\alpha = \frac{M_1\bar{V}_2 + M_2\bar{V}_1}{2(M_1x_1 + M_2x_2)x_1} \left(\frac{\Delta U_2^*}{\bar{V}_2} - \frac{\Delta U_1^*}{\bar{V}_1} \right) \left(\frac{\partial x_1}{\partial \mu_1} \right)_{T,P} \quad (19)$$

The heats of transport are related to the activation energy for molecular movement as follows,

$$\Delta U_i^* = \left(\frac{\partial(n\Delta U_m^*)}{\partial n_i} \right)_{T,P,n_j} \quad (20)$$

where ΔU_m^* is the total activation energy, and n and n_i are total number of moles and number of moles of component i , respectively. (ΔU_m^* is a function of viscosity and PVT behavior of the fluid system). This allows the use of the presumably more accurate mixture rather than pure component values for the evaluation of ΔU_i^* . In a similar way, analytical expressions for these terms can be derived from the appropriate equation of state and viscosity models once they have been selected.

The expression for the thermal diffusion factor from Kempers for a binary mixture is,

$$\alpha = \frac{\bar{V}_1 \bar{H}_2 - \bar{V}_2 \bar{H}_1}{(\bar{V}_1 x_1 + \bar{V}_2 x_2) x_1 \left(\frac{\partial \mu_1}{\partial x_1} \right)_{T,P}} \quad (21)$$

where \bar{H}_1 and \bar{H}_2 are the partial molar enthalpy of components 1 and 2. We have used the above equation to compute the thermal diffusion factor of binary hydrocarbon mixtures. The PR-EOS and the correlations by Paussat and Danner (1972) were used to calculate partial molar enthalpies. The subscript 1 refers to methane or the light component, and the sign convention is as described above. The experimental values of α , quoted by Kempers for the C₁-C₃ system are especially relevant to this study.

Fig. 9 shows the calculated results and data for C₁/C₃ at 72.8 °C and 5.59 MPa. In our calculations, the PR-EOS was used and the interaction coefficients between C₁ and C₃ was set at 0.01. Kempers used the Soave-EOS (Soave, 1972) but did not provide the parameters of this equation of state. Fig. 9 reveals that the version of the Soave-EOS used by Kempers provides better results than the PR-EOS. The data presented in Fig. 9 pertain to the gas state.

Fig. 10 depicts the results of calculations and data for the above system for a mixture containing 0.34 mole fraction methane at 72.8 °C vs. pressure. The calculated values by Kempers in the pressure range of 4.14 to 5.52 MPa are in better agreement with data than our calculated values using the PR-EOS. However, the calculated values by Kempers for pressure > 6.9 MPa are very different from data. Our calculated value at 7.75 MPa is in agreement with the data while Kempers' is off by an order of magnitude. It is possible that Kempers adjusted some parameters of the EOS; as a result, the high pressure values are predicted unreliably. Fig. 11 shows the phase envelope for the C₁/C₃ system at 72.8 °C. The data points are also shown on the figure. It is clear that some of the data points are in the two-phase region. Kempers used the Soave-EOS to calculate the thermal diffusion factor in the two-phase region. The two-phase state was not apparently recognized.

In order to further examine the reliability of the Kempers method, thermal diffusion factors for the C₁/nC₄ system were calculated. Rutherford and Root (1959) report experimental data for two compositions, one fluid system with a methane composition of 40 percent and another with a methane content of 49 percent at various pressures and temperatures. The calculated results and data are compared in Figs. 12 and 13. The interaction coefficient between C₁ and nC₄ was set equal to 0.027 in the PR-EOS. It is clear that the calculations are very different from the data. Even the sign is not the same. For the results presented in Fig. 5, the calculated α values were multiplied by 0.6 to bring them closer to the data.

Fig. 14 shows the thermal diffusion factor of nC₇-nC₁₆ liquid system at 35 °C and atmospheric pressure. The data are from Shieh (1969). This figure reveals that unlike the C₁/C₃ system, the variation of α with the composition is small. This figure also reveals that there is a fair agreement between data and predicted results from the PR-EOS.

Fig. 15 shows a comparison of Trevoy and Drickamer's (1949) data and calculated results of thermal diffusion factor for various hydrocarbon binary systems. In general, the agreement is fair except for C₇/C₁₄ and C₇/C₁₅ systems. Note that the sign is calculated properly.

For the above calculations, we used the PR-EOS without the volume translation; with volume translation, the results did not improve. On the whole, the calculation of partial molar volumes is very sensitive to the accuracy of the EOS to density predictions.

DISCUSSION AND CONCLUSIONS

One important parameter for the calculation of thermal diffusion is the thermal diffusion factor, α . Measured values of α are severely limited. The theory for the calculation of this parameter needs major improvement. In this paper, we have presented the results for calculating α using the most recent model. The examination of other models also gave unsatisfactory results.

Based on the measured thermal diffusion factors for the C_1/C_3 and C_1/nC_4 systems, it is very likely that α for the fluid systems of our interest could undergo a sign change for different conditions of compositions, pressure, and temperature.

The main conclusions derived from this paper are:

1. Gibbs criterion of segregation can be derived from the expression of the total diffusion flux at constant temperature. For nonisothermal conditions, Gibbs criterion of equilibrium cannot be invoked.

2. The Darcy velocity is the volume-average velocity. The velocity in the diffusion expression is often expressed in terms of mass-average or molar-average velocities. Therefore, one has to relate volume-average and mass-average velocities.

3. Thermal diffusion can both enhance and weaken the segregation in a hydrocarbon column.

ACKNOWLEDGMENT

We thank Sezai Ucan for his help in preparation of some of the graphs and calculations and Dr. Michael Riley for fruitful discussions on some of the concepts presented in this paper. This research was supported by the members of the research consortium on fractured and layered reservoirs of the Reservoir Engineering Research Institute and the US DOE grant DE-FG22-93BC14875. Their support is greatly appreciated.

NOMENCLATURE

- D - Molecular diffusion coefficient
- f_i - Fugacity of component i
- \bar{H}_i - Partial molecular molar enthalpy of component i
- $\bar{J}_i^{(0)}$ - Total diffusion mass flux of component i
- k - Permeability
- k_T - Thermal diffusion ratio

- l_x - Length in the x direction
- l_z - Length in the z direction
- M_i - Molecular weight of component i
- \bar{m}_i - Mass flux of component i
- n - Molar density (total), also total number of moles
- n_i - Molar density of component i, also number of moles of component i
- R - Gas constant
- P - Pressure
- T - Temperature
- \bar{v} - Mass-average velocity
- \bar{v}_i - Velocity of component i
- \bar{v}_d - Volume-average velocity or Darcy velocity
- \bar{v}_* - Molar-average velocity
- \bar{V}_i - Partial molar volume of component i
- x_i - Mole fraction of component i
- x - Spacial x-coordinate
- z - Spacial z-coordinate
- Z - Supercompressibility factor

GREEK LETTERS

- α - Thermal diffusion factor
- ΔU_i^* - Specific heat of transport of component i
- ΔU_m^* - Specific heat of transport of mixture
- ∇ - Vector operator, "nabla" or "del"
- μ - Viscosity
- μ_i - Chemical potential of component i
- ρ - Mass density (total)
- ρ_i - Mass density of component i
- ϕ - Porosity
- ϕ_i - Volume fraction of component i
- ω_i - Mass fraction of component i

SUPERSCRIPT

- \circ - Reference point

REFERENCES

1. Belery, P. and da Silva, F.V.: "Gravity and Thermal Diffusion in Hydrocarbon Reservoirs," Third North Sea Chalk Research Symposium, Copenhagen, June 11-12, 1990.
2. Bird, R.B., Stewart, W.E., and Lightfoot, E.N.: "Transport Phenomena," John Wiley and Sons, Inc. (1960) Part III.
3. Dougherty, E.L., and Drickamer, H.G.: "Thermal Diffusion and Molecular Motion in Liquids," J. Phys. Chem. (May 1955) 443-449.
4. Faissat, B., Knudsen, K., Stenby, E. H., and Montel, F.: "Fundamental Statements about Thermal Diffusion for a Multicomponent Mixture in a Porous Medium," Fluid Phase Equilibria (1994) 209-222.
5. Haase, R.: "Thermodynamics of Irreversible Processes," Addison-Wiley, (1969) Chapter 4.
6. Hamoodi, A.N., Abed, A.F., and Firoozabadi, A.: "Composition Modeling of Two-Phase Hydrocarbon Reservoirs," SPE 36244 paper to be presented at the 7th Abu Dhabi International Petroleum Exhibition and Conference, Abu Dhabi, UAE, Oct. 133-16, 1996.
7. Holt, T., Linderberg, E., and Ratkje, S.: "The Effect of Gravity and Temperature Gradients on Methane Distribution in Oil Reservoirs," SPE 11761, Unsolicited Paper, SPE, Richardson, TX, 1983.
8. Jacquemin, D.: "Interaction of Natural Convection and Gravity Segregation in Oil/Gas Reservoirs," SPE Reservoir Engineering J. (May 1990) 233-238.
9. Jones, A.L., and Foreman, R.W.: "Liquid Thermal Diffusion of Tall Oil," Ind. and Eng. Chem. (Sep, 1952) Vol. 44, No. 9, 2249-2253.
10. Jones, A.L., and Milberger, E.C.: "Separation of Organic Liquid Mixtures by Thermal Diffusion," Ind. and Eng. Chem. (Dec., 1953), Vol. 45, No. 12, 2689-2696.
11. Kempers, L.J.T.: "Thermodynamic Theory of the Soret Effect in a Multicomponent Liquid," J. Chem. Phys. (June 1989), Vol. 90, No. 11, 6541-6548.
12. Lira-Galeana, C., Firoozabadi, A., and Prausnitz, J.M.: "Computation of Compositional Grading in Hydrocarbon Reservoirs: Application of Continuous Thermodynamics," Fluid Phase Equilibria (Dec. 1994) 143-158.
13. Paussat, C.A., and Danner, R.P.: "Correlation of Ideal Gas Enthalpy, Heat Capacity, and Entropy," Ind. Eng. Chem. Proc. Res. Dev. (1972) Vol. 11, No. 4, 543-546.
14. Peng, D.Y., and Robinson, D.B.: "A New Two-Constant Equation of State," Ind. & Eng. Chem. (1976) Vol. 15, No. 1, 59-64.
15. Rutherford, W.M., and Roof, J.G.: "Thermal Diffusion in Methane-n-Butane Mixtures in the Critical Region," J. of Phys. Chem. (Sept. 1959) Vol. 63, 1506-1522.
16. Sage, B.H., and Lacey, W.N.: "Volumetric and Phase Behavior of Hydrocarbons," Stanford University Press (1949) Chapter VIII.
17. Shieh, J.J.C.: "Thermal Diffusion and Segmental Motion in Binary n-Alkane systems," J. of Phys. Chem. (1969), Vol. 73, No. 5, 1508-1513.
18. Soave, G.: "Equilibrium Constants from a Modified Redlich-Kwong Equation of State," Chem. Eng. Sci. (1972) Vol. 27, 1197-1203.
19. Tichacek, L.J., Knack, W.S. and Drickamer, H.G.: "Thermal Diffusion in Liquids; The Effect of Non-ideality and Association," J. Phys. Chem. (May 1956) 660-665.

20. Trevo, D.L., and Drickamer, H.G.: "Thermal Diffusion in Binary Liquid Mixtures," J. of Chem. Phys. (1949), Vol. 17, No. 11, 1120-1124.
21. Whitaker, S., and Pigford, R.L.: "Thermal Diffusion in Liquids, Measurements and a Molecular Model," Ind. and Eng. Chem. (July 1958) Vol. 50, No. 7, 1026-1032.

Appendix A: Mass- and Volume-Average Velocities

In binary and higher component mixtures, when various diffusion processes occur, and the chemical species are moving at different velocities, \bar{v}_i , one may define: 1) mass-average velocity, $\bar{v} = \sum \omega_i \bar{v}_i$, 2) molar-average velocity, $\bar{v}_* = \sum x_i \bar{v}_i$, and 3) volume-average velocity, $\bar{v}_d = \sum \phi_i \bar{v}_i$. The symbol ϕ_i represents the volume fraction. Bird, Stewart, and Lightfoot (1960) define the volume fraction of component i by (see Example 16.K3, page 518),

$$\phi_i = (\rho_i / M_i) \bar{V}_i \quad (\text{A-1})$$

where ρ_i is the mass density of component i . We question the validity of Eq. (A-1) for the representation of volume fraction, as we will explain shortly. In our understanding, the velocity given by the Darcy equation is the volume-average velocity. The volume-average velocity or the Darcy velocity is well defined as long as the volume fraction of species " i " is well defined. Note that when all species have the same velocity, $\bar{v} = \bar{v}_d = \bar{v}_*$.

Assuming that Eq. (A-1) is valid and noting that $v_d = \sum \phi_i \bar{v}_i$, the Darcy velocity is given by:

$$\bar{v}_d = \sum (\rho_i / M_i) \bar{V}_i \bar{v}_i \quad (\text{A-2})$$

The velocity of component " i " can be obtained from,

$$\bar{v}_i = \bar{v} + \bar{J}_i^{(i)} / \rho_i \quad (\text{A-3})$$

Combining Eqs. (A-2) and (A-3),

$$\bar{v}_d = \bar{v} \left(\sum \frac{\rho_i \bar{V}_i}{M_i} \right) - \sum \bar{J}_i^{(i)} \left(\frac{\bar{V}_i}{M_i} \right) \quad (\text{A-4})$$

By using the relationship $\sum (\rho_i \bar{V}_i) / M_i = 1$, Eq. 4 of the text is obtained.

The following example highlights the difference between various average velocities. Consider a mixture of 60 weight percent methane (C_1) and 40 weight percent propane (C_3) at 6.90 MPa and 37.8 °C for which the x -direction velocities of C_1 and C_3 are $V_{c_1} = 0.30$ m/day and $V_{c_3} = -0.30$ m/day. The partial molar volume of C_1 and C_3 in the above system are 0.359 and 0.0822 m³/kgmole, respectively (Sage and Lacey, 1949). The various average velocities in the x -direction are then $v_x = -0.244$ m/day, $v_{*x} = -0.162$ m/day, and $v_{dx} = -0.134$ m/day. There is an appreciable difference between these velocities. While there is no ambiguity in the calculation of \bar{v} and \bar{v}_* , the value of \bar{v}_d is based on calculated volume fractions of C_1 and C_3 from Eq. (A-1). For this example, Eq. (A-1) provides $\phi_{c_1} \approx 0.95$ and

$\phi_{c_3} = 0.05$ volume fractions. The low value of ϕ_{c_3} is unjustified because, in reality, the propane component takes up a larger volume fraction in the mixture. \bar{V}_{c_3} can be even negative which implies that volume fraction can be negative. In view of such an unphysical value, one should try to explore other methods for the calculation of volume fractions.

Appendix B: Derivation of Thermodynamic Equilibrium Expression from Total Diffusion Flux Expression

Let's write the expression for the total diffusion mass flux of component 1 (i.e., Eq. 6) in the z-direction for isothermal conditions,

$$J_{1z}^{(t)} = -\left(\frac{n^2}{\rho}\right) M_1 M_2 D_{12} \left[\left(\frac{\partial \ln f_1}{\partial \ln x_1} \right)_{T,P} \frac{\partial x_1}{\partial z} + \frac{M_1 x_1}{RT} \left(\frac{\bar{V}_1}{M_1} - \frac{1}{\rho} \right) \frac{\partial P}{\partial z} \right] \quad (\text{B-1})$$

At stationary state, $J_{1z} = 0$, and therefore,

$$\left(\frac{\partial \ln f_1}{\partial \ln x_1} \right)_{T,P} \frac{dx_1}{dz} + \frac{M_1 x_1}{RT} \left(\frac{\bar{V}_1}{M_1} - \frac{1}{\rho} \right) \frac{dP}{dz} = 0 \quad (\text{B-2})$$

Combining Eq. B-2 and the relationships $\frac{dP}{dz} = -\rho g$ and $\left(\frac{\partial \ln f_1}{\partial \ln x_1} \right)_{T,P} = x_1 \left(\frac{\partial \ln f_1}{\partial x_1} \right)_{T,P}$,

$$\left(\frac{\partial \ln f_1}{\partial x_1} \right) \frac{dx_1}{dz} + \frac{g}{RT} (M_1 - \rho \bar{V}_1) = 0 \quad (\text{B-3})$$

or

$$\left(\frac{\partial \ln f_1}{\partial x_1} \right)_{T,P} \frac{dx_1}{dz} = \frac{g}{RT} (\rho \bar{V}_1 - M_1) \quad (\text{B-4})$$

Eq. B-4 can be expressed in terms of the chemical potential,

$$(d\mu_1 = RT d \ln f_1)_T \quad (\text{B-5})$$

as,

$$\left(\frac{\partial \mu_1}{\partial x_1} \right)_{T,P} \left(\frac{dx_1}{dz} \right) = g(\rho \bar{V}_1 - M_1) \quad (\text{B-6})$$

Eq. (B-6) can also be written for component 2. These two equations will provide pressure and composition at any depth once pressure and composition at a reference depth are specified. Eq. (B-6) can be derived from $d\mu_i = -M_i g dz$ by expanding $d\mu_i(P, x_1)$ and using $dP = -\rho g dz$.

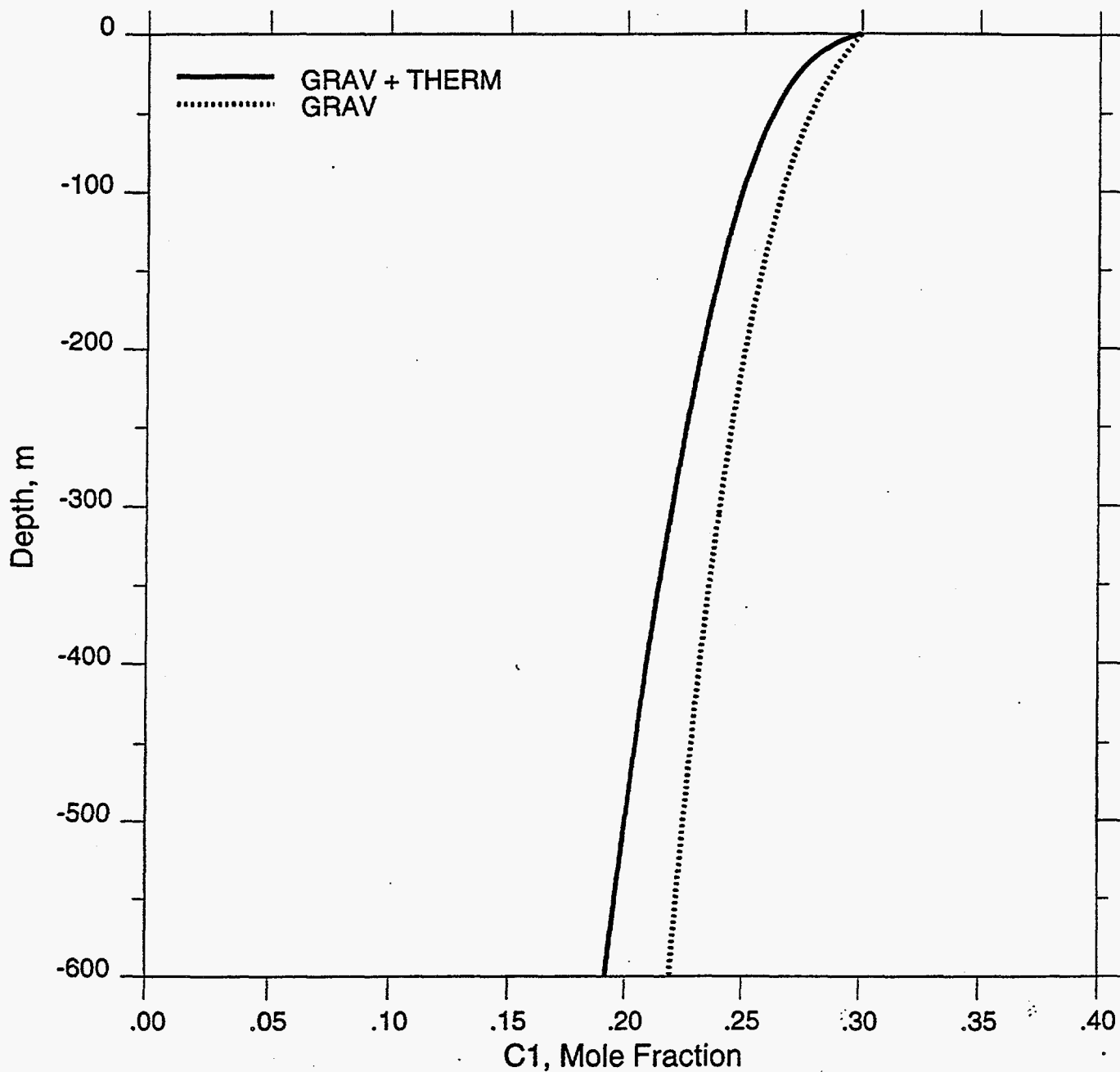


Fig.1- Depth vs. composition for a C1/C3 system in the liquid state
($P=7.24$ MPa, $T=346$ K @ depth=0).

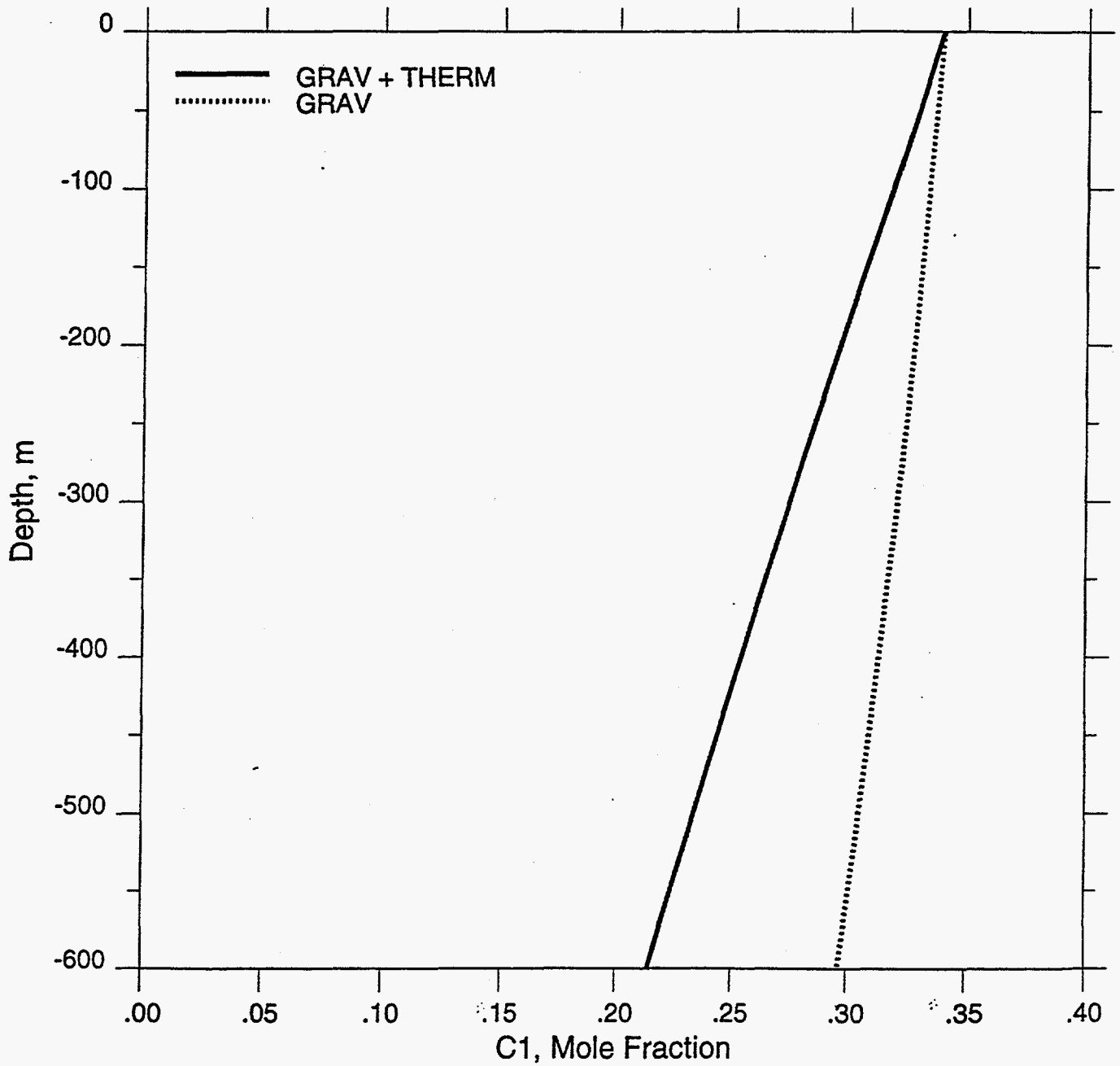


Fig.2- Depth vs. composition for a C1/C3 system in the gas state
(P=4.05 MPa, T=346K @ depth=0).

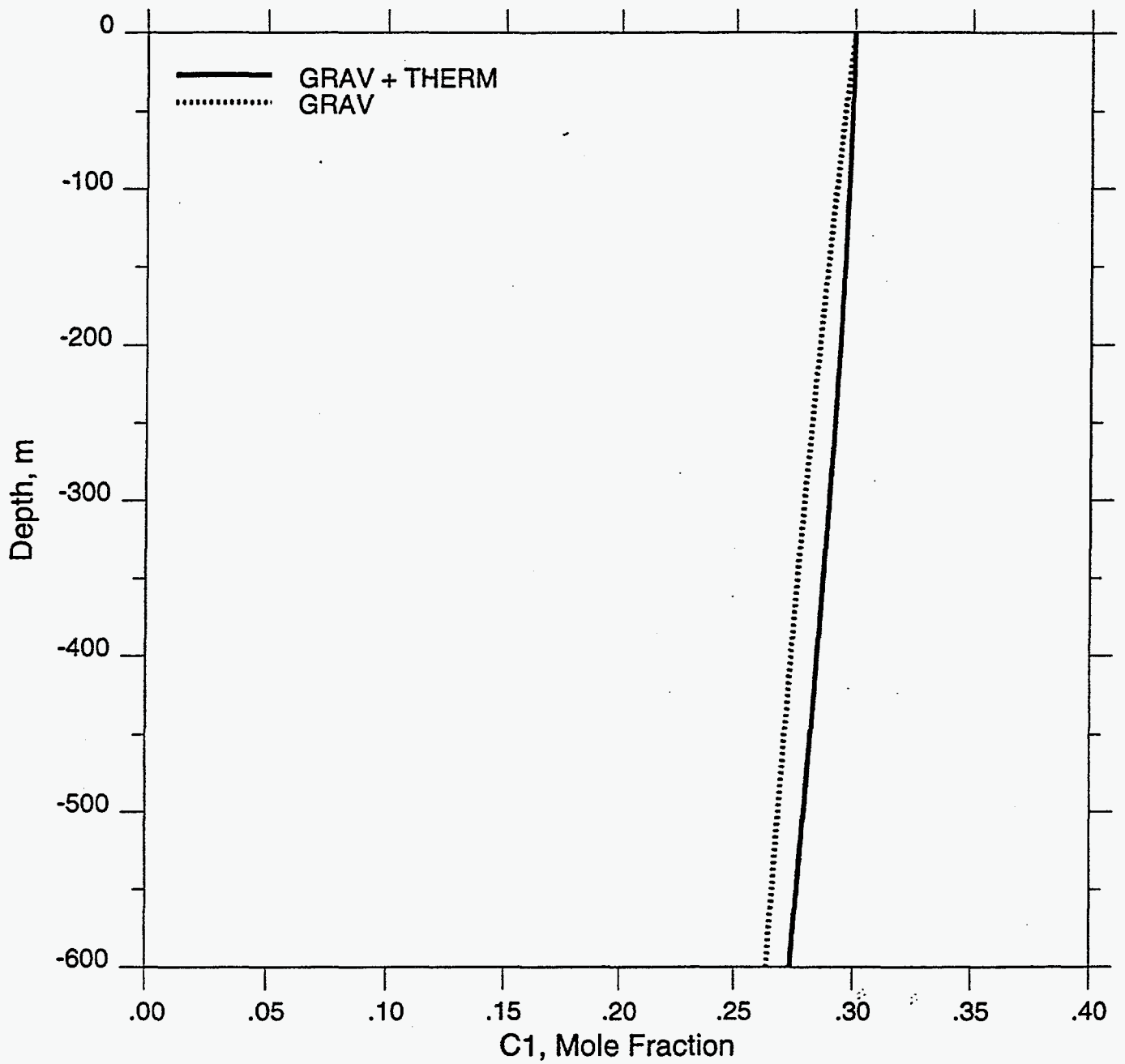


Fig.3- Depth vs. composition for the C1/C3 system in the liquid state
($P=10.3$ MPa, $T=346$ K @ depth=0).

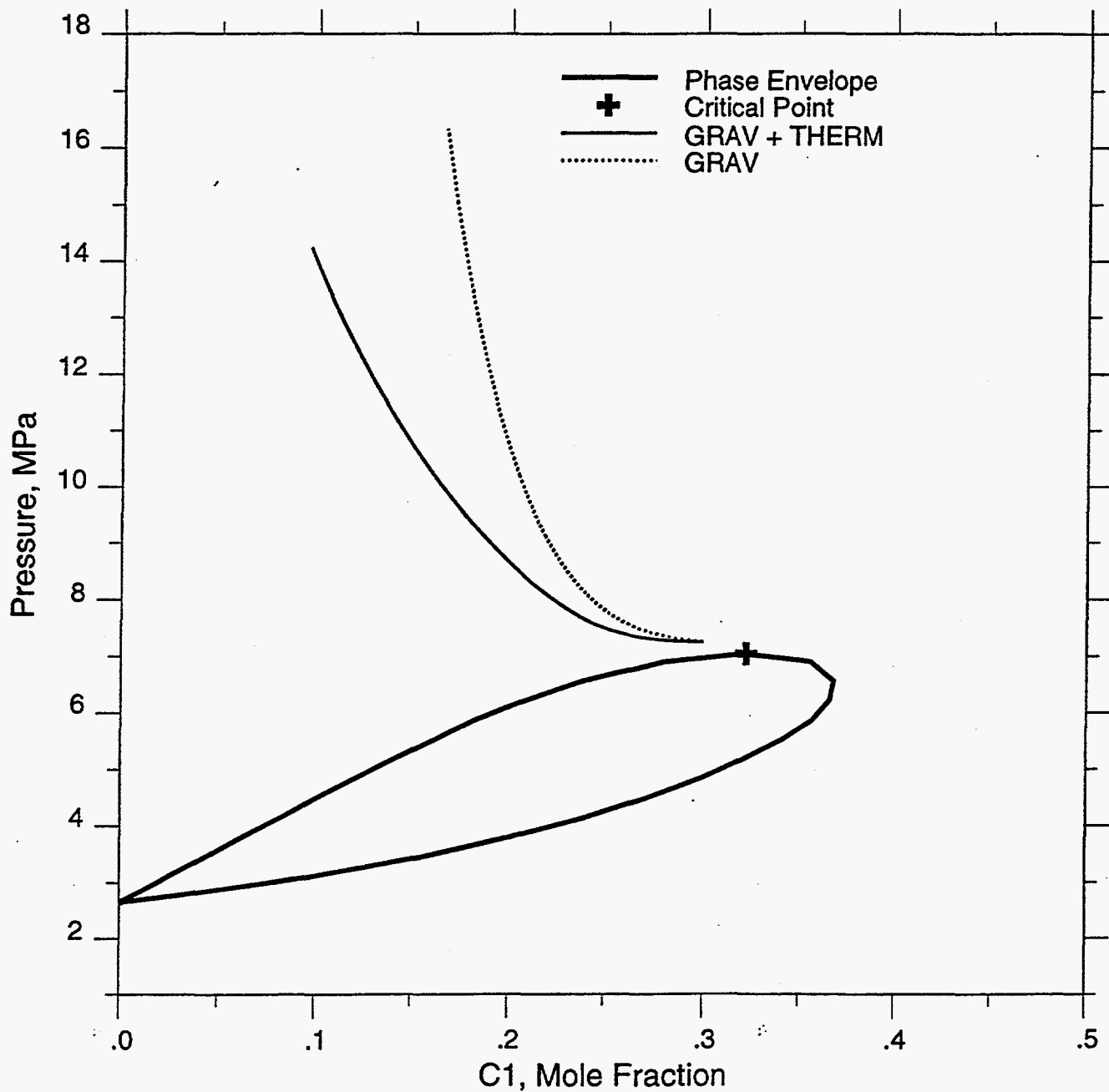


Fig.4- Phase envelope for the C1/C3 system at T=346 K, and pressure-composition relationship for the example of Fig. 1.

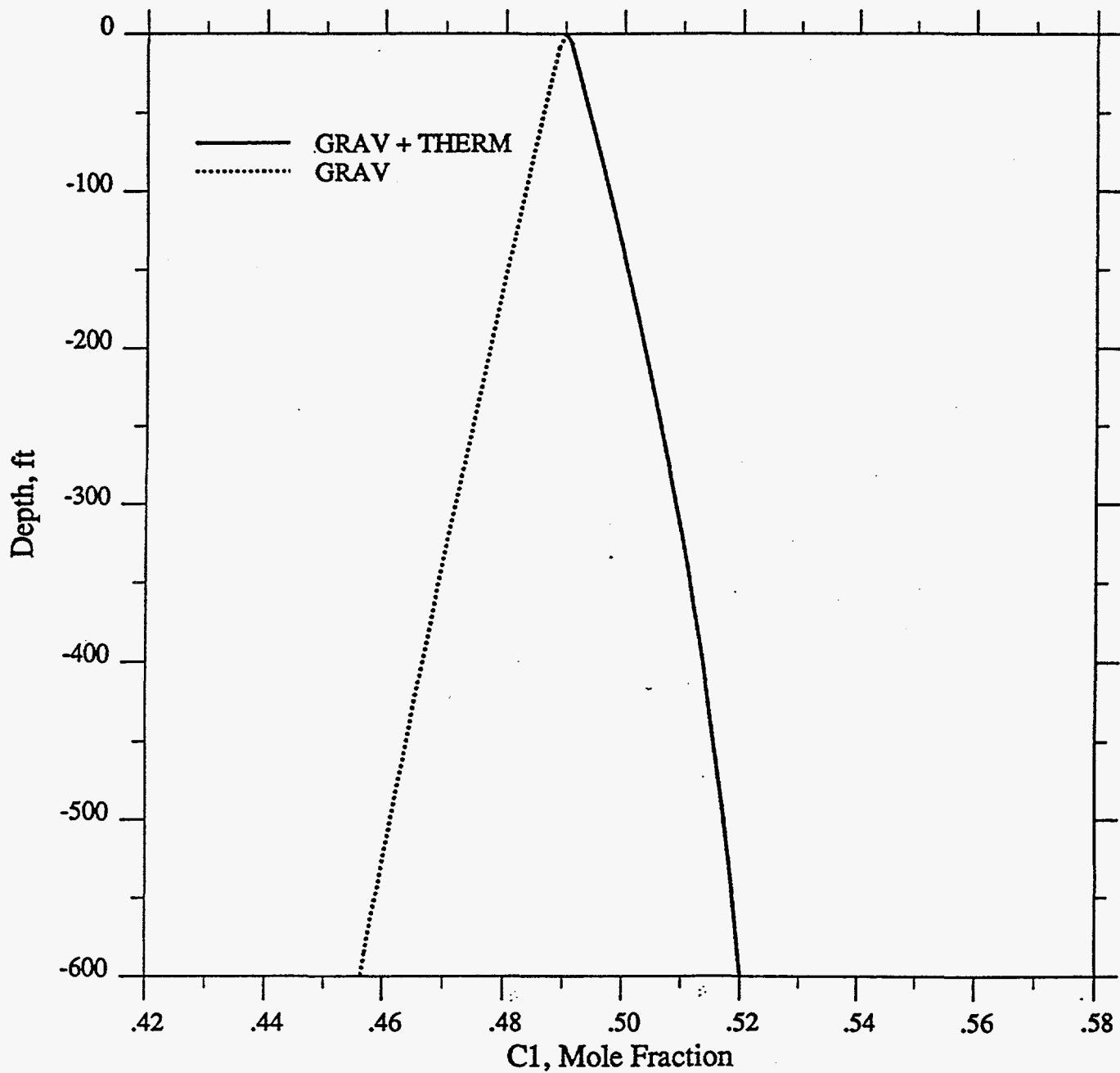


Fig. 5- Depth vs. composition for the C1/nC4 system in the liquid state (P=19.3 MPa, T=334 K @ depth=0).

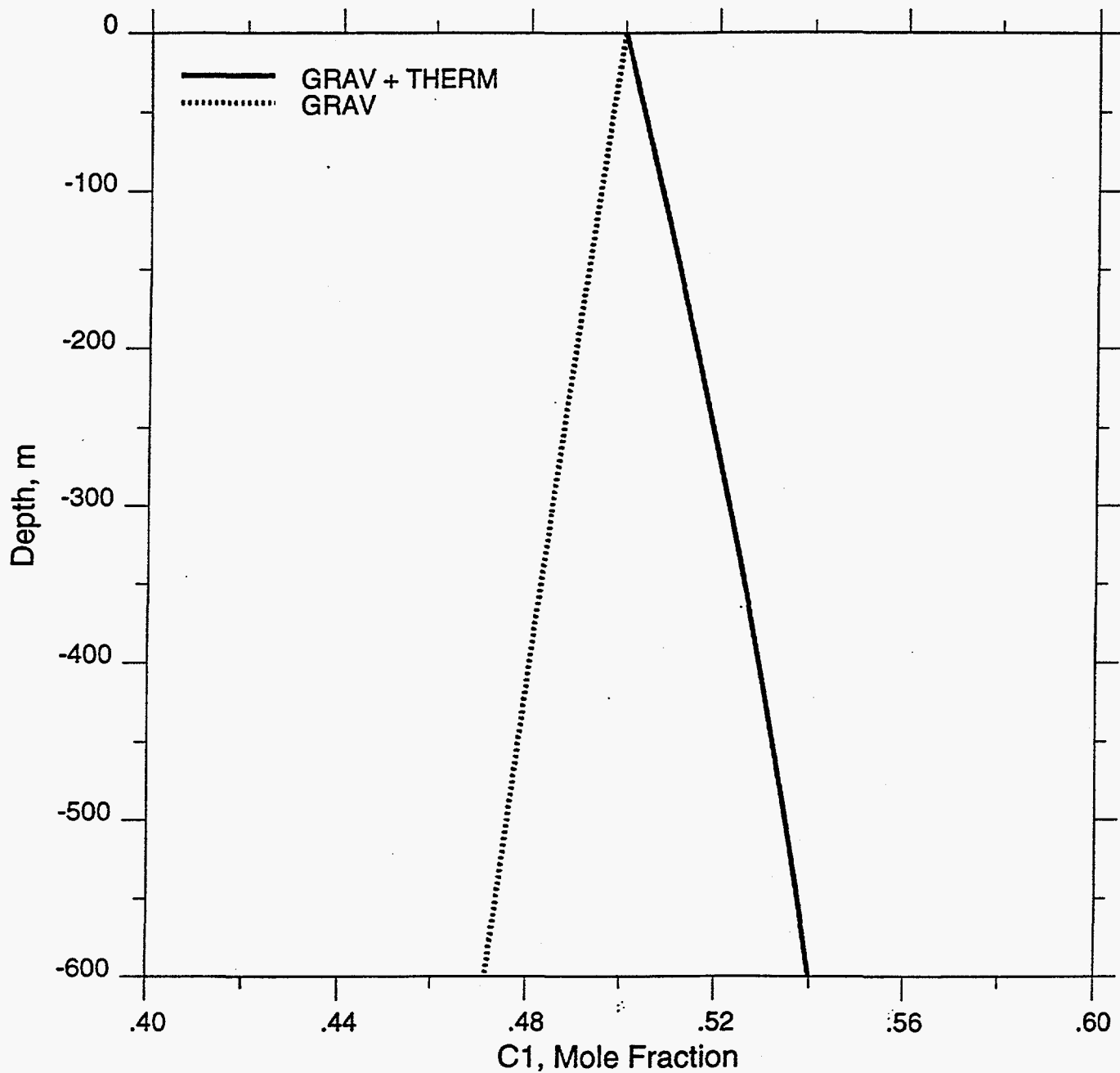


Fig.6- Depth vs. composition for the C1/nC10 system in the liquid state (P=20.7 MPa, T=346 R @ depth=0).

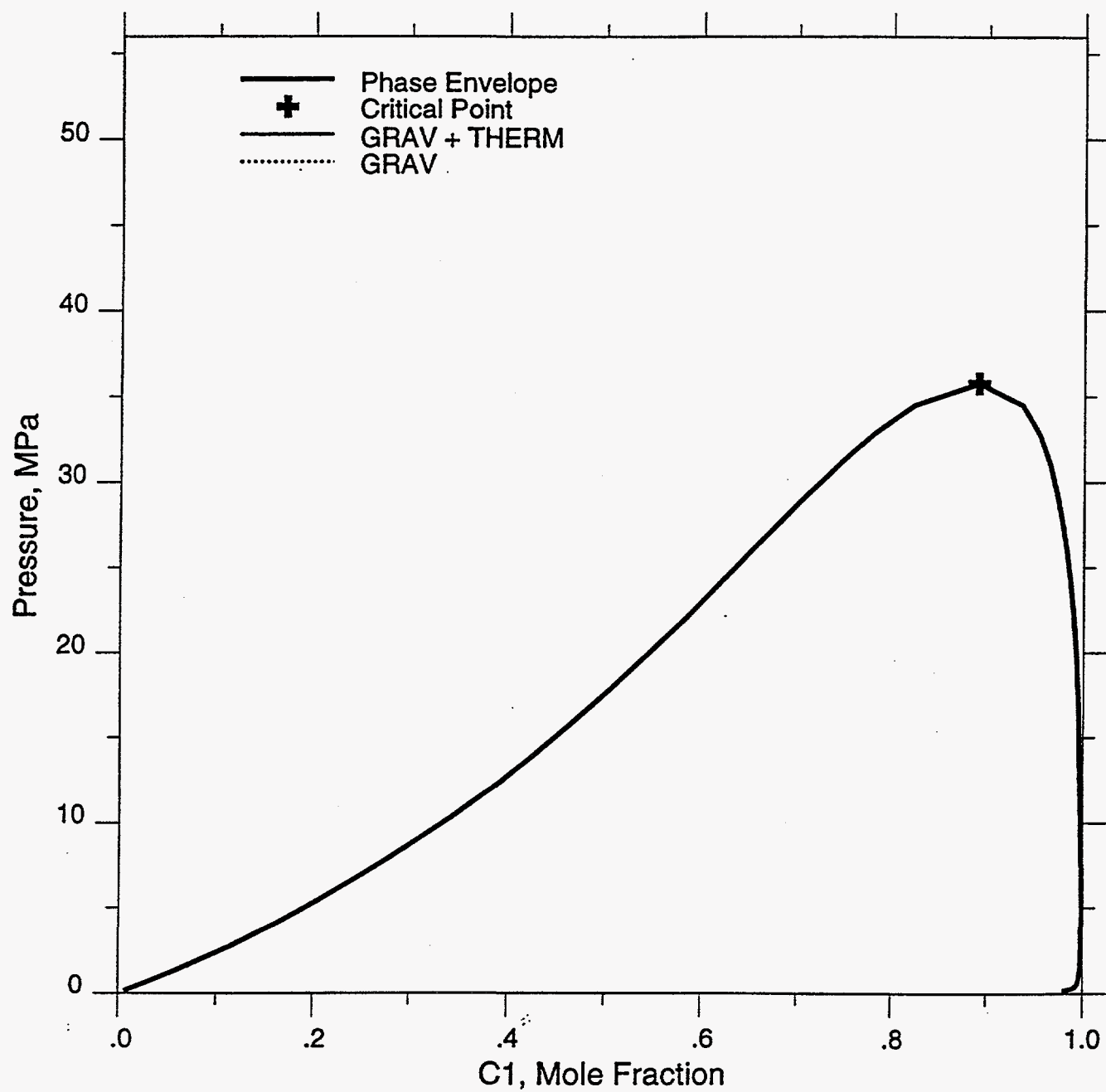


Fig.7- Phase envelope for the C1/nC10 system at T=344 K and pressure-composition relationship for the example of Fig. 6.

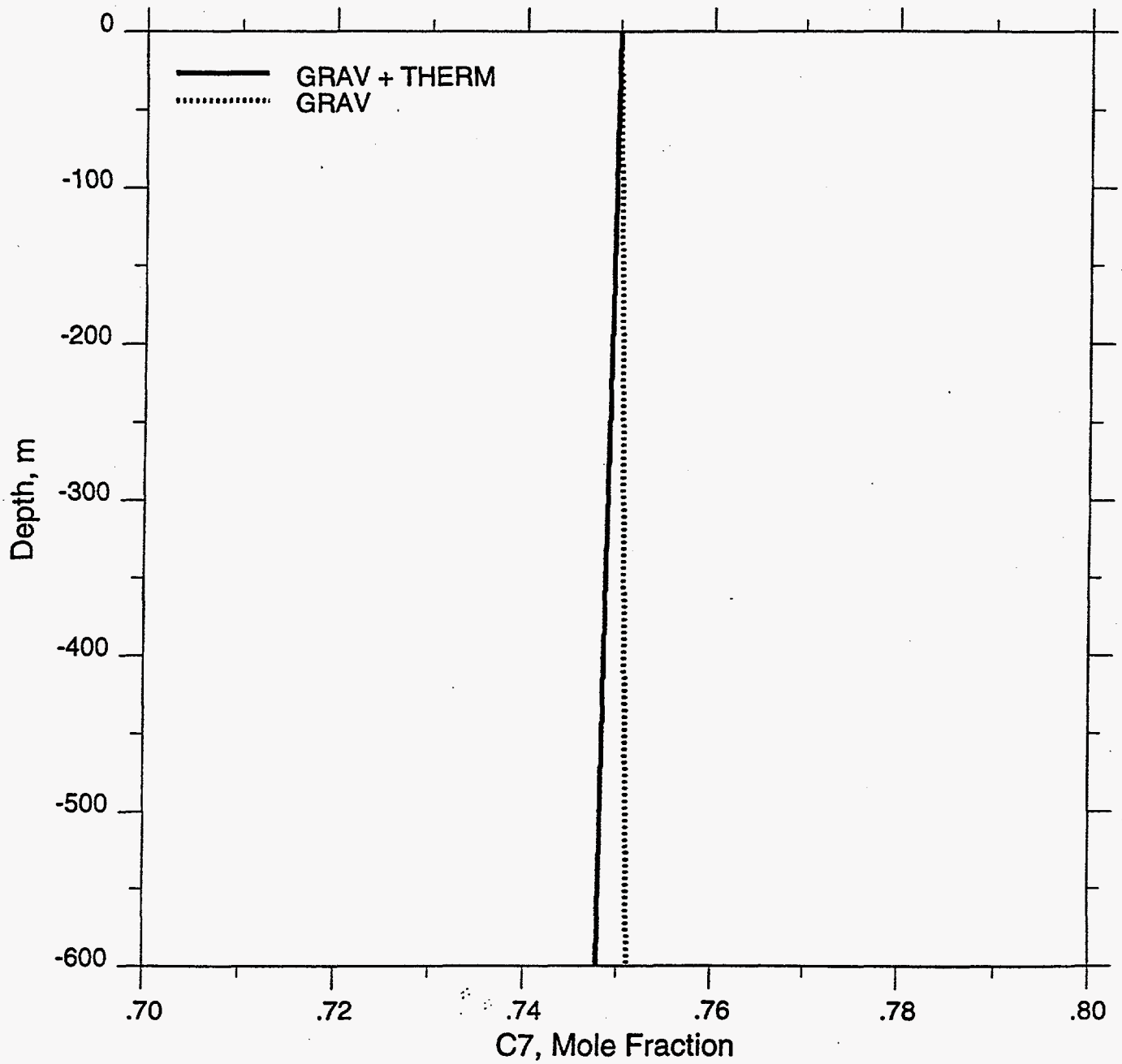


Fig.8- Depth vs. composition relationship for the nC7/nC16 liquid system (P=13.8 MPa, T=308 K @ depth=0).

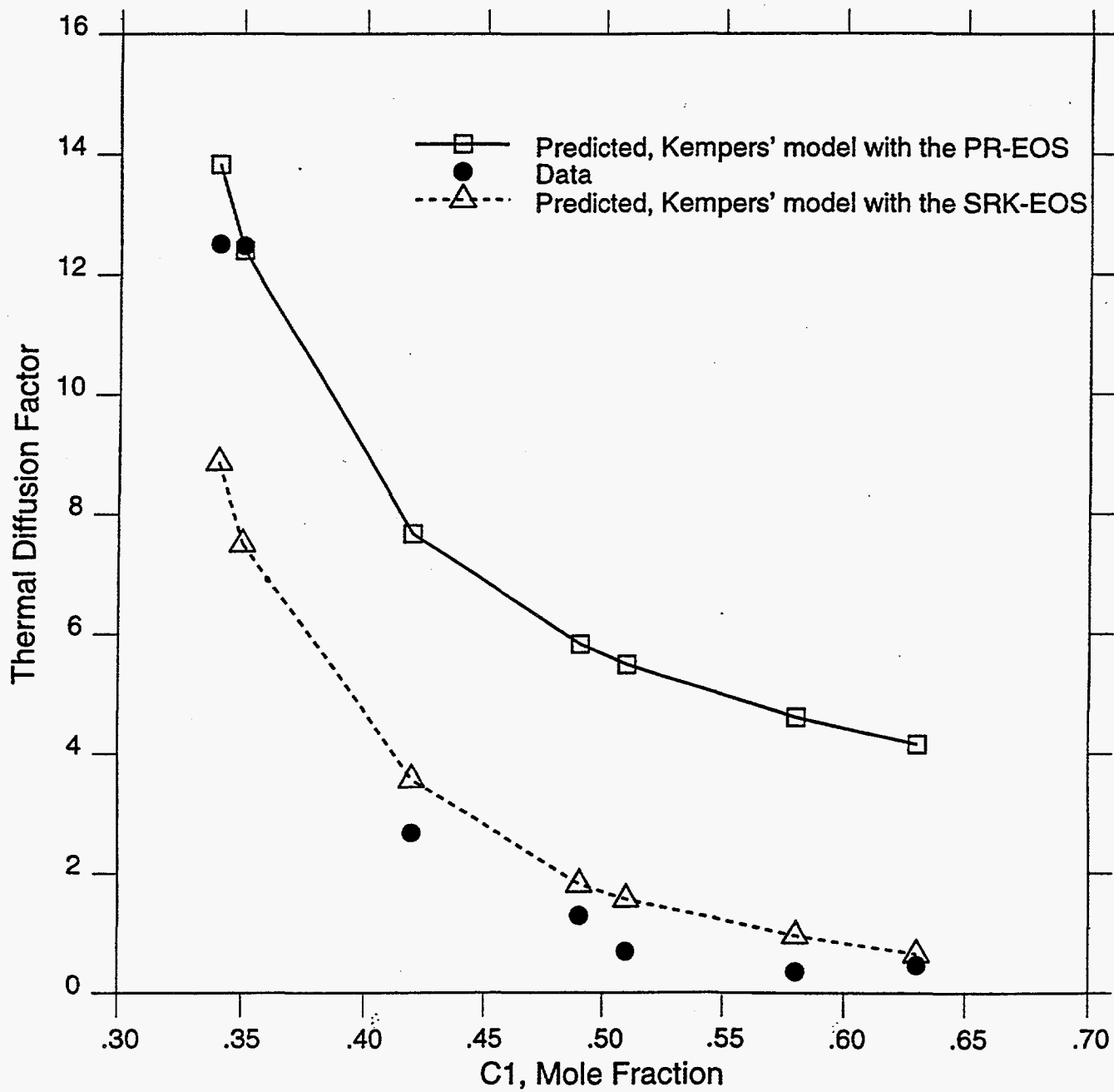


Fig.9- Thermal diffusion coefficient for the C1/C3 binary at 72.8 C and 5.59 MPa.

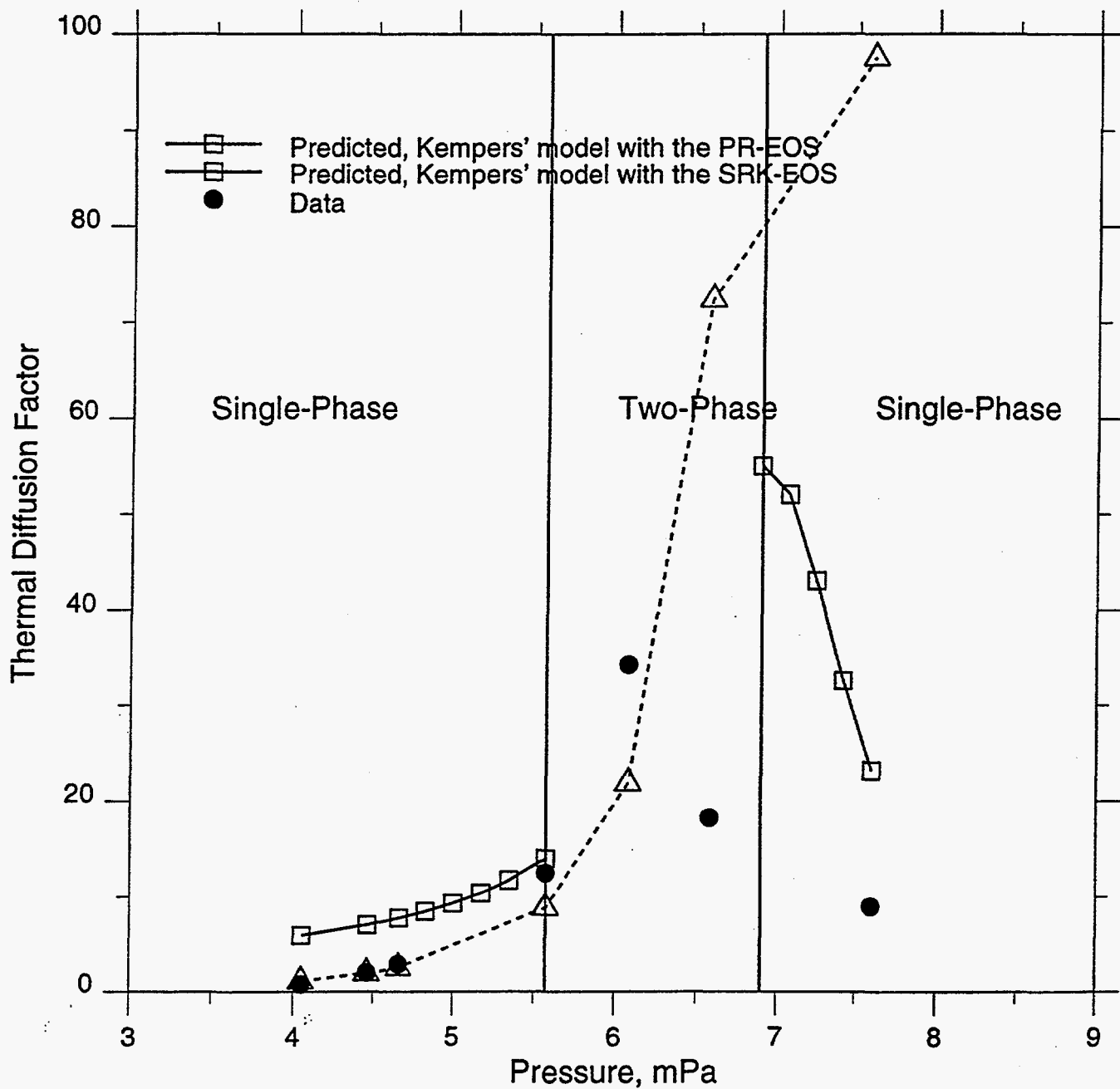


Fig.10- Thermal diffusion factors for the C1/C3 binary at 72.8 C and 0.34 mole fraction C1.

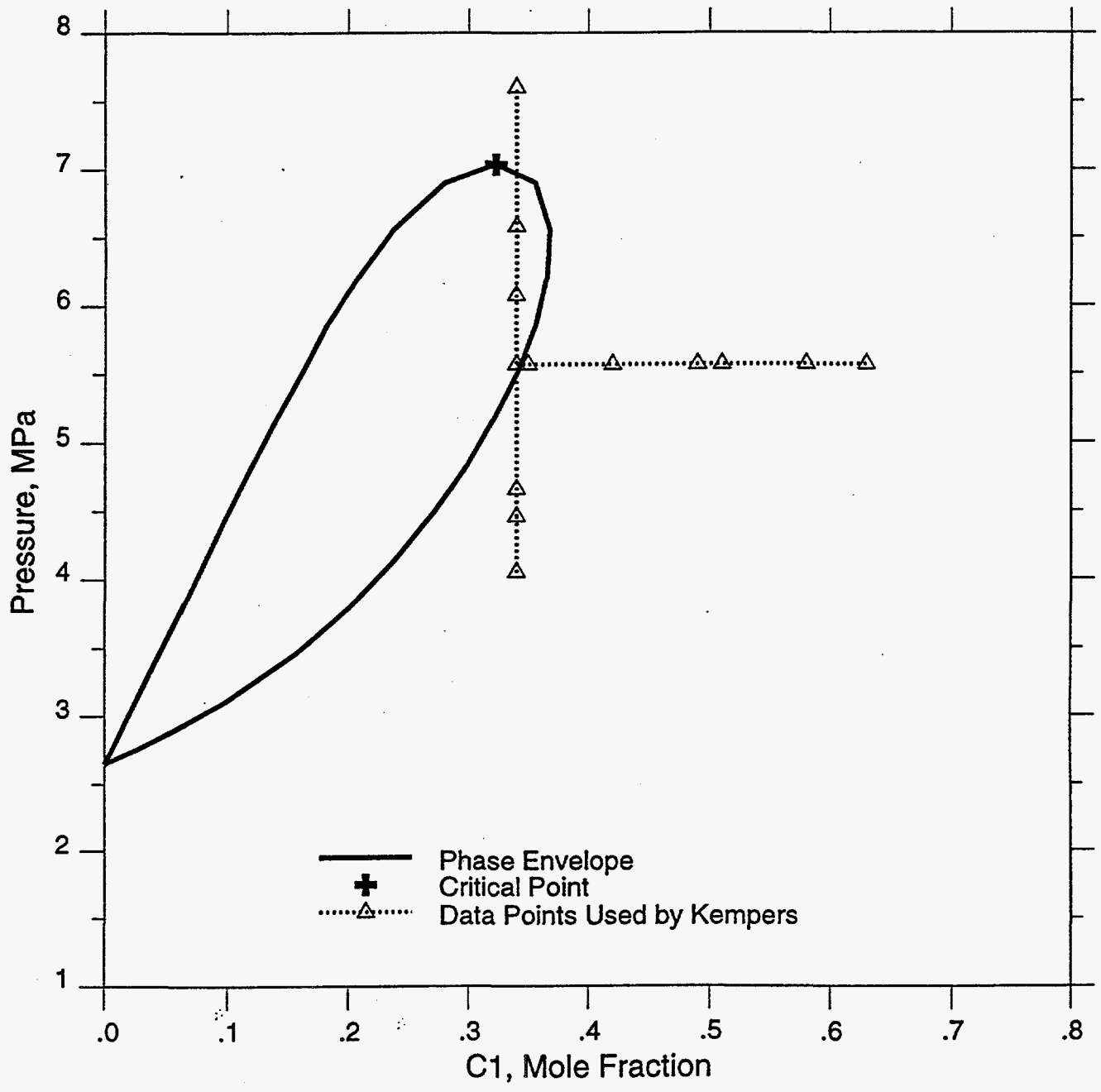


Fig.11- Phase diagram of the C1/C3 system at 72.8 C and the data points used by Kempers.

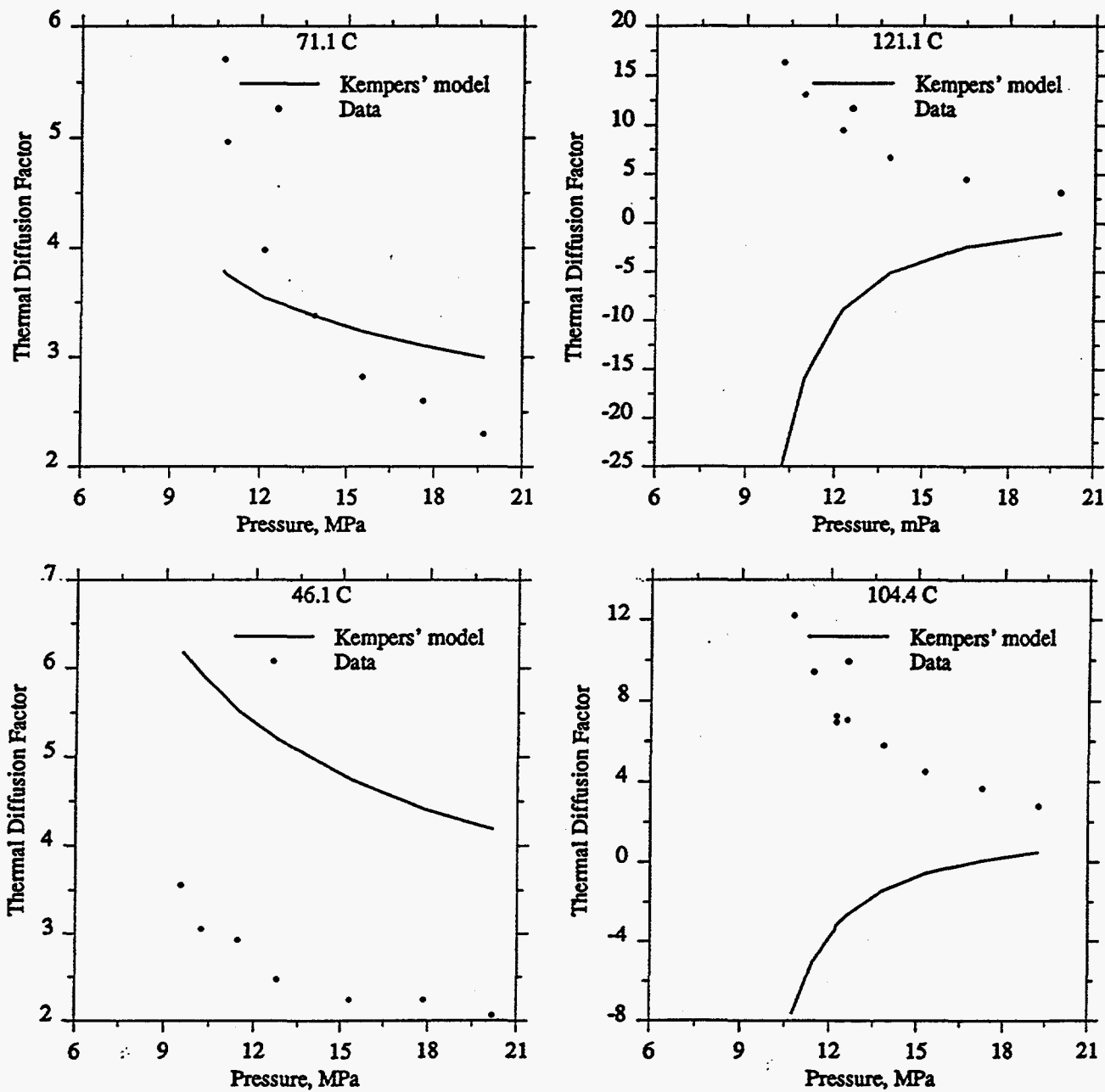


Fig. 12- Thermal diffusion factors for the C1/nC4 binary at 40 mole percent methane.

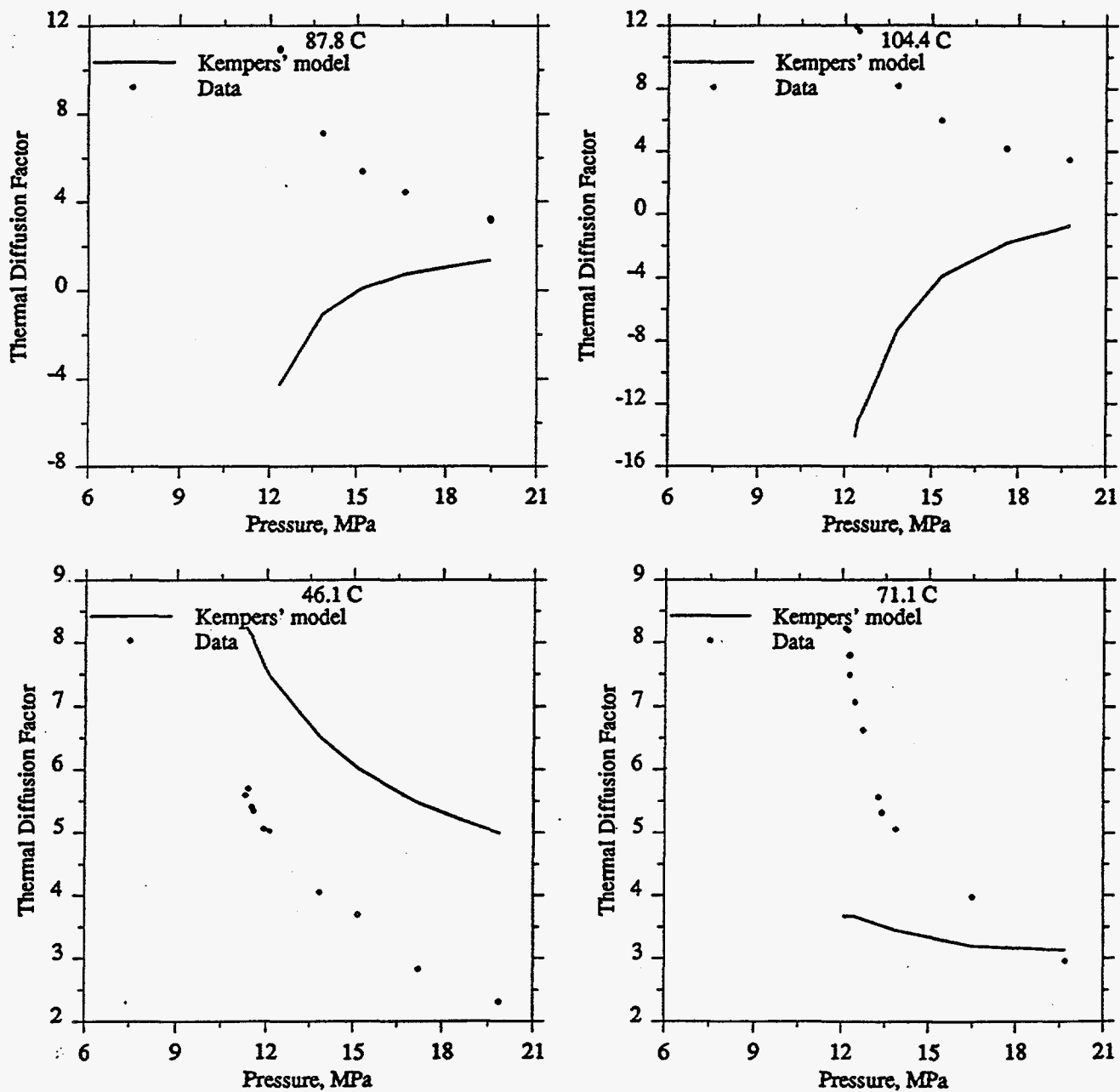


Fig. 13- Thermal diffusion factors for the C1/nC4 binary at 49 mole percent methane.

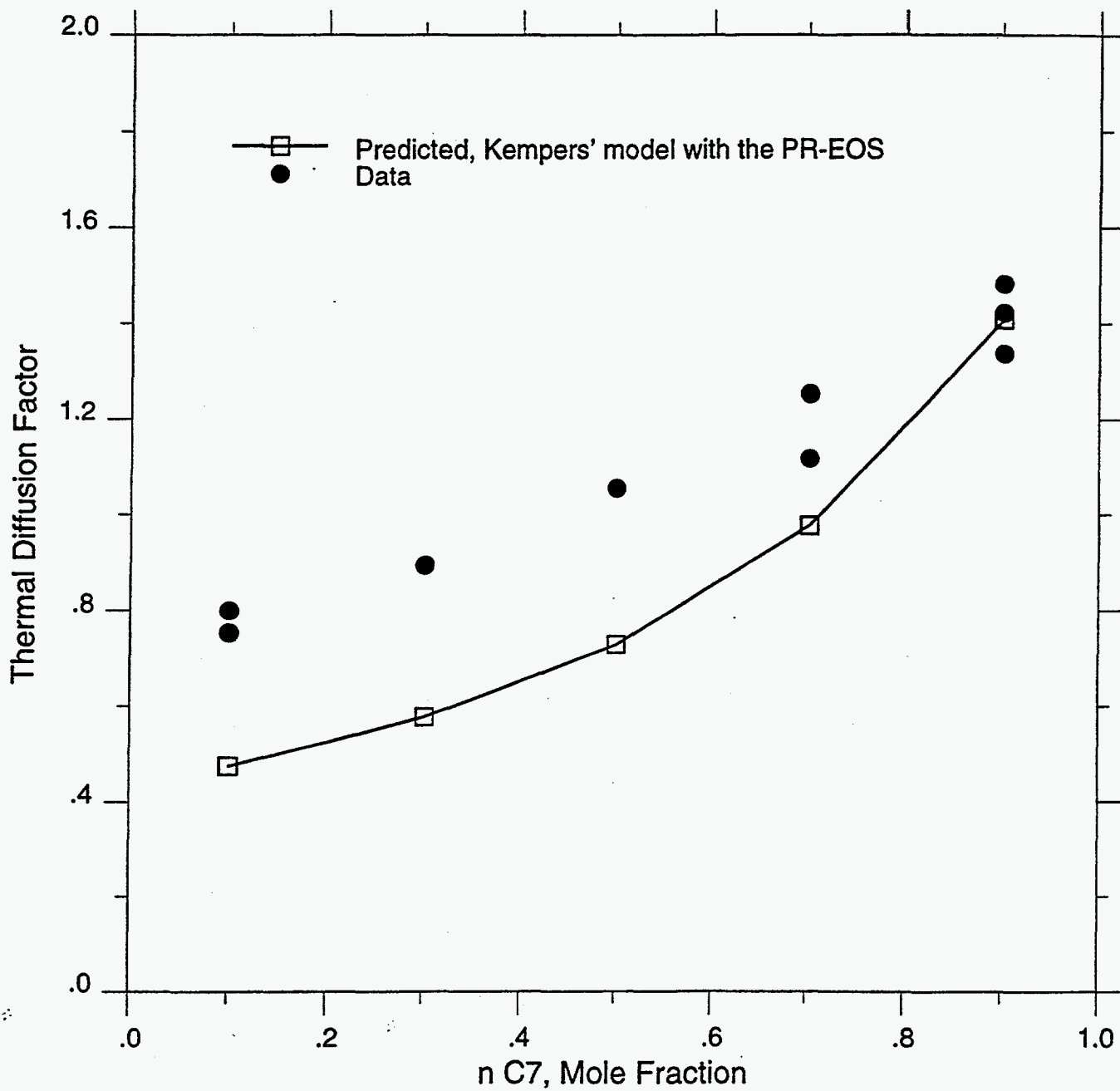


Fig.14- Thermal diffusion coefficient for the nC7/nC16 binary at atmospheric pressure and 35 C.

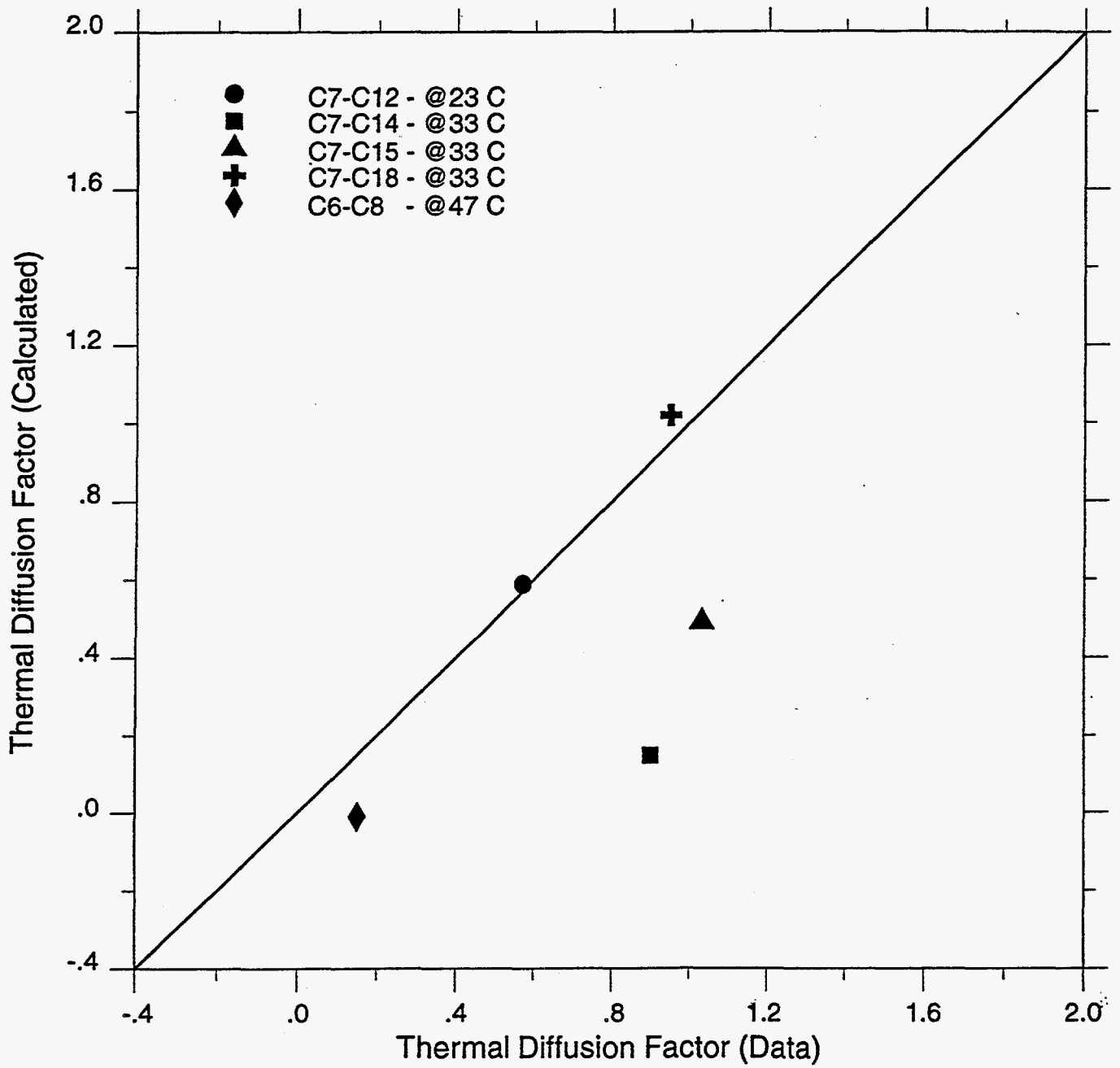


Fig.15- Thermal diffusion factors for various hydrocarbon systems.

CHAPTER VII

VISUALIZATION AND MEASUREMENT OF GAS EVOLUTION AND FLOW OF HEAVY AND LIGHT OIL IN POROUS MEDIA

Abbas Firoozabadi

Andrew Aronson

Reservoir Engineering Research Institute

SUMMARY

In a number of experiments, the efficiency of solution-gas drive for both light and heavy oils was studied. In these experiments a special coreholder was used to visually observe the formation of gas bubbles on the rock surface and the production from the core outlet. The results from all the experiments reveal that the critical gas saturation for the hydrocarbon liquids, 1) a light model oil, 2) an 11-API oil, and 3) a 35 API-oil, does not exceed 3 percent. However, the gas mobility for the heavy oil is very low and for the light model oil very high. Consequently, solution-gas drive for a heavy oil of 11 API gravity is more efficient than for a light oil.

INTRODUCTION

Solution-gas drive is a basic recovery mechanism. The two parameters that affect the efficiency of this process are: 1) critical gas saturation, and 2) mobility of the gas and liquid phases. A high critical gas saturation implies a high recovery; a 30 percent critical gas saturation would result in 30 percent oil recovery provided the oil shrinkage is negligible. On the other hand, a low critical gas saturation does not necessarily imply a low recovery; a low gas mobility or a high liquid mobility would result in high recovery.

Generally, solution-gas drive may not be efficient for very light oils. Factors which are believed to contribute to the low recovery are low critical gas saturation and high gas mobility. However, for a heavy oil, the recovery in solution-gas drive could be high either when the critical gas saturation is high or when the gas mobility is low and the liquid mobility is high. One purpose of this paper is to understand solution-gas drive for both light and heavy oils.

Solution-gas drive is initiated with the bubble nucleation, where at some critical supersaturation pressure (the pressure at which gas evolves from the supersaturated liquid) below the bubblepoint pressure, the formation of gas bubbles occurs. The bubbles may form instantaneously or according to the progressive nucleation theory. In

progressive nucleation, the rate of bubble formation is related to the supersaturation. Recently, based on theoretical analysis, we have postulated that bubble nucleation in porous media can be an instantaneous nucleation process; all bubbles form instantaneously at the critical supersaturation pressure.¹ Another objective of this work is to establish experimentally the instantaneous nature of nucleation in porous media.

It has been known for some time that a number of heavy oil reservoirs in Canada (viscosity in the range of 200 to 20,000 cp) have high recovery efficiencies - around 15 to 20 percent by primary depletion.^{2,3} The high recovery occurs in the absence of gravity drainage and water drive. A number of authors have made attempts to explain the high recovery from heavy oil reservoirs. In an early paper, Smith² hypothesized that solution-gas drive in heavy oil reservoirs is a two-phase flow with the gas in the form of tiny bubbles moving with oil. Based on the work of Ward, et al.,⁴ Smith argued that the radius of a stable bubble for a finite volume should be much smaller than the average pore throat. Ward, et al.⁴ had estimated that for a bubble density of 10^3 per cm^3 , the stable bubble may have a radius of 40 μm . These bubble densities and stable sizes may not apply to a heavy oil in porous media. Further theoretical work is needed to establish the bubble density and stable bubble size for the heavy oils.

In a later attempt, Islam and Chakma⁵ used both a long capillary tube and a horizontal core packed with unconsolidated sand to study mechanisms of bubble flow in heavy oil reservoirs. They used Dow Corning oils of 10, 1000, and 5000 cp viscosity and heavy oils to conduct flow experiments by simultaneous injection of gas bubbles and liquid. These experiments revealed that bubbles in a flowing stream of a viscous fluid will reduce the apparent viscosity. Islam and Chakma suggested a gas-oil relative permeability with a critical gas saturation of 40 percent. In-situ gas bubble formation and injection of gas bubbles in a liquid phase are fundamentally different processes. The work of these authors may not directly apply to solution-gas drive in heavy oil reservoirs.

In a more recent study, Maini, Sarma, and George⁶ have conducted many experiments using an unconsolidated sand and heavy oils to study solution-gas drive. A two-meter long sand-pack was employed by these authors. The recovery factor was obtained by dropping the pressure suddenly at the core outlet from the saturation pressure of some 700 psi to atmospheric pressure. More than 20 percent of the original heavy oil was produced in the primary depletion process. As has been observed by Islam and Chakma⁵ and others¹, a sudden drop in pressure may result in a higher recovery than a gradual pressure drop. From a number of tests, Maini, et al. concluded that the critical gas saturation for the formation of a continuous gas phase could be about 40 percent. The critical gas saturation for the heavy oils from the work of Islam and Chakma, et al., and Maini, et al., are much higher than the values for light oils.

The above brief review reveals that further work is needed to understand the solution-gas drive in heavy oil reservoirs. The main goals of this study are to: 1) resolve the issue of very high critical gas saturations, 2) find out whether tiny gas bubbles move with oil phase, and 3) determine the nature of bubble nucleation and bubble density and to better understand the efficiency of solution-gas drive for heavy oils in porous media. In this work, experiments with both light and heavy oils will be performed in order to compare the solution-gas drive for light and heavy oils. A new visual coreholder will be used to visually observe the appearance and flow of gas phase.

EXPERIMENTAL

A schematic of the experimental apparatus is shown in Figure 1. The setup, with slight differences, was used for the three sets of experiments. The main components of the apparatus include the visual coreholder, a high pressure chromatography pump, pressure transducers, a system for providing a constant temperature of 77° F ($\pm 0.3^\circ$ F) and a video recording system.

The specially-designed visual coreholder consists of an 8" long, 2" diameter Berea sandstone core (pore volume = 95 cm³, permeability \approx 500 md), capped at either end with a plexiglass cap (the top cap was machined with a dead-end for trapping gas evolved from the core) and sealed with a heat-shrunk teflon sleeve. Surrounding the core is a water-filled translucent chamber, which is pressurized and acts as an overburden sleeve. Plumbed to the coreholder is a constant flow/pressure pump. The pump is used both for saturating the core system and for pressure decline through volume expansion.

In a typical experiment, after assembling the coreholder in the vertical position and pressurizing the overburden sleeve to about 800 psia, the Berea core was exposed to methane at a pressure of approximately 500 psia to achieve adsorption on the rock surface. The methane was then displaced by the test fluid at test pressure, and extra pore volumes of fluid were passed through the core system to ensure that the core was saturated with the test fluid of the correct composition. The saturation period varied widely for the different fluids used, from less than one day to over two months for the heavy oil.

In each test the core system saturated with the test fluid at a pressure above the bubblepoint pressure, usually in the neighborhood of 650 psia, was expanded by a pump placed in the constant volume expansion mode. Then, the core surface was watched to observe bubble evolution and gas flow. The results of various tests are presented in the following.

RESULTS

A total of six tests were performed. Test fluids included a model light oil, a heavy oil, and a North Sea oil.

Model Light Oil. A mixture of C₁/C₃ -- 15.125 mole % C₁ and 84.875 mole % C₃ -- was used in the following two tests. The calculated bubblepoint pressure of the mixture at 77° F is 478 psia (using the Peng-Robinson equation of state⁸). The surface tension and the viscosity at the bubblepoint are 4.5 dyne/cm,⁹ and 0.08 cp,¹⁰ respectively.

Test 1: 0.3 cm³/hr Expansion Rate. In this test, the C₁/C₃ mixture at an initial pressure of 650 psia was expanded at a rate of 0.3 cm³/hr. At the top of the core, an open space of 10 cm³ captured the gas when flowed from the core. About 4 cm³ of this space (the cap) could be viewed.

Fig. 2 shows pressure-volume expansion data for this test. As the figure shows, in the single-phase liquid state, the pressure declines rapidly to an expanded volume of 1.25 cm³ (to 472 psia). Then the pressure rises slowly, indicating the evolution of the gas phase.

After the volume has expanded to 2.8 cm^3 , the pressure decreases with a slope of about -1.6 psi/cm^3 .

A total of nine small patches of gas were observed to form simultaneously on the front half of the vertical rock face at the volume expansion of 1.5 cm^3 . These patches were evenly distributed across the core. During the expansion from 1.52 to 2.57 cm^3 , the patches of gas increased in size, connected and formed larger patches until they were all connected at 2.57 cm^3 expansion.

At the volume expansion of 2.59 cm^3 , a filament of gas bubbles was observed flowing out of the top face of the core into the open space of the top cap. From then on, every 1 to 1.5 minutes, a filament of gas bubbles followed from the same face. The duration of the bursts varied from 0.7 to 1 second. All the bursts came from a single location on the core surface outlet. At a volume expansion of 8.9 cm^3 , the gas had filled a dead space of about 6 cm^3 in the open space outside the core. The gas saturation in the core is estimated to be around 1.8 percent at this volume expansion. The expansion was continued to 14 cm^3 . At this time, the gas nearly filled the open space at the top of the core (i.e., 10 cm^3 of gas). The amount of the gas in the pump was measured by pressurizing the fluids in the pump, and the gas in the core was estimated to be around 2 percent.

Based on the observation of the first continuous gas flow from the top face of the core (at volume expansion of 2.59 cm^3), the critical gas saturation is estimated to be around 1 percent of PV. Some authors¹¹ suggest that boundary effects may be the cause of ambiguity in critical gas saturation. This and other subsequent tests reveal that: 1) boundary effects may not be important, and 2) critical gas saturation is a measurable parameter. The displacement efficiency at the end of the test at 14 cm^3 expansion is approximately 2 percent. We measured a pressure increase of 2.5 psia at the termination of the test, which indicates a supersaturation of 2.5 psia. The pressure increase occurred in a period of 5 hours. Table 1 provides a summary of results for this and all the other tests to be discussed in the following.

Test 2: $0.06 \text{ cm}^3/\text{hr}$ Expansion Rate. This test is similar to Test 1 with the exception of expansion rate. Fig. 2 shows the pressure vs. volume expansion from a pressure of around 595 psia. The same figure also shows the pressure-expansion data of Test 1. Prior to gas evolution, Tests 1 and 2 have nearly identical expansion behavior. Around an expansion volume of 1.2 cm^3 , the slope of the pressure-expansion volume plot changes. The pressure has a slight increasing trend from an expansion of 1.2 to 2.8 cm^3 . Thereafter, it reduces linearly with a slope of about -1.1 psi/cm^3 . The critical supersaturation pressure is around 475 psia, which is slightly higher than the critical supersaturation pressure for Test 1. The maximum supersaturation for this test is, therefore, around 3 psi.

Visual observation of the core surface revealed gas forming first at one spot 2 cm from the bottom face of the core at 1.36 cm^3 volume expansion. The surface area of this first gas patch increased to 15 mm^2 at volume expansion of 1.4 cm^3 . The gas patch grew in a path upwards around the core and its width increased with time. Around 1.42 cm^3 expansion, another patch of gas appeared about 5 cm from the bottom face of the core. The first patch continued to "snake" around the core and at 1.5 cm^3 expansion, it had a distance of about 8 cm from the top face of the core and 1 cm from the bottom face. It is

possible that only one gas bubble was formed initially in this test. The second patch could be due to the growth of the bubble inside the core.

The flow of the gas from the core was first observed at 1.84 cm^3 expansion. For the remainder of the test, there were about 10 bursts of gas bubbles per hour. The duration of each burst of gas bubbles varied from 0.73 to 1 second. Similar to Test 1, all the gas bubbles flowed from the same point of the core top face. At the termination of this test, we continued to measure the pressure. There was no pressure increase, indicating negligible supersaturation.

Based on the observation of the first flow of gas, the critical gas saturation for Test 2 is estimated to be around 0.5 percent. The displacement efficiency of solution-gas drive seems to be very low -- around 1 percent of PV at the end. A high gas mobility precludes high recovery efficiency.

Heavy Oil. A heavy oil of 11 API gravity with a bubblepoint pressure of 445 psia at a temperature of 76° F was used for the two tests described in the following. It was prepared by mixing 10 cm^3 of methane to 1 cm^3 of stock tank oil ratio at standard conditions of 14.69 psia and 60° F . The viscosity of the saturated oil at 57° F was 17,000 cp. However, the experiments were performed at 76° F . The compressibility of the live oil above the bubblepoint pressure was measured to be about $1.8 \times 10^{-5} \text{ psia}^{-1}$. Likewise, the compressibility of the total rock fluid system in the single phase state at 76° F was $2.5 \times 10^{-5} \text{ psia}^{-1}$.

The saturation of the core with the heavy oil was a real challenge. It took more than two months to saturate the core; the pressure drop across the core was limited to 100 psi to avoid entering the two-phase region. This restricted the flow rate to about $15 \text{ cm}^3/\text{day}$ in saturating the core. By measuring the compressibility it was ensured that the fluid was in single phase state.

Test 3: $0.06 \text{ cm}^3/\text{hr}$ Expansion Rate. In the first test using heavy oil, the expansion was carried out from an initial pressure of 645 psia. The production was from the bottom end of the core. On the top, the volume of the cap (open space) was about 4 cm^3 . This whole volume could be viewed.

Fig. 3 shows the measured pressure-volume expansion data. The upper curve shows the pressure on the closed side, and the lower curve is the pressure on the expansion side of the core. In the early stage of expansion, the pressure declines rapidly, as expected. Both upper and lower pressures continue to decrease to pressures of 405 and 385 psia, respectively, at a volume expansion of 1 cm^3 . At this point, both curves flatten out, indicating the evolution of the gas phase. The supersaturations at expansion of 1 cm^3 are 40 and 60 psi for the top and bottom sides, respectively. Note that there is a substantial difference between the upper and lower pressures. The high pressure drop could be partly due to the narrow outlet tube at the bottom face of the core (diameter = 3 mm).

At an expansion of 1.45 cm^3 , some gas bubbles were visible on the outer surface of the core. We did not monitor gas bubbles on the surface of the core from 1 to 1.45 cm^3 volume expansion; therefore, gas bubbles might have appeared prior to volume expansion of 1.45 cm^3 . The bubbles were mainly located in the bottom 5 cm of the core, but several bubbles were observed as high as 15 cm from the bottom. There were approximately 50

to 60 small bubbles visible on the surface of the core. Further expansion to 1.7 cm^3 yielded a slight increase in the number and size of the existing bubbles. At this expansion, a gas pocket was observed in the transparent tube in the lower end cap of the core (see Fig. 5). The approximate volume of the gas slug₃ was 0.04 cm^3 . An interesting pressure fluctuation occurred at an expansion of 2.67 cm^3 . At this volume expansion the lower (expansion) pressure increased while the upper pressure decreased. The pressure change continued for one hour, at which time the lower pressure had increased by 10 psi and the upper pressure had dropped by 5 psi. The trend then reversed itself and the pressures returned to their previous levels and decline rates. This behavior was witnessed repeatedly at later times, where it was observed to coincide with the production of gas pockets from the core into the transparent outlet tube. A similar behavior has been observed by Maini, et al.⁶ At an expansion of 2.91 cm^3 , two gas slugs were observed in the core outlet tube. The upper slug was 3 mm in length, 18 mm below the bottom surface of the core. Below this slug was 5 mm of oil and then another gas bubble 2 mm in length. Based on a tube diameter of 3 mm, the volume from the bottom bubble to the bottom of the core is 0.22 cm^3 , which corresponds well with the volume expansion of 0.24 cm^3 (4 hours) from the time of the pressure fluctuation to the visual observation. At the volume expansion of 2.91 cm^3 , the core surface showed an increase in the number of gas bubbles towards the upper parts of the core. But, no bubbles were observed in the uppermost 2 cm of the core surface. Several more pressure spikes occurred at volume expansions of 3.52, 4.20, 4.56 and 6.03 cm^3 (see Fig. 3). From volume expansion of about 7.4 cm^3 , the fluctuations occurred much more often. This is displayed by the jagged appearance of the pressure volume curve from this point to the termination of the experiment at an expansion of 11.88 cm^3 . At the termination, the volume of gas in the pump was measured to be 1.3 cm^3 by compressing the fluids in the pump. This means that about 10.6 cm^3 of oil was produced from the core. Subtracting the contribution from fluid expansion, and since the formation volume factor is very close to unity, the oil recovery due to solution-gas drive to a pressure of 320 psi is about 10 percent. Such a high recovery confirms that solution-gas drive can be an important recovery process for some heavy oils.

While at an expansion of 1.7 cm^3 , gas was observed in the outlet tube; it may well have evolved from the oil outside the core, being that the lowest pressure in the system was near the expansion pump. A more logical choice for a gas flow might be at an expansion of 2.67 cm^3 where, as discussed above, gas slugs were produced from the core. Due to the uncertainty when gas flow from the core began, it can only be stated that the critical gas saturation is less than 3 percent.

Test 4: $0.06 \text{ cm}^3/\text{hr}$ Expansion Rate. In this test, the direction of flow was reversed with the expansion pump connected to the top of the coreholder, rather than the bottom. This change was made in order to measure the flow of the gas from the core in the cap at the top.

Fig. 4 shows the measured pressure-volume expansion data. The two curves correspond to the pressures on the closed side (bottom) and the expansion side (top) of the core. During the initial stage of expansion in the single phase liquid state, the pressures on both sides of the core were a few psi different. Both pressures continued to decrease to 404 and 395 psia at expansion of 0.86 cm^3 . This point corresponds to a local

minimum for both pressures, indicating the evolution of the gas phase. The critical supersaturation is, therefore, 40 to 50 psi. The data plotted in Fig. 4 are from manual readings and do not include data points where pressure fluctuations similar to Fig. 3 were observed. Fig. 4 shows that the difference between the two pressures increases with volume expansion.

At an expansion of about 1 cm^3 , many small gas bubbles (approximately 100 to 150) were visible on the outer surface of the core. These bubbles were mainly located in the top three-fourths of the core. The appearance of gas on the core surface at various volume expansions are displayed in Fig. 5. The pictures in this figure were taken at 1.28, 2.32, 5.30 and 12.90 cm^3 expansions. Fig. 5a corresponds to about 5 hours after the appearance of the gas bubbles. There was very little change in the number of bubbles from the time of their formation to the expansion of 1.28 cm^3 . At volume expansion of 2.32 cm^3 (i.e., time = 38.8 hr), gas bubbles grew considerably (see Fig. 5b). But, there was no gas in the cap at the top; therefore, the volume of the gas in the core is estimated to be about 1.5 cm^3 . At $t = 88.3 \text{ hr}$, volume expansion 5.3 cm^3 , the gas bubbles had grown further (see Fig. 5c), and there were no gas bubbles in the bottom 2 to 3 cm of the core. Finally, at 12.9 cm^3 expansion, gas bubbles had grown all over the core surface.

At the expansion of 2.4 cm^3 ($t = 40 \text{ hr}$), a small gas bubble was observed in the cap at the top. The volume of the gas in the cap grew to about 0.3 cm^3 at an expansion of 4.2 cm^3 . Further expansion to 5.3 cm^3 yielded an increase in the amount of gas in the cap to about 0.8 cm^3 . At 6.8 cm^3 expansion, there was approximately 2 cm^3 of gas in the cap. The oil recovery from solution-gas drive is equal to the gas saturation of the core; at 6.8 cm^3 expansion, about 4.8 cm^3 of oil has been produced from the core (the formation volume factor is very close to one). Therefore, the oil recovery (to an expansion of 6.8 cm^3) for the solution-gas drive mechanism is over 4 percent. Fig. 6 depicts the gas volume in the cap vs. the volume expansion for Test 4.

At an expansion of 11.26 cm^3 , the amount of the oil produced into the expansion pump was measured (by compression). It was found that about 5 cm^3 of oil had been produced from the core. At this expansion, the cap had already been filled with gas down to the production side arm, corresponding to about 3.4 cm^3 of gas. Similar measurements were made at further expansions. The data are shown in Table 2. This table shows that as pressure drops, oil continues to be produced from the core. The oil production from the core is about $0.02 \text{ cm}^3/\text{psi}$ pressure depletion, which implies that the oil mobility is significant.

The experiment was terminated at a volume expansion of about 30 cm^3 . Pressures at both ends of the core were measured as a function of the time after the expansion was stopped. The pressure for the top at the termination of expansion was 248 psia. It increased to 252 psia after about 80 hours. There were small pressure fluctuations for this top end. The pressure at the bottom end, both during the test and after expansion halt, fluctuated more. After expansion halt, the magnitude of the fluctuations was about 5 psi and showed a decreasing trend in the period of pressure monitoring (80 hours).

The critical gas saturation for this test is estimated to be around 2.5 percent (see Fig. 6). But, oil mobility seems to be significant even after gas flow. Comparison of Tests 3 and 4 reveals higher recovery from solution-gas drive when flow occurs from the bottom. But, even for Test 4, where the production was from the top, about 6.5 percent heavy oil

recovery was achieved to the pressure of 269 psia. As Table 2 shows, the oil recovery is still significant at this pressure.

Visual observation of the top cap in Tests 3 and 4 reveal that the solution-gas drive for this heavy oil is not from the simultaneous flow of oil and tiny gas bubbles.

Light Oil. For the following two tests, a 35 API gravity oil from the North Sea was mixed with pure methane; 16.2 cm³ of methane was mixed with 1 cm³ of stock tank oil at standard conditions of 14.69 psia and 60° F. The bubblepoint pressure of the mixture at 77° F is around 585 psia. The surface tension at the bubblepoint is estimated to be around 15 dyne/cm.¹² Viscosity at 77° F is not available. But, the viscosity of the saturated oil at 585 psia and 187° F is around 1 cp. The measured compressibility of the light oil used in the following two tests is 10⁻⁵ psia⁻¹ (at 77° F in the pressure interval of 625 to 700 psia). The measured compressibility of the total coreholder system with single phase oil is around 2.5 x 10⁻⁵ psia⁻¹.

Test 5: 0.3 cm³/hr Expansion Rate. In this test, as well as Test 6, the system pressure was initially 690 psia, and the expansion from the top started from this pressure. Fig. 7 shows the pressure-volume expansion data. The same figure also shows the data from the expansion of 120 cm³ of oil in the pump isolated from the core system. Due to different compressibilities, Test 5 and pump results in the single liquid phase state (from 690 to about 500 psia expansion) differ by a small volume. The critical supersaturation pressure for the oil in the pump (i.e., open space) is slightly less than the corresponding value of Test 5. The growth of gas phase is, however, faster in the pump; after gas evolution, supersaturation decreases very fast in the pump.

Around a volume expansion of 0.5 cm³ at a pressure of 505 psia, the slope of the pressure-expansion plot changes, indicating gas evolution (see Fig. 7). Gas bubbles on the surface of the core were first visible at a volume expansion of 0.9 cm³. The total number of bubbles was around 20 to 25. Further expansion to 1.2 cm³ yielded an increase in the size of the existing bubbles. Fig. 8 provides the photographs of the coreholder at various times during the expansion. At an expansion of 1.2 cm³, the bubbles are shown in Fig. 8a. This picture shows that the bubbles are distributed evenly across the core. At the expansion of 1.45 cm³, bubbles grow further, and there seems to be one new patch of gas at the top of the core; this new gas patch is possibly the result of bubble growth from the inside of the core. At the 2.1 cm³ expansion, the bubbles grow further (see Fig. 8c). The final photograph before gas flow from the core at a volume expansion of 2.7 cm³ shows that the gas bubbles have grown considerably and may be connected (see Fig. 8d).

Visual examination of the cap at the top showed very little gas until a volume expansion of 3.3 cm³. At this expansion, the volume of gas in the cap started to increase with expansion. Fig. 6 shows the volume of gas in the cap vs. volume expansion for Test 5. The contribution of the gas from the oil inside the cap is very small and can be neglected. Therefore, the gas in the cap can be assumed to be the result of gas flow from the core. From Fig. 6, one estimates the critical gas saturation to be around 3 percent. In two other duplicate tests, the same value of the critical gas saturation was also established. Fig. 6 also reveals that during the expansion from 3.3 to 7.8 cm³, about 1 cm³ of oil is also produced from the core. The solution-gas drive to a volume expansion of 7.8 cm³, results

in an oil production of 3.8 cm^3 , which is about 3.5 percent recovery (excluding liquid compressibility). After the gas in the cap reaches 3.4 cm^3 , it can flow out to the pump via the side arm (shown in Fig. 8). During the remaining course of the experiment at volume expansions of 8.1, 10.2, 15.0 and 22.8 cm^3 , the volume of the gas in the pump was measured (by compressing the pump fluids in a short time). This allowed an estimation of the oil production from the core. At expansion of 10.2 cm^3 , oil production from the core was about 5.0 cm^3 , but from 10.2 to 22.8 cm^3 , there was very little increase in the amount of liquid in the pump. This suggests that gas mobility is very high and liquid mobility (in the core) is very low. Note that the oil shrinkage in the 600 to 400 psia range is around 1 percent.

The supersaturation for Test 5 and the pump test were measured at the end. For the pump, the pressure increased about 6 psi after halting expansion. For Test 5, the supersaturation was 8 psi. There was practically no increase in pressure after one day.

Test 6: $0.06 \text{ cm}^3/\text{hr}$ Expansion Rate. Fig. 9 shows the pressure-volume expansion for both Tests 5 and 6. For Test 6, at about 0.5 cm^3 expansion, the pressure decline rate decreased considerably, but no gas bubbles were visible on the outer surface of the core until a volume expansion of about 0.9 cm^3 . At this expansion, some 7 to 10 gas bubbles were visible on the core outer surface. With further expansion, these bubbles grew. The growth of the gas bubbles was very similar to Test 5. The only difference is that the number of bubbles in Test 6 is less than that in Test 5. The decrease in bubble density is due to the rate effect. As Fig. 9 reveals, a major difference between Tests 5 and 6 is the high supersaturation of the latter test at the early stages of gas bubble growth, as expected.

Until an expansion of about 3 cm^3 , no sizable gas phase was visible in the cap at the top of the core. From this expansion, gas volume in the cap increased. Fig. 6 shows the accumulation of gas in the cap. At an expansion of 4.0 cm^3 , about 1 cm^3 of gas is present in the cap, which is mainly the result of gas flow from the core. The amount of gas in the cap increased to 3.4 cm^3 at an expansion of 6.7 cm^3 . Further expansion resulted in the flow of the gas from the side-arm to the pump. In the expansion period of 3.0 to 6.7 cm^3 , only 0.5 cm^3 of oil was produced from the core.

At expansions of 11, 14 and 17 cm^3 , the amount of the gas in the pump was measured and then the oil production from the core was estimated. At 11 cm^3 expansion, the total oil production from the core is estimated to be about 4 cm^3 . During further expansion, negligible oil production from the core occurred. Therefore, the total oil recovery at the termination of the test is around 4.2 percent. The critical gas saturation for this test is estimated to be 2.5 percent. Both the critical gas saturation and the recovery (at the same expansion) for Test 6 are less than for Test 5 due to rate effect.

At the end, the supersaturation was measured. Over a period of one day, the pressure increased from 438 to 442 psia, which gives a supersaturation of about 4 psi.

DISCUSSION AND CONCLUSIONS

An important issue in the interpretation of the experiments described above is whether the number of bubbles visible on the surface of the core represent the bubble density within the core. Based on the following reasoning, we believe the number of bubbles on the core surface and within the core are related. In the design of the coreholder, the core was tightly sealed with a heat-shrunk teflon sleeve and the overburden pressure was kept at a pressure of at least 200 psi higher than the pressure inside the core. Measurement of the permeability of the core within the setup and outside gave the same permeability. Since nucleation active sites are not believed to be initiated from the teflon surface, the bubble density on the rock surface and within the rock should be the same.

In this work it was observed that solution-gas drive for a heavy oil in comparison to a light oil can be an efficient process; the bubble density for heavy oil (number of bubbles per unit area or volume) is very high. Due to high oil viscosity, the pattern of bubble growth may be such that gas mobility is low; consequently oil mobility may be appreciable. Recovery of 10 percent of heavy oil with a bubblepoint pressure of 445 psia (Test 3) to a pressure of about 320 psia from solution-gas drive is an indication of high recovery efficiency.

Careful observation of the production from the transparent end face of the core and the open space on the top of the core reveals that the flow of heavy oil in porous media is not in line with the postulation of Smith⁶ that solution-gas drive is a two-phase flow with the gas in the form of tiny bubbles moving with oil. Prior to establishing critical gas saturation in the core, only oil was produced. When gas saturation in the core exceeded critical gas saturation, slugs of gas were produced along with oil. The production of slugs was accompanied by pressure fluctuations.

The visual observations in the experiments described in this paper also establishes the fact that critical-gas saturation is a measurable parameter. For the C_1/C_3 model light oil, heavy oil, as well as the 35 API oil, the onset of gas production after it has been formed in the core was by flow of a continuous stream of gas phase and not by isolated gas bubbles.

Other major conclusions drawn from this work are:

1. Critical gas saturation for heavy oil systems may not be very high; it may be within the range of lighter crudes.
2. The high efficiency of solution-gas drive for heavy oils may be related to the high bubble density and the low gas mobility. On the other hand, the low efficiency of solution-gas drive in very light oil systems could be the result of low bubble density and high gas mobility.
3. The nucleation process in porous media is of instantaneous nature, and does not follow the progressive nucleation.

ACKNOWLEDGMENTS

Mr. Tore Markeset carried out Tests 1 and 2, and Dr. Amrollah Mehdizadeh of the California Polytechnic State University, San Luis Obispo, California designed and constructed the visual coreholder. This work is supported by the members of the research consortium on fractured petroleum reservoirs of the Reservoir Engineering Research Institute and the U.S. Department of Energy (Grant No. DE-AC22-91BC14835). Their support is appreciated. Amoco Canada Petroleum Company, Ltd. provided the heavy oil.

REFERENCES

1. Firoozabadi, A. and Kaschiev, D., "Evolution of Gas Phase in Solution-Gas Drive Process," SPE 26286, paper available from SPE, Richardson, TX.
2. Smith, G.E., "Fluid Flow and Sand Production in Heavy Oil Reservoirs Under Solution Gas Drive," SPE Production Engineering (May 1988) 167-180.
3. Loughead, D.J. and Saltuklarouglou, M., "Lloydminster Heavy Oil Production - Why So Unusual," paper presented at the Ninth Annual Heavy Oil and Oil Sands Technology Symposium, Calgary, Canada, March 11, 1992.
4. Ward, C.A. Tikuisis, P., and Venter, R.D., "Stability of Bubbles in a Closed Volume of Liquid-Gas Solution," J. of Appl. Phys., (Sep. 1, 1982) Vol. 53, No. 9, 6076-6084.
5. Islam, M.R., and Chakma, A., "Mechanics of Bubble Flow in Heavy Oil Reservoirs," SPE 20070, paper presented at the 60th California Regional Meeting, Ventura, CA, April 4-6, 1990.
6. Maini, B.B., Sarma, H.K. and George, A.E., "Significance of Foam-Oil Behavior in Primary Production of Heavy Oils," Canadian J. of Petroleum Technology (Nov. 1993) Vol. 32, No. 9, 50-54.
7. Firoozabadi, A., Ottesen, B., and Mikklesen, M., "Measurement of Supersaturation and Critical Gas Saturation," SPE Formation Evolution J. (Dec. 1992) 337-344.
8. Peng, D.Y. and Robinson, D.B., "A New Two-Constant Equation of State," Ind. Eng. Chem. Fund. (1976) Vol. 15, No. 1, 59-64.
9. Weinaug, C.F. and Katz, D.L., "Surface Tensions of Methane-Propane Mixtures," Ind. and Eng. Chem. (1943) 239-246.
10. Bicher, L.B. and Katz, D.L., "Viscosity of the Methane-Propane System," Ind. and Eng. Chem. (1943) 754.

11. Li, X. and Yortsos, Y.C., "Critical Gas Saturations: Modelling and Sensitivity Studies," SPE 26662, paper presented at the 68th Annual Technical Conference and Exhibition of the Society of Petroleum Engineers, Houston, TX, Oct. 3-6, 1993.

12. Firoozabadi, A., Katz, D.L., Soroosh, H. and Sajjadian, V.A., "Surface Tension of Reservoir Crude-Oil/Gas Systems Recognizing the Asphalt in the Heavy Fraction," SPE Reservoir Engineering J. (Feb. 1988) 265-272.

Table 1. Gas and Oil Production Data for Test 4

Time, hr	Expansion, cc	Oil in Pump, cc	Gas in Pump, cc	Oil from Core, cc	Closed Side Pressure, psia	Expansion Side Pressure, psia
187.7	11.26	8.35	2.91	4.95	356	346
238.3	14.30	8.77	5.53	5.37	340	324
327.8	19.67	9.43	10.24	6.03	311	293
375.5	22.53	9.50	13.03	6.10	296	269
495.3	29.72	10.05	19.67	6.65	269	248

Figure 1. Apparatus diagram for critical gas experiments.

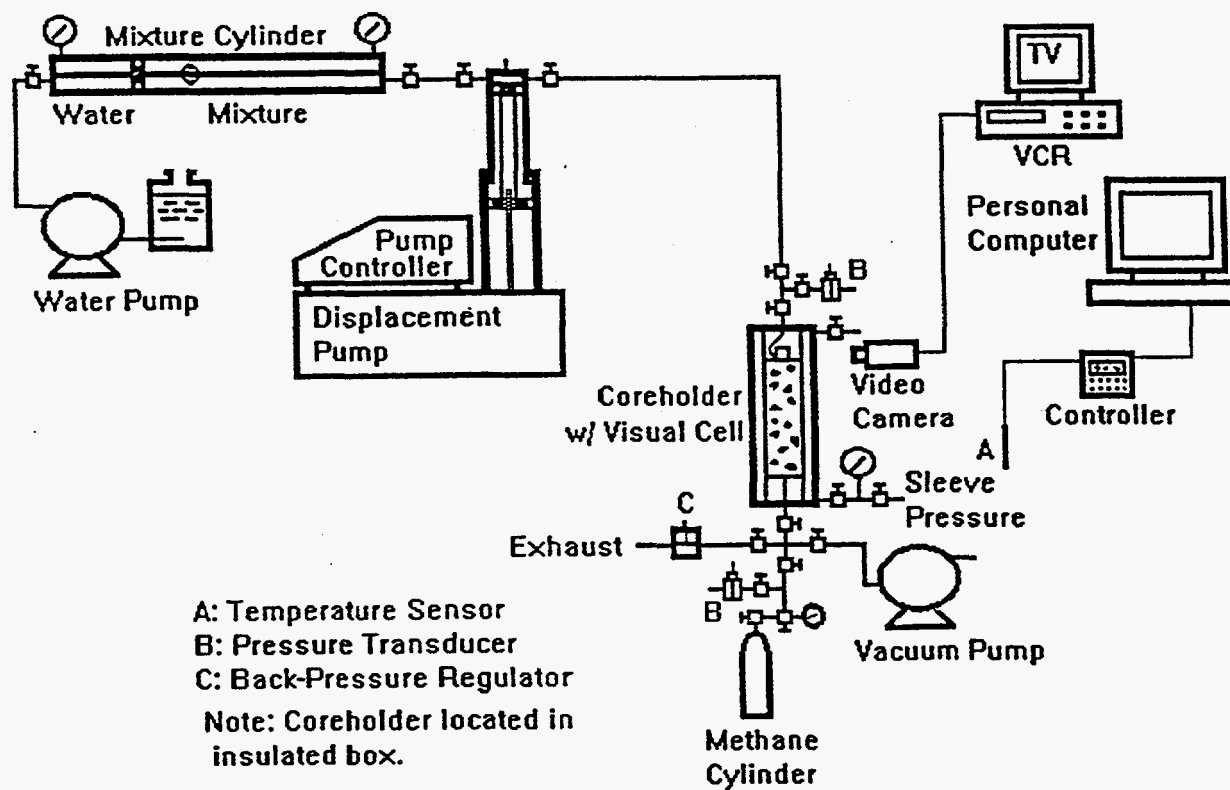


Fig.2-Pressure-volume expansion data for Tests 1 and 2.

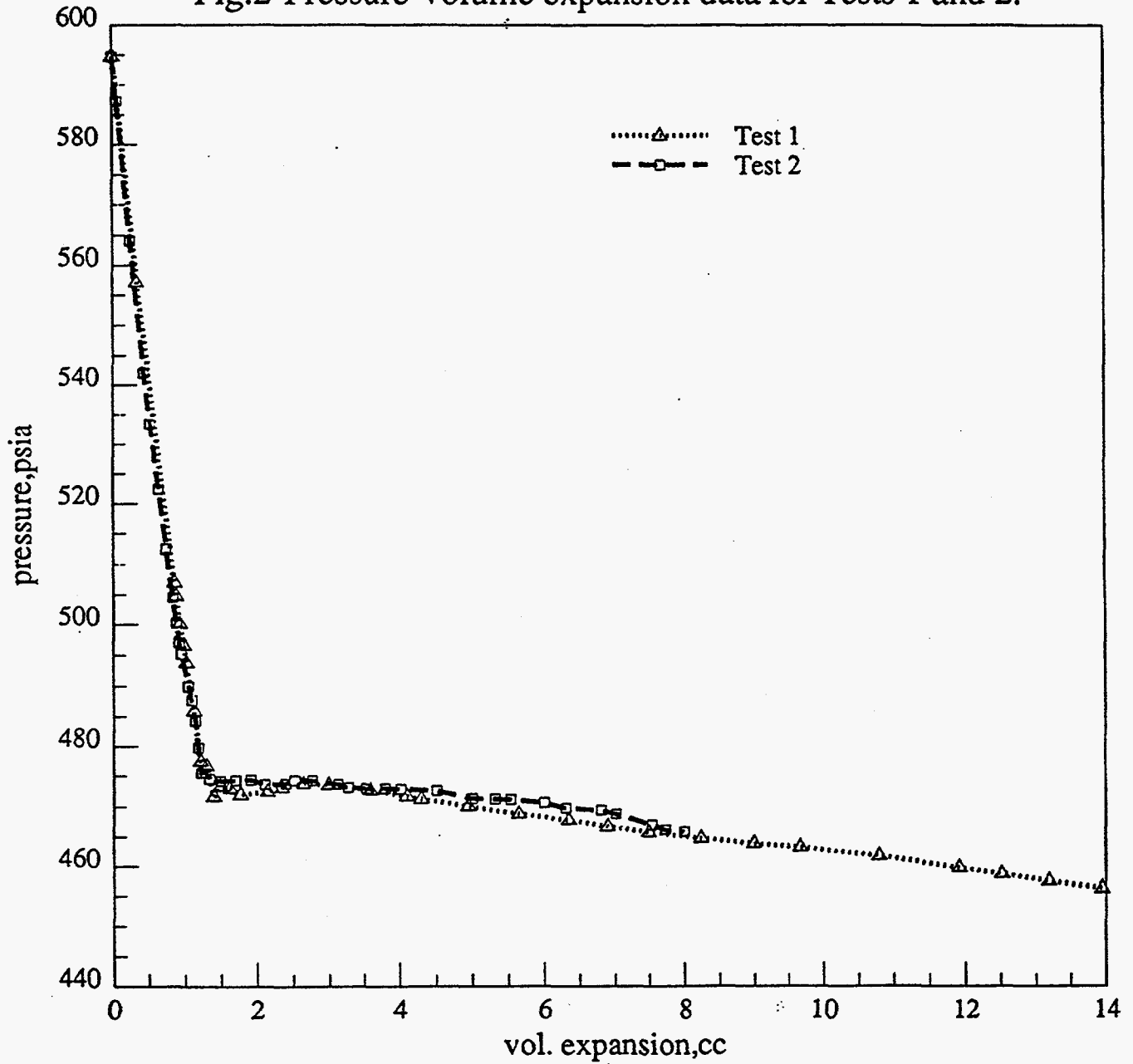


Fig.3-Pressure-volume expansion data for Test 3.

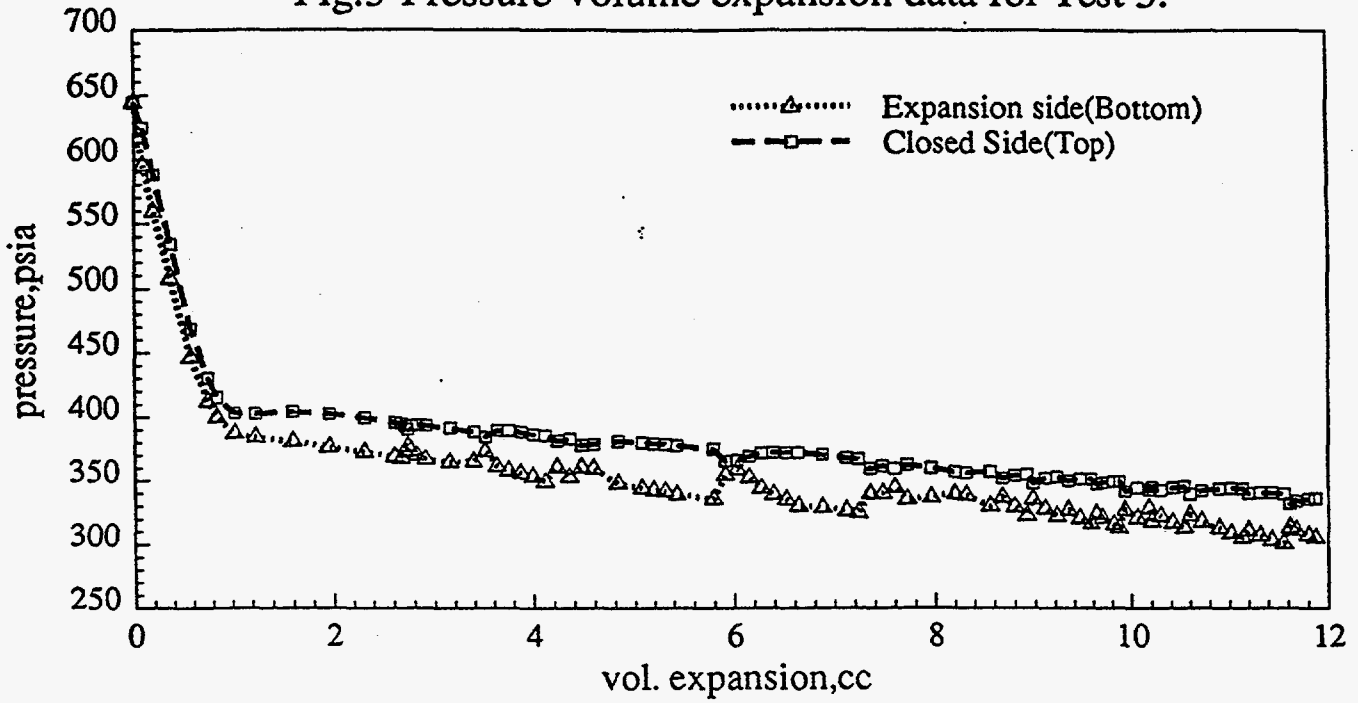
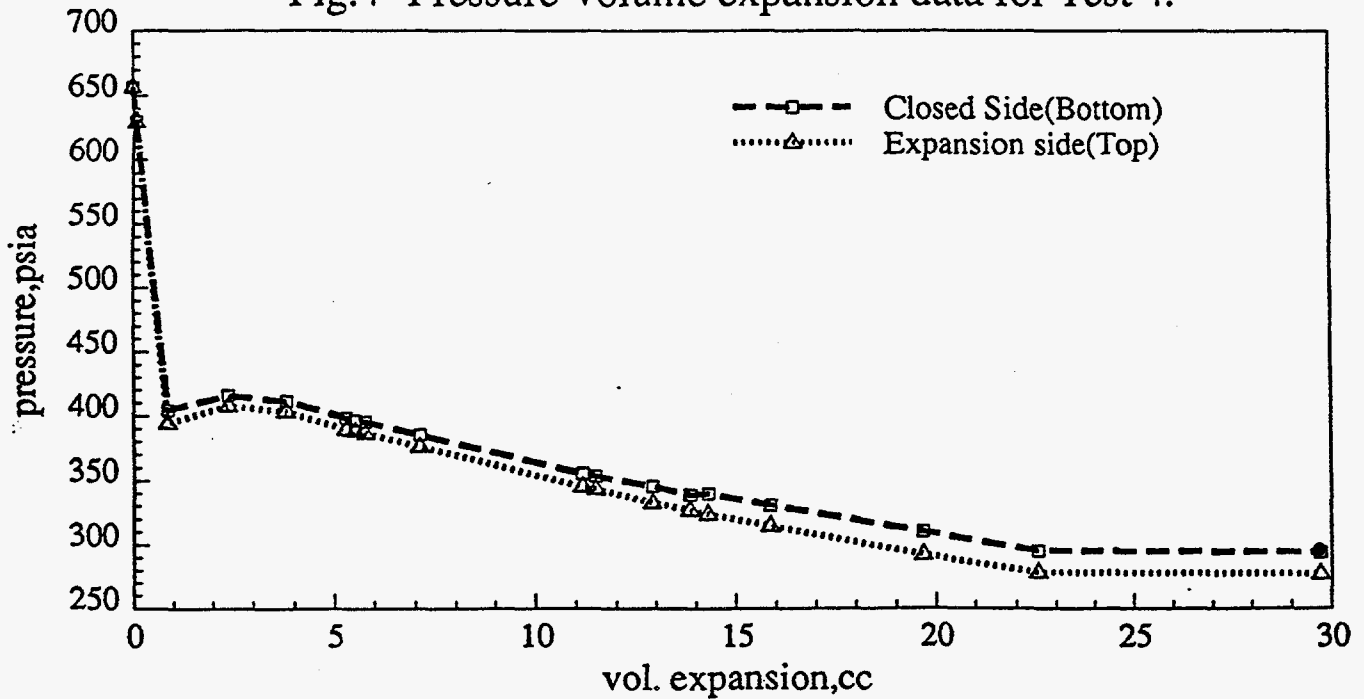
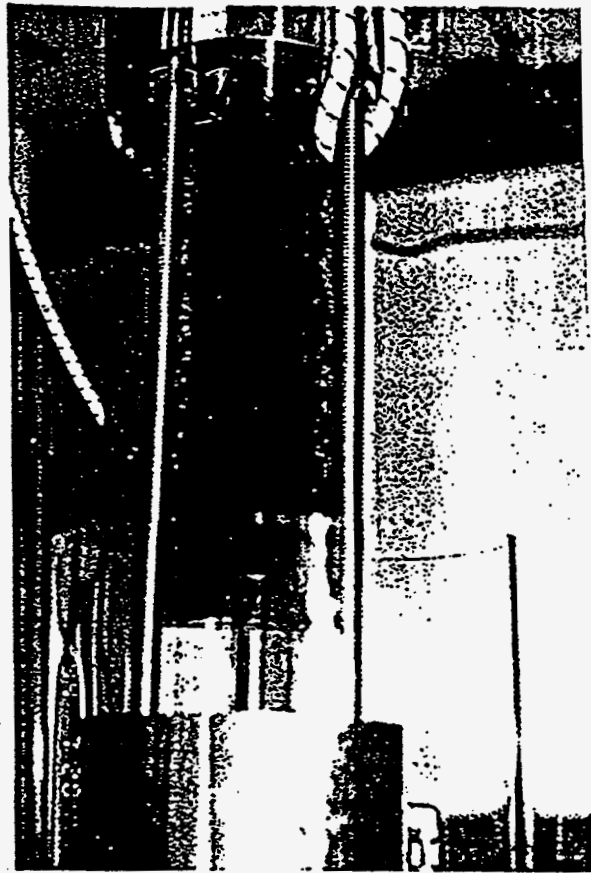


Fig.4- Pressure-volume expansion data for Test 4.

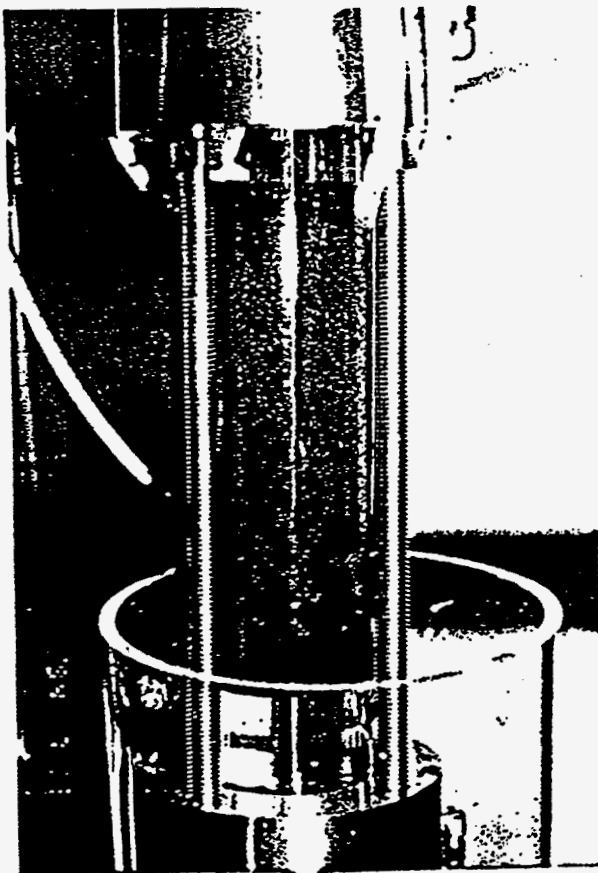




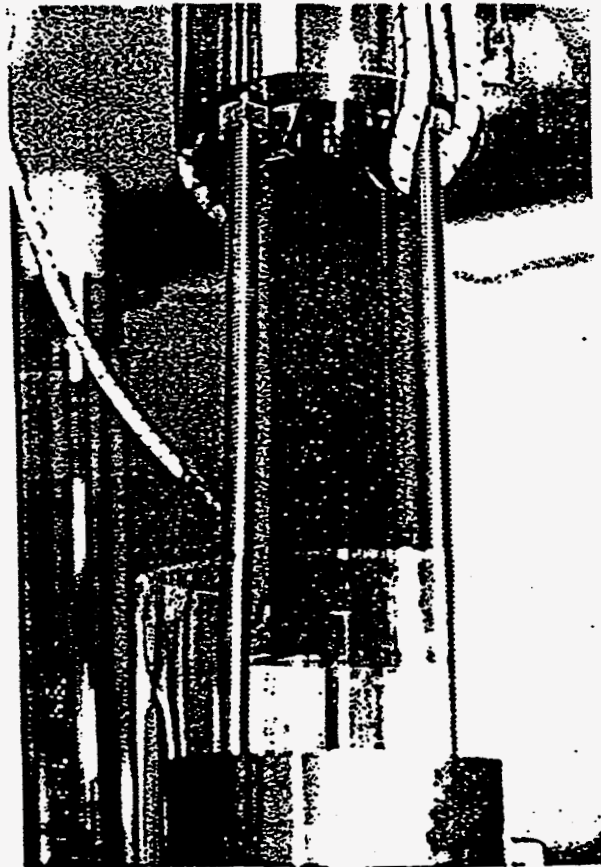
(a) expansion= 1.28 cc



(b) expansion= 2.32 cc



(c) expansion= 5.30 cc



(d) expansion= 12.9 cc

Fig. 5 - Growth of gas bubbles at various expansions for Test 4.

Fig.6- Gas production from the core into the top cap.

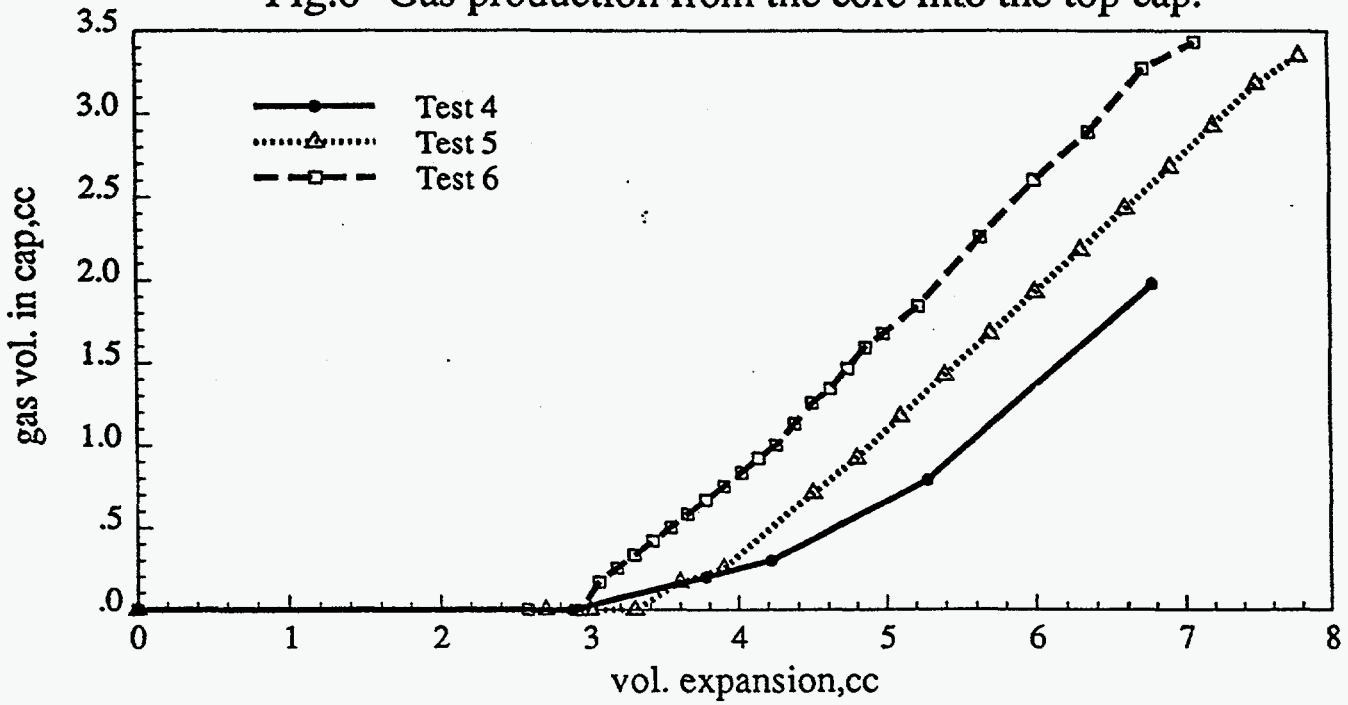
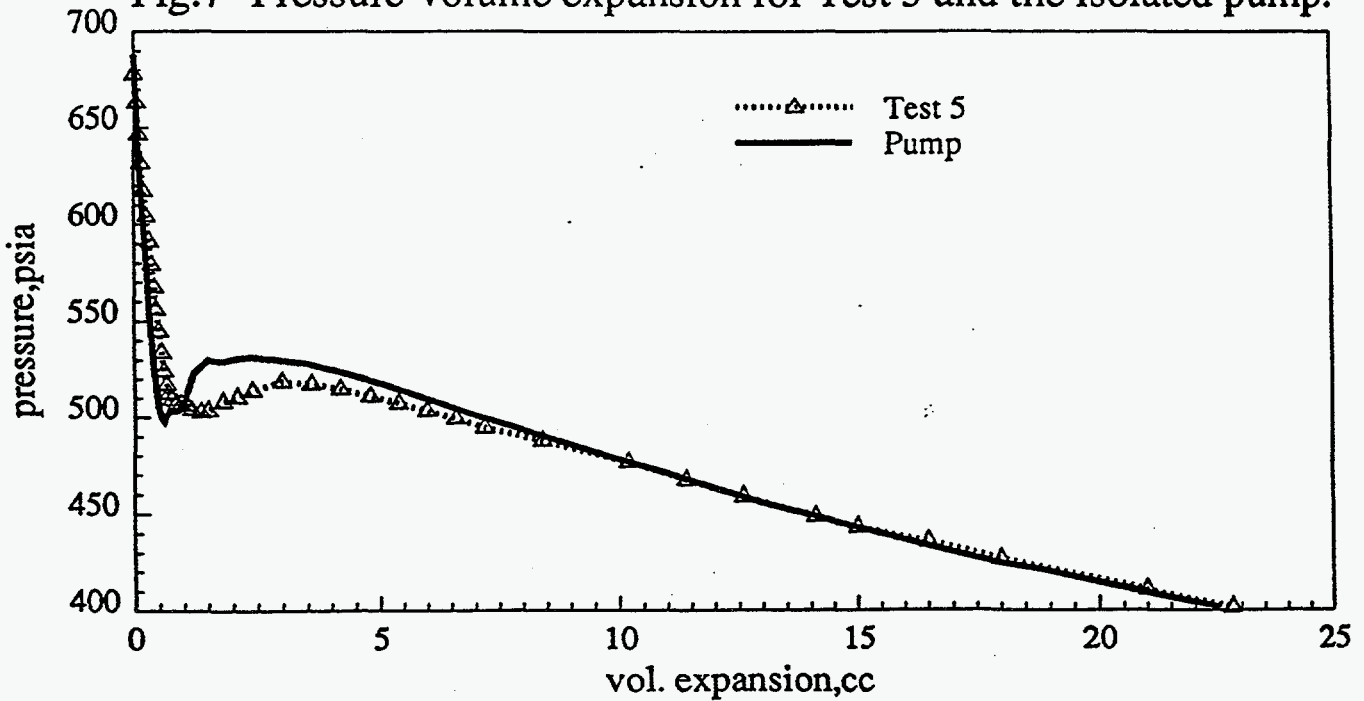
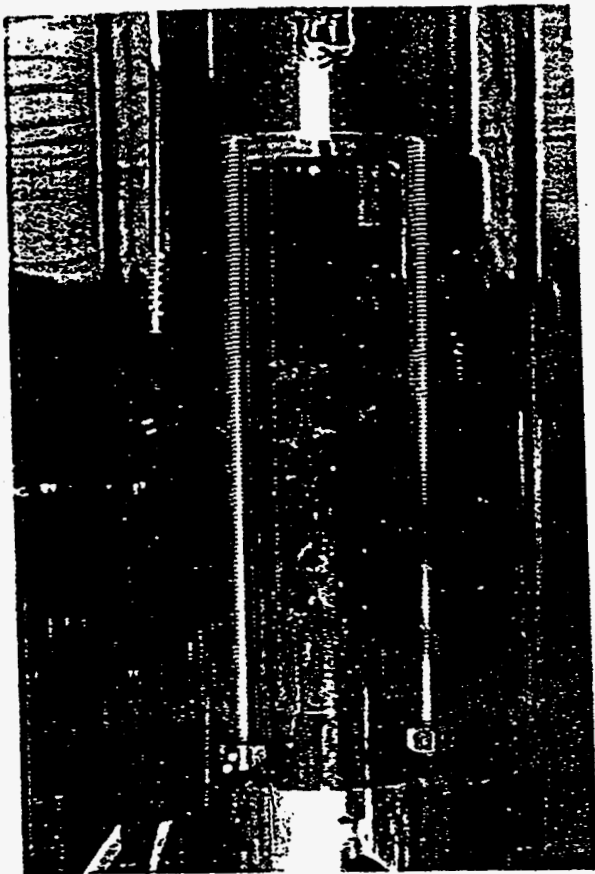
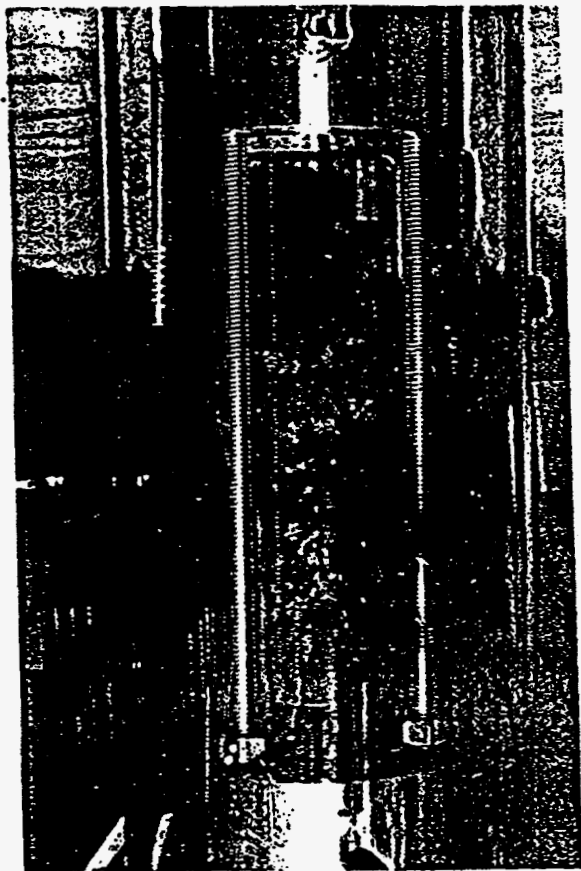


Fig.7- Pressure-volume expansion for Test 5 and the isolated pump.

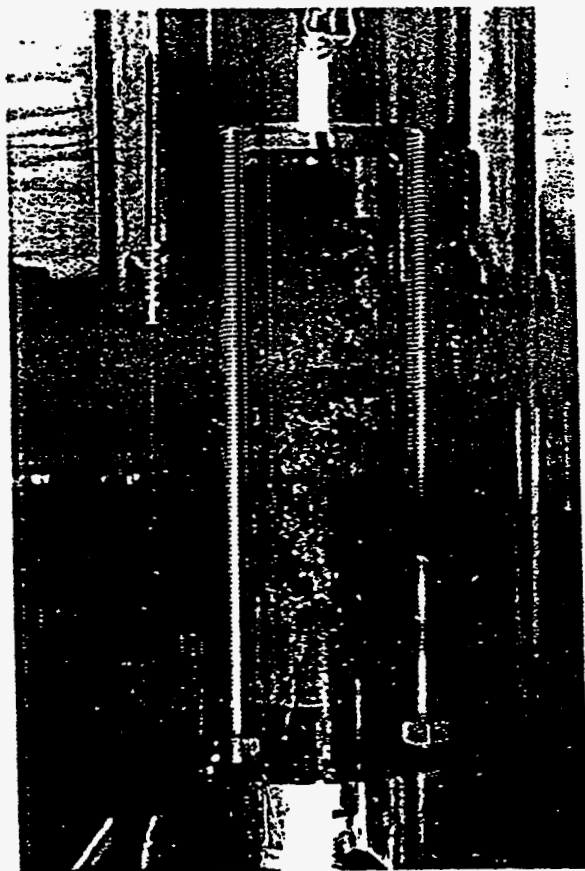




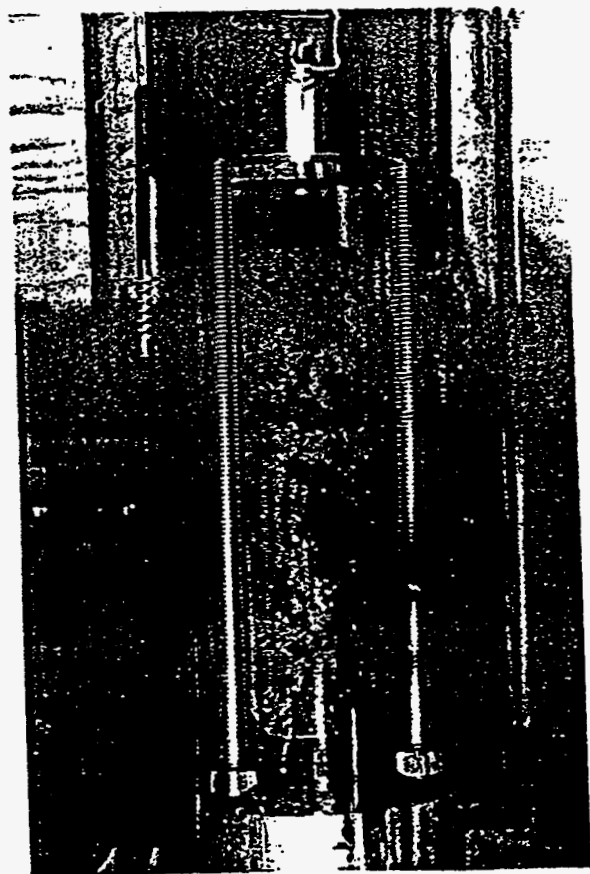
(a) expansion= 1.20 cc



(b) expansion= 1.45 cc

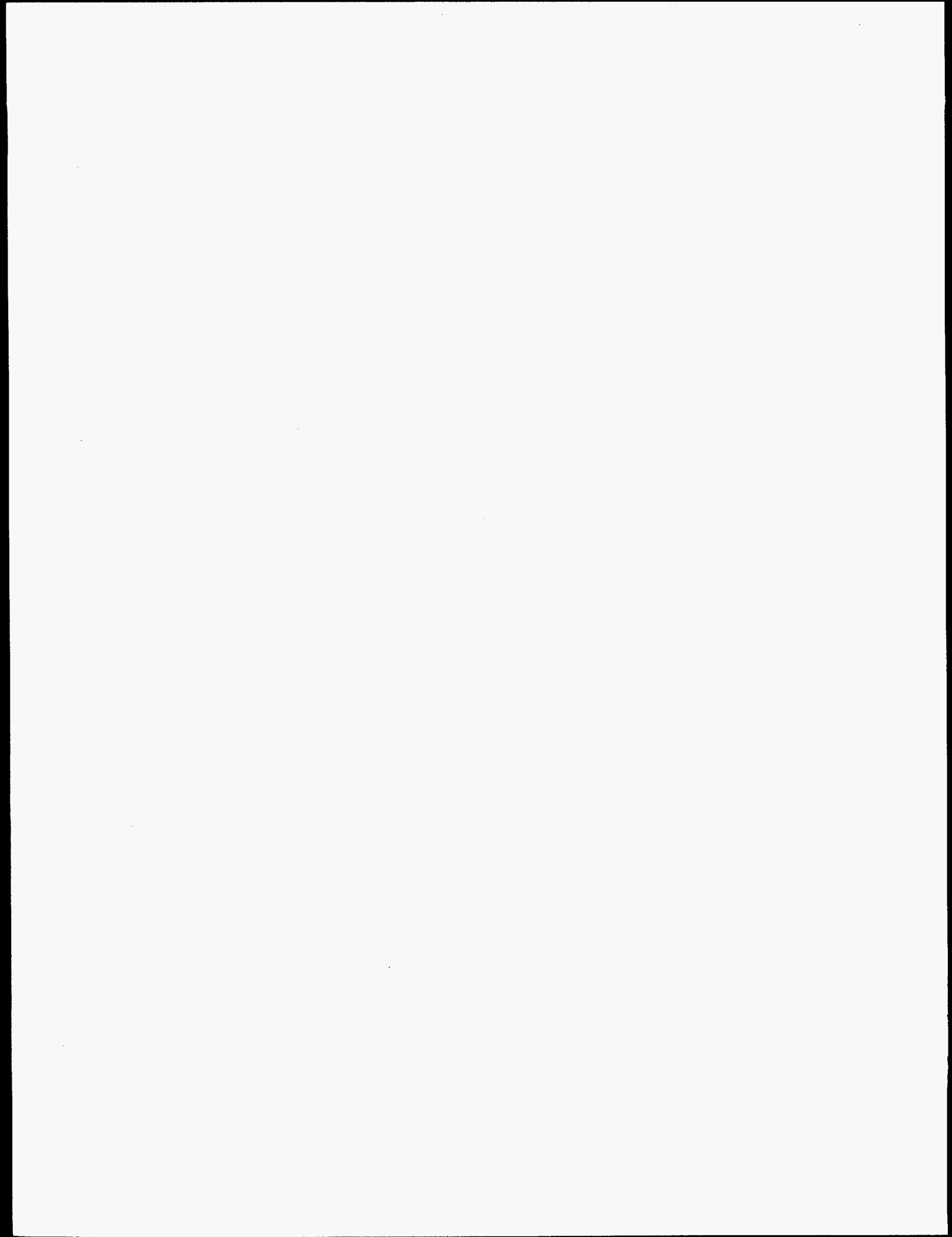


(c) expansion= 2.10 cc



(d) expansion= 2.70 cc

Fig. 8- Growth of gas bubbles at various expansions for Test 5.



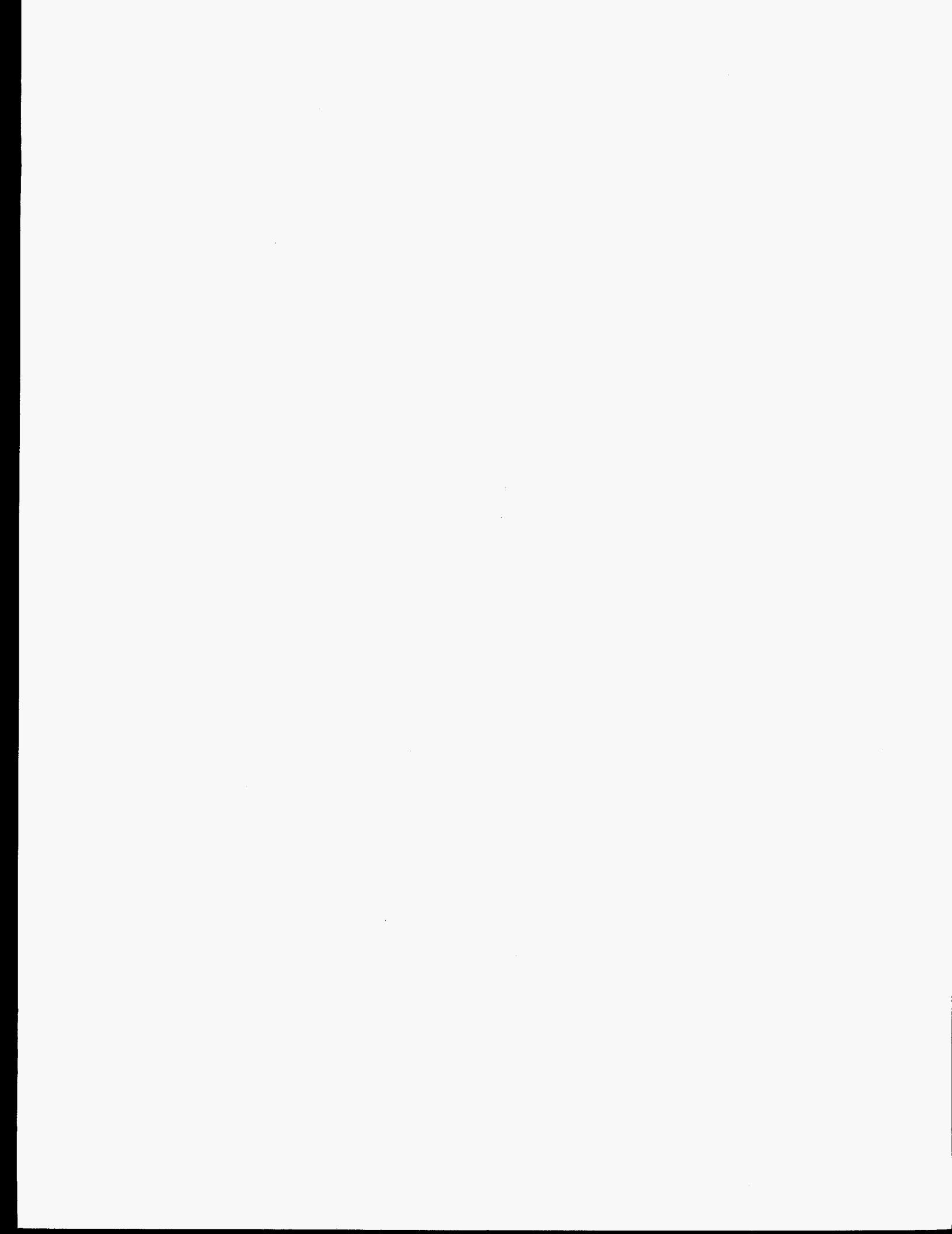
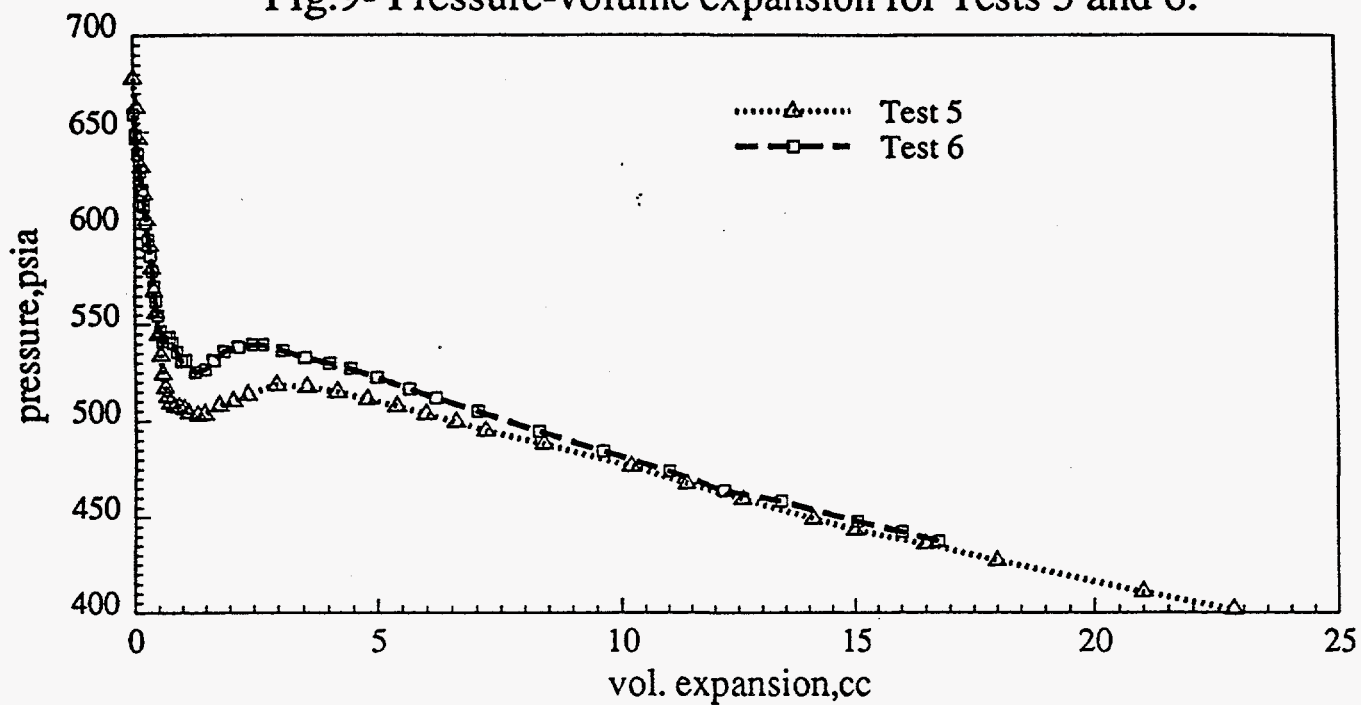


Fig.9- Pressure-volume expansion for Tests 5 and 6.



CHAPTER VIII

A Phenomenological Network Model of Critical Condensate Saturation

Fang Fang

Abbas Firoozabadi

Reservoir Engineering Research Institute

Maghsood Abbaszadeh

Japan National Oil Corporation

Clay Radke

University of California at Berkeley

SUMMARY

We have developed a phenomenological network model for critical condensate saturation. This model reveals that critical condensate saturation is a function of surface tension and contact angle hysteresis. On the other hand, residual oil saturation does not have such a dependency. Consequently, the selection of fluids in laboratory measurements for gas condensate systems should be made with care.

INTRODUCTION

Gas condensate reservoirs are becoming increasingly important; many new hydrocarbon reservoirs found in recent years are gas condensate reservoirs. These reservoirs, from a recovery and deliverability standpoint, may have significant differences from oil reservoirs. Prior to reaching the dew point pressure, the flow of gas in porous media is similar to that of undersaturated oil. When the pressure, either in the wellbore, or in the reservoir, drops below the dew point pressure, a new liquid condensate phase appears. The saturation of the new phase has to reach a threshold value in order to become mobile, provided the surface tension is higher than a critical value¹ (say $\sigma \geq 0.01$ dyne/cm). This threshold value is called critical condensate saturation, S_{cc} . When $\sigma < \sigma_c$, the critical contact angle, $\theta_c = 0^\circ$ and therefore the liquid condensate will perfectly wet the rock. The phenomenon of critical point wetting¹ for a near critical condensate fluid in porous media is very complicated due to the chemical heterogeneity of the rock surface and the presence of the interstitial water². For $\sigma < \sigma_c$, the new liquid phase spreads as a thin liquid film and film flow may occur. Consequently, S_{cc} may be very low, say less than 1 to 2 percent. For $\sigma > \sigma_c$, which is often the case, the new liquid phase is hypothesized to form liquid bridges between the walls of the pore network. For this case, the corresponding S_{cc} may be high.

The formation of a new gas phase, when the pressure of an undersaturated oil is lowered below the bubble point pressure, is followed by critical gas saturation, S_{cr} . There are fundamental differences between S_{cc} and S_{cr} . Critical gas saturation develops from the bubble nucleation in porous media³ and its value is often of the order of 1 to 5 percent. Critical condensate saturation results from retrograde condensation in porous media, and the measured values are in the range of 10 to 50 percent⁴⁻⁸. Such high values may imply that critical condensate saturation could be

similar to residual saturation in oil reservoirs. Residual oil saturation, S_{or} , is established by displacement. Since S_{cc} results from the in-situ liquid formation, and S_{or} is established by displacement, it is reasonable to believe that they are two different entities. S_{or} is not sensitive to the surface tension except at very low values. It stays constant with increasing surface tension above a certain value. However, the dependency of S_{cc} on surface tension is unknown. It is also highly desirable to examine the relationship between surface tension, gravity and critical condensate saturation. Currently, there is no theoretical model for critical condensate saturation. The main purpose of this work is to develop a phenomenological network model to understand the effect of surface tension and gravity on S_{cc} .

We have embarked on a theoretical investigation for the understanding of: 1) the mechanisms of in-situ liquid formation and flow, and 2) the difference between two-phase flow from external displacement and from in-situ liquid formation (internal). The first objective is mainly to address S_{cc} , and the second objective is well deliverability of gas condensate reservoirs. In this paper, the results of the work on S_{cc} is presented.

S_{or} In a Single Tube

It is well known that in a single tube, S_{or} and the $P_c - S_w$ relationship depend on the shape of the tube. Refs. 9 to 12 provide the capillary pressure saturation relationships for the circular, triangular, rectangular and curved triangular cross-section tubes. Fig. 1 displays various plots of the imbibition capillary pressure.

For a circular capillary tube of radius r , filled with a liquid and immersed in another fluid, if $P_c < 2\sigma \cos\theta / r$ is imposed, the tube will become empty; consequently, the concept of residual saturation does not apply to a capillary tube with a circular cross-section. The tube can be either empty or full.

Fig. 1a shows the imbibition capillary pressure-saturation for a triangular tube where $P_c / (\sigma / a)$ is the dimensionless capillary pressure, and a is the side length of the triangle. Note that residual nonwetting phase saturation, S_{or} , (shown by an open circle) is independent of the surface tension while capillary pressure, P_c , increases with surface tension.

The imbibition $P_c - S_w$ results for a square tube are shown in Fig. 1b. Parameter x on the y -axis denotes the side length of the square. Similar to a triangular tube, residual nonwetting phase saturation, S_{or} , is independent of the surface tension and changes with contact angle.

The imbibition $P_c - S_w$ relationship for a curved triangular tube which incorporates pore angularity is different from the shapes of triangular and rectangular tubes. Princen reasons that pore angularity is an important element of capillary pressure in porous media.¹¹ The examination of the $P_c - S_w$ plot shown in Fig. 1c (r is the radius of the side curve) reveals both positive and negative P_c for $\theta = 75^\circ$, but similar to previous shapes, S_{or} , is independent of the surface tension.

S_{cc} In a Single Tube

In the following, we will establish that the liquid holdup (i.e., critical condensate saturation, S_{cc}) in various tube geometries from the in-situ liquid formation, has features that are different from S_{or} :

Circular cross-section tube. Consider a circular capillary tube of radius r shown in Fig. 2. Assuming in-situ liquid condensation of height h in the tube, the force balance on the liquid column gives:

$$P_R - P_A = \frac{2\sigma}{r}(\cos\theta_R - \cos\theta_A) - \Delta\rho gh \quad (1)$$

where subscripts R and A stand for receding and advancing interfaces (i.e., θ_R receding contact angle), and P_R and P_A represent the pressures on the gas sides. In case of contact angle hysteresis, $\theta_A > \theta_R$. (The dashed interfaces in Fig. 2 have the same contact angle)

The liquid column will flow only when

$$h \geq \frac{2\sigma}{\Delta\rho gr}(\cos\theta_R - \cos\theta_A) - \frac{(P_R - P_A)}{\Delta\rho g} \quad (2)$$

Assuming the gas pressure difference on both sides of the liquid column to be small, $P_R - P_A \approx 0$, then Eq. 2 implies that if $\theta_R = \theta_A$, no matter how small the liquid height and how large the surface tension are, the liquid will flow. It also reveals that critical condensate saturation in a bundle of capillary tubes, 1) increases with an increase in the surface tension, 2) increases with a decrease in the diameter, and 3) increases with an increase in the contact angle hysteresis (the difference between the advancing and the receding contact angle).

Triangular cross-section tube. The height of the liquid column from the in-situ condensation in a triangular-shaped tube is given by (see Figs. 3b and 4)

$$h = \frac{4\sqrt{3}\sigma}{\Delta\rho ga}(\cos\theta_R - \cos\theta_A) \quad (3)$$

where gas pressure is assumed to be constant at both ends of the liquid column (see the derivation in the appendix). From the above equation, we note that the amount of liquid that a triangular-shaped tube can hold is also proportional to surface tension and is related to contact angle hysteresis which is similar to a circular tube.

Curved triangular cross-section tube. The height of the liquid holdup in a curved triangular tube is given by (see Figs. 3c and 4)

$$h = \frac{\sigma}{\Delta\rho gr} \left[\frac{(l_{1R} \cos\theta_R + l_{2R})}{A_R/r} - \frac{(l_{1A} \cos\theta_A + l_{2A})}{A_A/r} \right] \quad (4)$$

The parameters l_{1R} , l_{2R} , l_{1A} , l_{2A} , A_R and A_A are defined in the appendix together with the derivation of Eq. 4. In the above equation, similar to Eq. 3, the critical condensate saturation depends on the surface tension and the areal size of the tube. It is also related to the contact angle hysteresis.

A simple calculation may be useful to appreciate which of the tube geometries will hold more liquid. Let's assume $\sigma = 2$ dynes/cm, $\Delta\rho = 0.3$ g/cm³, $\theta_R = 0^\circ$, $\theta_A = 10^\circ$ and the cross-sectional area of the tube = 1 μm^2 . For a circular tube, $r = 0.56$ μm , and Eq. 2 provides $h = 3.6$ cm; for a triangular tube, $a = 1.52$ μm , from Eq. 3, $h = 4.64$ cm; for a curved triangular tube, from Eqs. A-12 and 4, $\alpha_A = 30^\circ$, $\alpha_R = 28.65^\circ$ and $h = 7.5$ cm. Therefore, the curved triangular tube can hold more liquid than circular or triangular tubes.

S_{cc} In a Network

A variety of network configurations and shapes are used to represent porous media. In this work, we use a very simple network composed of vertical interconnected circular capillary tubes. A size

distribution for the network can be assigned. To model the condensate formation and flow in a network, since there are no existing rules for in-situ liquid phase formation, we have to establish such rules for both a single tube and intersections of the network. Theoretical considerations guide us towards this end.

Liquid forming in a single tube. Consider two capillary tubes with radii r_1 and r_2 ; assume $r_1 < r_2$. The vapor pressure of a pure component in tube r_1 will be less than in tube r_2 . The decrease in vapor pressure for a curved interface is well known; the Kelvin equation provides the relationship between the vapor pressure and the interface curvature¹³. However, for hydrocarbon mixtures, the saturation pressure often increases as the interface curvature increases. In other words, the saturation pressure in tube r_1 will be more than the saturation pressure in tube r_2 . The effect of curvature on the saturation pressure of hydrocarbon mixtures is discussed in Ref. 14. In this work, we assume that when the radius of a circular capillary tube is smaller than a "threshold radius", r_p , the gas will condense in the tube and as a result, the condensate will form a liquid bridge provided $\sigma > \sigma_c$. Once a liquid bridge forms, it will grow. From the force balance:

$$h_1 = \frac{2\sigma}{\rho g r_1} (\cos \theta_R - \cos \theta_A) \quad (5)$$

where h_1 is the height of the liquid column when the gas pressure is constant and gas density is neglected. The advancing contact angle at the bottom interface θ_A can change from θ_{A0} to θ_{Amax} , where $\theta_{A0} \geq \theta_R$ and θ_{Amax} is the limiting advancing contact angle; $\theta_{A0} \leq \theta_A \leq \theta_{Amax}$. We assume that the receding contact angle θ_R at the top interface is constant. When the length of the liquid column, h_1 , exceeds $(2\sigma/\rho g r_1)(\cos \theta_R - \cos \theta_{Amax})$, it becomes unstable and moves downward to the end of the tube.

Liquid flow in the intersections. Figs. 5a-h depict the process of liquid formation, growth and flow in two connecting intersections. In this figure, the radii of the four intersecting ducts in intersection 1 and intersection 2 are r_1, r_2, r_3, r_4 and r'_1, r'_2, r'_3, r'_4 respectively. We assume that $r_2 < r_4$ and only $r_1 < r_p$; liquid first condenses in duct 1, and forms a liquid column, as shown in Fig. 5a.

Further gas condensation allows the length of the liquid column to increase, and the advancing contact angle will also increase. When the length of the liquid column, h_1 , exceeds $(2\sigma/\rho g r_1)(\cos \theta_R - \cos \theta_{Amax})$, the liquid column becomes unstable and moves downward to the end of the duct at point A and stops. Due to the edge effect, the advancing angle θ_A continuously increases from θ_{Amax} to 90° at point A, as more liquid forms in duct 1. This causes the liquid height, h_1 , to increase to a maximum, $(2\sigma/\rho g r_1)\cos \theta_R$ (see Fig. 5b). Further condensation causes the introduction of liquid to the intersection as shown in Fig. 5c, where the contact angle is θ_A . This step is accompanied by a small decrease in liquid height, h_1 . With more liquid condensing, the liquid column in duct 1 increases its height back to the maximum, $(2\sigma/\rho g r_1)\cos \theta_R$ and finally the liquid in the intersection expands to a maximum radius r_{max} . At r_{max} , the liquid touches corner C (see Fig. 5c) and becomes unstable and 1) its interface may break into two new interfaces; one interface in duct 2, and the other interface in the intersection as shown in Fig. 5d; or 2) the liquid in duct 1 may flow down immediately to provide liquid for the new configuration shown in Fig. 5e. The expression for r_{max} is obtained by using a force balance:

$$r_{\max} = \frac{2r_2 \cos \theta_{A_{\max}} + \sqrt{4r_2^2 + r_3^2 \sin^2 \theta_{A_{\max}}}}{\sin \theta_{A_{\max}}} \quad (6)$$

For the configuration in Fig. 5d, liquid flowing into duct 2 from duct 1 is determined from the new liquid column height in duct 1. From a force balance in duct 1 and duct 2, the maximum liquid height in duct 1 is found to be:

$$h_1' = \frac{2\sigma}{\rho g} \left(\frac{\cos \theta_R}{r_1} - \frac{\cos \theta_{A_{\max}}}{r_2} \right) \quad (7)$$

provided $R = r_2 / \cos \theta_A$ (see Fig. 5d). Once the liquid pressure in the intersection exceeds the liquid pressure in duct 2, the configuration shown in Fig. 5d becomes unstable and the configuration in Fig. 5e develops.

For the configuration shown in Fig. 5e, the fact that the liquid pressure in the interface may be higher than liquid pressure in duct 2, the liquid in intersection 1 is pulled into duct 2, until it breaks to two new interfaces in duct 1 and duct 2. When more gas condenses, the contact angle at the bottom interface of duct 1 changes from $\theta_{A_{\max}}$ to 90° as the height of liquid column in duct 1 increases to $(2\sigma/\rho g r_1) \cos \theta_R$. If there is still more gas condensing in duct 1, the condensed liquid flows into duct 2 through the corner while the height of liquid column in duct 1 remains the same. As more gas condenses, the liquid fills duct 2, and the contact angles at both edges increase to 90° . Finally liquid enters intersection 2 as shown in Fig. 5f. The curvature of the liquid interface in intersection 1 changes to the convex shape and the maximum height of the liquid column in duct 1 increases to $(2\sigma/\rho g)(\cos \theta_R / r_1 + 1/R_1)$ with further condensation. The liquid bridge in intersection 2 keeps growing until it touches corner D and breaks into new interfaces. The interface in intersection 1 also breaks to two new interfaces in ducts 1 and 2. If $r_1' < r_3'$, the stable configuration shown in Fig. 5g(1) realizes provided the liquid pressure in the intersection and duct 2 can be the same. If $r_1' > r_3'$, the new interface shown in Fig. 5g(2) with the dashed line is unstable. Liquid will be pulled into duct 3' and the stable configuration as shown with the solid line will evolve.

The interface in intersection 2 of Fig. 5g(1) with further condensation expands until it touches the other corner E, then it breaks to two new interfaces as shown in Figs. 5h(1a) and 5h(1b). The configurations in Figs. 5h(1a) and 5h(1b) are for different duct sizes as shown in these figures. In Fig. 5h(1a), with further condensation, duct 4' will be filled and then the vertical liquid column from ducts 1' and 3' will increase till it becomes unstable leading to the configuration in Fig. 5i.

When the liquid first forms in a horizontal capillary duct ($r < r_p$), the liquid bridge is stable until it reaches the intersections; then the contact angles at both edges increase to 90° (i.e., flat interface). There will be no further condensation on those flat interfaces. The maximum liquid length in a horizontal duct is the duct length.

In addition to the process described above, we also assume that when a liquid bridge first forms in a duct, it will appear in its middle. When two liquid bridges have been established in a single duct as result of flow from the neighboring ducts, these two liquid bridges upon touching each other form a single bridge or column. The rules governing the stability of a liquid column or a liquid bridge are based on the force balance which is the same as relating the pressures at various points in a liquid medium; in the horizontal direction, liquid pressure should be the same in a continuous liquid medium, and in the vertical direction, liquid pressure should be in hydrostatic equilibrium.

Network specification. We represent the porous media by a two-dimensional vertical square network with randomly sized circular capillary ducts. In this work, we use a network with dimensions of 20×20 intersections. The radius of each duct is randomly chosen from a log-normal size distribution function, shown in Fig. 6. The average radius of the ducts is $23.06 \mu m$, and the standard deviation is 5.74. For simplicity, we assume each capillary duct has the same length, $l = 6000 \mu m$. The total PV of the network is 8.89 mm^3 . Fig. 7 provides the network used in this work. The thickness of the lines is proportional to the duct diameter.

PROCEDURE AND RESULTS

Initially, the network is fully saturated with gas at a pressure above the dew point pressure. The gas pressure is then decreased to allow the liquid to form. In our simulation, we modify the continuous condensation process with discrete steps. During every step, a small amount of liquid forms. At the saturation point, those ducts with $r < r_p$ allow condensation in the form of a liquid bridge. Later on those ducts with radii larger than r_p which contain liquid bridges also serve as condensation sites. In this work, r_p is assumed to be $20 \mu m$, and the amount of condensation per step in a liquid bridge is $200 \mu m^3$. For simplicity we keep surface tension constant and assume that it is independent of pressure. This restriction on surface tension can be easily removed. We also assume that the gas pressure is constant in the entire network and the effect of gas pressure on the gas-liquid interface is also neglected.

Fig. 8 shows the liquid distributions in the network for $\theta_R = 0^\circ, \theta_{A_{\max}} = 10^\circ$, $\rho = 0.5 \text{ g/cm}^3$, $\sigma = 0.1 \text{ dyne/cm}$ at various stages of pressure depletion where liquid condensation increases.

Fig. 8a shows the condensate distribution in the network at $T = 10,000$ steps. The condensate saturation is 5.62%. Only small ducts have formed liquid bridges. There is little difference in condensate volume between vertical and horizontal ducts. This means that the liquid in most vertical ducts is still stable.

Fig. 8b shows the condensate distribution in the network at $T = 25,000$ steps. At this stage, the condensate saturation is $S_c = 16.6\%$. The small ducts and some nearby large ducts have formed liquid bridges, but the condensate is not well connected to the outlet.

Fig. 8c shows the condensate distribution in the network at $T = 35,183$ steps. At this stage, the condensate paths have been well established, the liquid is mobile, and the network produces condensate at a stable rate. The saturation is $S_c = 26.0\%$. Critical condensate saturation is defined as the liquid saturation at which the liquid production from the network becomes sustainable. Thus, in Fig. 8c the network has reached critical condensate saturation.

Critical condensate saturation, S_{cc} , of the network is obtained from

$$S_{cc} = \frac{V_{total} - V_{out}}{PV} \quad (8)$$

where V_{total} is the total liquid condensed in the network, V_{out} is the total liquid production of the network, and PV is the total porous volume. For this example, $V_{total} = 2.31 \text{ mm}^3$, $V_{out} = 7.25 \times 10^{-5} \text{ mm}^3$ and $PV = 8.89 \text{ mm}^3$.

Effect of various parameters. Fig. 9 displays the calculated results for critical condensate saturation, S_{cc} , for various values of surface tension and contact angle hysteresis. The calculations

are based on the 20×20 intersections network described above. The figure reveals that surface tension has a pronounced influence on critical condensate saturation. As surface tension increases, critical condensate saturation also increases. The effect of contact angle hysteresis is somewhat different. Contact angle hysteresis, when $\theta_R = 0^\circ$, and θ_{Amax} varies from 1° to 10° affects critical condensate saturation (Fig. 9a). However, contact angle hysteresis within the range of 10° to 30° seems to have a small effect on S_{cc} . The oscillations in S_{cc} for low values of surface tension are believed to be due to the network size (see Fig. 9b).

In order to study the sensitivity of the model to the network size, we increased the network size to 40×40 intersections. The advancing (maximum) and receding contact angles are $\theta_{Amax} = 20^\circ$ and $\theta_R = 0^\circ$. Other parameters are kept the same. The results of S_{cc} calculations are provided in Fig. 10. There is little effect of network size on S_{cc} values at high values of surface tension. The oscillations at low values of surface tension are due to the network size.

S_{or} In a Network

Many authors discuss the displacement process by using a wide variety of network models. Here, the simple network described above is also used to study two-phase displacement to establish S_{or} . The network for displacement is similar to the one used by Lenormand et al¹⁵; we use circular tubes rather than the rectangular tubes.

Similar to Lenormand et al's model, the imbibition displacement follows the rules that: 1) in any duct, if the capillary pressure is equal to or higher than the invasion pressure, the invading liquid enters the duct and stops at the other end; 2) every duct is either full of wetting phase or non-wetting phase. (i.e. piston-type motion as shown in Fig. 11a); 3) snap-off motion occurs only when the piston-type motion is not possible for topological reasons as shown in Figs. 11b, 11c; 4) when the non-wetting fluid is in one duct at the intersection, the imbibition I1-type motion occurs as shown in Fig. 11d; 5) when the non-wetting fluid is only in two adjacent ducts at the intersection, the imbibition I2-type motion occurs as shown in Fig. 11e.

PROCEDURE AND RESULTS

In our S_{or} network model, we first perform a major drainage, then decrease the capillary pressure by increasing the water pressure to accomplish imbibition. From the drainage-imbibition process, we can determine residual oil saturation. The effect of gravity on S_{or} is neglected.

We separate the ducts in the network into seven groups according to their sizes, as shown in Table 1. Initially, the network is fully saturated with water (i.e., wetting phase). The water reservoir is connected to the network at the top boundary. The oil (non-wetting phase) reservoir is connected to the network at the bottom boundary.

In the drainage process, oil is the invading phase while water is the invaded phase. We increase the oil reservoir pressure, P_o , and keep the water reservoir pressure, P_w , constant. At first, the oil pressure is increased gradually to the extent that it can enter the ducts which have sizes among groups 4 to 7. The oil phase does not form continuous paths to the top outlet at this pressure. We then increase the oil pressure to drain water in the ducts which have sizes in group 3. The oil at this pressure builds continuous paths to the top outlet. The oil pressure again is increased to allow water to be drained from all the ducts in which their paths have not been blocked. Some water is trapped no matter how much we increase the oil pressure. The trapped water is the residual water, and the water saturation is residual water saturation, S_{wr} . This is the end of the major drainage process.

After this initial drainage, we start an imbibition process where water is the invading phase and oil is the invaded phase. We keep increasing the water reservoir pressure, P_w , while keeping the oil reservoir pressure, P_o , constant. As we increase water pressure gradually, the capillary pressure allows water to enter the network. First, only piston-type displacement happens. We then increase water pressure further which causes the snap-off, imbibition I1- and I2-types displacements. When all the oil left in the network is the trapped oil, the imbibition process ends, and the oil saturation is residual oil saturation, S_{or} .

In order to investigate the relationship between S_{or} and surface tension, we change the surface tension and repeat the drainage-imbibition process; S_{or} values at different surface tensions are obtained which are shown in Fig. 12. The figure reveals that when surface tension is lower than 0.25 dyne/cm, S_{or} increases with increasing surface tension. When surface tension is higher than 0.25 dyne/cm, S_{or} is independent of surface tension. Fig. 13 shows residual oil saturation for a low water-oil interfacial tension of 0.25 dyne/cm ($S_{or} = 48.5\%$). Note the end effects on the right and left sides cause the oil to be trapped. Comparison of this figure with Fig. 8 reveals that S_{or} and S_{cc} are different entities.

DISCUSSION AND CONCLUSIONS

In this work, we have used simple tube geometries and a simple network for the representation of porous media. With these simple geometries, surface tension and contact angle hysteresis are key parameters of the critical condensate saturation model. Surface tension for gas condensate systems is often known. However, the current knowledge on contact angle hysteresis for gas condensate systems on a rock substrate is very little. Since a rock substrate is not smooth, one may expect contact angle hysteresis. In reservoir engineering calculation, it is often assumed that the contact angle between the oil and gas phases on a rock substrate is zero (θ measured through the oil phase). However, this does not mean that the contact angle hysteresis is zero. Very simple laboratory experiments using capillary tubes in the vertical position reveal that liquid in equilibrium with its vapor does not flow. The only reason for the liquid holdup is the contact angle hysteresis. Since contact angle hysteresis may depend on the type of hydrocarbons, one may speculate that the contact angle hysteresis for a model fluid such as C_1/nC_4 and an actual condensate may not be the same.

The phenomenological model described in this paper leads to the following conclusions:

1. Critical condensate saturation, S_{cc} , in a network of circular capillary tubes is similar to that of a single tube; S_{cc} increases with an increase in surface tension.
2. Critical condensate saturation in a network of capillary tubes is affected by contact angle hysteresis within the range of 0° to 10° ; when contact angle hysteresis increases, S_{cc} also increases. S_{cc} is only slightly affected by the contact angle hysteresis in the range of 10° to 30° .
3. There is an essential distinction between critical condensate saturation, S_{cc} , and residual nonwetting saturation, S_{or} . Above a certain value of surface tension, S_{or} is independent of this parameter in a capillary tube network. However, S_{cc} is a function of surface tension both in a capillary tube network and in a single tube.

The above conclusions are based on the balance between the capillary and gravity forces for S_{cc} . The conclusions, will, therefore, apply to critical condensate saturation in a vertical system, where viscous forces are neglected. S_{cc} in the horizontal direction when viscous forces are applied requires the examination of pressure effects, which are not covered in this work.

NOMENCLATURE

- a = side length of an equilateral triangular tube
- A = liquid cross-section area
- l = duct length
- l_1 = parameter defined by Eqs. A-4 and A-15
- l_2 = parameter defined by Eqs. A-5 and A-16
- h = height of liquid bridge
- P = pressure
- P_c = capillary pressure
- PV = pore volume
- r = radius of a tube, also radius of the side curve of curved triangle
- R = radius of interface
- r_p = threshold radius
- S = saturation
- S_{cc} = critical condensate saturation
- S_{or} = residual oil saturation
- S_{cr} = critical gas saturation
- V = volume of condensate

Greek letters

- α = angle defined for a curved triangular tube
- θ = contact angle
- θ_c = critical contact angle
- ρ = density
- $\Delta\rho$ = density difference between liquid and gas phases
- σ = surface tension
- σ_c = critical surface tension (corresponding to $\theta_c = 0^\circ$)

Subscripts

- A = advancing
- C = condensate
- CC = critical condensate
- max = maximum
- out = liquid flowing out of the network
- R = receding
- $total$ = total condensate that has been condensed

REFERENCES

1. Cahn, J. W.: "Critical Point Wetting," *Journal of Chemical Physics* (1977) 66, 3667-72
2. Williams, J. K., and Dawe, R. A.: "Near-Critical condensate Fluid Behavior in Porous Media - A Modeling Approach," *SPE Reservoir Engineering* (May 1989) 221-227.
3. Firoozabadi, A., and Kashchiev, D.: "Pressure and Volume Evolution During Gas Phase Formation in Solution Gas Drive Process," *SPE Journal* (Sept. 1996)
4. Saeidi, A., and Handy, L. L.: "Flow and Phase Behavior of Gas Condensate Volatile Oils in Porous Media," SPE 4891, Society of Petroleum Engineers, 1974.
5. Gravier, J. F., Lemouzy, P., Barroux, C., and Abed, A. F.: "Determination of Gas-Condensate Relative Permeability on Whole Cores Under Reservoir Conditions," *SPE Formation Evaluation J.* (Feb. 1986) 9-15.
6. Danesh, A., Henderson, G. D., and Peden, J. M.: "Experimental Investigation of Critical Condensate Saturation and its Dependence on Interstitial Water Saturation in Water-Wet Rocks," *SPE Reservoir Engineering* (Aug. 1991) 336-342.
7. Chen, H. L., Wilson, S. D., and Monger-McClure, T. G.: "Determination of Relative Permeability and Recovery for North Sea Gas Condensate Reservoirs," SPE 30769, Society of Petroleum Engineers, 1995.
8. Munkerud, P. K., and Toaster, O.: "The Effects of Interfacial Tension and Spreading on Relative Permeability in Gas Condensate Systems," Eighth European Symposium on Improved Oil Recovery, May 15-17, 1995, Vienna, Austria.
9. Princen, H. M.: "Capillary phenomena in Assemblies of Parallel Cylinders," (part 1), *Journal of Colloid & Interface Sci.* (1969) 69-75.
10. Princen, H. M.: "Capillary phenomena in Assemblies of Parallel Cylinders," (part 2), *Journal of Colloid & Interface Sci.* (1969) 359-368.
11. Princen, H. M.: "Capillary Pressure Behavior in Pores with Curved Triangular Cross Section: Effect of Wettability and Pore Size Distribution," *Journal of Colloid & Interface Sci.* (1992) 221-230.
12. Mason, G., and Morrow, N. R.: "Capillary Behavior of a Perfectly Wetting Liquid in Irregular Triangular Tubes," *Journal of Colloid & Interface Sci.* (1991) 262-273.
13. Defay, R., and Prigogine, I.: *Surface Tension and Adsorption*, Longmans, London (1966) Chapter XV and XVI.
14. Firoozabadi, A.: *Advanced Thermodynamics of Hydrocarbon Reservoirs*, Chapter 2, (in preparation).
15. Lenormand, R., Zarcone, C., and Sarr, A.: "Mechanisms of the Displacement of One Fluid by Another in a Network of Capillary Duets," *Journal of Fluid Mech.* (1983) 337-353.

ACKNOWLEDGEMENT

We thank Michael Riley for his help in the preparation of the paper. His comments are greatly appreciated.

Appendix: Critical Condensate Saturation (Liquid Holdup) Expressions

In the following derivations, the tube is assumed in a vertical position. First we will derive the expression for liquid holdup in an equilateral-triangular tube.

Triangular tube. Let's first derive the expressions for capillary rise in an equilateral triangular tube shown in Fig. 3 of the text (see Figs. 3a and 3b). For simplicity we will limit the derivations for $\theta < 60^\circ$. Fig. 3a depicts the vertical cross section across AD. The horizontal cross-section is shown in Fig. 3b. We assume that the interface is near-vertical for $h > h_1$, similar to the assumption made by Princen.⁹ When the whole column is at equilibrium, the force balance on the liquid column below $h = h_1$ is given by:

$$F_s = F_G \dots\dots\dots (A-1)$$

where the interfacial force F_s is given by

$$F_s = \sigma(l_1 \cos \theta + l_2) \dots\dots\dots (A-2)$$

and the gravity force F_G is given by

$$F_G = \Delta \rho g h_1 A_{h1} \dots\dots\dots (A-3)$$

In Eq. A-3 the gas density is neglected. l_1 is the length of the nonwetting phase-wetting phase interface in contact with the solid wall, l_2 is the length of the wetting phase in contact with the nonwetting phase and A_{h1} is the projected liquid cross-section area of the interface at $h = h_1$. From Fig. 3b

$$l_1 = 3 \left[a - 4R_1 \sin \left(\frac{\pi}{3} - \theta \right) \right] \dots\dots\dots (A-4)$$

$$l_2 = 3 \left(\frac{2}{3} \pi - 2\theta \right) R_1 \dots\dots\dots (A-5)$$

$$A_{h1} = \frac{\sqrt{3}}{4} a^2 - 3R_1^2 \left[\sqrt{3} \cos^2 \theta - \sin \theta \cos \theta - \left(\frac{\pi}{3} - \theta \right) \right] \dots\dots\dots (A-6)$$

The radius R_1 in Fig. 3b is given by the capillary pressure at $h = h_1$

$$P_{c1} = \Delta \rho g h_1 = \frac{2\sigma}{R_1} \dots\dots\dots (A-7)$$

Combining Eqs. A-1 to A-6 provides the expression for R_1

$$R_1 = \frac{a}{2\sqrt{3} \cos \theta} \quad (A-8)$$

The expression for h_1 is then readily obtained through $h_1 = 2\sigma / \Delta \rho g R_1$.

The next step is to obtain an expression for h , the liquid column in the vertical triangular tube (see Fig. 4). The basic concepts are the same as the capillary rise. There is a need to incorporate contact angle hysteresis so that the tube can hold a liquid column. We have to write the basic expression

$$P_{cA} = P_{cR} + \Delta\rho gh \dots\dots\dots (A-9)$$

where P_{cA} is the capillary pressure on the advancing meniscus and P_{cR} is the capillary pressure at the receding meniscus. Substitution of various parameters with appropriate contact angles in Eq. A-9 will provide Eq. 3 of the text.

Curved triangular tube. The capillary rise in an equilateral curved triangular tube is similar to that for an equilateral triangular tube but somewhat more complicated. Fig. 3a and Fig. 3c show the two cross sections. In the following, the derivations will be for a positive P_c .

The capillary pressure at $h = h_1$ (see Fig. 3a and Fig. 3c) is given by:

$$P_{c1} = 2\sigma/R_1 = \Delta\rho gh_1 \dots\dots\dots (A-10)$$

R_1 is obtained

$$R_1 = \frac{1 - \cos \alpha_1}{\cos(\alpha_1 + \theta)} r \dots\dots\dots (A-11)$$

where r is the radius of the curved triangle, and α_1 is obtained from

$$\left(\frac{\sqrt{3}}{3} - \frac{\pi}{6}\right) - (2 - \cos \alpha_1) \sin \alpha_1 - (1 - \cos \alpha_1)^2 \tan(\alpha_1 + \theta) + \alpha_1 - \left(\frac{\pi}{6} - \alpha_1\right) \cos \theta \frac{(1 - \cos \alpha_1)}{\cos(\alpha_1 + \theta)} = 0 \dots\dots\dots (A-12)$$

To obtain the capillary holdup height h in a curved-triangular tube, the force balance equations at the interfaces on both sides are written

$$F_{P_{cn}} = F_{\sigma n} \dots\dots\dots (A-13)$$

$$F_{P_{cn}} = P_{cn} A_n \dots\dots\dots (A-14)$$

where $n = A, R$; A and R represent advancing and receding interfaces, respectively and $F_{P_{cn}}$ is the capillary force balanced by the interfacial force $F_{\sigma n}$. The expression for F_{σ} is given by Eq. A-2 and parameters l_{1n} , l_{2n} , A_n ($n = A, R$) are given by

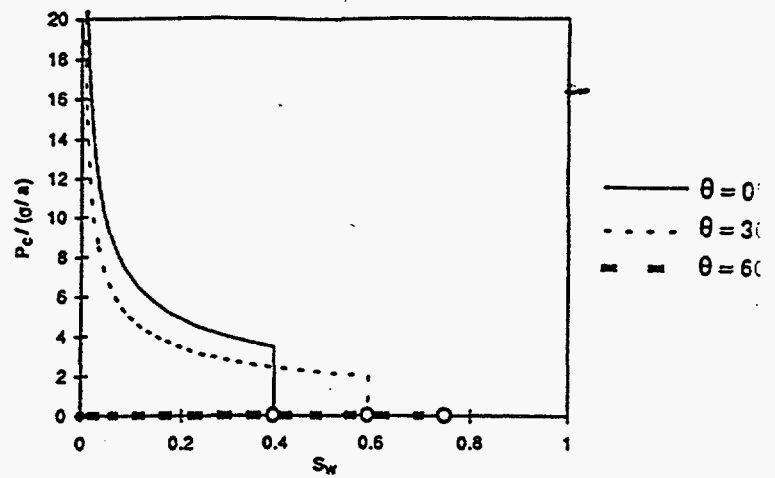
$$l_{1n} = 3r\left(\frac{\pi}{3} - 2\alpha_n\right) \dots\dots\dots (A-15)$$

$$l_{2n} = 3r[\pi - 2(\alpha_n + \theta)] \frac{1 - \cos \alpha_n}{\cos(\alpha_n + \theta)} \dots\dots\dots (A-16)$$

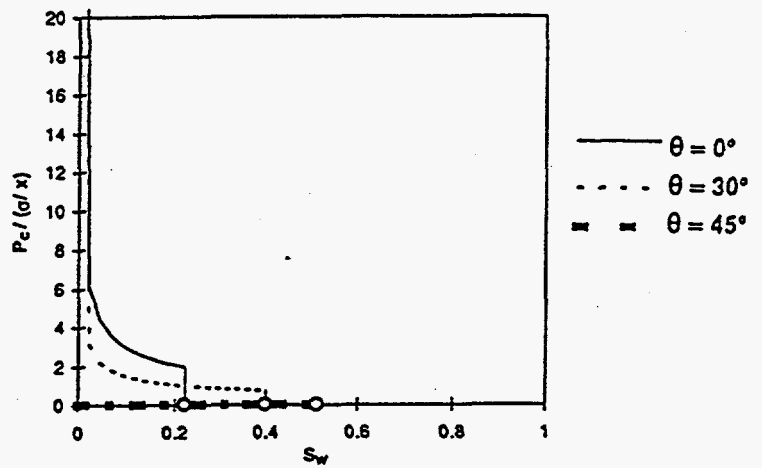
$$A_n = \left(\sqrt{3} - \frac{\pi}{2}\right)r^2 - 3r^2[(2 - \cos \alpha_n) \sin \alpha_n + (1 - \cos \alpha_n)^2 \tan(\alpha_n + \theta) - \left(\frac{\pi}{2} - (\alpha_n + \theta)\right) \frac{(1 - \cos \alpha_n)^2}{\cos^2(\alpha_n + \theta)} - \alpha_n] \dots\dots\dots (A-17)$$

Once the receding and advancing parameters are known, Eq. A-9 is used to obtain Eq. 4 of the text.

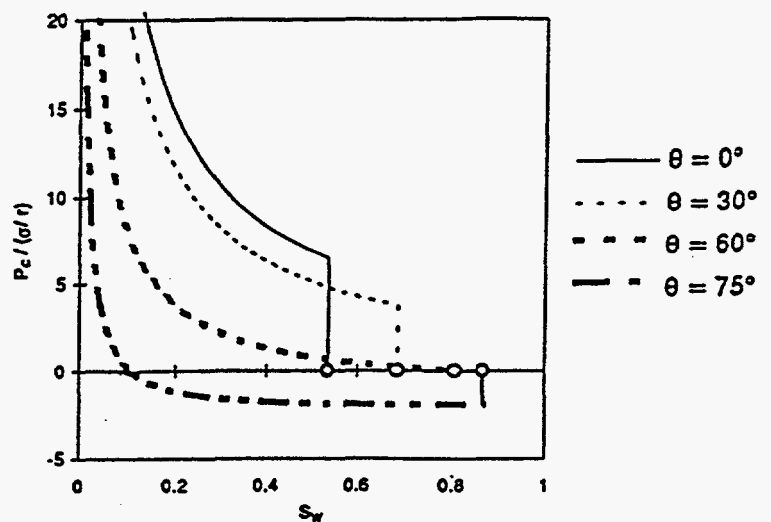
TABLE 1 – Different Groups of Radii (μm)	
Group 1	less than 10
Group 2	10 to 15
Group 3	15 to 20
Group 4	20 to 25
Group 5	25 to 30
Group 6	30 to 35
Group 7	larger than 35



(a) – Equilateral Triangle



(b) – Square



(c) – Curved Triangle

Fig. 1 – Imbibition P_c - S_w plots for a single tube of different shapes

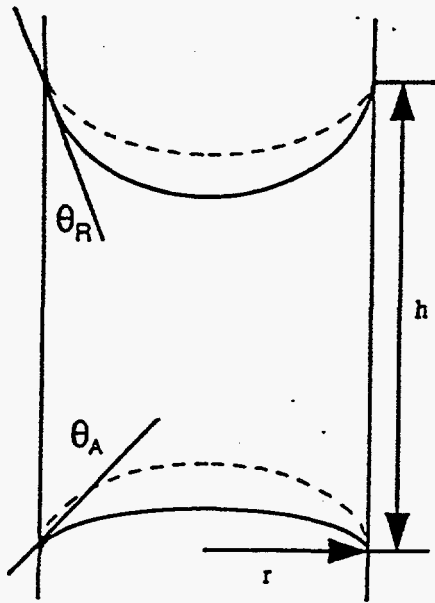


Fig. 2 – Advancing and receding interfaces of a liquid column in a Circular capillary tube

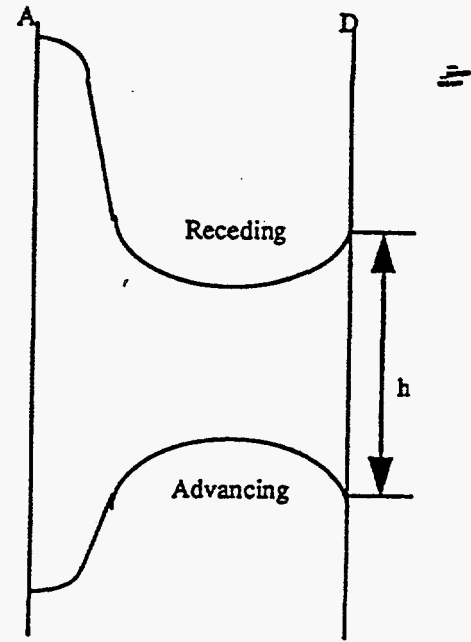
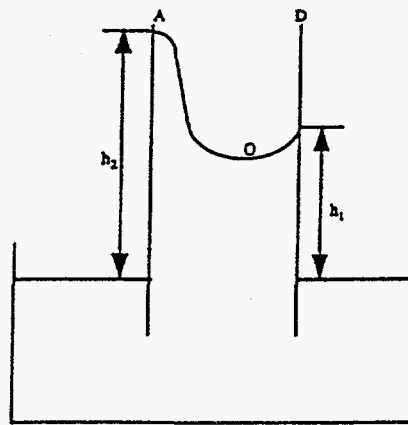
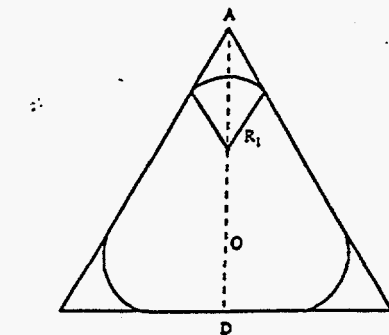


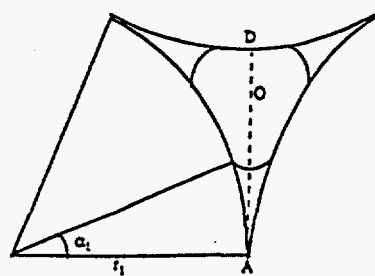
Fig. 4 – Liquid holdup in a triangular or curved triangular tube



(a) Capillary rise in a triangular and curved triangular tube

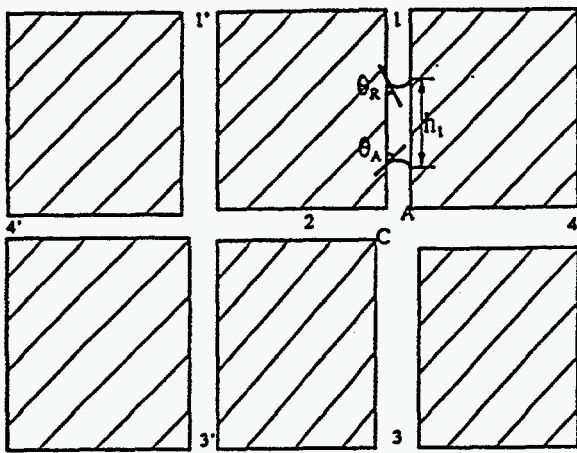


(b) Cross-section of liquid-gas interface in an equilateral triangular tube at $h=h_1$



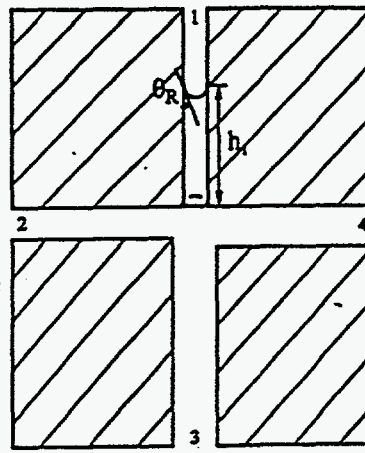
(c) Cross-section of liquid-gas interface in a curved triangular tube at $h=h_1$

Fig. 3 – Capillary rise in triangular and curved triangular tubes



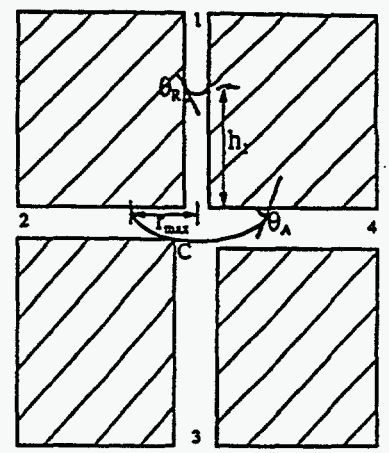
(a)

$$h_1 = \frac{2\sigma}{\rho g r_1} (\cos \theta_R - \cos \theta_A)$$



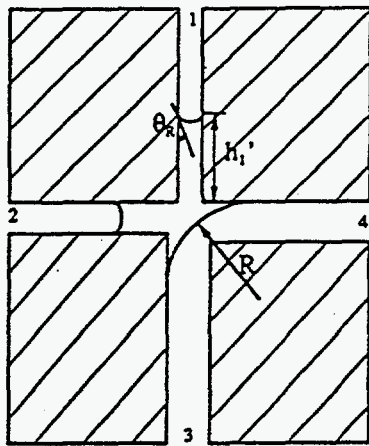
(b)

$$h_1 = \frac{2\sigma}{\rho g r_1} \cos \theta_R$$



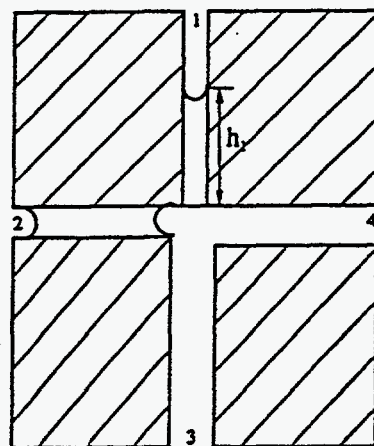
(c)

$$h_1 = \frac{2\sigma}{\rho g r_1} \cos \theta_R$$



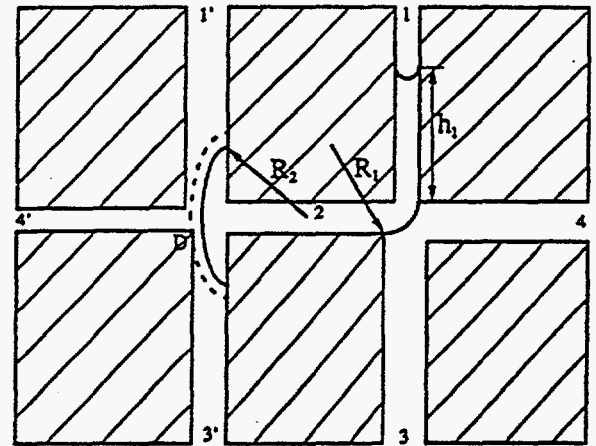
(d)

$$h_1' = \frac{2\sigma}{\rho g} \left(\frac{\cos \theta_R}{r_1} - \frac{\cos \theta_A}{r_2} \right)$$



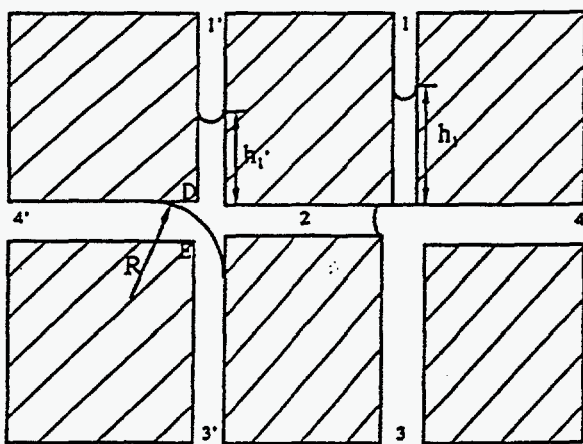
(e)

$$h_1 = \frac{2\sigma}{\rho g r_1} \cos \theta_R$$



(f)

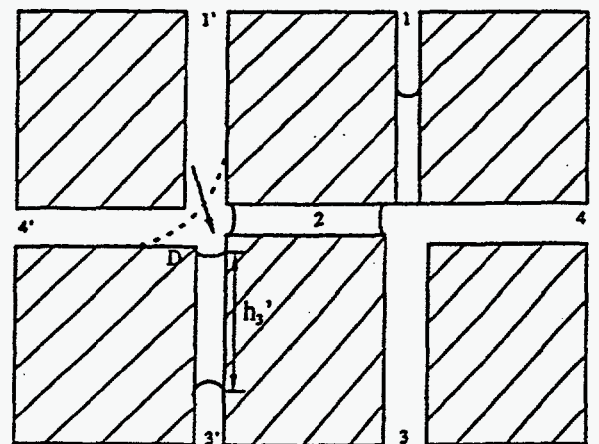
$$h_1 = \frac{2\sigma}{\rho g} \left(\frac{\cos \theta_R}{r_1} + \frac{1}{R_1} \right), R_1 = R_2$$



g(1)

$r_1' < r_2'$

$$h_1 = \frac{2\sigma}{\rho g r_1} \cos \theta_R, h_1' = \frac{2\sigma}{\rho g} \left(\frac{\cos \theta_R}{r_1} - \frac{1}{R} \right)$$

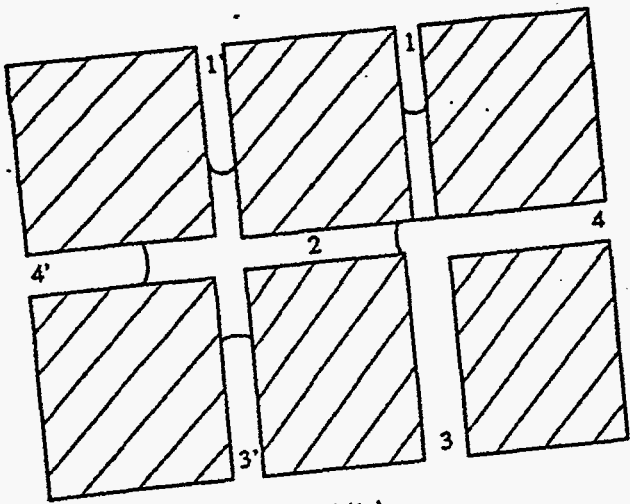


g(2)

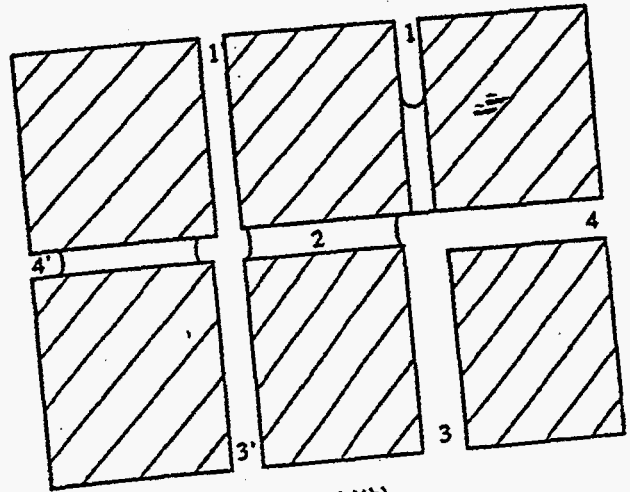
$r_1' > r_2'$

$$h_1 = \frac{2\sigma}{\rho g r_1} \cos \theta_R, h_3' = \frac{2\sigma}{\rho g r_2'} (\cos \theta_R - \cos \theta_A)$$

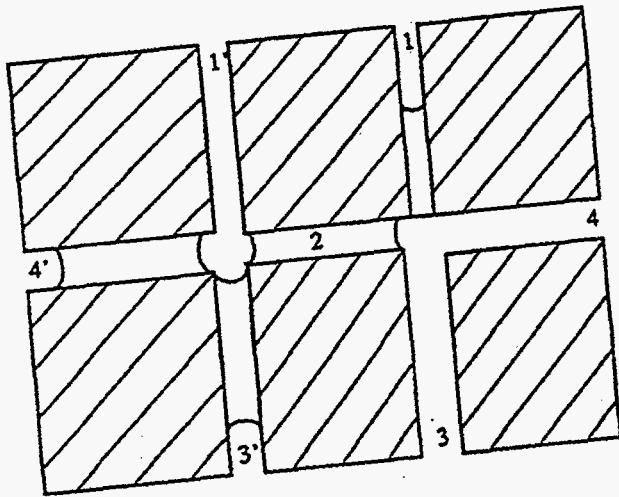
Fig. 5 - Schematics of liquid formation and flow in Intersections



h(1a)
 $r_3' > r_1', r_4' > r_2$



h(1b)
 $r_3' > r_1', r_4' < r_2$



h(1c)
 $r_3' > r_1', r_4' > r_2$

Fig. 5 - (Continued)

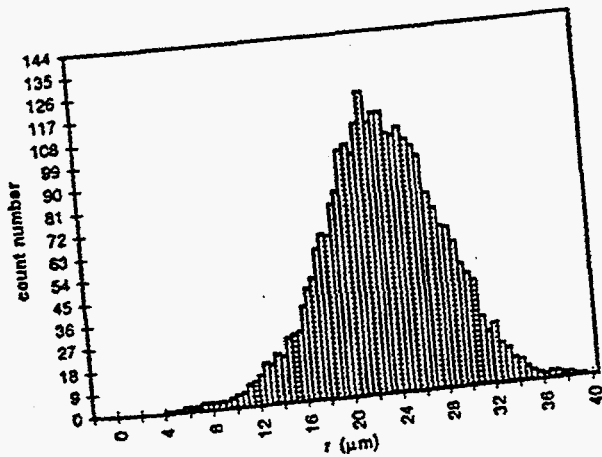


Fig. 6 - Radii's distribution of the network

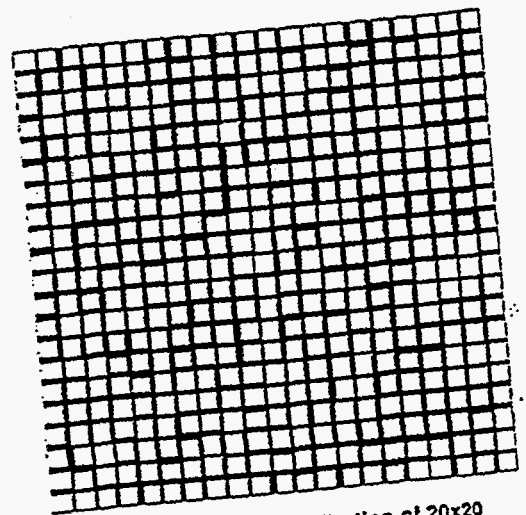
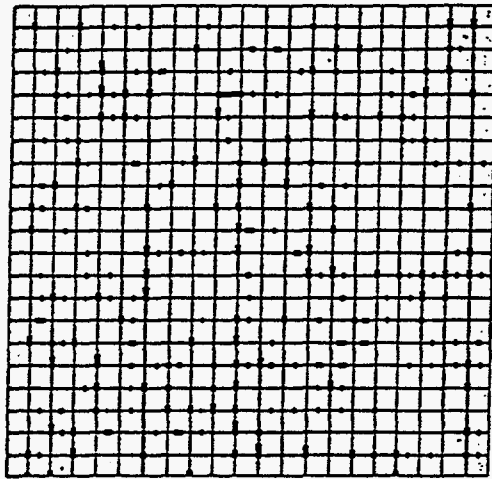
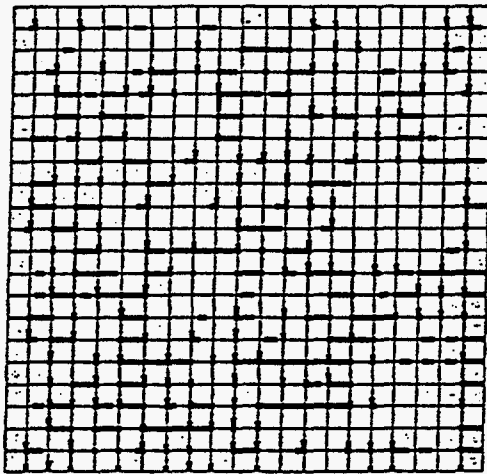


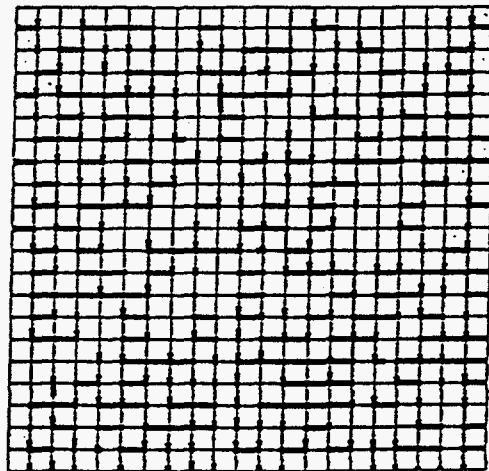
Fig. 7 - Network size distribution of 20x20



(a) $T = 10,000, S_c = 5.62\%$

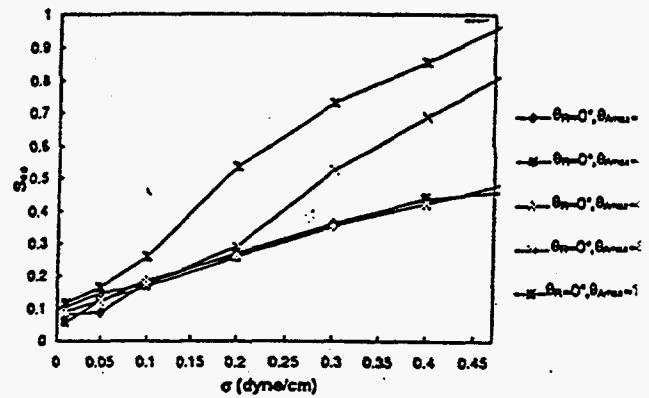


(b) $T = 25,000, S_c = 16.6\%$

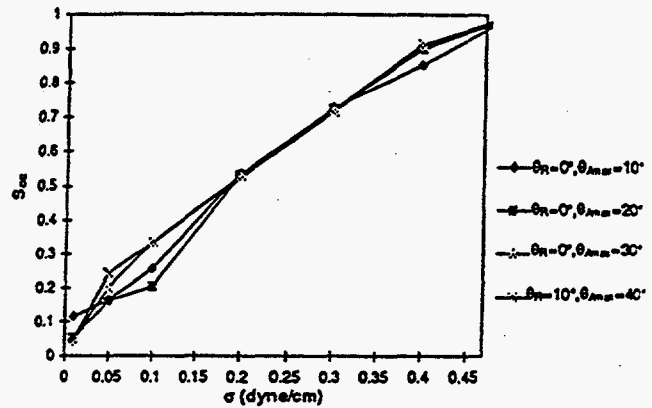


(c) $T = 35,183, S_c = 26.0\%$

Fig. 8 -- Liquid distributions at different stages of condensation
 $\sigma = 0.1 \text{ dyne/cm}, \rho = 0.3 \text{ g/cm}^3, \theta_R = 0^\circ, \theta_A = 10^\circ$



(a) -- Contact angle hysteresis $\leq 10^\circ$



(b) -- Contact angle hysteresis $\geq 10^\circ$

Fig. 9 -- S_{cc} vs. surface tension at different contact angle hysteresis network sizes 20 x 20

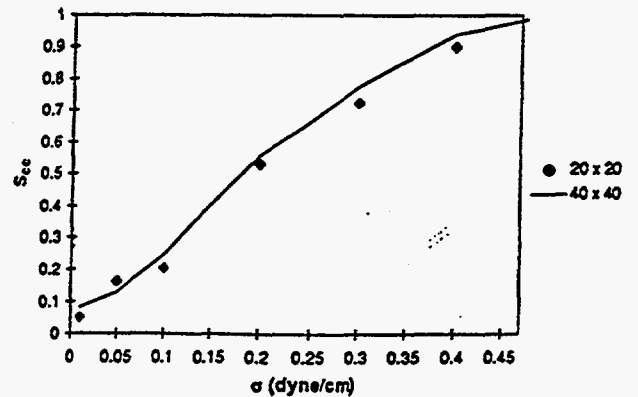


Fig. 10 -- S_{cc} vs. surface tension for two different network sizes

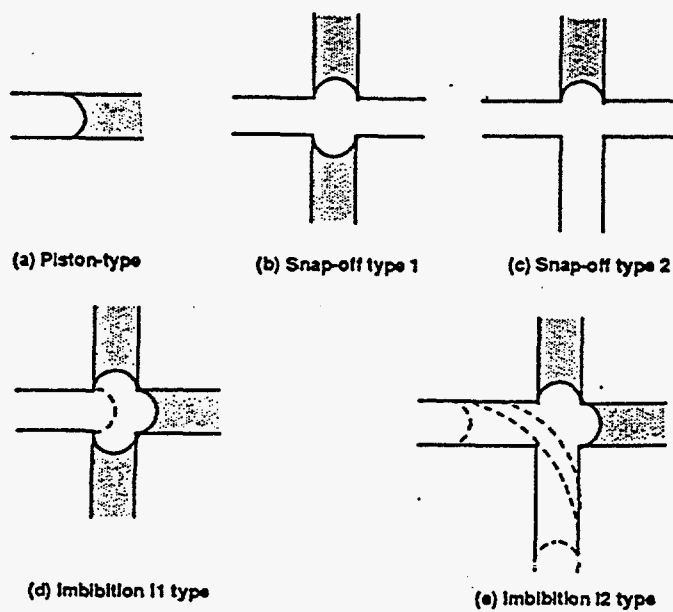


Fig. 11 - Basic mechanism of imbibition (after Lenormand, et al)

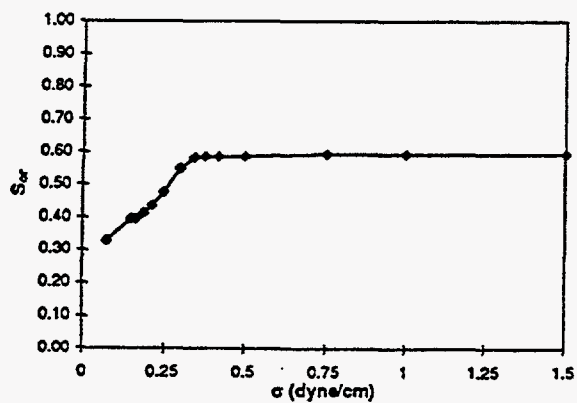


Fig. 12 - S_{or} vs. surface tension

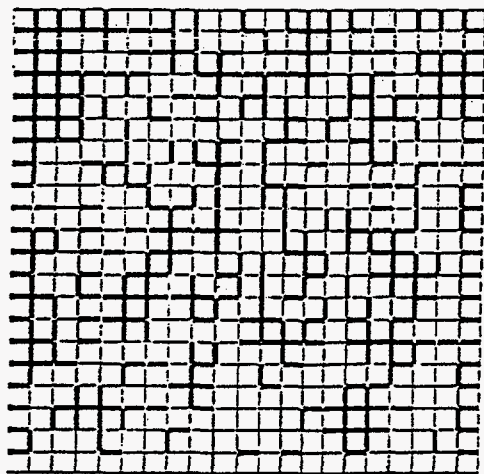


Fig. 13 - Liquid distribution at the end of imbibition